

Multi-scale computer models of lymphatic pumping

A Thesis

By

Christopher James Morris

Imperial College London

Department of Bioengineering

Prince Consort Road

London SW7 2AZ

This thesis is submitted for the degree of Doctor of Philosophy of Imperial College London

2021

ABSTRACT

The lymphatic system maintains fluid homeostasis by returning interstitial fluid to the veins.

Lymphatics pump fluid locally with contracting segments of the vessel (lymphangions) bounded by valves. Contractions are generated by specialized muscle exhibiting phasic and tonic contractions.

Deficient pumping can result in accumulation of interstitial fluid, called lymphoedema.

Lymphoedema treatments have limited effectiveness, partially attributable to a lack of understanding of contractions. A lumped parameter computational model of lymphangion pumping has previously been developed in the group. In this thesis I detail development of two multiscale models of lymphatic pumping to facilitate improved treatments for lymphoedema.

The first model captures subcellular mechanisms of lymphatic muscle contraction. This model is based on the sliding filament model and its smooth muscle adaptation. Contractile elements are combined with passive viscoelastic elements to model a cell. Many arrangements were trialled but only one behaved physiologically. The muscle model was then combined with the lymphangion model for comparison with experiments. This model captures mechanical and energetic aspects of both contraction types. I show that the model provides results similar to published experiments from rat mesenteric lymphatics. The model predicted a peak efficiency of 35%, in the upper range from other muscle types. In the range of frequencies and amplitudes simulated, the direct effect of calcium oscillations can increase lymphangion outflow by up to 40% of the flow in their absence.

The second model aims to improve our understanding of lymphangion interaction in large networks through computational homogenisation. In this model we do not directly simulate all lymphangions but sample lymphangions at evenly spaced intervals to reduce the computational intensity. We show through this model that increased external pressure at the network inlet collapses lymphangions and that this disruption of pumping for a few lymphangions reduces the outflow from the entire network.

CONTENTS

ABSTRACT.....	2
CONTENTS.....	3
ORIGINALITY AND STATEMENT OF CONTRIBUTION	6
COPYRIGHT DECLARATION.....	7
DEDICATION	8
ACKNOWLEDGEMENTS.....	9
LIST OF ABBREVIATIONS	10
LIST OF FIGURES.....	11
LIST OF TABLES.....	14
CHAPTER 1 – LYMPHATICS INTRODUCTION AND BACKGROUND.....	15
1.1. Introduction	15
1.2. Specific aims.....	18
1.3. Background	18
1.3.1. General anatomy and physiology of the lymphatic system.....	18
1.3.2. Pathologies associated with the lymphatic system	21
1.3.3. Lymphatic muscle.....	22
1.3.3.1. Excitation-contraction coupling	25
Chapter 2 – COMPUTATIONAL MODELLING BACKGROUND	29
2.1. Lymphatics	29
2.2. Muscle.....	41
2.3. Thesis structure.....	50
CHAPTER 3 – SUBCELLULAR MODEL OF LYMPHATIC MUSCLE	52
3.1. Introduction	52
3.2. Methods.....	55
3.2.1. Cell model	57
3.2.2. Molecular muscle modelling.....	59
3.2.2.1. Excitation-contraction coupling.....	69
3.2.3. Lumped parameter model of lymphatic pumping.....	74
3.2.3.1 Prescribed contractions	78
3.2.4. Solution method	81
3.3. Parameter Sensitivity Analysis	85
3.3.1. One-at-a-time analysis	86
3.3.2. Latin hypercube sensitivity analysis.....	87
3.4. Results.....	89
3.5. Conclusions and discussion.....	106

CHAPTER 4 – HOMOGENISED MODEL OF LYMPHATIC NETWORKS	115
4.1. Introduction	115
4.2. Methods	118
4.2.1. Microscale	120
4.2.1.1. Unadapted lymphangion RVE	122
4.2.1.2. Compliance RVE	124
4.2.2. Coupling the scales	126
4.2.2.1. Inlet RVE	126
4.2.2.2. Compliance RVE	127
4.2.3. Macroscale solution	129
4.3. Results	134
4.4. Discussion	138
CHAPTER 5 – CONCLUSIONS AND FUTURE WORK	142
5.1. Conclusions	142
5.2. Future work	144
REFERENCES	149
APPENDIX 1 – MUSCLE MODEL	165
Alternate CE arrangements (Original rate functions and values)	165
Parallel CEs	165
Series CEs phasic parallel spring, dashpot	167
Series CEs tonic parallel spring, dashpot	170
Original rate function (Before smoothed transition)	172
Constant detachment for $x > h$ (Before smoothed transition)	173
Smoothed varying g_{1Hux} (constant detachment for $x > h$)	173
Cell viscoelasticity	174
Time step check	176
Periodicity conditions check	177
Results from MacCormack predictor corrector	178
Muscle cell energy balance	179
Displacement discretisation insensitivity	180
One-at-a-time sensitivity analysis results	181
Distribution-moment approximation	182
APPENDIX 2 – PERMISSIONS DOCUMENTS FOR REPRINT	190

ORIGINALITY AND STATEMENT OF CONTRIBUTION

This thesis is my own work and all work previously performed is referenced.

Chapter 1 – This chapter summarises the literature from existing work by other researchers. This chapter is written by Christopher Morris.

Chapter 2 – This chapter also summarises the literature from existing work by other researchers and is written by Christopher Morris.

Chapter 3 – Model developed by Christopher Morris. Results obtained and prepared by Christopher Morris.

Chapter 4 – Homogenisation developed by Lowell Edgar and Christopher Morris. Adaptation of the lumped parameter model to a function taking inflow as well as inlet and outlet pressure boundary conditions from the macroscale and return microscale solution done by Christopher Morris, Lowell Edgar, and James Moore Jr. Results obtained by Christopher Morris.

Chapter 5 – Written by Christopher Morris.

COPYRIGHT DECLARATION

The copyright of this thesis rests with the author and is made available under a Creative Commons Attribution Non-Commercial No Derivatives licence. Researchers are free to copy, distribute or transmit the thesis on the condition that they attribute it, that they do not use it for commercial purposes and that they do not alter, transform or build upon it. For any reuse or redistribution, researchers must make clear to others the licence terms of this work.

DEDICATION

To my parents and brother for all their support and understanding.

ACKNOWLEDGEMENTS

I have had a great deal of support throughout the process of my PhD. I am extremely grateful to my academic supervisor, Professor James Moore Jr for his extensive expertise, and constant support and advice. I am grateful to Dr Lowell Taylor for his efforts in development of the homogenised model. My research greatly benefitted by some very productive work at conferences so I am grateful to the entire lymphatic research network. I would also like to thank Dr Bertram for his discussions during model development and Dr Zawieja for his input on muscle model writing. Finally, I wish to thank everyone in Prof Moore's research group for our group discussions.

LIST OF ABBREVIATIONS

AP – Action potential

ATP – Adenosine triphosphate

CaM – Calmodulin

CE – Contractile element

ECC – Excitation-contraction coupling

LEC – Lymphatic endothelial cell

LMC – Lymphatic muscle cell

NO – Nitric oxide

ODE – Ordinary differential equation

PDE – Partial differential equation

STD – Spontaneous transient depolarisation

TnC – Troponin C

LIST OF FIGURES

Figure 1: Schematic of the lymphatic system in relation to the cardiovascular system	17
Figure 2: Components of the lymphatic vasculature.....	21
Figure 3: Calcium kinetics in LMCs and LECs.....	25
Figure 4: Tracings of diameter and intracellular free calcium concentration in isolated vessels from the rat mesentery	27
Figure 5: Comparison of the axial discretisation showing four cells in each of Reddy's original model and Macdonald's refined model.....	31
Figure 6: Illustration of the geometry in the Rahbar model.....	36
Figure 7: Pressure-diameter tube laws of the Containo and Toro model under passive and peak intrinsic contraction conditions	37
Figure 8: Representative geometry of lymphatic valves	38
Figure 9: Schematic diagram of a lymph node	40
Figure 10: Hill models with contractile elements (CE) along with series and parallel elastic elements (SE and PE, respectively).....	42
Figure 11: Summary diagram for the Huxley-Hai Murphy model.....	46
Figure 12: Schematic of a model for an airway smooth muscle cell	49
Figure 13: Coupling of scales in the muscle model.....	56
Figure 14: Molecular models of phasic and tonic CE myosin states (upper row) and myosin head rates (middle row) and transitions between piecewise rate functions (lowest row).....	65
Figure 15: Figure summarising the energetics in the LMC model	68
Figure 16: Calcium plots (a) fit to the calcium concentration recording of (Zawieja et al., 1999) (b) calcium concentration recording of (Zawieja et al., 1999).....	69
Figure 17: Time-dependent saturations of (A) TnC and (B) calmodulin used in all results with the exception of calcium binding sensitivity.....	71
Figure 18: Plot of the passive tube law of a lymphangion.....	76
Figure 19: Schematic of a lymphangion.....	76
Figure 20: Plot of prescribed time-dependence of intrinsic tension	79
Figure 21: Plot of prescribed diameter-dependence of intrinsic tension.....	80
Figure 22: Plot of the resistance of the valve against the pressure difference across it.....	80
Figure 23: Flowchart of the solution algorithm for the coupled muscle-lymphangion models.....	84
Figure 24: Solution flowchart for the second-order Godunov solver.....	85
Figure 25: Boxplots of the PRCC for each parameter showing the variation between trials	88
Figure 26: Panel of plots summarising results for a single lymphangion contractile cycle under reference conditions	90
Figure 27: Comparing the diameter results of the muscle model at a transmural pressure 1 <i>cmH₂O</i> and no axial pressure difference to experimental data obtained from rat mesenteric lymphatics	91
Figure 28: Comparing the diameter-time shape for lymphangions recorded experimentally to coupled muscle-lymphangion model results	92
Figure 29: Comparison of the results obtained using the coupled muscle-lymphangion model and the prescribed intrinsic contractions model under reference pressure conditions	93
Figure 30: Panel of plots summarising the comparison between the muscle model developed here and the model of Contarino and Toro using the pressure conditions from Test 1 of (Contarino and Toro, 2018).....	94
Figure 31: Sensitivity of the model to phasic rates.....	95
Figure 32: Sensitivity of outflow to variations in the calcium binding properties of TnC.....	96

Figure 33: Panel of plots summarising the effect of increasing the outlet pressure for consistent inlet and external pressures.....	97
Figure 34: Panel of plots comparing the responses of the muscle model and prescribed contraction model responses to increases in adverse pressure	98
Figure 35: Panel of plots summarising the effect of simultaneously increasing inlet and outlet pressure	100
Figure 36: Panel of plots comparing the response of the muscle model and prescribed contractions model to variations in transmural pressure	101
Figure 37: Panel of plots showing the effects of varying both amplitude and frequency of calcium oscillations	103
Figure 38: Panel of plots summarising the results for a series chain of four simultaneously contracting lymphangions	106
Figure 39: Coupling of the macroscale and microscale showing the inlet and outlet pressure boundary conditions prescribed at the macroscale.	121
Figure 40: Schematic of the modified lymphangion pumping model as a microscale RVE.....	125
Figure 41: Plots showing the passive pressure-volume form of the passive tube law and the resultant compliance	125
Figure 42: Diagram of the interaction between macroscale and microscale times	126
Figure 43: Solution algorithm for the compliance RVE.....	129
Figure 44: Solution algorithm for the macroscale homogenisation.	133
Figure 45: Panel of plots comparing the time-dependence of results from the homogenised model and a direct pressure boundary condition lymphangion chain	135
Figure 46: Panel of plots showing the effects of varying external pressure in the homogenised model for a single vessel 25 lymphangions long.....	136
Figure 47: Panel of plots showing the effects of varying the parallel number of vessels at the inlet of the network 25 lymphangions long	137
Figure 48: Panel of plots showing the effects of varying the external pressure for a network 25 lymphangions long converging from 10 parallel vessels at the inlet to a single vessel at the outlet.	138
Figure 49: Diagram of an LMC with CEs in parallel	165
Figure 50: Panel of plots summarising the results for contractile elements in parallel	166
Figure 51: Diagram of an LMC with CEs in series. Phasic contractile elements have a spring and dashpot in parallel	167
Figure 52: Panel of plots summarising results from a dashpot and spring in parallel with phasic CEs	169
Figure 53: Diagram showing an LMC with series connections of CEs. Tonic contractile elements have a spring and dashpot in parallel.....	170
Figure 54: Panel of plots summarising the results for a muscle cell with a spring and dashpot in parallel with tonic contractile elements	171
Figure 55: Panel of plots summarising the effect of varying the phasic attachment and detachment rate constants in the original Huxley rate functions.....	172
Figure 56: Panel of plots summarising the effects of varying g_1 in a modified phasic rate function with constant detachment (g_1) for positive displacements greater than the powerstroke length ...	173
Figure 57: Panel of plots summarising the effects of varying g_1 in a modified phasic rate function with constant detachment (g_1) for positive displacements greater than the powerstroke length ...	174
Figure 58: Panel of plots showing the effects of varying cell viscoelasticity.	176
Figure 59: Panel of plots summarising the effects of halving the time step in simulations under reference conditions.	176

Figure 60: Panel of plots verifying that the periodicity conditions ensure that the results have reached periodicity	177
Figure 61: Panel of plots comparing model results under reference conditions when obtained with the second order Godunov solver and obtained with the MacCormack predictor-corrector	178
Figure 62: Energetics of an LMC model under reference conditions	180
Figure 63: Panel of plots showing that halving the displacement discretization had a negligible effect on the main output parameters of the model.....	181
Figure 64: Comparison of the fully-resolved displacement-distribution of myosin heads with the Gaussian distribution-moment model.....	189

LIST OF TABLES

Table 1: Rate constants used for phasic and tonic myosin head state transitions.....	68
Table 2: Muscle model parameters other than rate function constants.....	72
Table 3: Constants used in the prescribed intrinsic contraction model for comparison to muscle model results	81
Table 4: Overall sensitivity measures for each parameter	88
Table 5: Decreases in average flow with increasing half saturation concentration	96
Table 8: Effects of halving the time step on key model outputs	176
Table 7: Table of results showing the sensitivity measures obtained for each parameter from the one-at-a-time sensitivity analysis. Rows in bold indicate the variables considered sensitive and included in the Latin hypercube analysis.....	181

CHAPTER 1 – LYMPHATICS INTRODUCTION AND BACKGROUND

1.1. Introduction

The lymphatic system plays important roles in several aspects of normal physiologic function, particularly in fluid homeostasis, adaptive immune response, and lipid absorption. The involvement in immune response implicates the lymphatics in cancer, autoimmune diseases and atherosclerosis. Deficient lymphatic pumping can result in accumulation of protein-rich fluid in the interstitium, leading to a chronic debilitating condition called lymphoedema. There is currently no effective treatment to enhance the pumping of lymphatic vessels.

About 4 – 8 L of interstitial fluid enters the lymphatic system per day (Renkin, 1986, Levick and Michel, 2010), referred to as lymph once it has entered the lymphatic vessels. Lymph transport must work against an adverse pressure gradient from low or sub-atmospheric pressures in the interstitium (Jamalian et al., 2017, Aukland and Reed, 1993, Guyton et al., 1971) to central venous pressure at the subclavian veins (Bridenbaugh et al., 2003). Pumping is achieved by a combination of external compression and intrinsic contractions coupled with bi-leaflet valves to promote unidirectional flow towards the centre of the lymphatic tree (Figure 1). It is well established that external compressions arise from many sources including transient skeletal muscle contraction (White et al., 1932, McMaster, 1937, Yoffey and Courtice, 1956), respiration (Browse et al., 1971, Browse et al., 1974, Hall et al., 1965, Yoffey and Courtice, 1956, Schad et al., 1978), intestinal peristalsis (Unthank and Bohlen, 1988), and pulsation of adjacent blood vessels (Parsons and McMaster, 1938, Webb Jr and Starzl, 1953, Browse et al., 1971, Browse et al., 1974, Negrini et al., 2004). Intrinsic contractions arise from specialised muscle cells lining the vessels and are the main mechanism for lymph propulsion in many tissues (Olszewski and Engeset, 1980, von der Weid and Zawieja, 2004). The functional contractile units of the lymphatic vessels are regions bounded by valves, called lymphangions. Lymphatic vessels are formed from chains of lymphangions and a major remaining question is how the microscale lymphangions interact to generate the overall network flow. There is significant variation in the loads and demands on lymphatic vessels between different regions of the network

within an animal (Gashev et al., 2012, Gashev et al., 2004) and between species. Lymphatic pumping experiments are often performed using vessels from the rat mesentery because access is easy and these vessels are among the most intrinsically active (Gashev et al., 2004). Mouse lymphatics are not used much because they exhibit little contractility for reasons that are not known, but it is possibly due to the smaller size of mice compared to rats. A significant difference between the rat and human lymphatics is that the human lymphatics when standing must contend with gravity.

The specialised muscle lining lymphatic vessels exhibits properties of both cardiac and smooth muscles. This muscle is often referred to as lymphatic smooth muscle, but this can be misleading because of its hybrid nature. In this thesis it is referred to as lymphatic muscle. The demand for lymphatic muscle's hybrid nature is due to the lack of a central pump equivalent to the heart.

Lymphatic muscle must then both generate (cardiac muscle-like, phasic contractions) and regulate (vascular smooth muscle-like, tonic contractions) lymph flow (Quick et al., 2007, Bridenbaugh et al., 2003, von der Weid and Zawieja, 2004). The lack of effective treatment for lymphoedema can be attributed in part to a lack of understanding of lymphatic muscle (Scallan et al., 2016, Zhang et al., 2013).

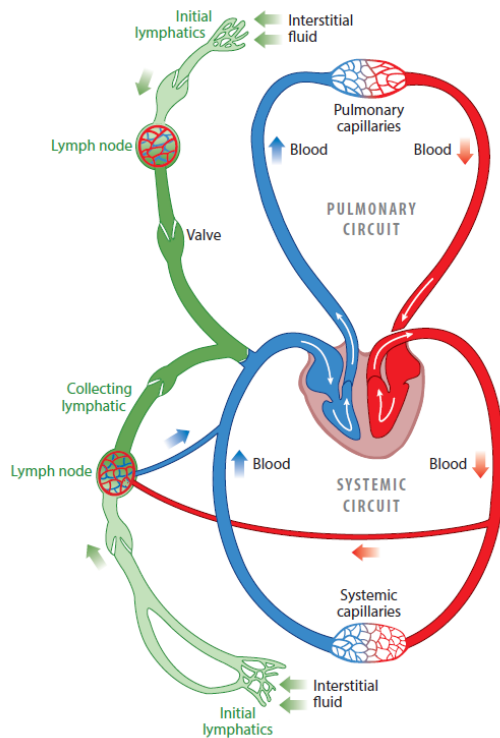


Figure 1: Schematic of the lymphatic system in relation to the cardiovascular system. Arrows indicate the direction of flow. (Moore Jr. and Bertram, 2018) Copyright permissions included in Appendix 2

In vivo experiments of lymphatic vessels allow visual observation of diameter and flow rate but there is little control over the pumping conditions and measuring pressure is prohibitively difficult. *In vitro* experiments of cannulated lymphangion chains allow better control of pressure conditions but is difficult because of their small diameter, particularly for determining flow rate. The difficulties with experimental studies motivated development of an ordinary differential equation (ODE)-based lumped parameter lymphangion model that has now been thoroughly validated (Bertram et al., 2011, Bertram et al., 2014a, Bertram et al., 2014b, Bertram et al., 2016b, Bertram et al., 2017, Jamalian et al., 2013, Jamalian et al., 2016, Jamalian et al., 2017). In a parameter sensitivity analysis minimum valve resistance, contraction frequency, lymphangion length, transmural pressure, active tension, and series number of lymphangions in a chain were identified as major determinants of lymphatic pumping. It is also impractical to cannulate large networks of lymphatic vessels. There is great difficulty directly studying lymphatic muscle because isolated lymphatic muscle loses its contractile phenotype.

1.2. Specific aims

This thesis covers the development of two computational models to improve our understanding of lymphatic muscle and large vessel networks by expanding on an existing lymphangion model.

1. **Develop a computational model for the subcellular mechanisms of lymphatic muscle**

contraction (Chapter 3). We combined molecular models of striated and smooth muscles in a structural arrangement to model lymphatic muscle cells (LMCs). This allows separation of the subcellular mechanisms involved in both types of contraction from lymphatic muscle, giving mechanical and energetic properties. We coupled this with an existing model of the lymphangion to understand how these subcellular mechanisms influence fluid transport.

2. **Develop a homogenised model of lymphatic networks (Chapter 4).** We developed on an existing lymphangion model to study the interaction of lymphangions in a large network. We then used the model to study the effect of spatial variations in steady external pressure on the pumping of large networks of lymphangions.

1.3. Background

1.3.1. General anatomy and physiology of the lymphatic system

The vasculature of the lymphatic system forms a converging tree which runs in parallel with the blood vasculature. Almost all tissues in the body have lymphatic drainage, including recently discovered presence in the central nervous system (Aspelund et al., 2015, Louveau et al., 2015) and eye (Schroedl et al., 2014, Aspelund et al., 2014).

Interstitial fluid is taken up by the smallest vessels of the lymphatic system (Figure 2). These vessels are typically called initial lymphatics, terminal lymphatics, or lymphatic capillaries in the literature. Throughout this thesis the term initial lymphatics will be used. Initial lymphatics are blind-ended vessels made of a single layer of endothelial cells (LECs) with a discontinuous basement membrane (Lutter et al., 2012, Paupert et al., 2011). Interstitial fluid, macromolecules and lymphocytes enter the initial lymphatics via button-like junctions formed of overlapping LECs (primary valves) (Trzewik et al., 2001).

The LECs of the initial lymphatics are attached to the surrounding tissue by anchoring filaments (Leak and Burke, 1968, Solito et al., 1997). Anchoring filaments prevent the initial lymphatics from collapsing and open the primary valves by transmitting forces from the surrounding tissue (Paupert et al., 2011, Heppell, 2013). Initial lymphatics do not have a muscle lining and rely on external forces for fluid flow. The diameter of initial lymphatics varies greatly between tissue beds and with species. Initial lymphatics from the rat mesentery have diameters in the range of 25 – 50 μm (Zweifach and Prather, 1975).

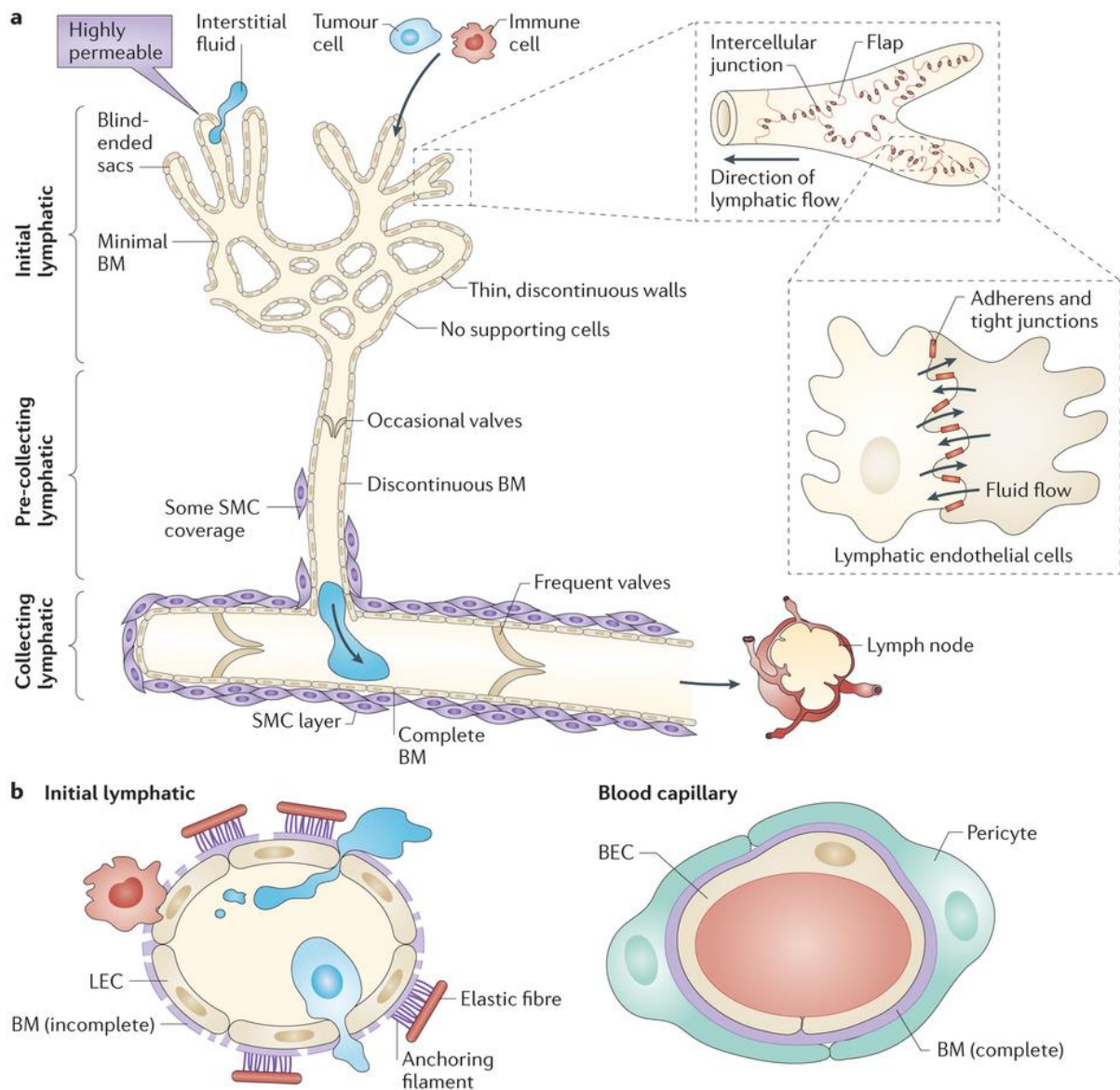
In some tissues such as the skin, initial lymphatics combine to form larger vessels called pre-collectors (Figure 2) which include occasional intraluminal bi-leaflet (secondary) valves (Schmid-Schönbein, 1990). There is some disagreement on the definition of pre-collectors, with some researchers considering them to have no muscle whilst others consider them to have few LMCs (Lutter et al., 2012).

Downstream from pre-collectors, lymphatic vessels are surrounded by multiple layers of LMCs (Figure 2) and have consistently present secondary valves (inter-valve spacing of approximately 600 – 1000 μm in the rat mesentery (Dixon, 2006)). Secondary valves are bi-leaflet and prevent retrograde flow along the lymphatics, as opposed to the primary valves which prevent flow out of the initial lymphatics. Secondary valves have a transmural pressure-dependent bias to the open position and complex dynamics (Wilson et al., 2015, Watson et al., 2017, Bertram et al., 2017). These vessels are called collecting vessels and are composed of chains of lymphangions. Collecting vessels therefore have an interaction between intrinsic contractions from the muscle cells and external compressions by surrounding tissue as mentioned in Section 1.1. The wall structure of collecting lymphatic vessels is like that of blood vessels with a tunica intima, tunica media, and tunica adventitia. In both blood and lymphatic vessels, the intimal layer is formed of endothelial cells, though these endothelial cells differ. The tunica media includes a single layer or several layers of LMCs interspersed with collagen and elastin fibres (Boggon and Palfrey, 1973, Yoffey and Courtice,

1970, Ohhashi et al., 1980). In lymphatic vessels, the adventitial layer contains fibroblasts, connective tissue elements and axons. Progressing centrally through the lymphatic network, the collecting vessels contain more muscle with a more circumferential orientation (von der Weid, 2019) to allow the larger vessels to contract and pump the greater quantities of lymph from the convergence of smaller vessels. In rat mesenteric lymphatic collecting vessels, the average pitch of LMCs is 6° from the circumferential direction (Zhang et al., 2007b, Zhang et al., 2013), resulting in 99% of force being transmitted circumferentially (Walmsley et al., 1982). The reason for this exact pitch value is unknown, but it is close to circumferential so that the main effects of contraction are reduction of diameter and propulsion of lymph. Collecting vessels from the rat mesentery have diameters in the range 80 – 200 μm . LECs in the collecting lymphatics are connected much more tightly than in the initial lymphatics by zipper-like junctions.

At multiple positions throughout the vascular tree there are kidney-shaped or spherical organs called lymph nodes (LNs). Rat mesenteric LNs have diameters on the order of 1 mm (Ohtani et al., 2003). There is a high concentration of immune cells in LNs, and they are where the adaptive immune response is stimulated by sampling of the antigen profile of lymph. Fluid transfer between the lymphatic and blood vascular systems occurs in LNs. Biologists have so far focused their fluid transfer research on specialised blood vessels called high endothelial venules where immune cells preferentially transmigrate. The fluid transfer results in a lower volume of lymph with higher protein concentrations leaving the LN than entering.

The vessels downstream of LNs combine to form the lymphatic ducts, the largest vessels of the lymphatic system. The right lymph duct drains the right upper quadrant (right side of the head, neck, right side of the thorax, and the right arm) and returns lymph to the blood at the right internal jugular and right subclavian veins. The thoracic duct drains the rest of the body and returns lymph to the blood at the left subclavian vein.



Nature Reviews | Cancer

Figure 2: Components of the lymphatic vasculature. (a) Progression of the lymph from uptake in the initial lymphatics, through pre-collectors and into the collecting vessels. (b) Comparison of the LECs from initial lymphatics and blood capillaries, including the attachment of anchoring filaments to initial lymphatics. (Stacker et al., 2014) Copyright permissions included in Appendix 2

1.3.2. Pathologies associated with the lymphatic system

Insufficient lymph transport can result in chronic tissue swelling from the accumulation of fluid and proteins in the interstitium, called lymphoedema. Lymphoedema can be classified as either primary (genetic) or secondary (acquired). Genes with associated mutations causing primary lymphoedema include PROX1, GATA2, FOXC2, and VEGFR3/FLT4 and can cause defects in vessel development, valve development, muscle recruitment and intercell electrical signal propagation (Brice et al., 2005, Mellor et al., 2011, Ferrell et al., 2010). Genetic mutations can also lead to an increased risk of

developing secondary lymphoedema (Finegold et al., 2012). Primary lymphoedema is less common than secondary lymphoedema. The overall population prevalence of lymphoedema has been estimated in the range of 1.3 – 1.4 per 1000, but estimates vary widely and are likely often underestimates (Rockson and Kahealani, 2008). The leading cause of secondary lymphoedema in the world is filariasis, caused by a parasitic worm (Rockson and Kahealani, 2008). Approximately 120 million people are infected with parasitic worms (Pfarr et al., 2009) and 1.3 billion people are at risk (WHO, 2008). In developed countries the leading cause is iatrogenic, particularly from surgical or radiation-based interventions for breast cancer (approximately 20% of breast cancer survivors develop lymphoedema (Bar Ad et al., 2010, Gillespie et al., 2018, DiSipio et al., 2013). The stasis of interstitial fluid in lymphoedema means that there is an accumulation of inflammatory signals and lowered macrophage infiltration, causing fibrosis and intense remodelling (Zampell et al., 2012, Zampell et al., 2011). In lymphoedema there is also impaired adaptive immune response, causing patients to be more susceptible to infections (Angeli et al., 2004, Karpanen and Alitalo, 2008). Studies of collecting lymphatic vessels in oedema showed enlarged vessels with inhibited contractions and higher diastolic pressure (Olszewski, 2002).

The other functions (besides maintaining fluid homeostasis) of the lymphatic system implicate it in many other diseases including cancer metastasis, autoimmune diseases, and metabolic disorders (Padera et al., 2016). A key factor in cancer metastasis via the lymphatics is the ability of primary valves to uptake cells and the lymphatics were widely considered passive routes of metastasis until recent research showed active involvement via chemokine gradients (Shields et al., 2007, Das and Skobe, 2008, Ben-Baruch, 2008, Podgrabinska and Skoba, 2014) and lymphangiogenesis (Podgrabinska and Skoba, 2014, Skobe et al., 2001, Stacker et al., 2001). Metastatic cancer tumours are commonly found in lymph nodes and have become an important tool for diagnosis and staging.

1.3.3. Lymphatic muscle

Lymphatic muscle adapts so that lymphangions act more like mini hearts or resistance vessels depending on the local lymphodynamic environment (Gashev et al., 2004, Gashev et al., 2012).

Lymphatic pumping can be divided into periods of systole and diastole (Benoit et al., 1989, Li et al., 1998, Scallan et al., 2012, Scallan et al., 2016) so indexes of lymphatic phasic pumping are often calculated using a cardiac pump analogy (particularly ejection fraction and stroke work) (Scallan et al., 2012, Scallan et al., 2016, Benoit et al., 1989).

The two contraction types exhibited by lymphatic muscle have been related to the isoforms of contractile proteins present, particularly the presence of striated (slow twitch β) and phasic smooth (SM1B and SM2B) myosin heavy chain isoforms (Muthuchamy et al., 2003). In the same paper, it was observed that the thoracic duct includes the tonic smooth (SM1A and SM2A) and phasic smooth (SM1B and SM2B) heavy chain isoforms. This reflects the different demands on the lymphatic vessels in different locations. The hybrid nature of lymphatic muscle results in distinct force-velocity (Zhang et al., 2013) and length-tension relationships (Zhang et al., 2007a, Zhang et al., 2007b). The maximum shortening velocity of lymphatic muscle (different for isotonic and isobaric conditions) is between that of cardiac and smooth muscles (Zhang et al., 2013).

Many factors including physical (e.g. stretch, shear, preload, afterload) (Scallan et al., 2012, Scallan et al., 2013, Davis et al., 2012, Davis et al., 2009b, Gashev, 2010, Gashev, 2008, Gashev, 2002), chemical (e.g. inflammatory mediators, endothelium-released mediators) (von der Weid, 2001, Bohlen et al., 2009, Bohlen et al., 2011, Nizamutdinova et al., 2014), and neural (reviewed in (Zawieja et al., 2011)) regulate lymphatic muscle contractions. Preload and afterload regulation of lymphatic muscle phasic contractions resemble cardiac muscle (Scallan et al., 2012, Scallan et al., 2016). Increasing preload increases phasic contraction strength (Frank-Starling effect) (Scallan et al., 2016, Scallan et al., 2012, Shirasawa and Benoit, 2003). Preload also increases the frequency of phasic contractions (Bainbridge effect) (Scallan et al., 2016, Scallan et al., 2012, Shirasawa and Benoit, 2003). Afterload increases phasic contraction strength (Anrep effect) (Davis et al., 2012, Scallan et al., 2012, Scallan et al., 2016). Afterload also causes a myogenic constriction of lymphatic vessels as observed in arterioles (Scallan et al., 2013, Davis et al., 2009a, Mizuno et al., 1997, von der

Weid, 2013). Preload and afterload are coupled between adjacent lymphangions, afterload of the upstream lymphangion forming preload of the downstream lymphangion(s).

Shear regulation of lymphatic muscle affects tonic contractions through the same signalling pathway as blood vessels (see Figure 2). Shear stress stimulates the production of nitric oxide (NO) by LECs, causing dilation (Gasheva et al., 2006, Bohlen et al., 2011, Munn, 2015, Bohlen et al., 2009, Wilson et al., 2013). Histamine also causes dilation of lymphatic vessels in response to increased shear stress (Nizamutdinova et al., 2017, Nizamutdinova et al., 2014, Munn, 2015). Shear also inhibits phasic contractions because the nitric oxide signalling cascade affects the calcium concentration, resulting in the lymphatics acting more as a passive conduit. Shear inhibition can be considered beneficial for two reasons: (1) when there is a pressure gradient driving flow the phasic intrinsic contractions are unnecessary, wasting energy, and (2) contractions of either type reduce diameter, causing higher resistance to and inhibiting flow (Quick et al., 2007, Gashev, 2008).

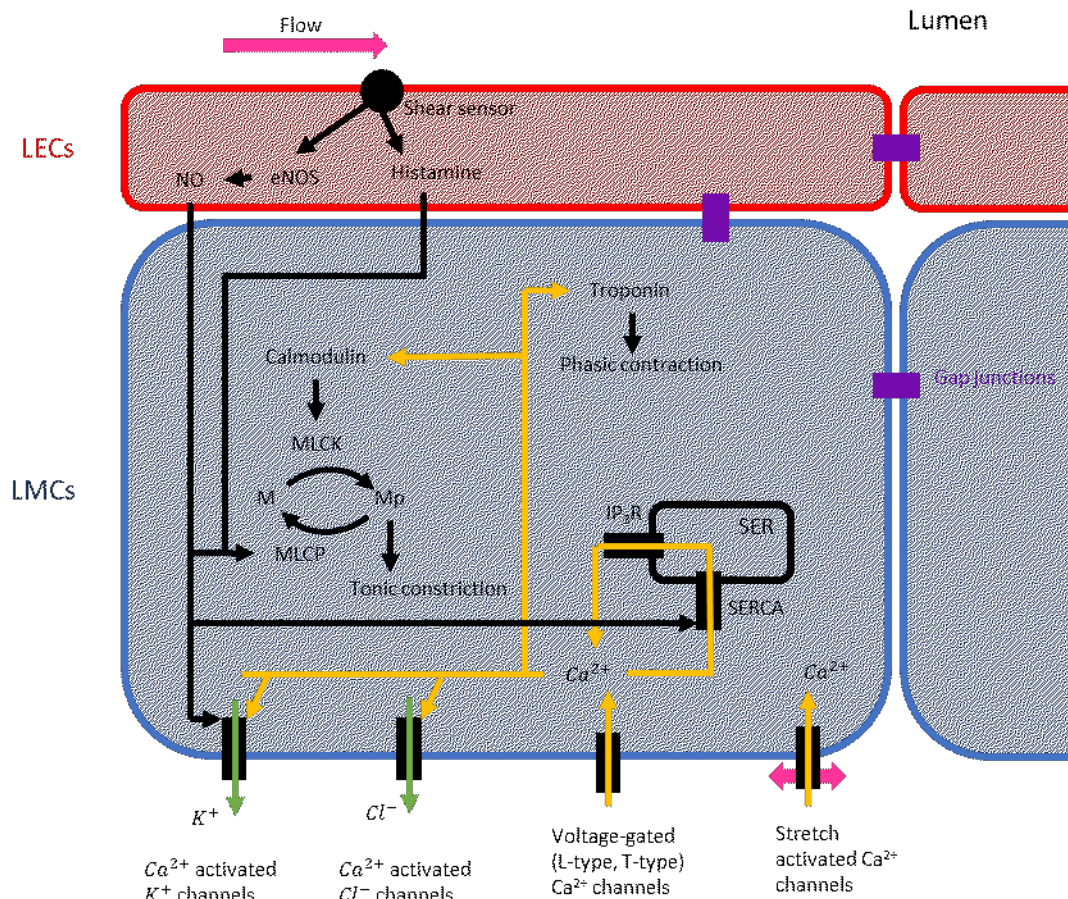


Figure 3: Calcium kinetics in LMCs and LECs. Calcium enters LMC cytosol through ion channels (voltage-gated and stretch activated) in the cell membrane or smooth endoplasmic reticulum (SER; ion channel SERCA – sarco endoplasmic reticulum calcium ion ATPase). Calcium binds to myosin light chain kinase (MLCK) to allow phosphorylation of myosin heads and tonic constriction, or troponin to generate phasic contractions. Calcium-activated chloride channels enhance the depolarisation of spontaneous transient depolarisations. LECs release relaxing factors in response to fluid shear. LECs are connected to each other and to adjacent LMCs by gap junctions. LMCs are also connected to each other by gap junctions. Pink arrows indicate physical input (shear, stretch), orange arrows indicate calcium ion movements, green arrows indicate movement of other ions. Adapted from (Munn, 2015) Copyright permissions included in Appendix 2

Many vasoactive substances in addition to nitric oxide and histamine have been shown to affect lymphatic muscle contraction (Hashimoto et al., 1994, Ohhashi et al., 1978, Takahashi et al., 1990).

The response of lymphatics to inflammatory mediators is of interest in understanding how they respond to oedema (von der Weid and Muthuchamy, 2010, von der Weid, 2001).

1.3.3.1. Excitation-contraction coupling

The excitation of lymphatic muscle results from changes in membrane voltage called spontaneous transient depolarizations (STDs) arising at pacemaker sites within the muscle layer (Zawieja et al., 1999, von der Weid and Zawieja, 2004, von der Weid, 2001). STDs of the membrane voltage result primarily from a release of calcium by intracellular stores activating calcium-dependent chloride channels for an outwards Cl^- current (Toland et al., 2000) (experiments performed on sheep

mesenteric lymphatics). STDs sum to depolarise the cell sufficiently for voltage-dependent calcium channels to be activated and generate action potentials (APs) (von der Weid et al., 2014) and after a single or group of APs, lymphatic vessels contract phasically (Azuma et al., 1977, Kirkpatrick and McHale, 1977, Allen et al., 1983, Ward et al., 1991). The calcium channels involved in lymphatic muscle APs again reflect its hybrid nature. Lymphatic muscle contains L-type (long-lasting) Ca^{2+} channels characteristic of smooth muscle and T-type Ca^{2+} channels which have been implicated as possible pacemaking components in cardiac muscle (Lee et al., 2014). It is likely that APs arise in LMCs, but possible that they are generated by interstitial cells in the muscle layer (McCloskey et al., 1999, Sanders and Ward, 2008, Briggs Boedtkjer et al., 2013). STDs are likely to be of myogenic origin because they still occur in the presence of the nervous inhibitor tetrodotoxin (McHale et al., 1980, van Helden, 1993) or after the endothelium is removed (Hanley et al., 1992, van Helden, 1993). Another potential cause of increased intracellular calcium is the suspected presence of stretch-activated calcium channels in LMCs (Munn, 2015) (see Figure 3). The frequency of STDs also increases with stretch (von der Weid et al., 2014), making it more likely that they will sum to generate APs and increasing the frequency of phasic contractions.

The calcium concentration and diameter within lymphatic vessels from the rat mesentery were simultaneously recorded by Zawieja and colleagues (Zawieja et al., 1999). Their recordings (Figure 4) show an AP prior to diameter constriction and fluctuations in the calcium concentration during the rest of the contractile cycle.

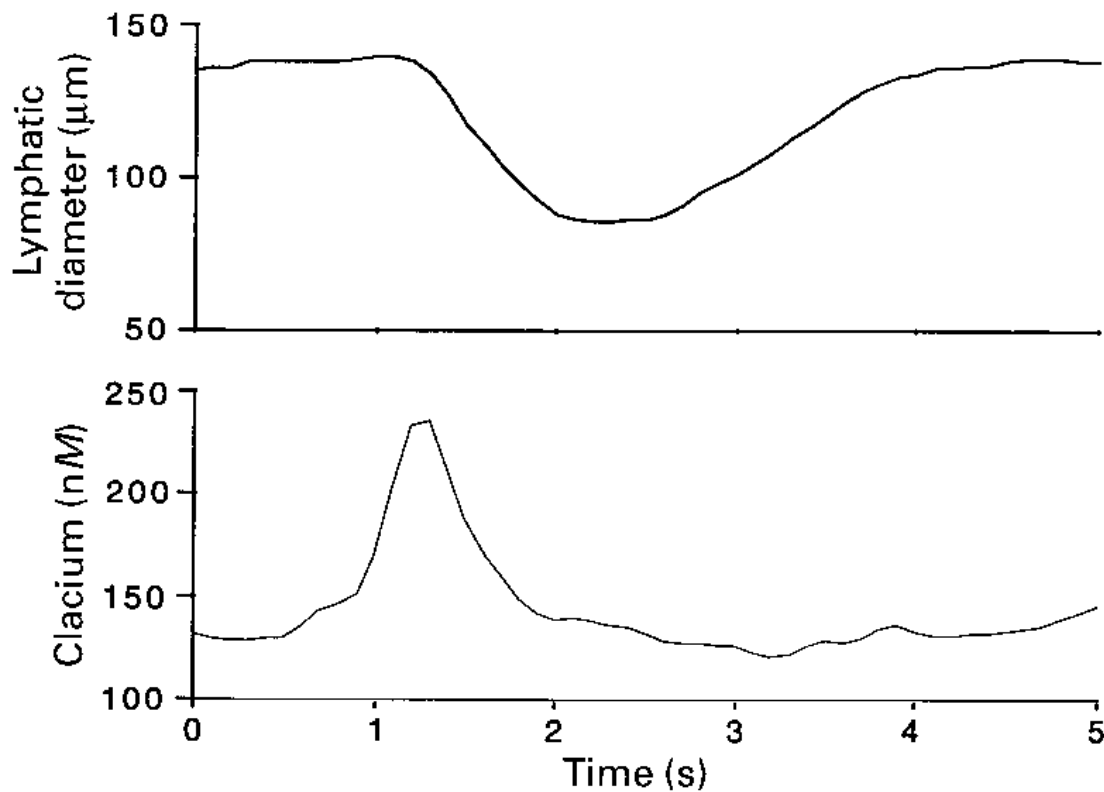


Figure 4: Tracings of diameter and intracellular free calcium concentration in isolated vessels from the rat mesentery. (Zawieja et al., 1999) Copyright permissions included in Appendix 2

Contractions of rat mesenteric lymphatics occur at a rate of approximately 8 – 12 per minute (contractile cycle duration of 5.0 – 7.5 s) and systole lasts for 0.5 – 0.7 s (Benoit et al., 1989) (see also Figure 4). APs propagate along the lymphangion in either direction (Scallan et al., 2016). There is some electrical decoupling between lymphangions, possibly due to the reduced density of LMCs around valve sinuses (Hald et al., 2018, van Helden, 1993).

For excitation-contraction coupling (ECC) in striated muscle, calcium binding to troponin C (TnC) causes a conformation change of the troponin-tropomyosin complex, exposing actin binding sites. There are two isoforms of TnC: one found in fast skeletal muscle and one found in both slow skeletal and cardiac muscles (Wilkinson, 1980, Lu et al., 2011). There is preliminary evidence for the presence of slow/cardiac TnC in lymphatic muscle (unpublished observation of M. Muthuchamy). Striated α -tropomyosin has also been observed in lymphatic muscle (Zhang et al., 2013).

It is generally accepted that the primary means of ECC for smooth muscle is calcium binding to calmodulin (CaM). Calcium-bound CaM activates myosin light chain kinase (MLCK) to phosphorylate

myosin heads, allowing binding to actin sites and contraction. Tonic contraction of lymphatic muscle appears to be MLCK dependent (Wang et al., 2009, Dougherty et al., 2014) and CaM has been observed in lymphatic muscle (Dougherty et al., 2008). Phosphorylation of myosin light chain 20 leads primarily to a modulation of tonic contraction of mesenteric lymphatics (Wang et al., 2009). Smooth muscle force generation is regulated by the ratio of activity between MLCK and myosin light chain phosphatase (MLCP), representative of the phosphorylation level of myosin. Smooth muscle, like striated muscle, contains tropomyosin but lacks the troponin complex, instead having calponin and caldesmon (Seow, 2016). Caldesmon has been observed in lymphatic muscle (Dougherty et al., 2014). The role of calponin is undetermined, but it has been shown that caldesmon may operate similarly to troponin I (Smith, 1985, Marston and Redwood, 1993) with the inhibition again being affected by the calcium saturation of CaM (Word et al., 1994). Previous models of smooth muscles with ECC have ignored caldesmon (Maggio et al., 2012, Laforêt et al., 2011).

There have also been several studies that describe calcium-independent mechanisms modulating the level of myosin light chain phosphorylation (Somlyo and Somlyo, 1994, Pfitzer, 2001).

Additionally, MLCK phosphorylation by Ca^{2+} /CaM-dependent protein kinase II increases its sensitivity to Ca^{2+} (greater calcium concentration required for the same saturation level) (Word et al., 1994).

The electrical signals in lymphatic muscle propagate between LMCs via gap junctions (von der Weid, 2001, Hald et al., 2018, Castorena-Gonzalez et al., 2018) (see Figure 3). An important distinction between arterioles and lymphatics is that there is weak electrical coupling between the LECs and LMCs in (von der Weid et al., 1996, Crowe et al., 1997, von der Weid and van Helden, 1997). This means that there is limited drainage of electrical signal to the LECs which act as an electrical sink (Scallan et al., 2016). APs thus propagate more rapidly along the lymphatic muscle layer (Scallan et al., 2016).

Chapter 2 – COMPUTATIONAL MODELLING BACKGROUND

2.1. Lymphatics

This thesis is focussed on the computational modelling of collecting lymphatics, so in this section I focus on a review of existing models of these vessels whilst mentioning some models of other lymphatic system components.

The first computer model of lymphatic vessel networks was developed by Reddy (Reddy, 1974, Reddy et al., 1977, Reddy, 1980). This was an ambitious model that attempted to simulate the major contractile lymphatic vessels of the human body through reduction of the Navier-Stokes equations. Only the main vessel from each organ is included and second generation or smaller vessels are assumed to be lumped into the main vessel as additional compartments. Vessels draining into the right thoracic duct are not included. Reddy assumed one-dimensional Poiseuille flow through a series of lymphangions with each lymphangion modelled as a single computational element (lumped parameter with one pressure p and one radius a value, computational elements indexed by i). This resulted in the following mass and momentum conservation equations (equations 1 and 2, respectively). Note that this model aimed to represent large networks in humans so included gravitational effects neglected in many lymphatic models based on the rat mesentery.

$$\frac{da_i}{dt} = \frac{1}{2\pi a_i l_i} (Q_{i-1} - Q_i) \quad (1)$$

where Q_i is the flow from lymphangion i to $i + 1$, l is the length of the lymphangion, t is time

$$\frac{dQ_i}{dt} = \frac{\pi(a_i^2 + a_{i+1}^2)}{(l_i + l_{i+1})\rho} (p_i + \rho g z_i - p_{i+1} - \rho g z_{i+1}) - \frac{4\mu}{\rho} \left(\frac{1}{a_i^2} + \frac{1}{a_{i+1}^2} \right) Q_i - \frac{Rv_i}{\rho} \quad (2)$$

where ρ is lymph density, g is gravitational acceleration, z is height, μ is lymph viscosity, Rv is the valve resistance

Valves were included as a constant resistance to forward flow when open and a condition that flow is never negative (there is no backflow). Valve resistance (equation 3) in the lymphatic system varies

with the size of the vessel, here represented through the resting radius (r_0). Intrinsic contractions were incorporated through prescription of a time-dependent stress (σ_{act}) represented by a half-sine with a refractory period and summed with hoop stress (σ_{hoop}) and external pressure (p_{ext}) to give the internal pressure (p) in equation 4.

$$Rv_i = 120\pi r_{0i}^2 \quad (3)$$

$$p_i = p_{ext,i} + \frac{h_i}{a_i} (\sigma_{hoop,i} + \sigma_{act,i}) \quad (4)$$

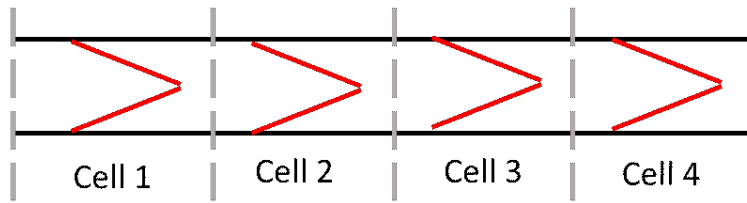
where h is the thickness of the lymphangion wall

More recently, Reddy's model has been updated to include damping and tension coefficients (γ and T , respectively), and changing from a thin wall to a thick wall model for a more accurate wall-force balance by incorporating variations in thickness of the lymphangion wall (Macdonald, 2008, Macdonald et al., 2008). In this study, the computer model was developed simultaneously with cannulation experiments on excised lymphatics from the rat mesentery to characterise passive wall mechanics and validate the model results. The tension coefficient was included to model axial bending of the lymphangion. The second term on the right-hand side of equation 5 is the thick wall model for passive forces, the third term is damping and the fourth is the tension term.

$$p = p_{ext} + E\Delta a_{out}^2 \frac{a_{out}^2 - a_{in}^2}{2(1-\sigma^2)a_{in}^2 a_{out}} + 2\pi a\gamma \frac{\partial a}{\partial t} - 2\pi aT \frac{\partial^2 a}{\partial x^2} \quad (5)$$

where E is the Young's modulus, a_{out} is the outer radius, a_{in} is the inner radius, σ is Poisson's ratio, γ is a damping coefficient, T is a tension term, x is axial distance

Reddy model



Macdonald model

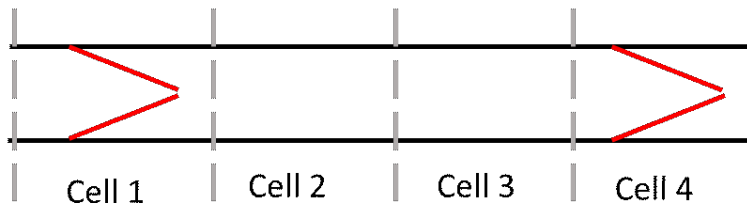


Figure 5: Comparison of the axial discretisation showing four cells in each of Reddy's original model and Macdonald's refined model. Valves are shown in red and cell boundaries are marked by grey dashed lines.

Inclusion of the damping coefficient served to make simulations more stable and suggested that some of the behaviour of Reddy's model was numerical rather than physical. In the more recent model, each lymphangion was sub-divided into six computational elements to give more spatial resolution, though this had little effect on results interpretation. In this model, the motion of secondary valve was imposed rather than calculated through fluid-structure interaction.

Venugopal, Quick and co-workers published a series of papers that used experimental and computational methods to investigate the combination of phasic and tonic contractions of lymphatics (Venugopal et al., 2003, Venugopal et al., 2004, Venugopal et al., 2007, Quick et al., 2008, Venugopal et al., 2010). The computational methods resulted in a lumped parameter model of a lymphangion. The model developed in these studies combined the time-varying elastance model (equation 6) originally developed to model the active contractions of the heart's left ventricle (Suga and Sagawa, 1974, Suga et al., 1973, Suga and Sagawa, 1972) with momentum conservation including both resistive and inertial terms (equation 7) under the assumption of Poiseuille flow. These were combined with mass conservation (equation 8). Valves were modelled as an additional

resistance (R_{valve}) when closed and were assumed to close when the valve's downstream pressure exceeded the upstream pressure.

$$E(t) = \frac{P(t)}{V(t)-V_0} \quad (6)$$

where V is volume and V_0 is the theoretical volume at zero pressure

$$\Delta P = \left(\frac{8\eta L}{\pi a^4} + R_{valve} \right) Q + \frac{\rho L}{\pi a^2} \frac{dQ}{dt} \quad (7)$$

where η is lymph viscosity and L is the axial lymphangion length

$$\frac{dV}{dt} = Q_{in} - Q_{out} \quad (8)$$

where Q_{in} is the inflow and Q_{out} is outflow

This model is a simple way to represent lymphangions from their fundamental properties but is limited by the very simple model of valves (as in the Reddy model and its adaptation by MacDonald) and inaccuracies in the time-varying elastance calculation.

The combined phasic and tonic contractions were also included by Caulk and colleagues (Caulk et al., 2016, Caulk et al., 2015) and Razavi and co-workers (Razavi et al., 2017). These models used a constitutive model (four fibre strain energy density W function) for the passive properties of an incompressible thin-walled cylinder (equation 9). Intrinsic contractions were included using constant tone and a part cosine for the increase in force during phasic contraction. These models were used to represent the rat thoracic duct in the research of Caulk and rat tail lymphatics in the work of Razavi. The passive tension was calculated for the circumferential and axial directions. It is, however, worth noting that the thoracic duct has significantly different contractile properties compared to the rat mesenteric collecting lymphatics typically used for studies on contractile lymphatic vessels.

$$\sigma_{\theta\theta}^{pas} = 2C_{\theta\theta}^e \frac{\partial W}{\partial C_{\theta\theta}^e} - 2C_{rr}^e \frac{\partial W}{\partial C_{rr}^e} \quad (9a)$$

$$\sigma_{zz}^{pas} = 2C_{zz}^e \frac{\partial W}{\partial C_{zz}^e} - 2C_{rr}^e \frac{\partial W}{\partial C_{rr}^e} \quad (9b)$$

$$\mathbf{W} = b(\text{tr}(\mathbf{C}^e) - 3) + \sum_{k=1,2,3,4} \frac{b_1^k}{b_2^k} \left(\exp \left\{ b_2^k \left[\lambda^{k^2} - 1 \right]^2 \right\} - 1 \right) \quad (9c)$$

$$\lambda^{k^2} = \mathbf{C}_{\theta\theta}^e (\sin \alpha^k)^2 + \mathbf{C}_{zz}^e (\cos \alpha^k)^2 \quad (9d)$$

where σ^{pas} is the passive normal stress, \mathbf{C}^e is the right Cauchy-Green strain tensor, b, b_1^k, b_2^k are material parameters, α^k is the direction of fibre k

Moore Jr., Bertram, and co-workers then developed another lumped-parameter model to examine the function of lymphangions (Bertram et al., 2011, Bertram et al., 2014a, Bertram et al., 2014b, Bertram et al., 2016b, Bertram et al., 2017, Jamalian et al., 2013). This model has been well validated through comparison with cannulation experiments (Davis et al., 2011, Davis et al., 2012, Scallan et al., 2012) and in vivo recordings (Dixon et al., 2006, Zawieja et al., 1993). In this model, conservation of mass was used to give an ordinary differential equation for the lymphangion diameter. Three pressures within the lymphangion (upstream, middle and downstream) were calculated to allow for the model to simulate valve prolapse. The mid-lymphangion pressure was calculated using a passive tube law and prescribed intrinsic contractions combined with an assigned external pressure. Throughout its development, the model has been through several forms of the passive tube law, valve resistance, and diameter-dependent intrinsic tension. The first form of the relation (equation 10a) was used in (Bertram et al., 2011) and a second, improved form (equation 10b) that changed to negative curvature at exactly zero transmural pressure and $D/D_a = 1$ in (Jamalian et al., 2013). The third form (equation 10c) was adopted in (Bertram et al., 2014a) and the most recent form (equation 10d) in (Jamalian et al., 2017). There have also been two versions of the valve resistance model, with the first version (equation 10e) being a single sigmoid for valve opening used in (Bertram et al., 2014a) and the second (equation 10f) including another sigmoid for valve failure used in (Jamalian et al., 2017). Additionally, alternate forms of the diameter-dependence of intrinsic contractions have been used with one version (equation 10g) in (Bertram et al., 2016b) and another (equation 10h-k) in (Jamalian et al., 2017).

$$f_{pas,1} = P_d(\exp(D/D_d) - (D_d/D)^3) \quad (10a)$$

$$f_{pas,2} = \frac{4}{15}P_d(12\exp(D/D_d - 1) - 11 - (D_d/D)^3) \quad (10b)$$

$$f_{pas,3} = P_d \left[c_1 \left(\frac{D}{c_9} - c_2 \right)^2 + c_3 \exp \left(c_4 \left(\frac{D}{c_9} - c_5 \right) \right) + c_6 + c_7 \left(\frac{D}{c_9} - c_8 \right) + c_{10} \left(\frac{c_9}{D} \right)^3 \right] \quad (10c)$$

$$f_{pas,3} = c_1 \exp(c_2 D) + c_3 \exp(c_4 D) + c_5 D + c_6 - c_7/D^3 \quad (10d)$$

$$R_{valve,1} = R_{Vn} + \frac{R_{Vx}}{1 + \exp(-s_o(\Delta p_v - \Delta p_o))} \quad (10e)$$

$$R_{valve,2} = R_{Vn} + R_{Vx} \left(\frac{1}{1 + \exp(-s_f(\Delta p - p_f))} + \frac{1}{1 + \exp(s_o(\Delta p - p_o))} - 1 \right) \quad (10f)$$

$$M_{d,1} = \left(\frac{1}{1 + \exp(-s_d(D - D_a))} + \frac{1}{1 + \exp(s_d(D - D_b))} - 1 \right) \quad (10g)$$

$$M_{d,2} = \frac{M_a + M_b + M_c - 2}{6} \quad (10h)$$

$$M_a = 5.5 / \left(1 + \exp(-s_{d0}(D_i - D_0)) \right) \quad (10i)$$

$$M_b = 0.5 / \left(1 + \exp(-s_{d1}(D_i - D_1)) \right) \quad (10j)$$

$$M_c = 2 / \left(1 + \exp(s_{d2}(D_i - D_2)) \right) \quad (10k)$$

where P_d is a pressure constant (sets the local passive stiffness), D_d is a diameter constant (sets the size of the unpressurised and relaxed lymphangion), $c_{1,2,3,4,5,6,7,8,9}$ are constitutive parameters, R_{Vn} is the resistance of an open valve, R_{Vx} is the additional resistance on valve closure, s_o is the opening slope of valve resistance, Δp is the pressure difference across the valve (upstream-downstream), Δp_o is the pressure difference for valve opening, s_f is the slope of valve failure, p_f is the pressure difference for valve failure, $s_{d0,1,2}$ and $D_{0,1,2}$ are constitutive parameters

Upstream and downstream pressure were calculated based on momentum conservations relating pressure differences to the valve and Poiseuille lymphangion body resistances. In this model the

boundary conditions were pressure at either end of the lymphangion as these were the input control variables in cannulation experiments. A major contribution of this model was a more realistic consideration of valve behaviour, and the inclusion of a passive tube law to incorporate the passive properties of the lymphangion wall. The more realistic valve behaviour resulted from using a pressure difference-resistance relationship obtained experimentally to include bias of the valves to the open position and more accurate backflow values during valve closure. Throughout this series of papers, the core of the model remained the same whilst the passive tube law, valve resistance and intrinsic contraction equations have been updated to capture experimental results more realistically. A parameter sensitivity analysis of this model identified contraction frequency, external pressure, intrinsic tension, and lymphangion length as key parameters for further study. We make adaptations to this model in this thesis, so more detail is provided in the methods sections for Chapters 3 and 4. This model has since been used to represent small idealised networks (Jamalian et al., 2016) and to investigate the theory that suction pressure generated by the contracting lymphatics extends into the initial lymphatics to facilitate fluid uptake (Jamalian et al., 2017). Shear stress-dependent feedback has also been studied by incorporation into this model for lymphangion chains (Bertram et al., 2019) and valve failure has been studied again for lymphangion chains without shear feedback (Bertram et al., 2017). This model is the state-of-the-art for lumped parameter models of lymphangion function.

A three-dimensional model of a tubular lymphangion has also been developed (Rahbar and Moore Jr., 2011) with the main finding that Poiseuille flow is an appropriate assumption for collecting lymphatics. This model consisted of a contracting segment that maintained a circular cross-section but varied in radius bounded by stationary inlet and outlet regions and was run using Star-CCM+. Contractions were imposed as radial wall motion and the inlet boundary condition was parabolic flow (steady and unsteady) with a static outlet pressure boundary condition.

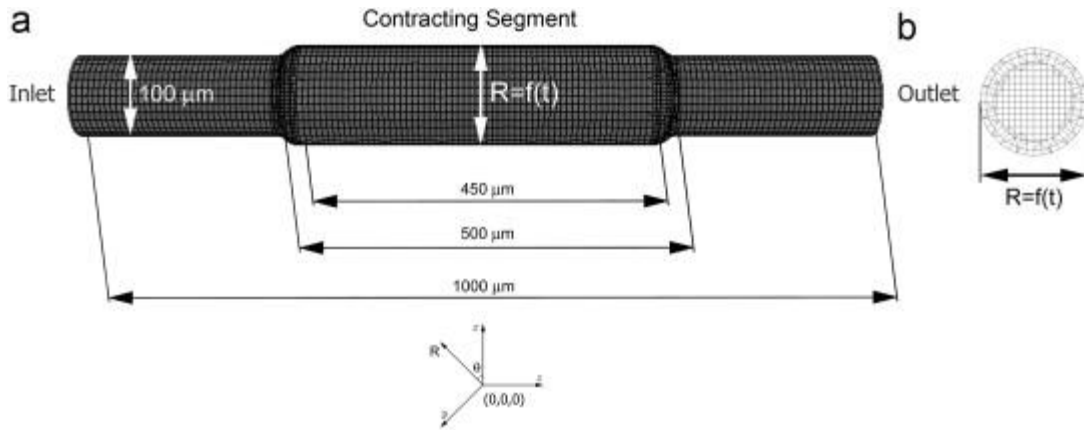


Figure 6: Illustration of the geometry in the Rahbar model. (a) The contracting segment is prescribed radial motion in time with the variation occurring between $40\text{ }\mu\text{m}$ and $120\text{ }\mu\text{m}$ (b) Cross-sectional view at the centre of the contracting segment. A trimmed hexahedral mesh was used to accommodate wall motion (cell sizes $10\text{ }\mu\text{m}$ and thickness of the prism layer $15\text{ }\mu\text{m}$) (Rahbar and Moore Jr., 2011) Copyright permissions included in Appendix 2

Several models have also been developed that investigate the signalling and regulation of intrinsic contractions in lymphatics. In one of these models the concentrations of NO and calcium were implemented as the only two signalling molecules involved in lymphatic contractions, and it was shown that calcium and NO levels alternate spatiotemporally for complementary feedback loops (Kunert et al., 2015, Baish et al., 2016). This model reproduced experimentally observed responses to pressure variations and manipulations of signalling pathways. In another paper, a modified FitzHugh-Nagumo model for action potentials was coupled with a non-linear system of hyperbolic PDEs to give a one-dimensional model of the electrical and fluid mechanical aspects of collecting lymphatics (Contarino and Toro, 2018). Contractions were incorporated by varying between phenomenologically derived passive and contracted pressure-diameter functions. In this paper, the effects of valve failure (stenosis and regurgitation) were also modelled. The model results showed that the regurgitant valve was incapable of preventing backflow and caused the lymph pump to be inefficient with an adverse pressure difference. When modelling stenotic valves, the model showed an unexpected decrease in efficiency of the downstream lymphangion with increasing contraction rate.

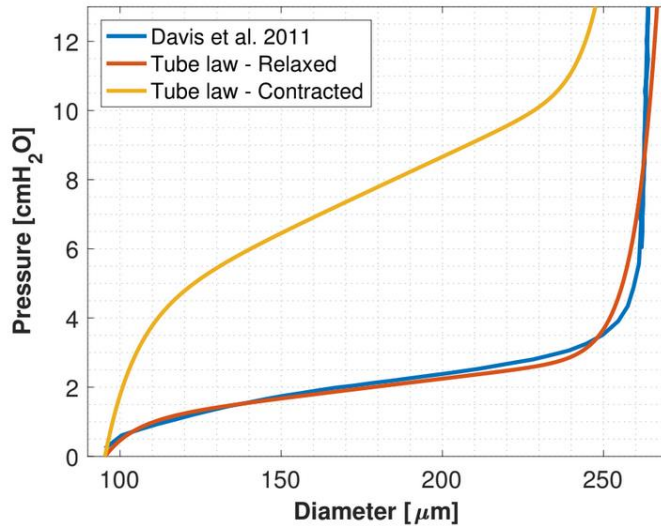


Figure 7: Pressure-diameter tube laws of the Containo and Toro model under passive and peak intrinsic contraction conditions. The external pressure was set to 0 cmH₂O so the y axis represents transmural pressure. Also included is the passive tube law previously reported by Davis and colleagues (Davis et al., 2011). Figure reference (Contarino and Toro, 2018) Copyright permissions included in Appendix 2

A more detailed model of NO concentration has also been developed (Wilson et al., 2013). Wilson and co-workers used confocal images from rat mesentery to generate realistic geometry and investigate the distribution of NO. This model combined flow and mass transfer equations in steady and unsteady analyses using Star-CCM+. Parabolic inflow was assumed with a Dirichlet inlet concentration boundary condition and a zero-flux outlet boundary condition. End effects were avoided by adding 200-micron long inlet and outlet regions. These simulations revealed areas of flow stagnation near valve leaflets, providing a potential explanation for experimental observations of high NO concentration in this region. This model also supported the theory of shear-dependent NO production since removing this dependence yielded unphysiological concentrations.

Secondary valves are a complex component of the lymphatic network due to their bias to the open position and dependence on transmural pressure, so have warranted some detailed models to examine their functionality (Wilson et al., 2015, Watson et al., 2017, Bertram, 2020). The difference in these models from the lymphangion models covered above is that those models use lumped-parameter representations whilst these models study the effects of valve geometry in more detail. Wilson and co-workers used idealised geometry of secondary valves for a finite element analysis study aimed at understanding the effect of valve and sinus size on leaflet deflection and the open

valve resistance. Watson and co-workers (Watson et al., 2017) used confocal images of rat mesenteric secondary valves (geometry in Figure 8) to perform a finite element analysis study to gain further understanding of the pressure for valve closure, and the retrograde flow during valve closure. (Bertram, 2020) developed a 3D finite element fluid-structure interaction model of secondary lymphatic valves that incorporates the effect of transmural pressure to study valve resistance and flow during opening and closing. The geometry was defined using confocal images of rat mesenteric secondary valves and the model was run using ADINA software. Both the leaflets and lymphangion wall were modelled as neo-Hookean.

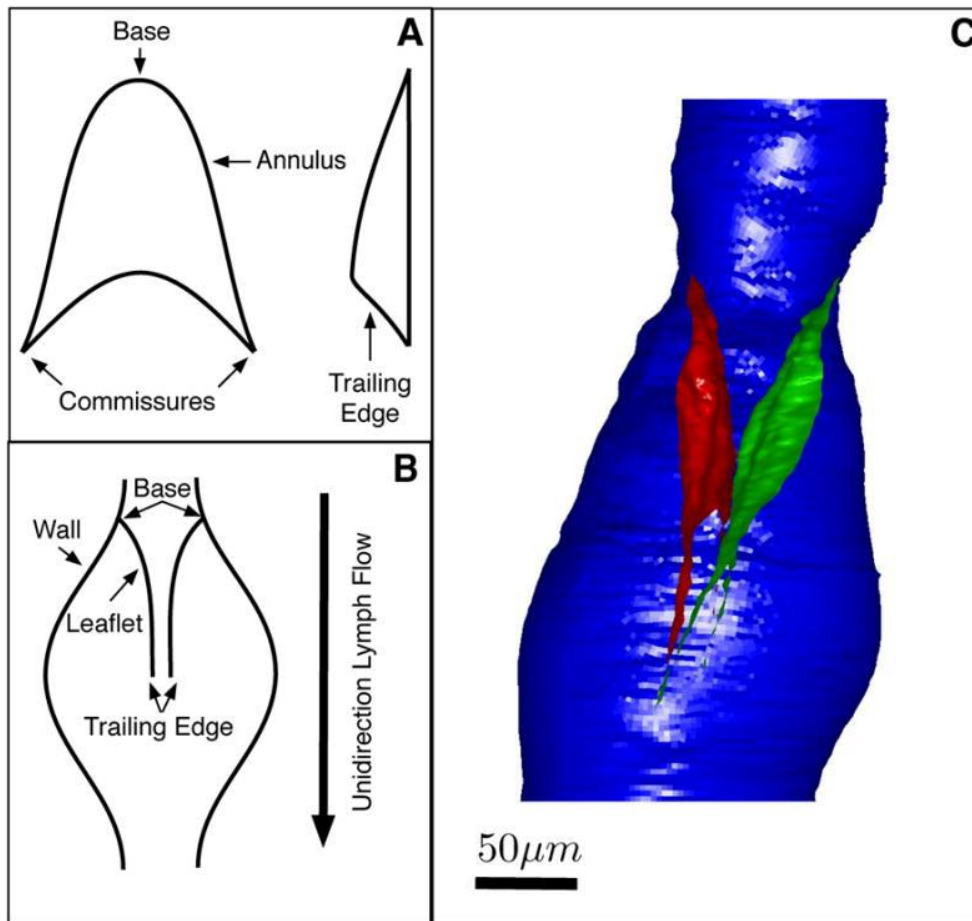


Figure 8: Representative geometry of lymphatic valves (A) shows the leaflet shape (B) is a cross-section showing the geometry of valve leaflets and sinus (C) is a 3D geometry of the lymphangion (blue) and valve leaflets (red and green). (Watson et al., 2017) Copyright permissions included in Appendix 2

Mathematical models have also been developed for primary valves (Mendoza and Schmid-Schönbein, 2003, Galie and Spilker, 2009, Heppell et al., 2013). (Mendoza and Schmid-Schönbein, 2003) modelled a pair of endothelial cells with one firmly attached to the surrounding tissue and one

unattached. The unattached cell was able to bend into the lumen of the vessel to allow inflow and was assumed to be purely elastic. The aim of this model was to investigate the theory that the overlap of endothelial cells was the function of primary valves and suggested that this was the case. (Galie and Spilker, 2009) built on the model of (Mendoza and Schmid-Schönbein, 2003) by using a finite element approach and using parameters more accurately defined by experimental results. (Heppell et al., 2013) simulated fluid leakage from blood vessels, transport through the interstitium, and uptake by initial lymphatics. This was accomplished using a basic unit including one blood capillary, one initial lymphatic and an interstitial space in between using COMSOL Multiphysics. The interstitial space was modelled as a porous medium, the blood capillaries as permeable membranes and the. They used this model to investigate the effects of Young's modulus of interstitium, the pressure difference between blood and lymphatic vessels, the permeability of the blood vessel, and the primary lymphatic valves as either open or closed by comparing the vessel circumference to a threshold value. This model of primary valves was used because it captures their response to expansion or contraction of the interstitium. These variations are then discussed in relation to changes in the body during aging and pregnancy.

There have been a few models developed for lymph nodes, such as (Jafarnejad et al., 2015, Cooper et al., 2016, Baldazzi et al., 2009, Gong et al., 2013) with the main two objectives being to determine the resistance to flow and study activation of immune response. Jafarnejad and co-workers (Jafarnejad et al., 2015) used commercial software (STAR-CCM+) to simulate an idealised model of mouse LNs, finding that about 90% of lymph flows around the outer edge of the lymph node whilst the fluid that gets deeper into the lymph node is absorbed into blood vessels with the magnitude of transfer being highly dependent on the surface area of blood vessels. Cooper and co-workers (Cooper et al., 2016) used images of mouse lymph nodes for the geometry for simulations in COMSOL Multiphysics. They found that the lymph flows directly between afferent and efferent vessels, and the amount that is absorbed or extravasated depends on the pressure in efferent lymphatics. The difference in predicted flow paths likely arises from the subdivision of different

regions of the LN (see Figure 9) with different permeabilities in the model of Jafarnejad. Both models combined flow through open spaces with porous sections and Starling's law for the entry/exit of flow into/out of blood vessels. Inflow was prescribed for the afferent vessels and outlet pressure for the efferent vessels. (Baldazzi et al., 2009) presented a hybrid discrete/continuous model of the lymph node. This model includes three types of cells and four chemokines. Cells were modelled as discrete agents residing in a 3D Cartesian mesh and interactions between cells as probabilistic rules. Chemokine concentration is modelled as uniform diffusion with degradation. (Gong et al., 2013) used a systems biology approach in a 3D agent-based cellular model of a lymph node. This model allows for the simultaneous simulation of T cell trafficking, activation, and production of effector cells under different antigen conditions. The model produced three important predictions: (1) T cell encounters with dendritic cells are more efficient in 3D, suggesting the need for 3D modelling (2) lymph nodes are able to produce CD4+T cells at the same efficiency over multiple cognate frequencies (3) reducing the time that naïve T-cells are required to bind DCs before becoming activated increases the rate of effector cell production.

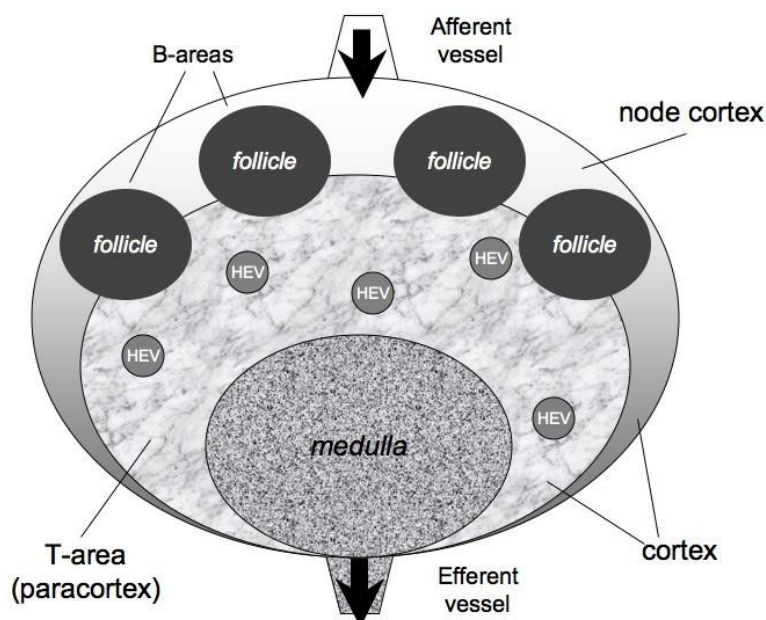


Figure 9: Schematic diagram of a lymph node, highlighting the different regions as considered by (Jafarnejad et al., 2015). Afferent and efferent vessels are the inflow and outflow pathways for lymph, and HEVs are blood vessels that exchange fluid with lymph. Figure originally published in open source article (Baldazzi et al., 2009) Copyright permissions included in Appendix 2

The electrical and calcium dynamics of lymphatic endothelial cells have also been modelled (Behringer et al., 2017) to test the hypothesis that these dynamics facilitate lymph flow. This study combined experimental and computational approaches. The computational model used the Hodgkin-Huxley membrane model incorporating the major ions (Ca^{2+} , Cl^- , Na^{2+} and K^+) through their Nernst potentials. The key advantage of the computational approach is that it can simultaneously calculate currents of ion channels, pumps, transporters, and exchangers that cannot be feasibly done experimentally.

2.2. Muscle

There are many models of muscle function, so this section does not aim to review all of them.

Instead, I cover the two commonly used classes of muscle model, the Hill model (Hill, 1938) and the Huxley sliding filament model (Huxley, 1957), with some examples of their uses in modelling cardiac, skeletal, and smooth muscle. Whilst these models were initially developed a long time ago, they are still the basis for many state-of-the-art models today. I also include some of the important modifications that have been used since the original models founding these classes were published.

Hill was the first to observe that there was a hyperbolic relationship between force (F) and velocity (v), yielding the famous Hill equation of muscle function (equation 11).

$$(v + b')(F + a') = b'(F_0 + a') \quad (11)$$

where b' is a constant, a' is the coefficient of shortening heat, F_0 is the isometric force generation

There are many adaptations of the Hill model that use a more complex representation of the series elastic component and include passive elastic elements or dashpots. The most used form of the Hill model includes a contractile element, a series elastic element, and a parallel elastic element (Figure 10. The series elastic element most likely represents a combination of the actin and myosin filament backbones, nonuniformity of sarcomeres, and other connective components in the sarcomere

(Knudson, 2007). The parallel elastic element represents the passive stiffness of the muscle from components of the muscle besides the sarcomeres, primarily the cytoskeleton.

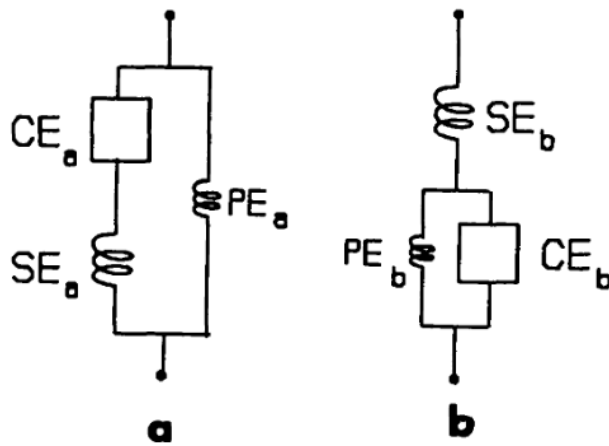


Figure 10: Hill models with contractile elements (CE) along with series and parallel elastic elements (SE and PE, respectively) (a) PE in parallel with both SE and CE (b) PE in parallel with CE only (Winters, 1990) Copyright permissions included in Appendix 2

The Hill model is a simple model, and this has been a factor in its ongoing popularity despite the generally accepted major limitation of the Hill model that is the lack of mechanistic insight into the molecular mechanisms and their relation to the metabolic aspects of muscle function. Comparison of the Hill equation to the Huxley model, however, has shown that there are insights into the actomyosin cycling rates from the Hill equation (Seow, 2013) made possible by the state-of-the-art study on mechanical motors resolved at the piconewton and nanometer scales (Piazzesi et al., 2007).

In the Huxley model, also known as the sliding filament model, muscle is modelled as a large population of myosin heads. Each myosin head is modelled as a linearly elastic spring (stiffness K) with force generation (F) proportional to its displacement (equation 12a) with the equilibrium fixed to the myosin filament. Huxley assumed that the myosin heads could occupy either of two states: attached or detached with attachment and detachment rates (f and g , respectively) depending on the displacement of the head. Huxley tried a few different rate functions and the chosen rate functions were based on simple intuition. The attachment rate function was intuitively made to increase so that the heads are most likely to attach at the powerstroke length and the muscle is doing the most work per actomyosin cycle. The heads do not attach at negative displacements

(resisting muscle contraction) and cannot attach at greater displacements than the powerstroke length. The detachment was high for negative displacements to reduce the heads that resist contraction and increased with increasing displacement so that heads do not reach too higher displacement and get damaged. The key equation in this model is a hyperbolic partial differential equation (equation 12b) governing how the displacement-distribution of myosin heads varies in time.

$$F = K \int nx \, dx \quad (12a)$$

$$\frac{\partial n}{\partial t} - v \frac{\partial n}{\partial x} = f(1 - n) - gn \quad (12b)$$

The use of linearly elastic springs was motivated by the fact that experiments showed the difference in force generation was linearly proportional to rapid length changes (extending or shortening). A key conceptual insight of Huxley in developing his model was the mechanistic explanation of the maximum shortening velocity (for zero force) being when the resistive force from heads with negative displacement equals the force from heads with positive displacement. Huxley showed that under isovelocity conditions, his model gave results that were equivalent within experimental error to the Hill equation. Huxley also showed that his model fit the energy liberation data, but that data has been subsequently questioned leading to improvements to the Huxley model as covered later in the next paragraph. There are several other potential choices for the rate functions in the Huxley model as he noted in his initial publication (Huxley, 1957) and discussed by (Keener and Sneyd, 2009). There is also a general binding site model (equation 13) which can be simplified to continuous binding site (where the myosin heads can bind anywhere, the opposite situation to the one binding site per myosin head assumed in the Huxley model) and discrete binding site (myosin heads each have a few binding sites available) by taking different limits in actin binding site spacing.

$$\frac{\partial n}{\partial t} - v \frac{\partial n}{\partial x} = f[1 - \sum_{i=-\infty}^{\infty} n(x + ml_a, t)] - g(x)n \quad (13)$$

where m indexes the lattice spacing of actin binding sites (distance l_a)

There have been many studies that attempt to improve on the limitations of the Huxley model (e.g. energetics, eccentric contraction, initial response to quick-release) by including additional myosin head states and/or transition functions (Huxley and Simmons, 1971, Hill, 1974, Eisenberg et al., 1980, Piazzesi and Lombardi, 1995, Barclay, 1999). The two-state Huxley model can be viewed as lumping multiple different attached states together, leading to the explicit modelling of these attached states for more accurate modelling of the experimental data. Huxley also published a paper stating that the inclusion of additional states could better represent the energetics than the original model (Huxley, 1973). Another conceptual improvement to the Huxley model was the simultaneous consideration of thermodynamics and mechanics (Eisenberg and Greene, 1980). Eisenberg and co-workers modelled heads as having an initial weak attached state with subsequent transition to a strongly attached state, these attached states having different equilibrium positions (i.e. different strains for zero force). A common concept for improved energetics modelling in Huxley-type models is weak coupling between ATPase activity and cross-bridge cycling. The important distinction between the strongly and weakly attached states is the ability of the weakly attached state to detach without hydrolysing ATP.

Based on the latch-state hypothesis of smooth muscle, Hai and Murphy published a series of papers in which they developed a four-state model of smooth muscle myosin head conformations with first-order kinetics for transitions between states (Hai and Murphy, 1992, Hai and Murphy, 1988a, Hai and Murphy, 1988b). Most quantitative models of smooth muscle are developments of this initial model. This model was validated against data from swine carotid vascular smooth muscle under isometric and isovelocity conditions. It was assumed that phosphorylation was a prerequisite for attachment of myosin heads (direct attachment of unphosphorylated myosin occurred at a negligible rate), and that once attached heads were dephosphorylated, they took a lot longer to detach than phosphorylated heads (they are in the latch state). They also assumed that the load bearing properties of both phosphorylated and dephosphorylated heads are the same and that the

only regulatory effect was calcium facilitating phosphorylation. The main limitation of this model was the lack of the displacement dependence present in the Huxley model.

Mijailovich and Fredberg published two papers (Mijailovich et al., 2000, Fredberg et al., 1999) that extended the Hai and Murphy model of myosin head states by incorporating the myosin heads' extension-dependence of the Huxley sliding filament model as shown in Figure 11A. They used this model to study the effects of length oscillations on airway smooth muscle in a more complete model of smooth muscle function than the isovelocity or isometric conditions in the original Hai and Murphy model. In their first model publication they combined the Huxley and Hai-Murphy models and applied length oscillations to study their effects on muscle force. The combination of Huxley and Hai Murphy models yielded four partial differential equations for the development of displacement-distribution of myosin heads in each of the four states over time. This set of equations was written in terms of a vector for the state populations and a four-by-four matrix of transition rates. Their second model included calculations of the ATP hydrolysis under sinusoidal length oscillations. In their second publication they also included an alternative conservation of myosin heads (equation 14) because the Huxley conservation is not technically true under non-isometric conditions because of convection of attached heads beyond the powerstroke region they attached in. Following models adapting the Huxley-Hai Murphy model, however, neglect this alternate conservation equation.

$$n_{Mp}(\xi, t) + n_M(\xi, t) + \sum_m [n_{AMp}(\xi + ml_a) + n_{AM}(\xi + ml_a)] = 1 \quad (14)$$

where n_{Mp} is the fraction of myosin heads in the detached phosphorylated state, ξ is the local displacement (within the range 0 to the maximum possible for head attachment), t is time, n_{Mp} is the fraction of myosin heads in the detached dephosphorylated state, n_{AMp} is the proportion of heads in the attached phosphorylated states, n_{AM} is the fraction of heads in the attached dephosphorylated state

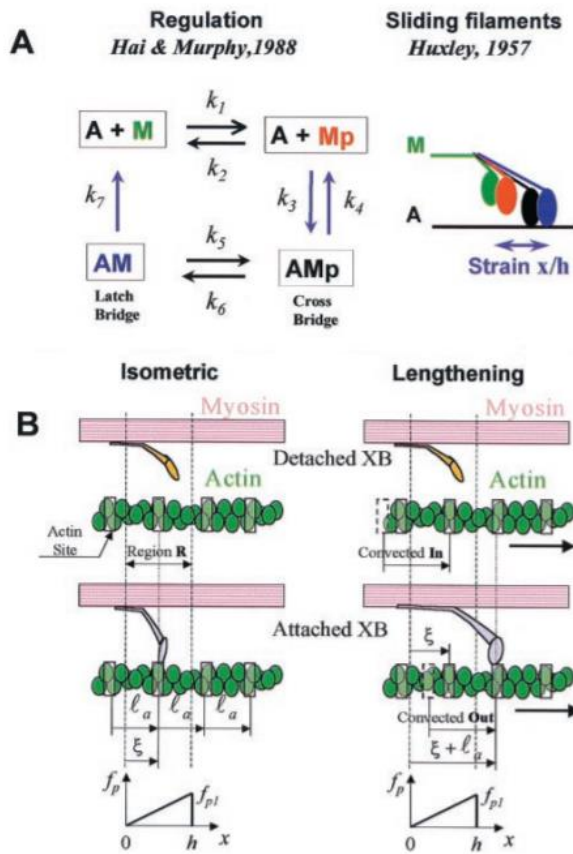


Figure 11: Summary diagram for the Huxley-Hai Murphy model (A) shows the four different states of myosin heads in the model with transition rates and the physical position of the myosin heads in the four different states and defines strain/displacement and (B) shows the difference in head conservations between isometric and lengthening cases due to convection of heads between actin binding site regions (Mijailovich et al., 2000) Copyright permissions included in Appendix 2

The computational intensity of the Huxley model has led to a series of papers that use a method called distribution-moment, originally developed by Zahalak in the 1980s (Zahalak, 1986, Zahalak, 1981). This method involves assuming a distribution (typically Gaussian, equation 15a-c) of myosin heads to allow for the derivation of ordinary differential equations for the macroscale properties of muscle function (stiffness, force and elastic energy storage). Using these ordinary differential equations greatly reduces the demand of this model despite increasing error in force and velocity estimates. Advances in computing power, however, have made the Huxley model much more feasible (Lemaire et al., 2016). More recently, the distribution-moment approximation was applied to the Huxley-Hai Murphy model (Rampadarath and Donovan, 2018) to study airway smooth muscle in asthma.

$$n(x, t) = \frac{M_0(t)}{\sqrt{2\pi}\sigma(t)} \exp\left(-\frac{(x - \mu(t))^2}{2\sigma^2(t)}\right) \quad (15a)$$

$$\sigma(t) = \sqrt{\frac{M_2(t)}{M_0(t)} - \left(\frac{M_1(t)}{M_0(t)}\right)^2} \quad (15b)$$

$$\mu(t) = \frac{M_1(t)}{M_0(t)} \quad (15c)$$

where n is the proportion of heads that are attached, x is displacement, t is time, M_0 is the zeroth moment of attached heads in displacement (representative of the total fraction of attached heads), M_1 is the first moment of attached heads in displacement, M_2 is the second moment of attached heads in displacement

There have also been multiple studies that use multiscale simulations to incorporate muscle function into the greater function of organs or organ systems. Larger-scale models of skeletal muscle often couple Huxley or phenomenological models of tension generation with finite element methods (Röhrle et al., 2012, Ivanović et al., 2016, Fernandez et al., 2005) and often involve the addition of passive elements to represent tendons. In (El Makssoud et al., 2011) they coupled the Huxley model with macroscale passive elements to model rabbit medial gastrocnemius. Multiscale modelling of skeletal muscle was reviewed in (Jung and Buehler, 2017) and continuous model methods in (Dao and Ho Ba Tho, 2018). In the continuous model review, it was highlighted that models were either for generic muscle tissue or specific muscles including detailed geometric and fibre orientation details. There are also many models of skeletal muscle that examine its role in locomotion.

There have been a few models that use the Huxley model for cardiac muscle (Wong, 1971, Wong, 1972, Negroni and Lascano, 1996, Wong, 1976, Rice and de Tombe, 2004). A cardiac muscle Hill model has also been developed (Grood et al., 1974). Other models take a phenomenological approach (Washio et al., 2012, Fung, 1993, Landesberg and Sideman, 1994) and constitutive relations have also been used (Guccione and McCulloch, 1993, Guccione et al., 1993). A very simple lumped parameter model of ventricular function, as mentioned in the previous section, is time-

varying elastance. Many recent models of cardiac function use commercial software (for example ANSYS, Comsol, Star-CCM+, Solidworks) for fluid-structure interaction with a trend towards patient-specific modelling (Lopez-Perez et al., 2015, Khalafvand et al., 2011) which is inappropriate for lymphatic vessel studies at this time. These types of models also reflect the greater base of knowledge acquired over the longer duration of cardiac studies and the more complex flow profiles in the heart due to the higher Reynolds number of the flow. For recent reviews of mathematical models of cardiac muscle see (Niederer et al., 2019, Regazzoni et al., 2021).

Several models have coupled Huxley-Hai Murphy models with constitutive solid mechanics for passive soft tissue in the lung (Hiorns et al., 2014, Politi et al., 2010, Brook, 2014, Brook and Jensen, 2014, Tawhai and Bates, 2011, Lauzon et al., 2012), bladder (Laforêt et al., 2011), and various blood vessels (Wang et al., 2008, Yang et al., 2003, Coccarelli et al., 2018, Murtada et al., 2017). Another study looked into length adaptation of smooth muscle through a phenomenological model (Lambert et al., 2004). Brook and co-workers expanded on the Huxley-Hai Murphy model to investigate length-adaptation of airway smooth muscle (Brook, 2014, Brook and Jensen, 2014, Hiorns et al., 2014). Brook and Jensen developed a structural model of an airway smooth muscle cell (Figure 12) to study CE reorganisation in length adaptation by arranging HHM CEs in series and parallel (row A in parallel with the cell nucleus, modelled as a linearly elastic spring, and row B directly tethered to the cell membrane) and applying an instantaneous rearrangement of the CEs, modelled as a change in the linear density of available actin binding sites.

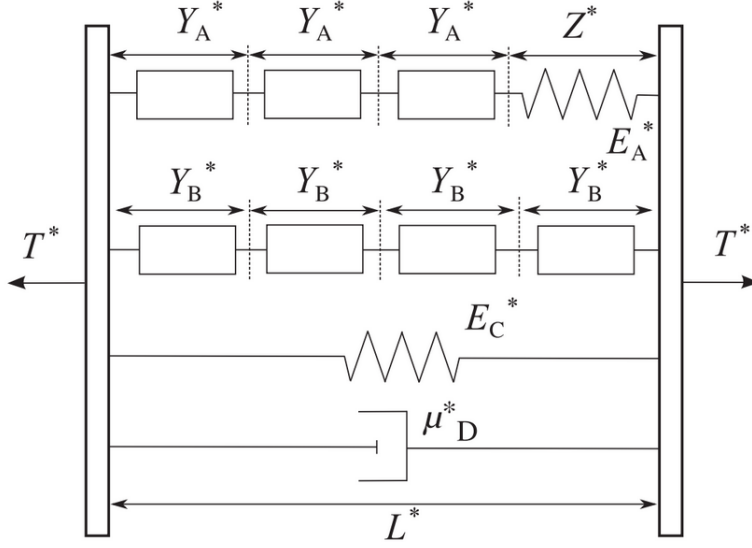


Figure 12: Schematic of a model for an airway smooth muscle cell. The model contains two parallel rows of contractile elements (lengths Y_A^* and Y_B^*). The cell nucleus is modelled as a Hookean spring with length Z^* and stiffness E_A^* . In parallel with the rows of contractile elements are a Hookean spring (stiffness E_C^*) and Newtonian dashpot (viscosity μ_D^*). The overall cell length is L^* and the total force generated by the cell is T^* (Brook and Jensen, 2014) Copyright permissions included in Appendix 2

The key equations for this model are the series length balance

$$L^* = N_A^* Y_A^* + Z^* E_A^* = N_B^* Y_B^* \quad (16)$$

where N_A^* is the series number of row A contractile elements, N_B^* is the series number of row

B contractile elements

the series force balance between row A contractile elements and the nuclear spring

$$F_A^* = E_A^* (Z^* - Z_{ref}^*) \quad (17)$$

where Z_{ref}^* is the reference length for zero force from the nuclear spring

and the parallel force summation

$$T^* = F_A^* + F_B^* + E_C^* (L^* - L_{ref}^*) + \mu_D^* \frac{dL^*}{dt^*} \quad (18)$$

where L_{ref}^* is the reference length for zero force from the cell stiffness and t^* is time

An important factor in modelling muscle function is excitation-contraction coupling, relating the stimulus of muscle to force generation through intracellular calcium concentration and its binding to

regulatory proteins. The calcium concentration within the muscle affects the transition rates of attachment and/or phosphorylation through a Hill function that represents the binding of calcium to regulatory proteins (Yochum et al., 2015, Bursztyn et al., 2007, Laforêt et al., 2011, Yang et al., 2003, Wang et al., 2008). Calcium concentration is either a prescribed function fit to experimental recordings of the free calcium or is the sum of various fluxes into and out of extracellular and intracellular stores (Rice and de Tombe, 2004, Rice et al., 2008, Koenigsberger et al., 2004, Parthimos et al., 1999). Modelling the calcium concentration through fluxes provides greater insight into the relative importance of different channels but requires significantly more model parameters. There are also models that include additional compartments for more detailed representation of the various calcium-bound states of regulatory proteins (Zahalak and Ma, 1990, Fajmut et al., 2005a, Fajmut et al., 2005b).

Another factor in muscle function is the dependence of force generation on the muscle length, representing the overlap of actin and myosin filaments. This is typically incorporated through the inclusion of a function relating muscle length and the number of myosin heads available to attach. These functions are obtained from the shape of the force-length relationship that is often obtained in isometric muscle experiments (see, for example, (Kocková and Cimrman, 2009, Yu et al., 1997)).

2.3. Thesis structure

Chapter 1 provides a general introduction to the lymphatic system paying particular attention to the biomechanics of pumping and lymphatic muscle contractility.

Chapter 2 provides a background on existing computational models of the lymphatics and muscle.

Chapter 3 discusses a model of lymphatic muscle from an article submitted to *Biomechanics and Modeling in Mechanobiology*.

Chapter 4 discusses a homogenised model of lymphatic networks from an article to be submitted to the *Journal of Engineering in Medicine* pending some recommended adjustments to allow the model to capture properties of lymphatic networks.

Chapter 5 is a discussion of the findings obtained in this PhD and recommends some future research based on the models developed.

CHAPTER 3 – SUBCELLULAR MODEL OF LYMPHATIC MUSCLE

3.1. Introduction

Fluid homeostasis is maintained by the converging vessels of the lymphatic system that return 4 – 8 L of interstitial fluid per day to the venous system at the subclavian veins. Lymph transport works against an adverse pressure gradient from low or subatmospheric pressures in the interstitium (Jamalian et al., 2017, Aukland and Reed, 1993, Guyton et al., 1971). Since there is no central lymph pump, each lymphatic vessel must impart energy through active contraction of specialised lymphatic muscle cells (LMCs). Retrograde flow is prevented by closely spaced one-way intraluminal valves (Margaris and Black, 2012, Gashev, 2008, Moore Jr. and Bertram, 2018). In addition to intrinsic contractions, external forces such as from skeletal muscle contraction, respiration, and contraction of the heart, among others can impart energy to lymph propulsion. The relative contributions of intrinsic contractions and external compression vary throughout the lymphatic tree.

Deficiencies in lymph transport can result in a chronic, debilitating condition involving tissue swelling from accumulation of interstitial fluid and proteins called lymphoedema. The effectiveness of lymphoedema management strategies is limited, so it is generally said that it has no cure (Fu, 2014). The absence of lymphoedema treatments can be attributed in part to a lack of understanding of LMC contraction dynamics (Scallan et al., 2016, Zhang et al., 2013).

The dual roles of lymphatic vessels serving as both pumps and conduits means that intrinsic contractions from LMCs must perform the tasks of both cardiac muscle (phasic contractions to generate flow) and vascular smooth muscle (tonic constriction to regulate flow through diameter-based resistance) (Quick et al., 2007, Bridenbaugh et al., 2003, von der Weid and Zawieja, 2004). Lymphatic muscle contractions can adapt in the manner of a heart or a resistance artery, depending on the local lymphodynamic environment (Gashev et al., 2012, Gashev et al., 2004).

The dual behaviours of LMCs are grounded in the presence of two isoforms of contractile proteins. These cells possess both striated (slow twitch β) and phasic smooth (SM1B and SM2B) myosin heavy chain isoforms (Muthuchamy et al., 2003). The key difference between heavy-chain isoforms is that

tonic myosin heads can enter a slowly-cycling latch state (Seow, 2016, Murphy and Rembold, 2005). Similar to other types of muscle cells, the excitation of LMCs results from STDs arising at pacemaker sites within the muscle layer (Zawieja et al., 1999, von der Weid and Zawieja, 2004, von der Weid, 2001). These depolarisations sum to generate APs which cause changes in the intracellular calcium concentration (von der Weid et al., 2014, Zawieja et al., 1999).

For striated muscle, calcium binding to TnC causes a conformation change of the troponin-tropomyosin complex. This exposes actin sites for myosin head attachment. There is preliminary evidence for the presence of slow/cardiac TnC in lymphatic muscle (unpublished observation of M. Muthuchamy). It is generally accepted that the primary means of ECC for smooth muscle is calcium binding to CaM. This activates myosin light chain kinase to phosphorylate myosin heads, allowing binding to actin sites and force generation. Tonic contraction of LMCs is likely myosin light chain kinase dependent given the presence of CaM (Wang et al., 2009, Dougherty et al., 2008).

No model for the subcellular mechanisms of lymphatic muscle contractility exists. Existing models of lymphangions prescribe the intrinsic contraction forces. Computational research into lymphatic muscle has focused on the regulation of contractions and the electrical properties of lymphatic muscle (Contarino and Toro, 2018, Kunert et al., 2015, Baish et al., 2016). Whilst there have been multiple computer models phenomenologically incorporating both phasic and tonic contractions of lymphatic muscle (Kunert et al., 2015, Caulk et al., 2016, Caulk et al., 2015, Razavi et al., 2020, Razavi et al., 2017), the different effects of the contraction types was the focus of only one series of computational modelling papers. This model used the time-varying elastance model of the heart combined with the transmission line equations for blood vessels (Venugopal et al., 2003, Venugopal et al., 2004, Venugopal et al., 2007, Quick et al., 2008, Venugopal et al., 2010). Contarino and Toro published a phenomenological one-dimensional model of lymphangions with action potentials incorporated through a modified FitzHugh-Nagumo model and allowed the inclusion of shear- and pressure-dependent effects on contractions. The model consists of a system of nonlinear hyperbolic

PDEs and four ODEs. The key advantage/progress of this model is the ability to simulate lymph flow in one dimension with contractile responses to mechanical feedback. Kunert and colleagues developed a lattice-Boltzmann type model to show that oscillations in nitric oxide and calcium concentration can explain lymphatic contractions. Their model predicted that the concentrations of calcium and nitric oxide oscillate spatiotemporally and that the periodic contractions result. Baish and colleagues simplified the model presented by Kunert and co-workers and noticed the similarities of the shear-dependent NO oscillator to the van der Pol oscillator and applied stability methods to identify the key parameters. The model is dependent on phenomenological environmental calcium influx, stretch-induced calcium influx, and shear-dependent contraction inhibition. The only previous computer model focusing on the dual nature of lymphatic muscle used the time-varying elastance model of the heart combined with the transmission line equations for blood vessels (Venugopal et al., 2003, Venugopal et al., 2004, Venugopal et al., 2007, Quick et al., 2008, Venugopal et al., 2010). Whilst this model was important in developing an understanding of the hybrid nature of lymphatic muscle it did not incorporate the subcellular mechanisms that give rise to the dual behavior. The phenomenological nature of these models combined with the fact that they do not explicitly model the subcellular components limits their applicability in studying the effects of modulating subcellular components in health and disease.

Many muscle models are based on those of A.F. Huxley (Huxley, 1957) or of A.V. Hill (Hill, 1938). Huxley's model is a mechanistic model of the molecular interactions of actin and myosin filaments of muscle (described in more detail below). Whilst these models are founded in research that has existed for a while, the fundamental concepts remained unchanged and Hill's model is a black-box model that relates velocity and force generation. Hill's model lacks a direct relationship between mechanical and metabolic behaviour (Huxley's includes such a relationship). Computational intensity initially hindered use of the Huxley model but this has become less of an issue (Lemaire et al., 2016).

3.2. Methods

The sub-cellular muscle model is based on the molecular sliding filament model of Huxley (Huxley, 1957) and its adaptation for smooth muscle (Fredberg et al., 1999, Mijailovich et al., 2000). The fully coupled model consists of three scales: molecular, cell, and lymphangion. Scales are coupled by iteratively passing down the velocity from a larger scale to a smaller scale and returning the contractile force, as shown by Figure 13. The cell model is loosely based on the work of Brook and Jensen (Brook and Jensen, 2014) with rows of contractile elements in parallel with a Kelvin-Voigt viscoelastic element to represent the passive properties of the cell. The model is adapted to account for the phasic and tonic contractions of LMCs, and additionally to include the effects of excitation-contraction coupling. The little existing knowledge of LMC microstructure meant that a simple representation of the CEs and passive viscoelasticity was a good start, with the Brook and Jensen model providing a good basis. Accounting for the presence of both phasic and tonic contractions in lymphatic muscle resulted in a significant change of the cell structure model from that of Brook and Jensen. The effects of ECC are included in the muscle model to induce periodic contractions. We base the model parameters on rat mesenteric collecting lymphatics.

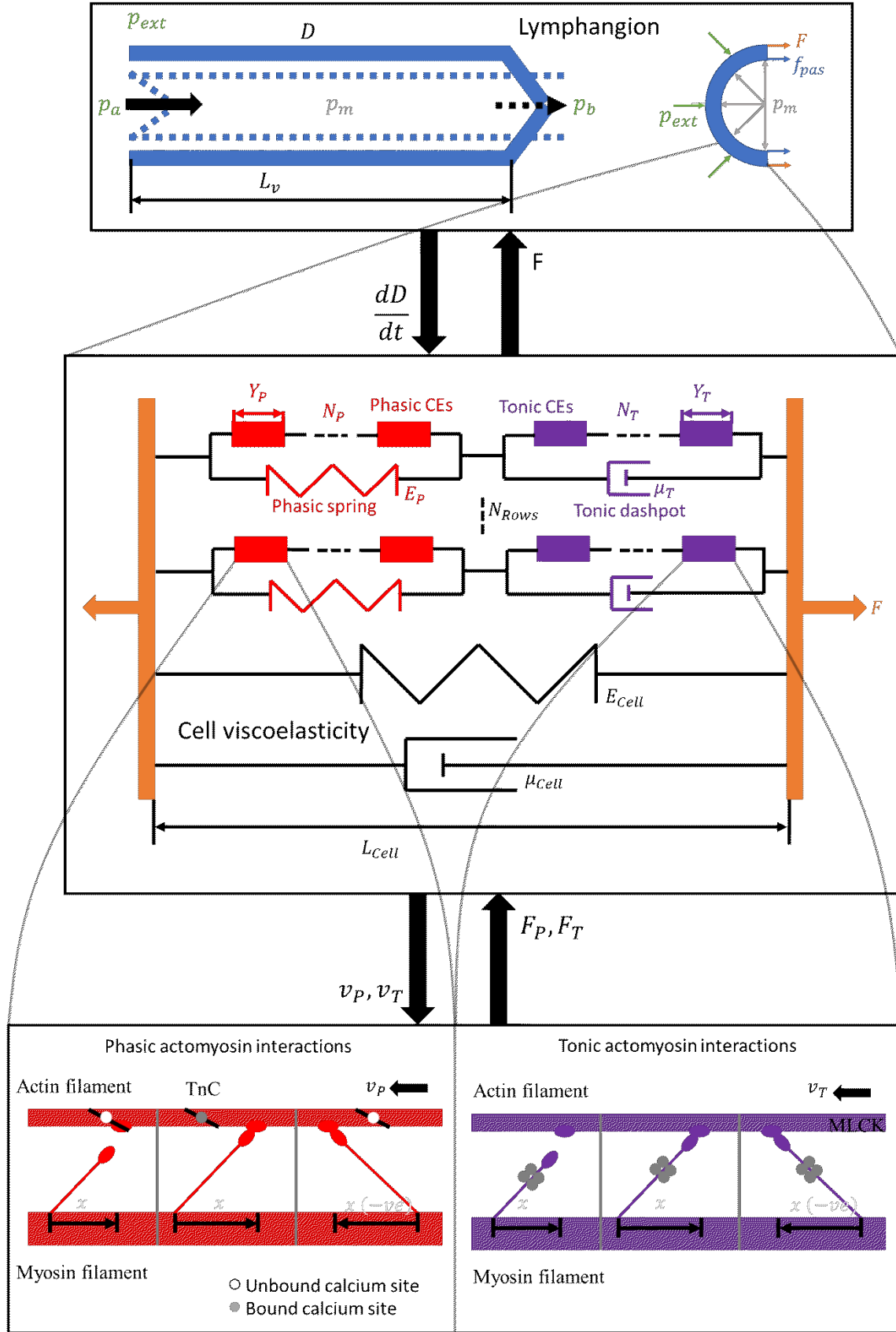


Figure 13: Coupling of scales. The largest scale in the model is based on a lumped parameter model of lymphangion pumping, which yields macroscale pressure-flow relations. Intrinsic muscle contractions are incorporated through a wall-force balance to calculate the pressure in the centre of a lymphangion. LMC contractile force is calculated from a model that includes two types of contractile elements (CEs) connected in series with a spring in parallel with phasic elements and dashpot in parallel with tonic elements. There is also a parallel viscoelasticity representing cell properties. The molecular

force generation of CEs is calculated from the sliding filament model with ECC incorporated using a prescribed periodic function of intracellular free calcium concentration.

3.2.1. Cell model

The combination of tonic and phasic contractions is captured at the cell scale through two types of molecular contractile elements (CEs). Viscoelasticity of LMCs is modelled using a Kelvin-Voigt viscoelastic element in parallel with the CEs as a simple case with only two parameters without evidence for the use of alternative methods (Figure 13), based on the work of Brook and Jensen (Brook and Jensen, 2014) discussed in Chapter 2. Brook and Jensen developed their model to study the effects of length adaptation in human airway smooth muscle. CEs provide a velocity- and calcium-dependent force modelled as described in Section 3.2.2.

CEs of both types are connected in series. A strain-stiffening spring is included in parallel with phasic CEs (referred to as phasic spring) and a Newtonian dashpot in parallel with tonic CEs (referred to as tonic dashpot). The phasic spring allows the tonic force during diastole to be transmitted across passive or minimally active phasic CEs and affect the cell force. This is necessary to allow tonic constriction of the lymphangion. The tonic dashpot allows phasic contractions to rapidly reduce the cell length without causing a significant change in tonic CE length. This is necessary to allow the tonic CEs to attach enough heads for physiologic force generation. In the development of this model, several series and parallel arrangements of contractile units and mechanical elements were trialed, but this was the only arrangement that yielded physiologic behaviors because it allowed for both phasic and tonic contractions to influence the overall force, unlike the other arrangements (see Appendix 1). The other arrangements that were tried were parallel rows of contractile elements, series CEs with passive elements (spring and dashpot) in parallel with phasic CEs only, and series CEs with passive elements in parallel with tonic CEs only. The key problem with the parallel arrangement was that the faster velocity of phasic CEs was also the velocity of the tonic CEs so the tonic CEs could not attach enough heads for physiologic force generation. Having passive elements in parallel with the phasic CEs meant that the overall force of the CE row was the tonic force (the passive elements simply made up the difference so that the combination of phasic CEs and passive elements was the

tonic force). Similarly, with passive elements in parallel with the tonic CEs the row force was the phasic force. LMC viscoelasticity was included in addition to the phasic spring and tonic dashpot because the phasic spring and tonic dashpot affect the dynamics of the interaction between the two types of contractile element whereas the cell viscoelasticity affected the overall force of the cell.

A force balance between CEs with contributions from the phasic spring and tonic dashpot results in the following equation for the force developed by a single row (F_{Row}) containing the CEs (Figure 13).

$$F_{Row} = F_P + E_P(N_P Y_P - N_P Y_{P,ref}) = F_T + \mu_T N_T \frac{dY_T}{dt} \quad (19)$$

where F_P is the force generated by phasic CEs, E_P is the stiffness of the phasic spring, N_P is the number of phasic CEs in series, Y_P is the length of phasic CEs, $Y_{P,ref}$ is the reference length for zero force from the spring in parallel with phasic CEs, F_T is the force generated by tonic CEs, μ_T is the viscosity constant for the tonic dashpot, N_T is the number of tonic CEs in series, Y_T is the length of tonic CEs, t is time.

The strain-stiffening of the phasic spring is given by the exponential equation

$$E_P = a \times \exp(b N_P Y_P) \quad (20)$$

where a, b are constitutive parameters

It is essential for the phasic spring to be in extension during diastole when there is little phasic force, and tonic CEs pull on the phasic CEs so that the spring provides an additional contractile force and the row force is higher than the phasic force and includes tonic CE effects during diastole. This means that the phasic spring needs to resist overextension of phasic CE (otherwise the lymphangion would be unable to overcome the pressure demand imposed upon it. Both types of CE are initialized to the same length (see Section 3.2.3).

The total combined length of phasic and tonic CEs corresponds to the cell length (L_{Cell})

$$L_{Cell} = N_P Y_P + N_T Y_T \quad (21)$$

The total contractile force of the cell (F) is the sum of the overall parallel contributions

$$F = N_{Rows}F_{Row} + E_{Cell}(L_{Cell} - L_{Cell,ref}) + \mu_{Cell} \frac{dL_{Cell}}{dt} \quad (22)$$

where N_{Rows} is the number of parallel rows of CEs, E_{Cell} is the stiffness of the LMC, $L_{Cell,ref}$ is the length of an LMC with zero force from the cell stiffness, μ_{Cell} is the viscosity constant for the LMC

The shortening velocity of tonic CEs (v_T) is obtained by rearranging the series force balance (equation 13a), and the shortening velocity of phasic CEs (v_P) by differentiating and rearranging the length balance (equation 13b)

$$v_T = -\frac{dY_T}{dt} = \frac{F_P + E_P(N_P Y_P - N_P Y_{P,ref}) - F_T}{\mu_T N_T} \quad (23a)$$

$$v_P = -\frac{dY_P}{dt} = \frac{dL_{Cell}/dt - N_T dY_T/dt}{N_P} \quad (23b)$$

3.2.2. Molecular muscle modelling

The molecular models for CE force generation are based on adapting the sliding filament model to include the effects of ECC. In the sliding filament model, myosin heads are modelled as linearly elastic springs (Huxley, 1957) and can occupy different chemical states. Each myosin head has its own equilibrium position that moves with the myosin filament, and its contractile force when attached is proportional to the displacement from equilibrium (Figure 14). The maximum displacement at which a myosin head can still attach to actin is called the powerstroke length (assumed consistent between myosin isoforms). Detachment is possible at all displacements. We assume that there is an actin site:myosin head ratio of 1: 1 and sufficient spacing between actin sites that each myosin head has only one actin site in attachment range. In phasic CEs, ECC is included via TnC which affects the attachment rate (Wong, 1971, Wong, 1972). In tonic CEs, ECC is included via CaM which affects the phosphorylation rate (Wang et al., 2008, Yochum et al., 2015).

It is assumed that phasic myosin heads can occupy two states with the head either attached and generating force or detached (see Figure 14). The rate myosin head attachment (f) or detachment (g) is dependent on its displacement using the functions of A.F. Huxley (Huxley, 1957) modified so that the detachment rate is constant for positive displacements greater than the powerstroke length as shown in Figure 14. Constants for transition rates of both myosin isoforms are listed in Table 1. In the model presented here, the attachment rate is also dependent on the saturation of cardiac TnC with calcium ions, modelled as described in Section 3.2.2.1. Smooth transitions between the piecewise rate functions in equations 24a,b and 27a,b are provided by part sines as considered by the original rate functions:

$$f = \begin{cases} 0 & \text{if } x/h < 0 \\ S_{Trop} f_1 x/h & \text{if } 0 \leq x/h < 0.9 \\ S_{Trop} f_1 0.9 \left(\frac{\sin\left(\frac{2\pi x}{0.4h}\right) + 1}{2} \right) & \text{if } 0.9 \leq x/h \leq 1.1 \\ 0 & \text{if } x/h > 1.1 \end{cases} \quad (24a)$$

where S_{Trop} is the saturation of TnC, f_1 is a constant, x is displacement, h is powerstroke length,

$$g = \begin{cases} g_2 & \text{if } x/h < -0.1 \\ (g_2 - 0.1g_1) \left(\frac{\sin\left(\frac{2\pi x}{0.4h} - \pi\right) + 1}{2} \right) + 0.1g_1 & \text{if } -0.1 \leq x/h \leq 0.1 \\ g_1 x/h & \text{if } 0.1 < x/h \leq h \\ g_1 & \text{if } x/h > h \end{cases} \quad (24b)$$

where g_1, g_2 are constants obtained from a general fit to the shape of diameter and pressure tracings obtained experimentally (see Table 1)

The displacement-distribution of attached phasic heads can be affected by either detachment or mechanical convection to a different displacement. Convection is the result of all heads being attached to the same actin filament so heads with different extensions are dragged at the rates. Using the sign convention of shortening velocity being positive, the convection results in a partial

differential reducing the displacement of attached heads during shortening. Using first-order kinetics for myosin head state transitions the attached proportion of myosin heads is governed by

$$\frac{\partial n_P}{\partial t} - v_P \frac{\partial n_P}{\partial x} = (1 - n_P)f - n_P g \quad (25)$$

where n_P is the proportion of phasic myosin heads with displacement x that are attached. Conservation of the total number of myosin heads dictates that the fraction of detached heads is $(1 - n_P)$. The minus sign arises from the sign convention of shortening velocity being considered positive. The force per phasic CE (F_P) is then calculated as in (Huxley, 1957) by integrating Hooke's law over all displacements with constants for the number of myosin heads and density of actin binding sites.

$$F_P = Num_P \rho K_P \int_{-\infty}^{\infty} x n_P dx \quad (26)$$

where Num_P is the number of myosin heads in a phasic CE, ρ is the length density of actin binding sites along the thin filament, K_P is phasic myosin head stiffness

The force of phasic contractile elements is directly dependent on the density of actin binding sites because this limits how many heads can attach and forces from different heads add in parallel. In practice the integral has finite bounds with displacements that are large enough (in both positive and negative directions) that there is no convection of myosin heads beyond the limits. The integral was, in practice, bounded by finite values of $-15h$ to $15h$ which were far enough from the attachment region that all heads were detached before reaching these bounds, so the force was unaffected and increasing these bounds would have no effect on the results. Displacement discretisation was twenty cells per powerstroke length with the sine region ($0.1h$ on either side of the rate transitions at $x = 0$ and $x = h$) subdivided by ten. See Appendix 1 for a check that the model results are unaffected by halving displacement discretisation under reference conditions.

Tonic CE mechanics are also modelled using the sliding filament model, but with additional states motivated by the presence of the slowly cycling latch state of smooth muscle (Dillon et al., 1981,

Murphy and Rembold, 2005) (Figure 14). The models for these additional states come from Hai and Murphy (Hai and Murphy, 1988a, Hai and Murphy, 1988b, Hai and Murphy, 1992). Tonic CE transition rate functions for attachment and detachment (plotted in Figure 14) are similar to those for phasic CEs, except with increased detachment rates for heads with greater displacement than the powerstroke length (Brook and Jensen, 2014). Transitions between the piecewise functions are again given by part sines.

Attachment k_3

$$k_3 = \begin{cases} 0 & \text{if } x < 0 \\ K_{3,1} x/h & \text{if } 0 \leq x < 0.9 \\ 0.9K_{3,1} \left(\frac{\sin\left(\frac{2\pi x}{0.4h}\right) + 1}{2} \right) & \text{if } 0.9 \leq x/h \leq 1.1 \\ 0 & \text{if } x/h > 1.1 \end{cases} \quad (27a)$$

Phosphorylated detachment k_4

$$k_4 = \begin{cases} K_{4,2} & \text{if } x/h < -0.1 \\ (K_{4,2} - 0.9K_{4,1}) \left(\frac{\sin\left(\frac{2\pi x}{0.4h} - \pi\right) + 1}{2} \right) + 0.9K_{4,1} & \text{if } -0.1 \leq x/h \leq 0.1 \\ K_{4,1} x/h & \text{if } 0.1 < x/h < 0.9 \\ (0.9(K_{4,1} + K_{4,3}) - 1.1K_{4,1}) \left(\frac{\sin\left(\frac{2\pi x}{0.4h} - \pi\right) + 1}{2} \right) + 0.9K_{4,1} & \text{if } 0.9 \leq x/h \leq 1.1 \\ (K_{4,1} + K_{4,3}) x/h & \text{if } x/h > 1.1 \end{cases} \quad (27b)$$

Dephosphorylated detachment k_7

$$k_7 = \begin{cases} K_{7,2} & \text{if } x/h < -0.1 \\ (K_{7,2} - 0.1K_{7,1}) \left(\frac{\sin\left(\frac{2\pi x}{0.4h}\right) + 1}{2} \right) + 0.1K_{7,1} & \text{if } -0.1 \leq x/h \leq 0.1 \\ K_{7,1} x/h & \text{if } 0.1 < x/h < 0.9 \\ (1.1(K_{7,1} + K_{7,3}) - 0.9K_{7,1}) \left(\frac{\sin\left(\frac{2\pi x}{0.4h} - \pi\right) + 1}{2} \right) + 0.9K_{7,1} & \text{if } 0.9 \leq x/h \leq 1.1 \\ (K_{7,1} + K_{7,3}) x/h & \text{if } x/h > 1.1 \end{cases} \quad (27c)$$

where $K_{3,1}, K_{4,1}, K_{4,2}, K_{4,3}, K_{7,1}, K_{7,2}, K_{7,3}$ are constants

The phosphorylation/dephosphorylation rates (k_1 and k_6 , respectively) are assumed to be independent of displacement and the same for both attached and detached heads (Brook and Jensen, 2014). The phosphorylation rate of tonic myosin heads is dependent on the saturation of CaM.

$$k_1 = S_{CaM}K_1 \quad (27d)$$

$$k_6 = S_{CaM}K_6 \quad (27e)$$

where S_{CaM} is the saturation of CaM, K_1, K_6 are constants

The resulting set of partial differential equations (PDEs) describing the displacement-distribution of tonic heads in different states can be written as a single equation with a vector of attachment states and a matrix of transition rates (Fredberg et al., 1999) as given here in equations 28a,b.

$$\frac{\partial \mathbf{n}_T}{\partial t} - v_T \frac{\partial \mathbf{n}_T}{\partial x} = \mathbf{T} \mathbf{n}_T \quad (28a)$$

$$\mathbf{n}_T = \begin{Bmatrix} M \\ Mp \\ AMp \\ AM \end{Bmatrix} \quad (28b)$$

where M is the proportion in the detached dephosphorylated state, Mp is the proportion in the detached phosphorylated state, AMp is the proportion in the attached phosphorylated state and AM is the proportion in the attached dephosphorylated state.

$$\mathbf{T} = \begin{bmatrix} -k_1 & k_2 & 0 & k_7 \\ k_1 & -(k_2 + k_3) & k_4 & 0 \\ 0 & k_3 & -(k_5 + k_4) & k_6 \\ 0 & 0 & k_5 & -(k_6 + k_7) \end{bmatrix} \quad (28c)$$

The total number of heads must again be conserved, resulting in an algebraic equation to replace one of the PDEs

$$\sum \mathbf{n}_T = 1 \quad (28d)$$

In this model AM was replaced, meaning that the final row of the transition matrix is not used

$$AM = 1 - M - M_p - AM_p \quad (28e)$$

The force generated by tonic CEs is given by the integral of attached states over all displacements (Brook and Jensen, 2014) again with constants of the number of myosin heads and density of actin binding sites.

$$F_T = \rho Num_T K_{HHM} \int_{-\infty}^{\infty} x \times AM_p dx + \rho Num_T K_{HHM} \int_{-\infty}^{\infty} x \times AM dx \quad (29)$$

where Num_T is the number of myosin heads in a tonic CE, K_{HHM} is the stiffness of tonic myosin heads

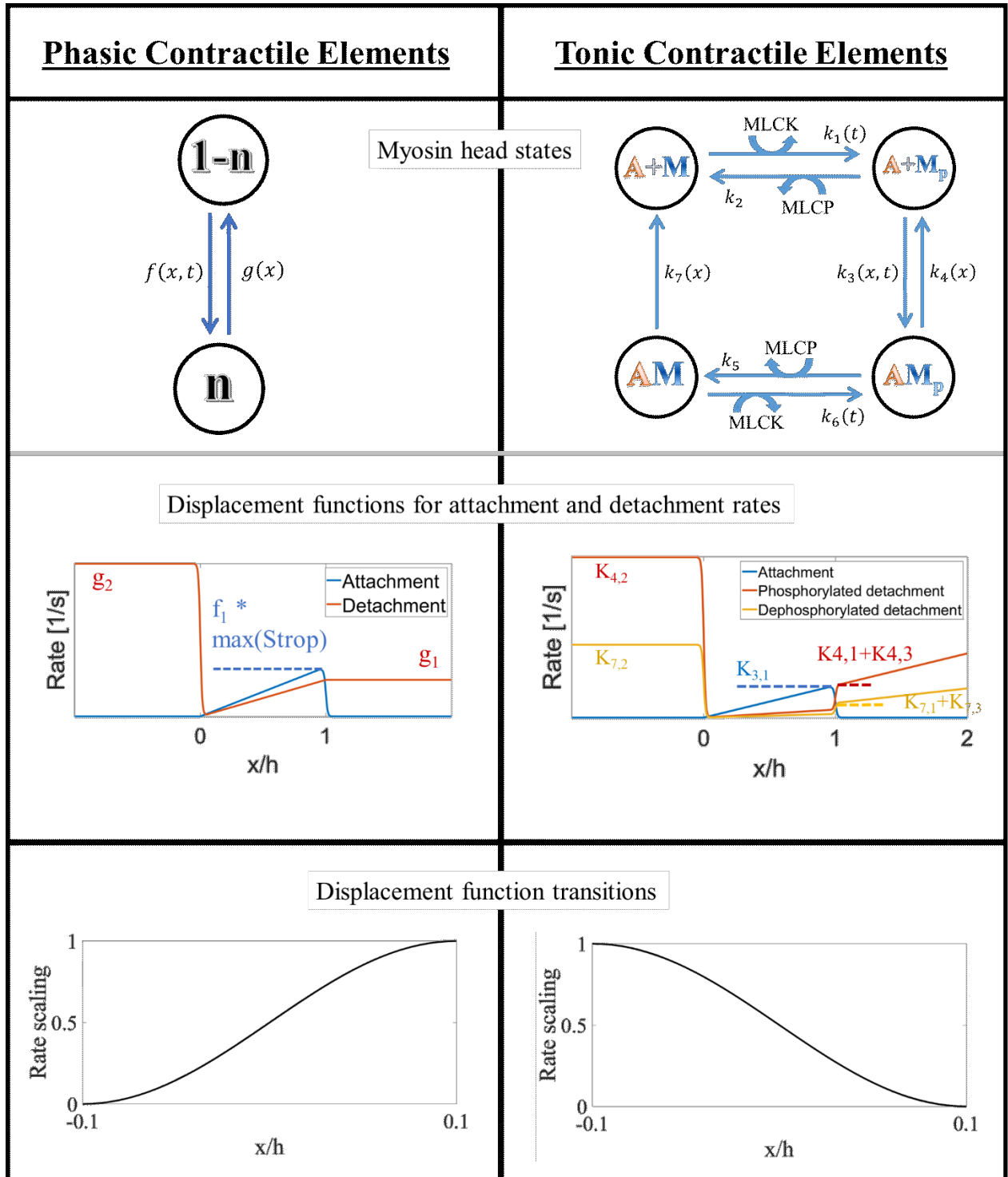


Figure 14: Molecular models of phasic and tonic CE myosin states (upper row) and myosin head rates (middle row) and transitions between piecewise rate functions (lowest row)

To analyse the system's efficiency (see Figure 15 for an overview of model energetics calculations), the rate of energy liberation is calculated. One molecule of ATP is hydrolysed per detachment or phosphorylation process. The energy liberated by detachment is calculated from the myosin detachment rate and number of attached heads. The number of attached heads is given by the

proportion of heads attached integrated over all displacements and multiplied by the density of actin sites. The total energy liberation rate is the product of the number of CE rows and the energy liberated from a single row, then summed over all LMCs.

$$\frac{dEnergy_P}{dt} = N_{Cell} N_{Rows} \rho e N_{um_P} N_P \int_{-\infty}^{\infty} g \times n_P dx \quad (30)$$

where $Energy_P$ is the energy liberated by detachment of phasic myosin heads, N_{Cell} is the circumferential number of LMCs, e is the energy liberated by hydrolysis of one ATP molecule

The rate of energy liberation in phasic CEs is due solely to the energy liberated in detachment. The energy liberation in tonic CEs is the sum of detachment and phosphorylation events (Mijailovich et al., 2000). The liberation rates here are summed over all CEs to give the energy liberated by each LMC and then summed over all LMCs.

$$\frac{dEnergy_{T,PhosDetach}}{dt} = N_{Cell} \rho e N_{Rows} N_{um_T} N_T \int_{-\infty}^{\infty} k_4 \times AM_p dx \quad (31a)$$

$$\frac{dEnergy_{T,UnphosDetach}}{dt} = N_{Cell} \rho e N_{Rows} N_{um_T} N_T \int_{-\infty}^{\infty} k_7 \times AM dx \quad (31b)$$

$$\frac{dEnergy_{T,DetachPhos}}{dt} = N_{Cell} \rho e N_{Rows} N_{um_T} N_T k_1 \int_{-\infty}^{\infty} M dx \quad (31c)$$

$$\frac{dEnergy_{T,AttachPhos}}{dt} = N_{Cell} \rho e N_{Rows} N_{um_T} N_T k_6 \int_{-\infty}^{\infty} AM dx \quad (31d)$$

$$\frac{dEnergy_T}{dt} = N_{Cell} \rho e N_{Rows} N_{um_T} N_T \left(\int_{-\infty}^{\infty} k_4 \times AM_p dx + \int_{-\infty}^{\infty} k_7 \times AM dx + k_1 \int_{-\infty}^{\infty} M dx + k_6 \int_{-\infty}^{\infty} AM dx \right) \quad (31e)$$

where $Energy_{T,PhosDetach}$ is the energy liberated by detachment of phosphorylated tonic myosin heads, $Energy_{T,UnphosDetach}$ is the energy liberated by detachment of unphosphorylated myosin heads, $Energy_{T,DetachPhos}$ is the energy liberated by phosphorylation of detached myosin heads, $Energy_{T,AttachPhos}$ is the energy liberated by phosphorylation of attached myosin heads, $Energy_T$ is the total energy liberated by tonic CEs.

The rate of doing work per LMC, dW/dt , is given by the force multiplied by the shortening velocity, which is then summed over all cells.

$$\frac{dW}{dt} = N_{Cell} F \times -\frac{dL_{Cell}}{dt} \quad (32)$$

The cell work is overall work done by LMCs (contributions of phasic and tonic CE works, temporary storage in the phasic spring and cell stiffness, losses to tonic dashpot and cell viscosity).

The total energy liberated and work done comes from integrating their rates over the duration of a cycle. The overall energy liberated by LMCs is the sum of energy liberation by phasic and tonic CEs. Whatever liberated energy not used to do useful work is lost as heat. The energy efficiency (η) is the useful work done divided by the energy liberated.

$$\eta = \frac{W}{Energy_P + Energy_T} \quad (33)$$

Plots for the energy balance for an LMC under reference conditions are given in Appendix 1.

Energy loss rates due to viscosity are calculated as

$$\frac{dE_{TDloss}}{dt} = P N_{Cell} \mu_T \left(N_T \frac{dY_{HHM}}{dt} \right)^2 \quad (34a)$$

where E_{TDloss} is the loss of energy to viscosity of the tonic dashpot

$$\frac{dE_{CSloss}}{dt} = N_{Cell} \mu_{Cell} \left(\frac{dL}{dt} \right)^2 \quad (34b)$$

where E_{CSloss} is the loss of energy to viscosity of the cell. An additional loss (E_{lymph}) occurs at the lymphangion level due to the behaviour of the lymph being pumped

$$\frac{dE_{lymph}}{dt} = \frac{64\mu L_v}{\pi D^3} (Q_1^2 + Q_2^2) \quad (34c)$$

At the sliding filament level, energy is lost because not all heads complete the entire powerstroke (E_{PS}). Incomplete powerstrokes liberate the same amount of energy but cannot convert all of the energy liberated to work (Barclay and Loiselle, 2020, Eisenberg et al., 1980). This is combined with

the fact that ATP hydrolysis is irreversible so the excess liberated energy is not re-captured and is lost to entropy as heat (Loiselle et al., 2010, Chapman and Loiselle, 2016). The conversion to heat is likely via internal friction between the myosin heads and actin binding sites (Chapman and Loiselle, 2016).

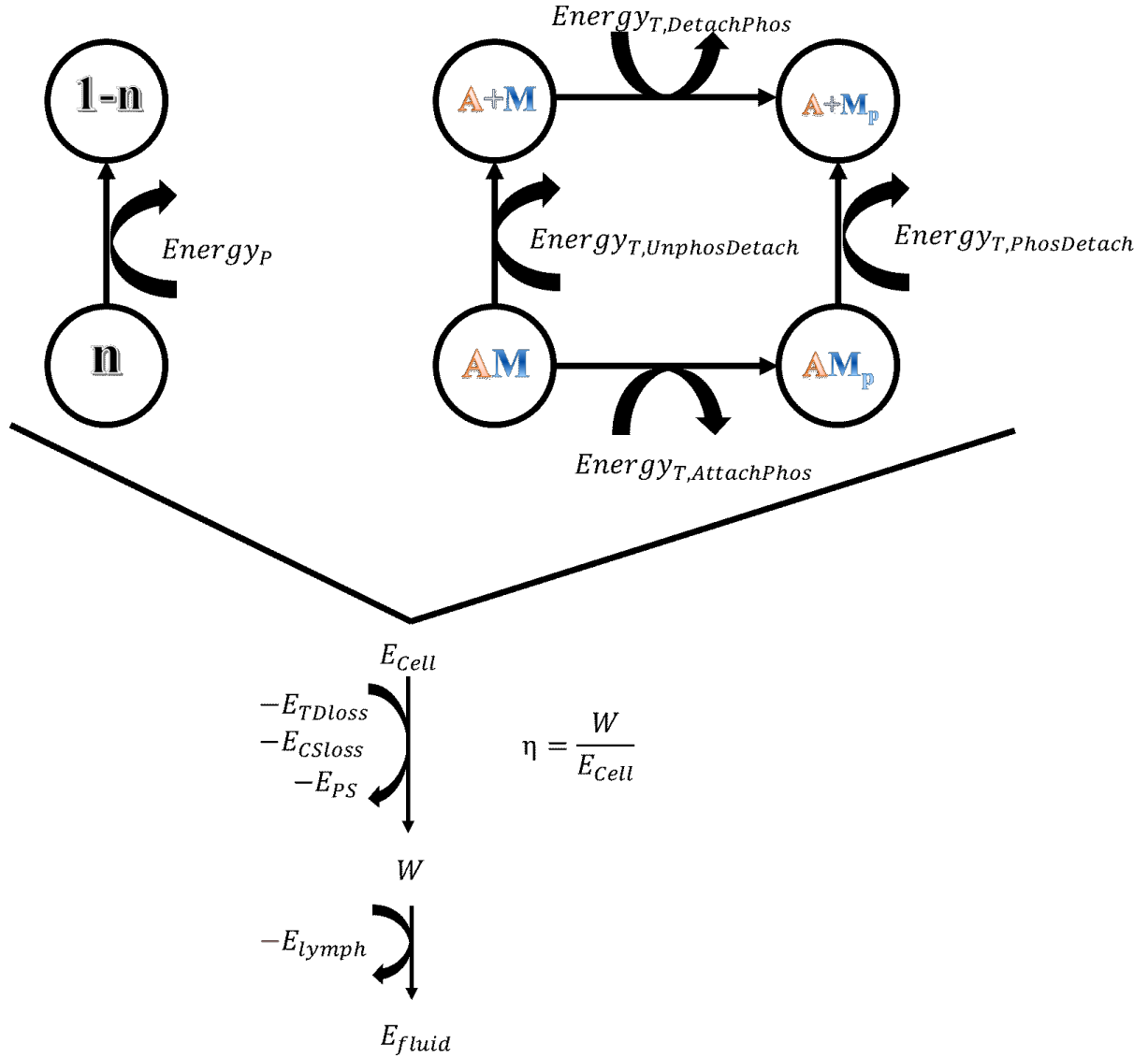


Figure 15: Figure summarising the energetics in the LMC model. Energy is liberated by detachment in both the phasic and tonic components, and additionally by phosphorylation in the tonic component. The liberation by LMCs is the sum of contributions from tonic and phasic components, which is then reduced by losses to the viscosities of the tonic dashpot, the cytoskeleton, and incomplete powerstrokes, giving the work done by the cell (the efficiency of the muscle cell is the ratio of cell work and total energy liberation). The cell work then loses energy overcoming the lymph viscosity to give energy transfer to lymph.

Table 1: Rate constants used for phasic and tonic myosin head state transitions

Constant symbol	Value [1/s]	Source
f_1	620	Fit to general features
g_1	50	(pressure, diameter, flow) of

g_2	210	rat mesenteric lymphangion experiments (Davis et al., 2008, Davis et al., 2011, Davis et al., 2012, Scallan et al., 2016, Zawieja et al., 1999)
$K_{3,1}$ $K_{4,1}$ $K_{4,2}$ $K_{4,3}$ $K_{7,1}$ $K_{7,2}$ $K_{7,3}$ K_1 K_2 K_5 K_6	0.88 0.22 $4(K_{3,1} + K_{4,1})$ $3K_{4,1}$ 0.1 $20K_{7,1}$ $3K_{7,1}$ 0.35 0.1 K_2 K_1	Airway smooth muscle cells (Fredberg et al., 1999)

3.2.2.1. Excitation-contraction coupling

To induce contractions, ECC was initiated via a periodic intracellular free calcium concentration (c).

This concentration was used to calculate the saturation of binding proteins. Saturations alter the transition rates between myosin head states to influence force generation (Wang et al., 2008, Yochum et al., 2015, Wong, 1971, Wong, 1972). The calcium concentration in this model is not affected by the regulatory mechanisms operating in lymphatic muscle (e.g. shear- and pressure-dependent changes in calcium concentration levels and timing) for simplicity in this first implementation of the model, and future work underway to capture such effects.

The rat mesenteric lymphatic vessel calcium measurements of Zawieja and colleagues (Zawieja et al., 1999) were fit (Figure 16) and calcium oscillations modelled as sinusoidal oscillations about the average diastolic concentration.

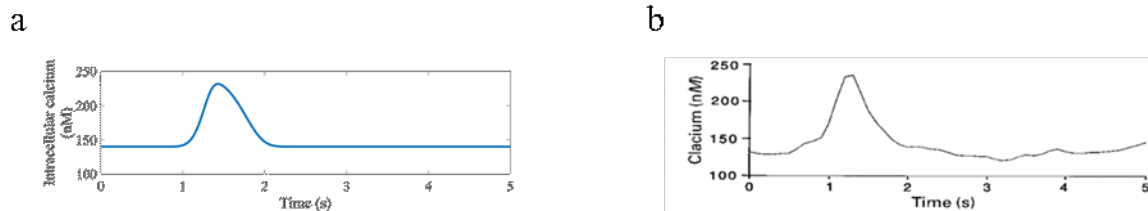


Figure 16: Calcium plots (a) fit to the calcium concentration recording of (Zawieja et al., 1999) (b) calcium concentration recording of (Zawieja et al., 1999)

$$c(t) = \begin{cases} (Ca_{amp} - Ca_d) \frac{a_2}{b_2 - a_2} [\exp(-a_2 t_p^6) - \exp(-b_2 t_p^6)] + Ca_d & \text{if } t_p < t_{ca} \\ Ca_d (1 + Ca_{amp} \sin(\omega_{ca} 2\pi(t_p - t_{ca}))) & \text{if } t_p \geq t_{ca} \end{cases} \quad (35)$$

where Ca_{amp} is the peak calcium concentration, Ca_d is the diastolic calcium concentration, a_2, b_2 are constitutive parameters, t_p is the time from the beginning of the current cycle, t_{ca} is the time in the current cycle for onset of calcium oscillations, Ca_{amp} is the amplitude of calcium oscillations as a fraction of the average diastolic calcium, ω_{ca} is the frequency of calcium oscillations

Calcium oscillations were modelled as sinusoidal fluctuations in diastolic calcium concentration with various amplitudes and frequencies. Amplitudes were expressed as a percentage of the average diastolic calcium concentration. Frequencies were included as the number of oscillations per diastolic period. This model of calcium transient was chosen because it allows specification of peak and resting calcium levels, as well as timings. This model can therefore be manipulated to provide many different forms of calcium concentration without many parameters and gives a smooth peak in calcium concentration which is more biological than other functions used to model calcium transients in other muscle models (Bursztyn et al., 2007). A sinusoidal approximation was chosen for fluctuations from spontaneous transient depolarisations despite their randomness as this allowed reproducibility of results and the comparison of results with different myosin head compositions, pressures, or timing can be compared.

The calcium saturations of TnC and CaM were modelled using Hill functions following published models from bladder smooth muscle (Laforêt et al., 2011), uterine smooth muscle (Yochum et al., 2015) and rabbit skeletal muscle (Grabarek et al., 1983). The calcium binding/unbinding rates for both TnC and CaM are much faster than the rates of actomyosin cycling (Robertson et al., 1981, Cannell and Allen, 1984, Faas and Mody, 2012), so a quasi-steady state can be assumed. Calcium-independent regulatory mechanisms affecting myosin phosphorylation are not considered here. Calcium saturations for TnC and CaM with reference binding properties (see Table 2) are shown in Figure 17.

TnC saturation (S_{Trop}) is calculated using

$$S_{Trop} = \frac{c^{n_{mTrop}}}{c^{n_{mTrop}} + c_{0.5,Trop}^{n_{mTrop}}} \quad (36a)$$

where n_{mTrop} is the Hill coefficient for TnC, $c_{0.5,trop}$ is the half saturation concentration for TnC

CaM saturation (S_{CaM}) is calculated using

$$S_{CaM} = \frac{c^{n_{mCaM}}}{c^{n_{mCaM}} + c_{0.5,CaM}^{n_{mCaM}}} \quad (36b)$$

where n_{mCaM} is the Hill coefficient for calmodulin, and $c_{0.5,CaM}$ is the calcium concentration at which half of the calmodulin calcium binding sites are occupied, representing the affinity of the protein to calcium

The phosphorylation and attachment rates were multiplied by the saturation of the regulatory proteins because the overall saturation is representative of the probability that any given protein will be saturated. The probability of state transition is then the product of the probability that the myosin site is “active” (regulatory protein saturated) and the probability of transition given that a site is “active”.

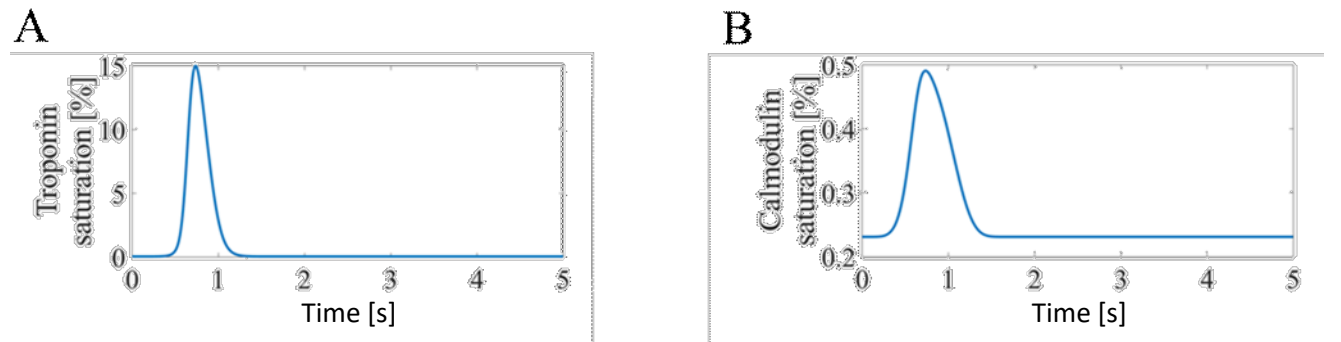


Figure 17: Time-dependent saturations of (A) TnC and (B) calmodulin used in all results with the exception of calcium binding sensitivity.

Table 2: Muscle model parameters other than rate function constants

Symbol	Description	Value [dimension]	Source
N_{Cell}	Number of LMCs around lymphangion circumference	4 [-]	Unpublished estimate of D. Zawieja
N_{Rows}	Total number of parallel rows of CEs	3 x 6e3 [-]	Reference value chosen Estimate from SEM image of rat mesenteric lymphatic (Muthuchamy et al., 2003)
Num_p	Number of myosin heads per phasic CE	4500 [-]	Reference value chosen Combined volume estimate from cultured LMCs in (Muthuchamy et al., 2003) with concentration of heads from (Bagshaw, 1993)
Num_T	Number of myosin heads per tonic CE	1000 [-]	Reference value chosen Assumed slight reduction in head number from phasic due to less structural organization
E_{Cell}	Stiffness of LMC cytoskeleton	75 [dyne/cm]	Reference value chosen so that the pressure shape resembles published recordings from rat mesenteric lymphangions In range of (Trepap et al., 2007) for human airway smooth muscle
μ_{Cell}	Dynamic viscosity of (one-dimensional) LMC	50 [(dyne s)/cm]	Reference value chosen

			In range of (Treat et al., 2007) for human airway smooth muscle
N_{phasic}	Series number of phasic CEs	14 [-]	Made to give approximate lengths of striated CE lengths observed in other muscles
N_{tonic}	Series number of tonic CEs	14 [-]	Made to give approximate lengths of smooth muscle CE lengths observed
ρ	Length density of actin binding sites	6e5 [1/cm]	Assumed consistent between CE types. (Huxley, 1957) gave an actin site separation of 153Å for frog sartorius muscle (equivalent to density of 6.5e5[1/cm], 8% difference) Airway smooth muscle (Brook and Jensen, 2014)
h	Powerstroke length	15.6 [nm]	Assumed consistent between CE types Frog sartorius muscle (Huxley, 1957)
K_{Hux}	Stiffness constant of phasic myosin heads	0.4 [dyne/cm]	Frog sartorius muscle (Huxley, 1957)
K_{HHM}	Stiffness constant of tonic myosin heads	1.8 [dyne/cm]	Airway smooth muscle (Brook and Jensen, 2014)
$Ca_{1/2,Trop}$	Calcium concentration for half saturation of cardiac TnC	0.27 [μM]	Reference value chosen
$Ca_{1/2,CaM}$	Calcium concentration for half saturation of CaM	8 [μM]	Reference value chosen
n_{mTrop}	Hill exponent for CaM calcium saturation	12 [-]	Reference value chosen

n_{mCaM}	Hill exponent for CaM calcium saturation	1.5 [-]	Reference value chosen
$cycletime$	Duration of total contractile cycle	5 [s]	Rat mesenteric lymphatic muscle (Zawieja et al., 1999)
Ca_{amp}	Peak calcium concentration	240 [nM]	Rat mesenteric lymphatic muscle (Zawieja et al., 1999)
Ca_d	Diastolic calcium concentration	140 [nM]	Rat mesenteric lymphatic muscle (Zawieja et al., 1999)
a	Constitutive parameter for intracellular free calcium concentration	24.17 [s ⁻⁶]	Rat mesenteric lymphatic muscle (Zawieja et al., 1999)
b	Constitutive parameter for intracellular free calcium concentration	0.5278 [s ⁻⁶]	Rat mesenteric lymphatic muscle (Zawieja et al., 1999)
L_{ref}	Length of an LMC with zero storage by the cytoskeleton	0 [cm]	Will vary with length adaptation
μ_T	Tonic dashpot (one-dimensional) viscosity constant	10 [(dyne s)/cm]	Reference value chosen
a_p	Constitutive parameter for strain-stiffening of phasic spring	5.1282e-23 [dyne/cm]	Fit to titin (in range from various references) (Kellermayer et al., 2003, Labeit et al., 2003, Linke and Grützner, 2008)
b_p	Constitutive parameter for strain-stiffening of phasic spring	7.3838e+3 [1/cm]	Fit to titin (in range from various references) (Kellermayer et al., 2003, Labeit et al., 2003, Linke and Grützner, 2008)

3.2.3. Lumped parameter model of lymphatic pumping

To test the response of the muscle model, it was incorporated into the latest version of an existing one-dimensional ODE-based lumped parameter model that has been extensively validated (Bertram et al., 2011, Bertram et al., 2014a, Bertram et al., 2014b, Bertram et al., 2016b, Bertram et al., 2017,

Jamalian et al., 2013, Jamalian et al., 2016, Jamalian et al., 2017). This model has been through several iterations with different versions of the passive tube law, the valve resistance and the prescription of intrinsic contractions. This model includes conservation of mass (equation 37), conservation of axial momentum (equations 38a-d) and a circumferential wall-force balance (equation 39) from the latest iterations of the model (Jamalian et al., 2017) into which the intrinsic contractions from the above cell model were incorporated through the LMC force. Momentum conservation includes terms for resistances of the lymphangion body and valves. Pressure boundary conditions are applied at the inlet and outlet of a single lymphangion or chain of lymphangions. The wall force balance is based on the central lymphangion pressure (p_m) and includes a passive elasticity term (pressure-diameter tube law fitted to experimental data), intrinsic contractions, and the pressure external to the lymphangion. In previous iterations of this lymphangion model, the intrinsic contractions were based on prescribed diameter- and time-dependencies. This work replaces the applied intrinsic contractions with the lymphatic muscle model. Passive viscoelasticity of LMCs was included in addition to the passive pressure-diameter fit (plotted in Figure 18) because the passive, purely elastic tube law is dominated by collagen and elastin fibers in the vessel wall rather than cytoskeletal stiffness of the LMCs. Cytoskeletal stiffness was still included because it affects the force generated by LMCs. Appendix 1 shows the effects of varying the cytoskeletal stiffness and that this had a significant impact on the model output. Here we use i to index the lymphangion in a chain of z simultaneously contracting lymphangions

$$\frac{dD_i}{dt} = 2(Q_i - Q_{i+1})/\pi D_i L_v \quad (37)$$

$$p_{down,i-1} - p_{up,i} = Q_i R_{Vi} \quad (38a)$$

$$P_{up,i} - P_{mid,i} = Q_i R_{ves,i} \quad (38b)$$

$$P_{mid,i} - P_{down,i} = Q_{i+1} R_{ves,i} \quad (38c)$$

$$P_{down,i} - P_{up,i+1} = Q_{i+1} R_{Vi+1} \quad (38d)$$

$p_{down,i-1} = p_a$ and $p_{up,i+1} = p_b$ are the inlet and outlet boundary conditions, respectively

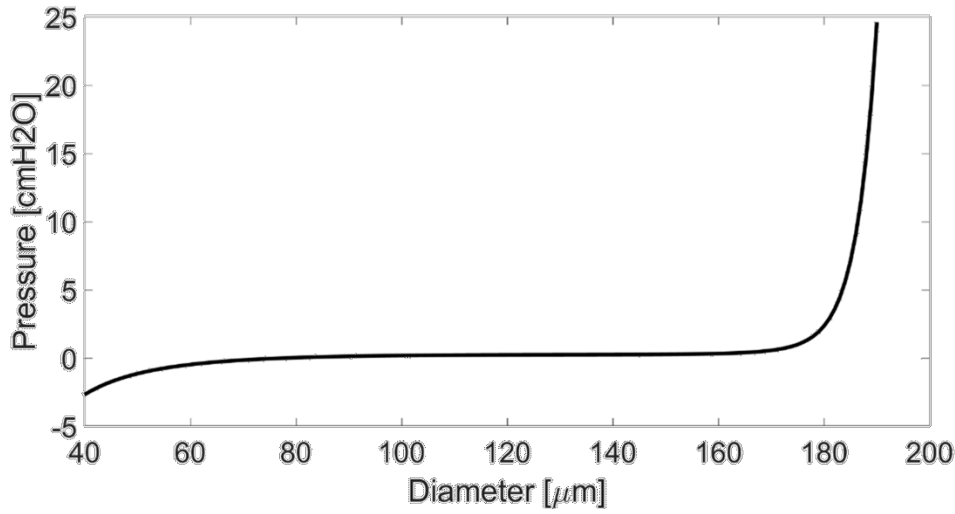


Figure 18: Plot of the passive tube law for the pressure of the lymphatic wall at different diameters

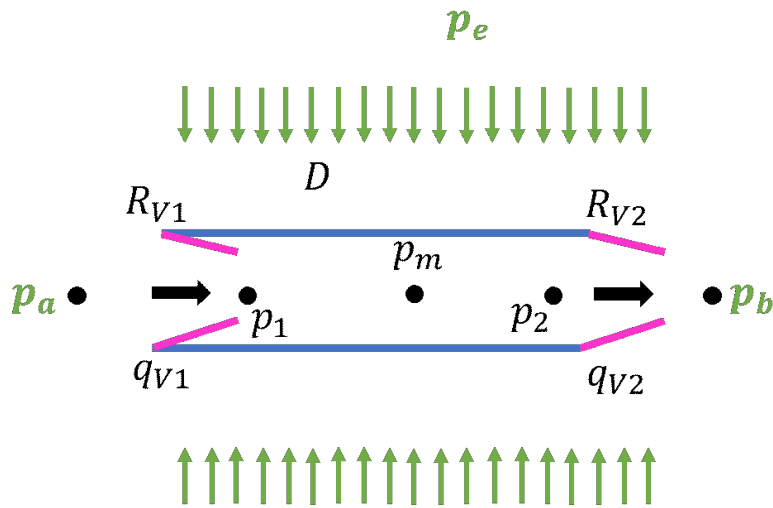


Figure 19: Schematic of a lymphangion. Boundary conditions on pressure are given in green, valves are in pink

Several LMCs around the lymphangion are assumed to be circumferentially oriented. Direct transmission of force between LMCs is assumed (no viscous losses or elastic storage in the extracellular matrix). Here a single layer of LMCs is modelled, but multiple layers could be modelled. Modelling multiple layers would require summing the forces of different layers. The resulting wall-force balance for mid-lymphangion pressure is

$$p_{m,i} = p_{ext} + f_{pas}(D_i) + \frac{2F_i}{D_i L_v} \quad (39)$$

where p_{ext} is the pressure external to the lymphangion, f_{pas} is the passive tube law, D is lymphangion diameter, L_v is the axial length of a lymphangion

The length of each LMC (L_{cell}) is assumed to be the same for all cells in a single layer surrounding a lymphangion. Cell length is calculated from a circumferential length balance.

$$L_{Cell,i} = \frac{\pi D_i}{N_{Cell}} \quad (40)$$

The wall-force balance with zero intrinsic force is

$$p_m - p_e = f_{pas}(D_0) \quad (41a)$$

The reference length (for zero force) of the phasic parallel spring is therefore set to be the phasic CE length with zero intrinsic force and multiplied by a reducing factor $\vartheta = 0.1$ to ensure contractile force giving a reference phasic spring length of

$$Y_{P,ref} = \vartheta \frac{\pi D_0}{N_{Cell}(N_P + N_T)} \quad (41b)$$

The ejection fraction (EF), a commonly used metric for lymphatic pumping, was calculated from the minimum and maximum diameters to compare the simulation pumping with published experiments.

$$EF_i = \frac{\max(D_i)^2 - \min(D_i)^2}{\max(D_i)^2} \times 100 \quad (42)$$

The useful energy transferred to fluid movement was calculated from the volumetric outflow rate and the adverse pressure difference following (Bertram et al., 2016b)

$$\frac{dE_{fluid}}{dt} = \bar{Q}_{z+1}(p_b - p_a) \quad (43)$$

The muscle model was then run for a chain of four lymphangions with the head states updated independently with identical calcium input and the only difference being the pressure conditions with alternate velocities.

3.2.3.1 Prescribed contractions

Results obtained using the coupled muscle-lymphangion model were compared to results from the lymphangion model with prescribed intrinsic contractions, the only difference being that the intrinsic contraction term in the wall-force balance depending on prescribed time- and diameter- dependencies of tension (comparison of equations 39 and 44). The wall-force balance for mid-lymphangion pressure with prescribed contractions is

$$p_{m,i} = p_e + f_{pas}(D_i) + \frac{2M_t M_d(D_i)}{D_i} \quad (44)$$

so the intrinsic force for comparison to the cell force from the muscle model is $F = M_t M_d L_v$

The time-dependent input function for tension (Figure 20) is the latest version as in (Jamalian et al., 2017)

$$t_{temp} = \text{mod}(t, \text{cycletime}) \quad \text{cycletime} = 0.5(t_r + t_c) + t_d$$

$$M_t = \begin{cases} M_0 & \text{if } t_{temp} > 0.5(t_r + t_c) \\ M_a \left(1 - \cos\left(\frac{2\pi t_{temp}}{t_c}\right) \right) / 2 + M_0 & \text{if } t_{temp} > 0.5t_c \\ M_a \left(1 - \cos\left(\frac{2\pi (t_{temp} + 0.5(t_r + t_c))}{t_r}\right) \right) / 2 + M_0 & \text{if } 0.5t_c < t_{temp} < 0.5(t_r + t_c) \end{cases}$$

(45)

where M_t is the time-dependence of contractions, M_0 is the tonic tension, M_a is the peak tension, t_{temp} is the time in the current cycle, t_c is twice the duration of contraction and t_r is twice the duration of relaxation

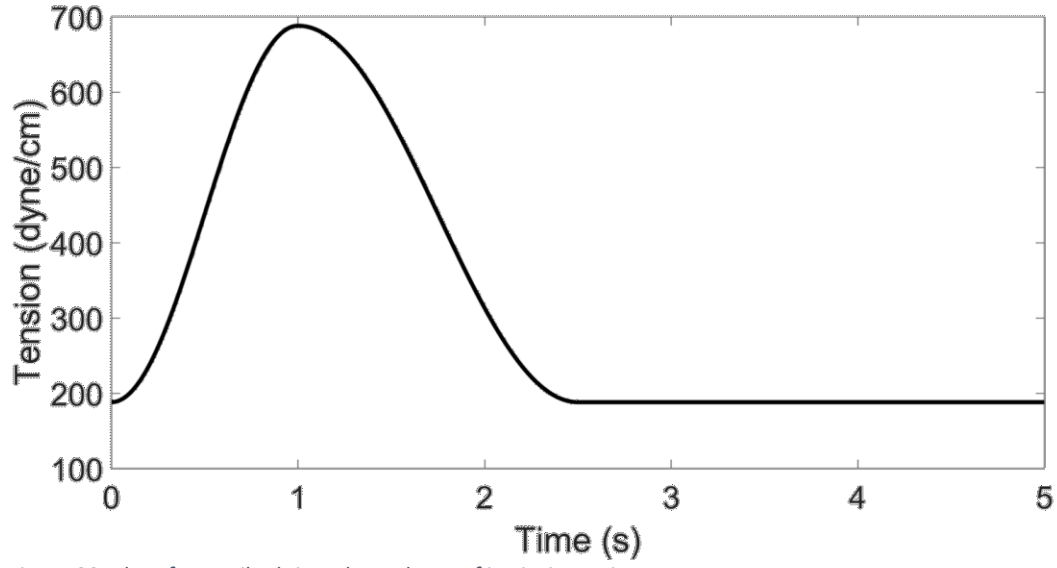


Figure 20: Plot of prescribed time-dependence of intrinsic tension

The diameter-dependent input function (Figure 21) is also the latest version used in (Jamalian et al., 2017)

$$M_{d0,i} = 5.5 / (1 + \exp(-s_{d0}(D_i - D_0))) \quad (46a)$$

$$M_{d1,i} = 0.5 / (1 + \exp(-s_{d1}(D_i - D_1))) \quad (46b)$$

$$M_{d0,i} = 2 / (1 + \exp(s_{d2}(D_i - D_2))) \quad (46c)$$

$$M_{d,i} = \frac{M_{d0,i} + M_{d1,i} + M_{d2,i} - 2}{6} \quad (46d)$$

where M_d is the diameter-dependence of intrinsic contractions, s_{d0} , s_{d1} , s_{d2} , D_0 , D_1 and D_2 are constitutive constants

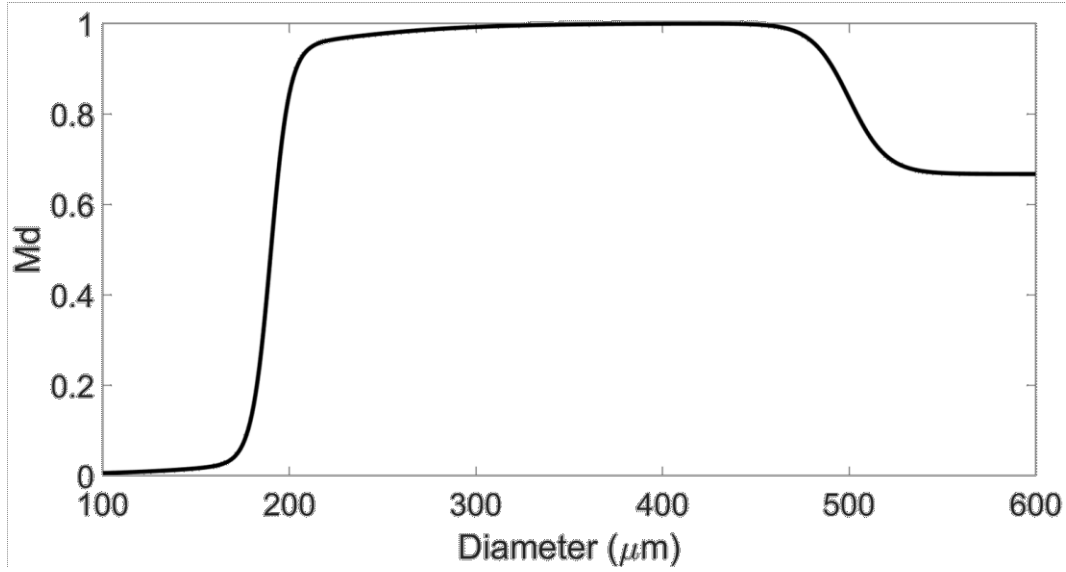


Figure 21: Plot of prescribed diameter-dependence of intrinsic tension

Valve resistance (Figure 22) is calculated from the sum of two sigmoids (one for opening and one for failure)

$$R_{v,i} = R_{v,min} + R_{v,max} \left[\frac{1}{1 + \exp(s_o(\Delta p_i - p_o))} + \frac{1}{1 + \exp(-s_f(\Delta p_i - p_f))} \right] \quad (47)$$

where $R_{v,min}$ is the resistance of the open valve, $R_{v,max}$ is the additional resistance on valve closure, s_o is the slope of the valve opening, Δp is the pressure difference across the valve (upstream minus downstream), p_o is the pressure for valve opening, s_f is the slope of failure, p_f is the pressure of valve failure

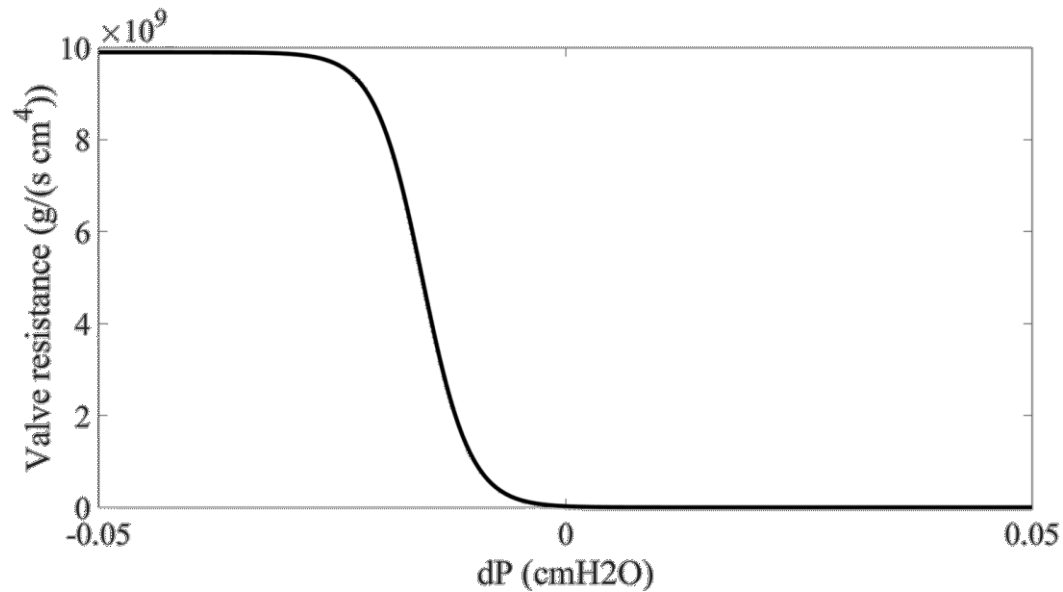


Figure 22: Plot of the resistance of the valve against the pressure difference across it (upstream - downstream)

The calculations for work done in the prescribed contraction model were the equivalent to equation 32 for the muscle model as given by (Bertram et al., 2016b)

$$W_{in,i} = \pi L_v \oint M_d M_t dt \quad (48)$$

where W_{in} is the work done by intrinsic contractions

The constants in time-dependence of intrinsic contractions (contracting, relaxing diastolic durations, peak and tonic tension) were varied to obtain the best match with reference results for the coupled muscle-lymphangion model but diameter-dependent constants were left at the previously published values of Jamalian and colleagues with values given in Table 3.

Table 3: Constants used in the prescribed intrinsic contraction model for comparison to muscle model results

Symbol	Value [units]
M_0	188 [dyne/cm]
M_a	500 [dyne/cm]
t_c	2 [s]
t_r	4 [s]
t_d	1 [s]
s_{d0}	2000 [1/cm]
D_0	0.019 [cm]
s_{d1}	250 [1/cm]
D_1	0.021 [cm]
s_{d2}	1000 [1/cm]
D_2	0.050 [cm]

3.2.4. Solution method

The solution to this system of equations was obtained in two stages. In the first stage, the resting (zero muscle force) equilibrium diameter was calculated based on the mid-lymphangion pressure.

This was followed by solution of the full coupled model of lymphangion and muscle (algorithm flowchart Figure 23). The initial conditions for the lymphangion were diameter (0.02 cm), upstream pressure ($= p_a$) and downstream pressure ($= p_b$). Equilibrium diameter was obtained using the adaptive time step MATLAB solver ODE15S. Phasic and tonic myosin heads were initialised as all detached, and tonic myosin heads all dephosphorylated. CEs were initialised to equal lengths. The reference lengths for the spring in parallel with phasic CEs and LMC stiffness were calculated as fractions of the initial length. This was done to ensure that the phasic parallel spring and the LMC stiffness contributed contractile forces. A second solver was then used to develop periodic contractions with the coupled lymphangion and muscle equations. The ODE for diameter (equation 37) was solved using first-order forwards differencing as a simple method with low computational intensity. The PDEs for myosin head states of both isoforms (equations 26 and 28) were solved using a second-order Godunov solver (Brook and Jensen, 2014, Hiorns et al., 2014) (see Figure 24). The second-order Godunov was chosen for reasons of stability (Harten et al., 1983, Roe, 1986). This solver is an explicit upwind finite volume scheme. A first-order half time step is calculated with the effects of head transitions neglected in calculating the convective fluxes. This uses Riemann solutions at the boundaries of each displacement cell, and a separate source/sink term is used for transitions. The head distributions after this first half step are used to calculate updated fluxes through a spatial gradient for calculation of a full time step. The time step was determined using a Courant-Friederichs-Lewy condition ($dt = 0.8 dx / \max(\text{abs}[v_{Phasic}, v_{Tonic}])$) and a maximum step size of 10^{-4} s. The validity of this time step was checked by comparing the results under reference conditions with this time step to when the time step was halved, yielding negligible changes in the average flow (order $10^{-3}\%$, see Appendix 1 for details). Simulations were also run using a MacCormack predictor-corrector method instead of the Godunov and differences in the results were negligible (see Appendix 1). Displacement integrals were evaluated using trapezoidal integration. Algebraic equations for lymphangion pressures were solved at each time step using the force

resulting from updated head states to give updated pressures used in the following time step.

Simulations were considered periodic when all the following conditions were met:

$$\left| \frac{\bar{Q}_2 - \bar{Q}_1}{\bar{Q}_2} \right| \times 100 < 1 \quad (49a)$$

$$\left| \frac{dY_T}{dt} \right| \times \text{cycletime} < 2 \times 10^{-2} \text{ cm} \quad (49b)$$

$$\left| \frac{\bar{F}_T - \bar{F}_{T_{Prev}}}{\bar{F}_T} \right| \times 100 < 2 \quad (49c)$$

where $\bar{F}_{T_{Prev}}$ is the average of tonic CE force over the previous cycle

Refer to Appendix 1 for details on verification of periodicity conditions under reference conditions.

The simulation under reference conditions took 6.7 hours on a laptop with an AMD Ryzen 7 3700U processor (quad core 2.3GHz per core) and 8GB of RAM. Periodicity was reached after 10 contractile cycles. With the use of different input values, the duration of simulations varied in the range of approximately 4-10 hours (9-16 contractile cycles). Simulations struggled to reach these periodicity conditions when the lymphangion was chronically constricted, so simulations were run for a maximum of 10 cycles. For the simulations run for 10 cycles, the magnitude difference in valve flows was $< 0.09 \text{ mL/hr}$, change in tonic CE length during the final cycle was $< 2.5 \times 10^{-6} \text{ }\mu\text{m}$ and the difference in average tonic force between the final two cycles was $< 2.3\%$. These values represent minor changes between contractile cycles, relative to the magnitude of cyclic variations, that do not affect overall conclusions from the model. The simulations struggled to reach periodicity under these conditions because the flow had small values, so even a negligible difference in flows was a significant percent change.

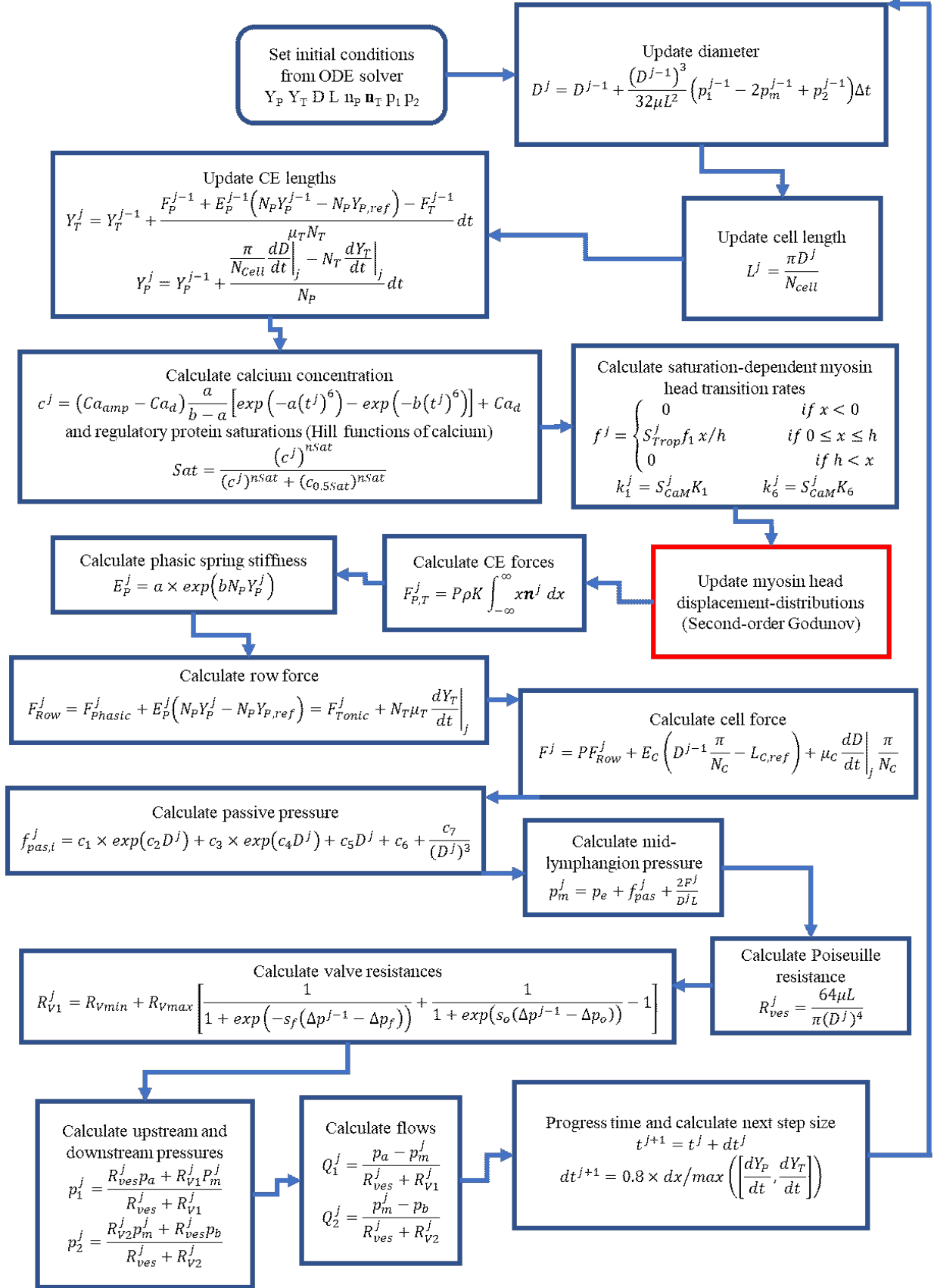


Figure 23: Flowchart of the solution algorithm for the coupled muscle-lymphangion model. j indexes the time step. The red box indicates use of a Godunov solver (algorithm in Figure 24). Note that not every variable calculated is used directly in the following step, and arrows indicate the steps rather than equation relationships

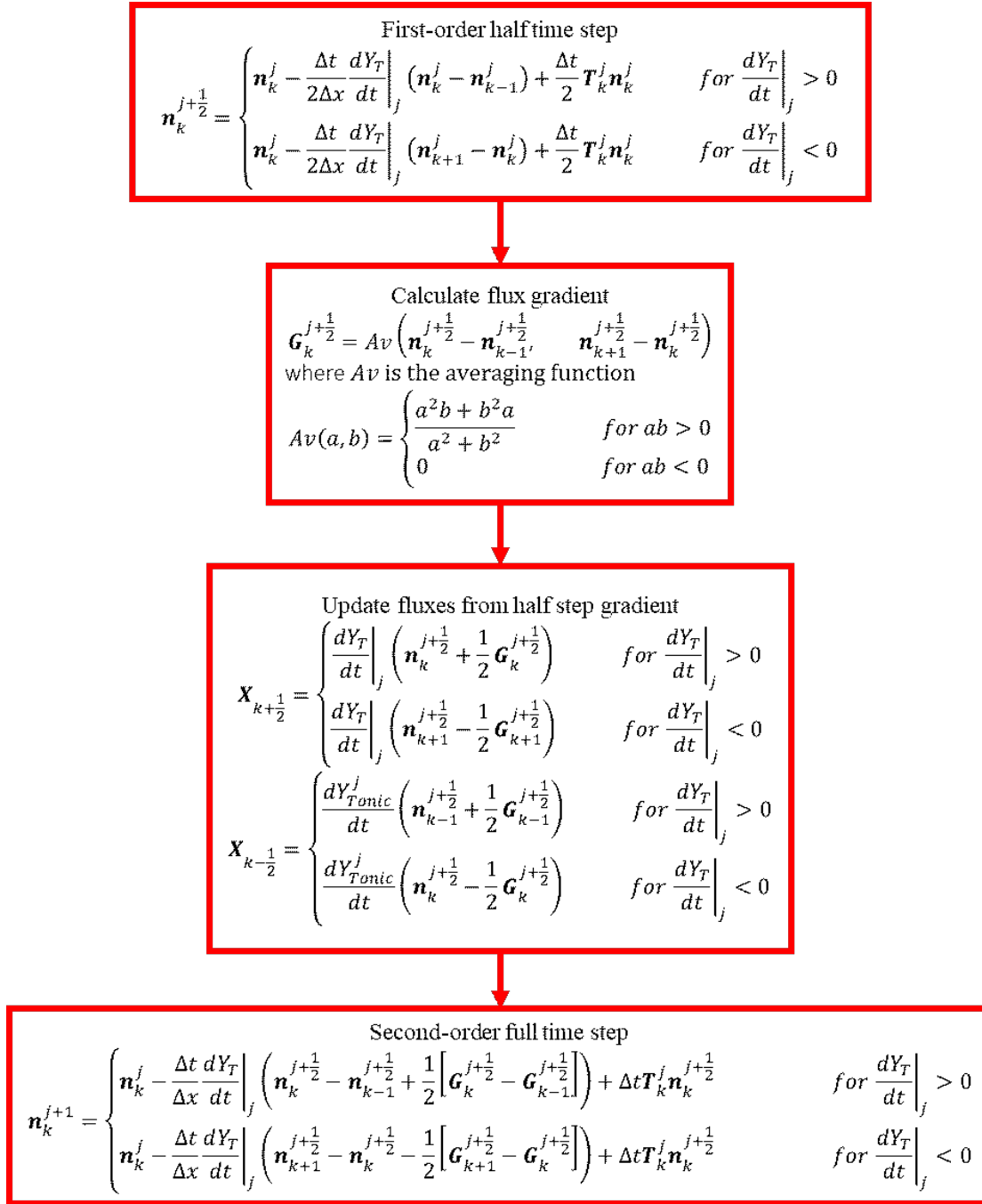


Figure 24: Solution flowchart for the second-order Godunov solver. k indexes the discretised displacement value

3.3. Parameter Sensitivity Analysis

This sensitivity analysis focusses on the parameters of the muscle model only, without the parameters involved in the lymphangion model. Our model has many independent parameters ($p = 32$), and the runtime is significant (7 hours under reference conditions). For the full set of parameters, a Latin hypercube sensitivity analysis with 100 trials would take approximately 30,800 days to run without any parallelisation. This time scales with p^{p+1} so screening was used to reduce the dimensionality of the parameter sensitivity analysis and make it more practical.

The most commonly used screening method in engineering applications is one-at-a-time sensitivity analysis (Iooss and Lemaître, 2015). We therefore ran an initial screening sensitivity analysis by individually varying parameters from their reference value and examining the effect on the average outflow. The parameters with the greatest effect on the average flow were considered the most sensitive and a more detailed general sensitivity analysis was run with this reduced set of parameters.

3.3.1. One-at-a-time analysis

One-at-a-time is a local sensitivity analysis relating model outputs for altered parameter values to results from the reference condition. The pressure conditions were maintained at $p_a = 3 \text{ cmH}_2\text{O}$, $p_b = 3.1 \text{ cmH}_2\text{O}$ and $p_{ext} = 2 \text{ cmH}_2\text{O}$. Sensitivity of the results to variations in the parameter were assessed using the ratio of the normalised change in average flow to the normalised change in input.

$$S_{i,j} = \frac{(\bar{Q}_{ref} - \bar{Q}_{i,j})/\bar{Q}_{ref}}{(Parameter_{ref,j} - Parameter_{i,j})/Parameter_{ref,j}} \quad (50)$$

where i indexes the adjusted parameter values, j indexes the parameter, \bar{Q}_{ref} is the average outflow with reference parameter values, $\bar{Q}_{i,j}$ is the average outflow with the adjusted parameter value, $Parameter_{ref,j}$ is the reference value of the parameter and $Parameter_{i,j}$ is the adjusted parameter value

This sensitivity index can be positive (increase in average flow with increase in parameter) or negative (decrease in average flow with increase in parameter) and an absolute value of one represents a linear increase, absolute value greater than one represents a superlinear relationship and less than one a sublinear relationship. See Appendix 1 for a table of results obtained from this analysis.

Designating parameters with a maximum $|S| > 1.2$ as sensitive yielded five parameters for a more in-depth global sensitivity analysis using Latin hypercube sampling. These were the peak calcium, the

phasic calcium binding properties, the phasic detachment rate for negative displacements, and the series number of LMCs around the lymphangion.

3.3.2. Latin hypercube sensitivity analysis

The range of possible values for the $k = 5$ parameters were each divided into $s = k + 1 = 6$ regions as required by Latin hypercube sampling (Marino et al., 2008). We assumed a uniform probability distribution for the range of values of each parameter. The Latin hypercube sampling method randomly takes values from each parameter's probability distribution (one value from each region) without repetition to ensure that the entire range of values for each parameter is sampled. These random values for each parameter are then assembled into a matrix with r rows for the number of samples (equivalently model runs) and k columns. One matrix represents a single Latin hypercube trial that provides a single measure of the correlation between the parameters and the average outflow. Each trial therefore involved 6 model calls and resulted in 6 sample values of average flow. Multiple trials are then required to allow for statistical separation of the influence of each parameter as they are being simultaneously randomly sampled.

Sensitivity of the model outflow on each of the parameters was calculated using the partial rank correlation coefficient (PRCC). The PRCC measures the linear relationship between the input and the output, varying between -1 and 1 . Negative values mean that the output decreases with increasing input and positive increasing with increasing output with larger magnitudes indicating stronger relationships. One PRCC value was calculated for each trial using the 6 samples. These correlation coefficients were then plotted using box plots and an overall sensitivity measure calculated from their mean over all trials.

The equation for the PRCC for a single trial is calculated as

$$PRCC_j = \frac{Covariance}{\sqrt{Variance(x_j)Variance(y)}} \quad j = 1, \dots, k \quad (51a)$$

$$Covariance = \frac{\sum_{i=1}^n (x_{ij} - \bar{x})(y_i - \bar{y})}{n-1} \quad (51b)$$

where x is input (overbar is averaged over the r samples), y is output (overbar is averaged over the n samples), i indexes the sample (combination of randomised parameter values for a single model run), j indexes input parameter

$$Variance(x_j) = \frac{\sum_{i=1}^n (x_{ij} - \bar{x})^2}{n-1} \quad (51c)$$

This analysis showed that the model was most sensitive to the peak calcium concentration (PRCC value of 0.489) with the next two sensitive parameters of $c_{0.5,Trop}$ and N_{cell} showing PRCC values approximately half of that for the peak calcium concentration (0.251 and 0.234, respectively).

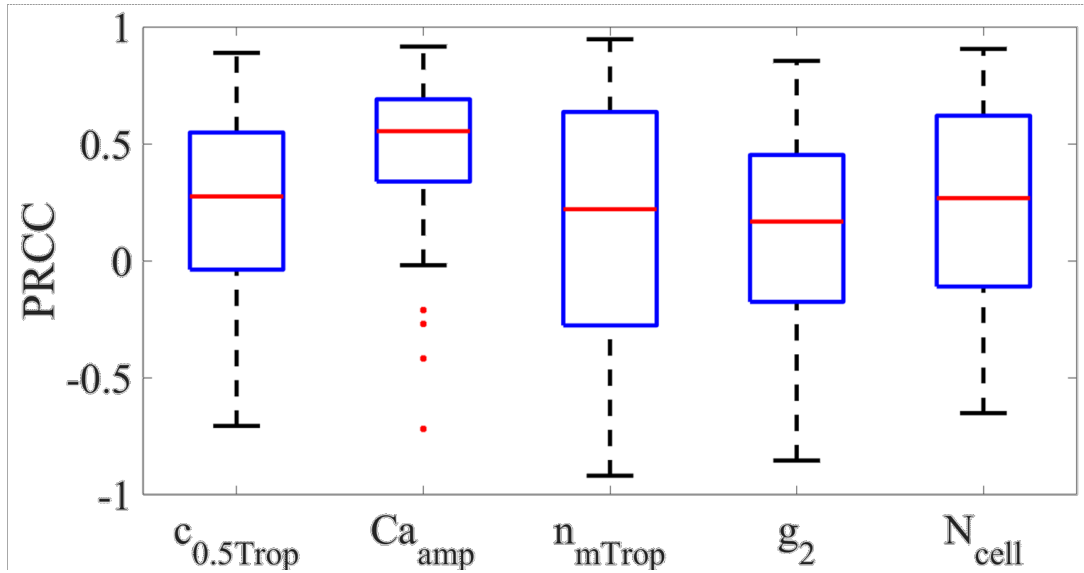


Figure 25: Boxplots of the PRCC for each parameter showing the variation between trials

Table 4: Overall sensitivity measures for each parameter

Variable	$c_{0.5,Trop}$	Ca_{amp}	n_{mTrop}	g_2	N_{cell}
Average PRCC	0.251	0.489	0.166	0.130	0.234

3.4. Results

Plots of the CE row forces (note that these are the total values for the lymphangion) against time show that tonic force is almost constant throughout the contractile cycle with a range of 2.7% the average value under reference conditions (Figure 26a). The small variation in tonic force is due to the resistance of the tonic dashpot to any changes in tonic CE length. In the absence of a tonic dashpot the phasic CEs would cause too much convection for the tonic CEs to form sufficient cross-bridges for physiologic force generation. The phasic spring provides a means for the tonic CE force to be transmitted over the whole cell when the phasic CE force drops in diastole, thus setting the diastolic diameter. The phasic force (Figure 26a) increases by 1.4 dyne in response to increased calcium concentration to cause the lymphangion to propel fluid downstream, resulting in a peak cell force of approximately 2.4 dyne (Figure 26g). The mid-lymphangion pressure increased to a peak value of 0.21 cmH₂O above the outlet (Figure 26c) and reduced to 0.06 cmH₂O below the inlet pressure to create a suction effect for diastolic filling (Figure 26c). The time-averaged flow rate was 0.02 mL/hr with a peak of 0.200 mL/hr (Figure 26e), resulting from a decrease in diameter of 41 μ m below the diastolic value of 165 μ m for an ejection fraction of 44% (Figure 26f). Muscle cells converted approximately 9.3% of free energy from ATP to work. The peak rate of energy liberation by the lymphangion was 0.30 erg/s and peak rate of muscle work was 0.055 erg/s and, during diameter recovery, the inflowing lymph performed work lengthening the muscle with a peak value of 0.011 erg/s (Figure 26h). Useful output work for fluid motion reached a peak value of 0.005 erg/s and 30.3% of the muscle work was transferred to the fluid (corresponding to 2.8% of energy liberated).

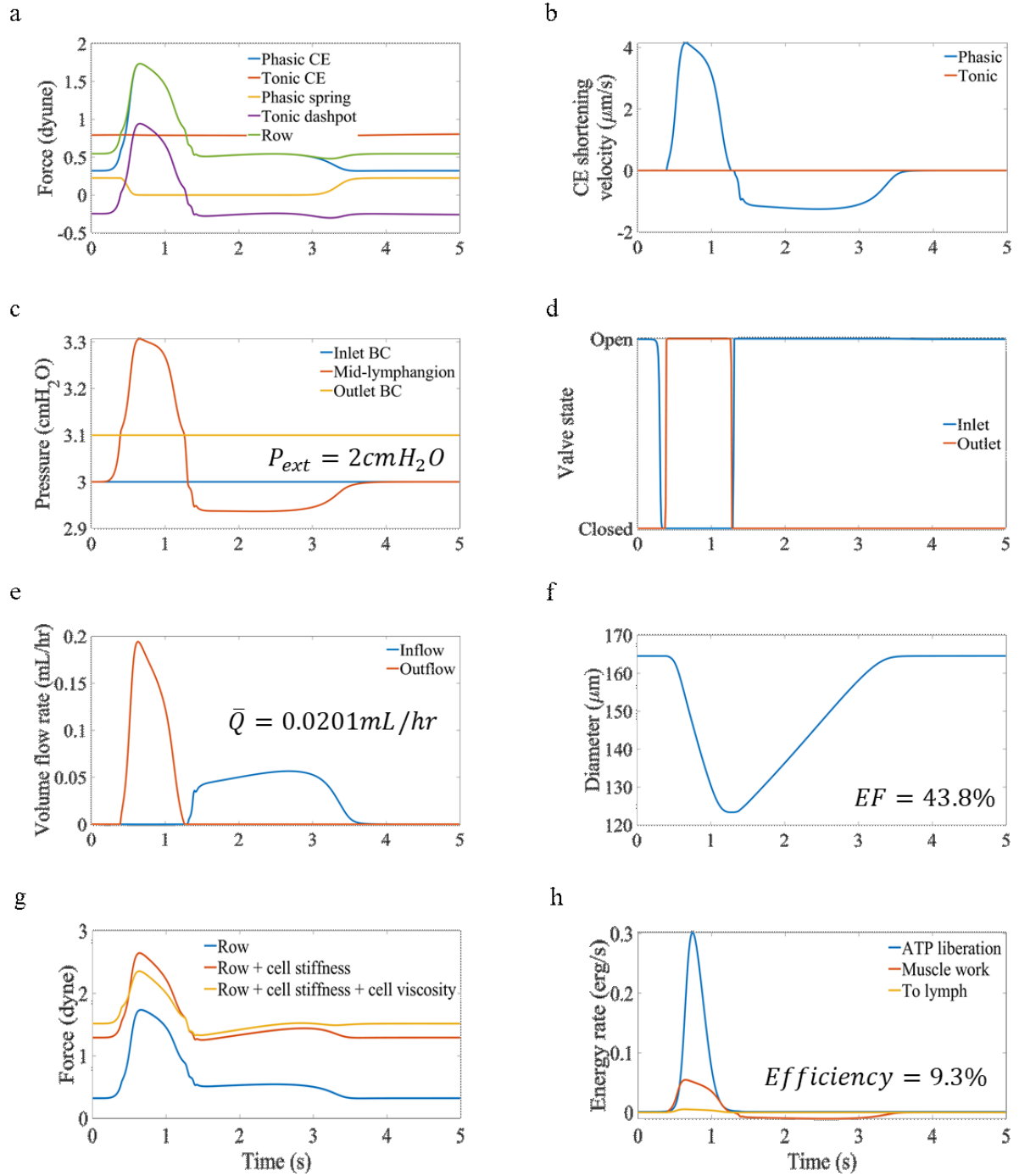


Figure 26: Panel of plots summarising results for a single lymphangion contractile cycle under reference conditions ($P_a = 3.0 \text{ cmH}_2\text{O}$, $P_b = 3.1 \text{ cmH}_2\text{O}$ and $P_{ext} = 2.0 \text{ cmH}_2\text{O}$). (a) summarises the force contributions from subcellular components (CEs, phasic spring and tonic dashpot) (b) is the shortening velocity of CEs showing the greatly reduced tonic CE velocity resulting from the presence of the tonic dashpot (c) is the pressure in the lymphangion compared to boundary conditions showing the increase to expel fluid and the decrease to refill the lymphangion (d) shows the opening and closing of the valves (e) shows the volume flow rates (f) shows the diameter of the lymphangion (g) shows the contributions of the cell viscoelasticity and CEs to the overall force generated by an LMC (h) shows the rates of useful work done by the muscle compared to the energy liberated by ATP hydrolysis to model the metabolic efficiency of lymphatic muscle and the useful energy imparted to the fluid

Model results under conditions of transmural pressure $1 \text{ cmH}_2\text{O}$ and constant axial pressure ($p_a = p_b$) were primarily compared to the results of Zawieja (Zawieja et al., 1999) obtained from

cannulated rat mesenteric lymphatics. The calcium input for the model was a fit of the calcium tracing of Zawieja's results, allowing for closer comparison of the results (Figure 27). The shape of the diameter-time plot was similar to that recorded by Zawieja, and the ejection fraction was very close to the Zawieja results obtained at 1 cmH₂O (46% from model, 45% in experiments). This similarity in ejection fraction represents similar normalized volume change and therefore the average flow output as a percentage of the diastolic volume. Normalizing the diameter values to the diastolic value showed that the muscle model generated smaller changes than recorded in Zawieja's experiments (normalized contracted diameter 0.73 compared to 0.60).

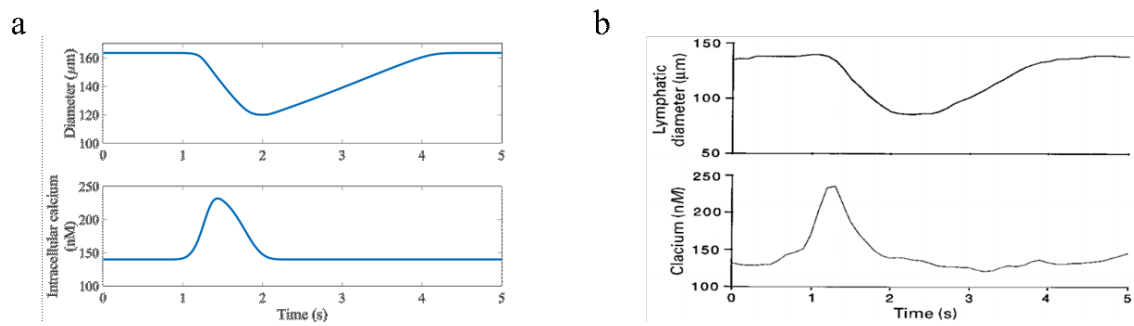


Figure 27: Comparing the diameter results of the muscle model at a transmural pressure 1 cmH₂O and no axial pressure difference to experimental data obtained from rat mesenteric lymphatics. (a) diameter and calcium from the coupled muscle-lymphangion model (b) diameter and calcium tracings from the experimental results of (Zawieja et al., 1999)

In a series of experiments (Zawieja, 2009) increased the transmural pressure applied to cannulated rat mesenteric lymphatics (1, 2, 3, 5, 7 cmH₂O) every 30 s the diameter-time relationship during recovery appeared exponential at lower transmural pressures (1 cmH₂O) and more linear after increasing the transmural pressure (2 cmH₂O and higher) as shown in Figure 28a. The reported ejection fraction for the transmural pressure results at 1 cmH₂O in this set of experiments was higher than the previous experimental results and the model results at 65%. At decreased transmural pressure (0.4 cmH₂O) the model exhibited a more exponential diameter-time shape during recovery (Figure 28b).

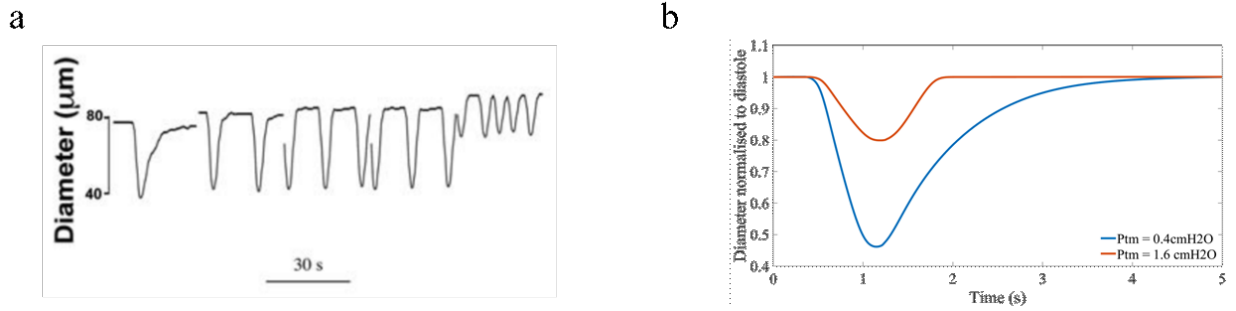


Figure 28: Comparing the diameter-time shape for lymphangions recorded experimentally to coupled muscle-lymphangion model results (a) diameter of cannulated rat mesenteric lymphatics at various transmural pressures (1,2,3,5,7 cmH_2O , increasing in 30 s intervals) (Zawieja, 2009) showing that the linear recovery of diameter occurs at higher transmural pressures (b) results from the muscle-lymphangion model transmural pressures of 0.4 cmH_2O showing the exponential shape of diameter-time during recovery and 1.6 cmH_2O showing the more linear diameter-time recovery shape

Comparing the muscle model under reference conditions to the adjusted model with prescribed contractions (Figure 29) showed a more rapid diameter recovery in the prescribed contraction model (approximately 1.4 s compared to 2.1 s) whilst the difference in average flows was negligible (approximately 0.5%). The diastolic diameters were the same for both the muscle model and the model with prescribed contractions at 165 μm whilst the systolic diameter was slightly different at 123 μm for the muscle model and 124 μm for the prescribed contractions model Figure 29a. The diameter returned to the diastolic value at virtually the same time, but the prescribed contraction model remained at the systolic value for a longer period (approximately 0.4 s compared to 0.1 s). It has been found experimentally that the recovery duration is longer than the contraction period (Scallan et al., 2016), indicating that the muscle model better represents lymphangion behaviour in this case. The prescribed contraction model exhibited slower pressure reduction (0.26 $\text{cmH}_2\text{O/s}$ compared to 0.39 $\text{cmH}_2\text{O/s}$) with a slightly lower peak pressure (0.17 cmH_2O compared to 0.21 cmH_2O) and a larger peak amplitude of suction pressure (0.17 cmH_2O below the inlet pressure, compared to 0.63 cmH_2O), see Figure 29b. This difference could be reduced by altering the form of the time-dependent relaxation of intrinsic tension but is not included here. The other key differences were that the prescribed contraction model did not allow for separation of the tonic and phasic forces of lymphatic muscle (a constant assumed tone was applied which did not reflect interactions between the phasic and tonic components) and the subcellular energetics was not calculable. Using the calculation of work by intrinsic contractions and the fluid power for both

models, however (equations 32, 43 and 48), showed that the peak work rate of the muscle model was higher in the muscle model (0.055 erg/s compared to 0.043 erg/s) and the work done on the lymphangion by fluid was lower (0.011 erg/s compared to 0.021 erg/s) as shown by Figure 29d. The peak rate of energy transfer to lymph was higher for the muscle model (0.005 erg/s compared to 0.004 erg/s). The efficiency of transfer of work done by intrinsic contractions to the energy imparted to lymph, was similar in both models (29% in the prescribed contraction model compared to 30% in the muscle coupled model).

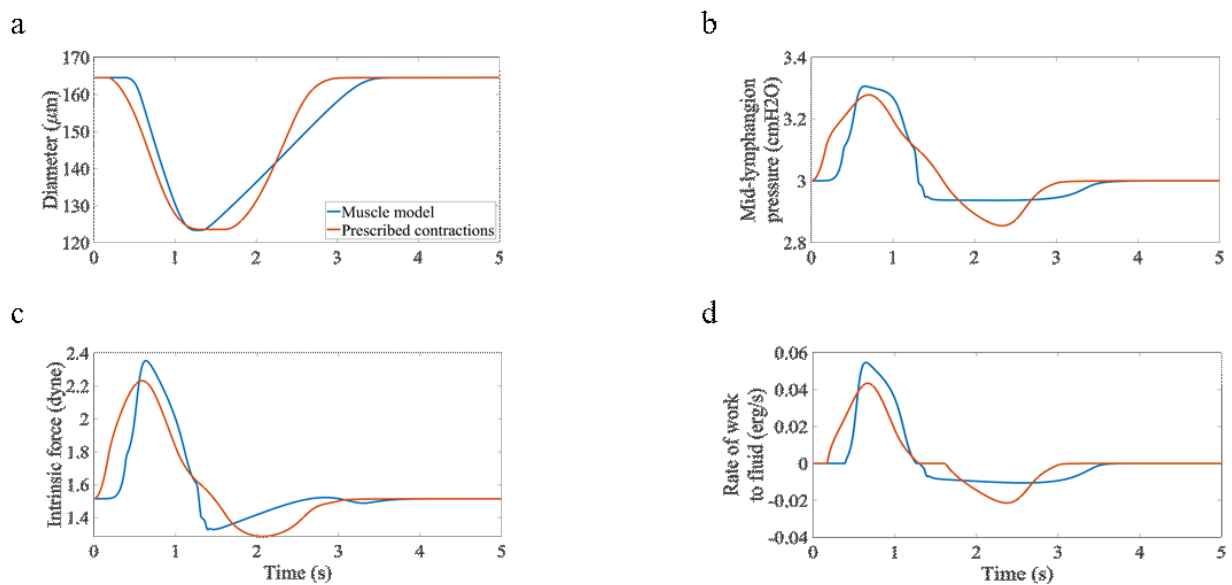


Figure 29: Comparison of the results obtained using the coupled muscle-lymphangion model and the prescribed intrinsic contractions model under reference pressure conditions (inlet 3 cmH_2O , outlet 3.1 cmH_2O and external 2 cmH_2O). (a) diameter and (b) mid-lymphangion pressure (c) intrinsic force (cell force of the muscle model, prescribed force from the other model) (d) Rate of work transfer to lymph

Comparing the results of the muscle model to the first test case of Contarino and Toro (single lymphangion with inlet pressure 5 cmH_2O , outlet pressure 7 cmH_2O and external pressure 2 cmH_2O) showed significantly different results. The lymphangions considered by the two models are of different size (diastolic diameters of approximately 180 μm in the muscle model and 240 μm in the Contarino and Toro model shown by Figure 30a,b, note the difference in the y-axis). At these greater pressures, the muscle model did not generate much of a decrease in diameter (the contracted diameter normalised to the diastolic diameter was approximately 0.9 in the muscle model compared to approximately 0.5 in the model of Contarino and Toro) and the return in

diameter was much more rapid (0.4 s compared to 1 s). There was therefore little flow from the muscle model 0.01 mL/hr. This corresponded to only a small increase in the pressure above the outlet pressure (0.15 cmH₂O) and a sharper downwards spike in pressure (to 0.50 cmH₂O below the inlet pressure) when it came to refilling. Comparing the reference results of the muscle model (Figure 26), however, with the results of Contarino and Toro showed much greater agreement with the main difference being the pause of the Contarino and Toro model at the outlet pressure before the suction-based refilling, corresponding to a pause in the diameter at the contracted value.

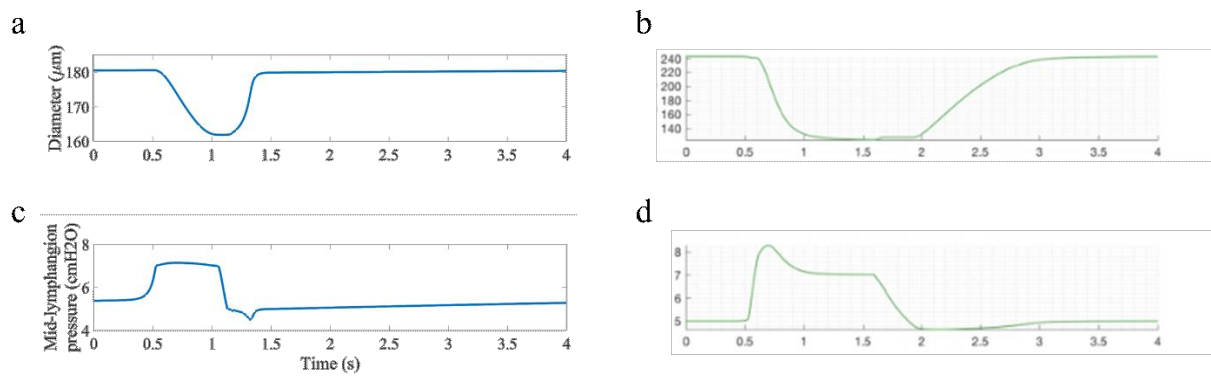


Figure 30: Panel of plots summarising the comparison between the muscle model developed here and the model of Contarino and Toro using the pressure conditions from Test 1 of (Contarino and Toro, 2018) with an external pressure of 2 cmH₂O, and inlet pressure of 5 cmH₂O and an outlet pressure of 7 cmH₂O. (a) shows the mid-lymphangion pressure predicted by the muscle model (b) shows the mid-lymphangion pressure from the model of Contarino and Toro (c) shows the diameter of the muscle model, and (d) shows the diameter of the model of Contarino and Toro

The average outflow was more sensitive to f_1 than g_1 , decreasing by 15% with halving f_1 and by 2% with doubling g_1 . Outflow decreased by approximately 60% when f_1 was doubled and 69% when g_1 halved. This was due to the increased maintenance of cross-bridges causing continuous constriction of the lymphangion (Figure 31a,b). The average flow increased by 46% when g_2 was doubled and decreased by 38% when g_2 was halved (Figure 31a).

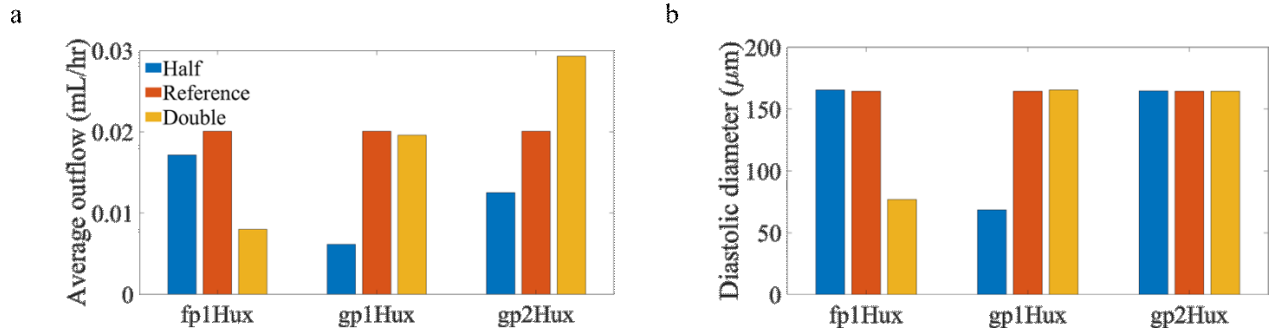


Figure 31: Sensitivity of the model to phasic rates (a) rate of fluid output (b) diastolic size of the lymphangion. When the attachment is too high (f_1 double) or the detachment is too low (g_1 half), the phasic force during diastole causes constriction of the diameter, so there is greatly reduced flow

The average outflow varied by $< 0.4\%$ when the tonic head rate constants were doubled or halved.

The insensitivity of flow to changes in tonic rates was because variations in tonic force mainly altered the force borne by the tonic dashpot (the greatest change in tonic CE force was 0.34 dyne increase with halving k_{1HHM} corresponding to a 0.33 dyne decrease in tonic dashpot force). The resulting change in the average row force from all tonic rates was up to approximately 2%. Doubling or halving μ_T resulted in $< 0.5\%$ variation in the average outflow (results not shown).

There was an optimal range of combinations of troponin Hill coefficient and calcium saturation for half saturation that generated a high average flow (Figure 32). This optimal range of n_{mTrop} , $c_{0.5,Trop}$ combinations occurred where the peak concentration is large (between 4.2% and 38.1%) with a low enough diastolic saturation (in the range of 0.003% to 0.06%) to prevent constant constriction. Constant constriction to diameters $< 86 \mu m$ occurred when both n_{mTrop} and $c_{0.5,Trop}$ were low. This was due to an increased diastolic saturation ($> 0.07\%$) causing an increased diastolic force (phasic CE force > 0.59 dyne). High combinations of n_{mTrop} , $c_{0.5,Trop}$ caused a low peak saturation and small phasic contraction amplitudes so the lymphangion was unable to generate significant flow. Neglecting constricted results, the average outflow decreased with increasing half saturation concentration and this decrease in flow was because of a decreasing peak saturation and peak phasic CE force (see Table 5). Varying $c_{0.5,CaM}$ between 4 μM and 20 μM caused variations in the average flow of $< 1\%$.

Table 5: Decreases in average flow with increasing half saturation concentration

n_{mTrop}	Decrease in \bar{Q} [mL/hr]	Decrease in peak S_{Trop} [%]	Decrease in peak F_P [dyne]
11	0.0017	3.29	0.027
12	0.0052	13.8	0.082
13	0.0075	22.1	0.122
14	0.0099	33.9	0.166
15	0.0105	34.0	0.197

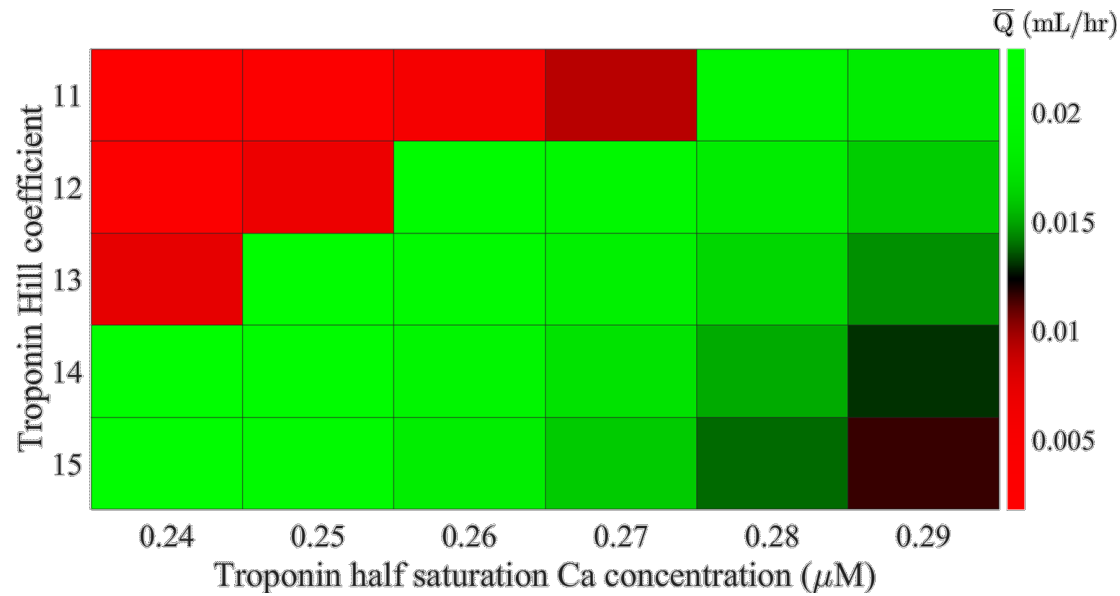


Figure 32: Sensitivity of outflow to variations in the calcium binding properties of TnC. There is a combination of TnC Hill coefficients that result in effective pumping

The efficiency of LMCs increases with increasing adverse pressure difference to a peak value of 65% at 7 cmH₂O (Figure 33a) before decreasing to 56.5% at 10 cmH₂O. Energy losses to viscosity are much lower than to inhomogeneities in cross-bridge attachment/detachment displacements (Figure 33c). Energy losses due to incomplete powerstrokes decrease with adverse pressure due to the decrease in convection, and due to viscosity also decrease because of the reduced velocities and the greatest viscous losses are from cell viscosity which has the greatest viscous constant and the greatest shortening velocity. The efficiency increases with p_b because there is reduced outflow (Figure 33d), meaning that there is less convection and more heads can complete the powerstroke. Comparing the muscle work and fluid pumping work shows a similar form for both with a peak cell work of 0.0566 erg at 6 cmH₂O and a peak fluid work of 0.0440 erg at 4 cmH₂O (Figure 33b). This, combined with the decreasing energy liberation, resulted in a peak of 86% work transfer from

muscle to fluid at 2 cmH₂O and 48% efficiency of energy liberated to fluid work at 5 cmH₂O (Figure 33b). The decreased convection also increases the peak force generation by phasic CEs (Figure 33e) from 1.52 dyne at an adverse pressure difference of 0 cmH₂O to 25.40 dyne at 10 cmH₂O. The increased phasic force caused an increase in the peak cell force (Figure 33f) from 2.13 dyne at an adverse pressure difference of 0 cmH₂O to 26.32 dyne at 10 cmH₂O. The force increase was linear because the outlet pressure was increased linearly, and the maximum mid-lymphangion pressure barely increased above the outlet pressure in each case, meaning that the required force increase was linear. A maximum flow of 0.021 mL/hr was achieved when the outlet pressure was the same as inlet pressure (Figure 33d) and pumping had failed (no net outflow) at 10 cmH₂O.

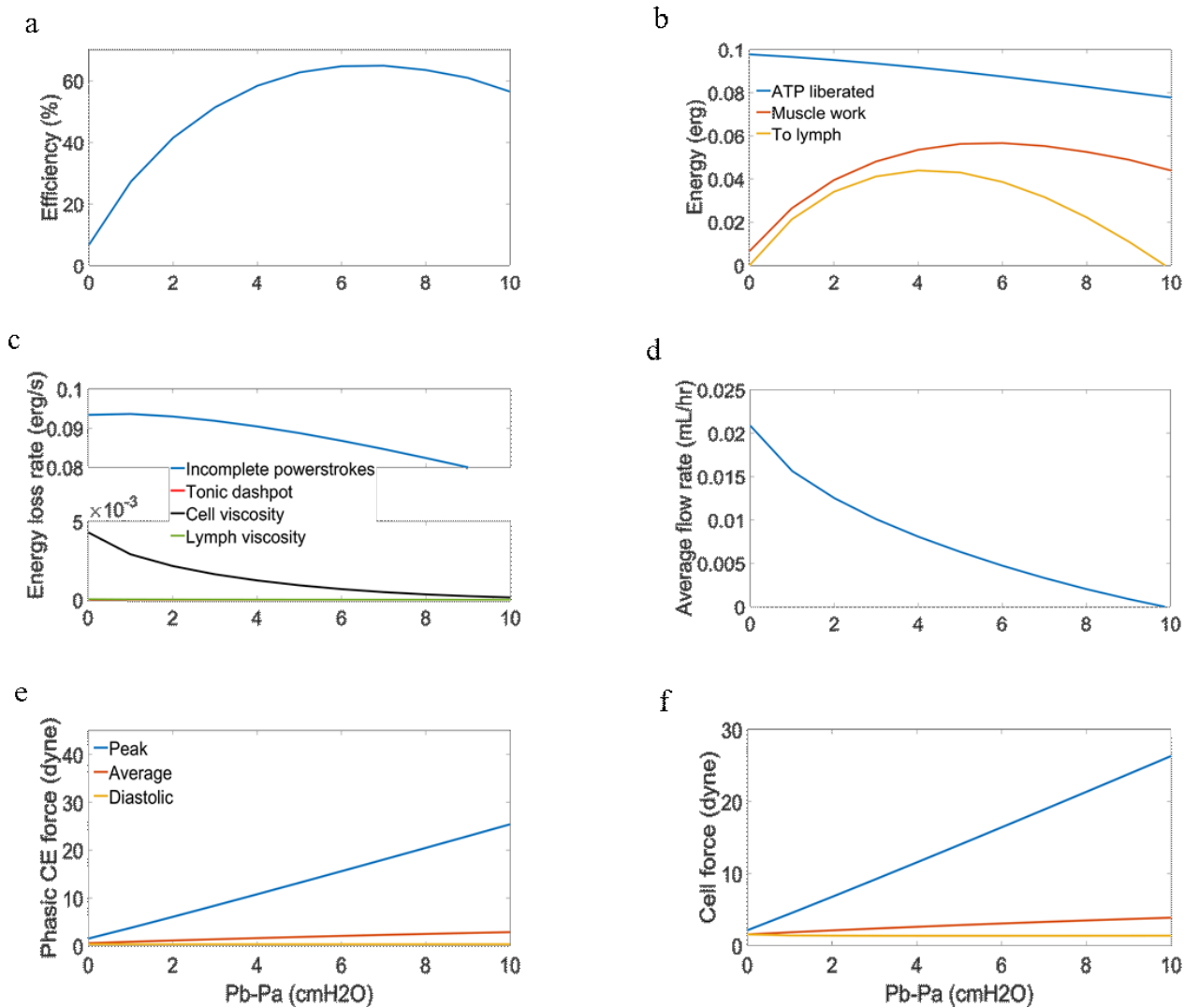


Figure 33: Panel of plots summarising the effect of increasing the outlet pressure for consistent inlet (3 cmH₂O) and external pressures (2 cmH₂O). (a) shows an increase in efficiency with increased afterload until a point after which there is

a slight decrease until pump failure (defined as zero net outflow) (b) compares the energy liberated to the work done by the muscle and the useful work done on the lymph (c) shows that the viscous losses were much lower than losses to incomplete powerstrokes (d) shows the decrease in outflow from the increased load (e) shows the response of increasing phasic force to increasing load (f) shows that the increasing phasic force causes an increasing cell force

The prescribed contraction model fails at much lower adverse pressure (Figure 34b) than the muscle model (approximately 2 cmH₂O compared to 10 cmH₂O) because the muscle model is better capable of increasing its force generation in response to higher pressure demand (Figure 34d). The failure of pumping in the prescribed contraction model was due to an inability of the lymphangion to refill with suction-based flow. This meant that the diastolic diameter increased (Figure 34a) with outlet pressure (172 μ m at 10 cmH₂O for the muscle model and 179 μ m for the prescribed contractions model) and the peak force increased through reduced convection in the muscle model (from 2.13 dyne at 0 cmH₂O to 26.32 dyne at 10 cmH₂O) as discussed above and through Md in the prescribed contraction model (from 2.03 dyne at 0 cmH₂O to 22.1 dyne at 10 cmH₂O). The muscle model work (Figure 34c) response to increased outlet pressure is opposite in the prescribed contraction and muscle models. The hyperbolic pressure-flow relationship is somewhat similar to force-velocity curves of muscle, and the muscle work is similar to power, with the response of the muscle model behaving like the reported response of muscles.

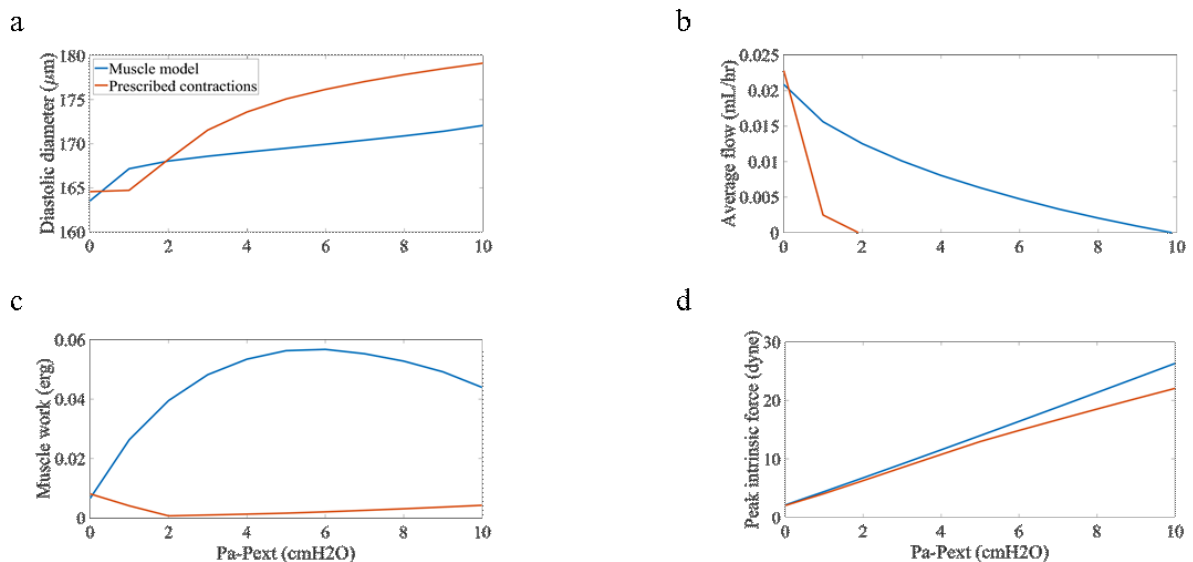


Figure 34: Panel of plots comparing the responses of the muscle model and prescribed contraction model responses to increases in adverse pressure whilst the inlet and external pressures were maintained at 2 cmH₂O and 3 cmH₂O, respectively (a) compares the change in diastolic diameter (b) compares the change in average outflow (c) compares the changes in work done by the intrinsic contractions (d) compares the peak intrinsic force

Varying the transmural pressure by simultaneously changing p_a and p_b showed that the efficiency of lymphatic muscle followed an inverse relation to average flow (Figure 35a,c) with collapse at low transmural pressures (0.8 cmH₂O and lower) causing low stroke volume (< 14 nL compared to 28 nL at 1 cmH₂O) (Figure 35c,d). The value of this transmural pressure for optimal flow is primarily dependent on the passive tube law, but also depends on the diastolic intrinsic force. This was because of the reduced velocity resulting in lower myosin turnover (Figure 35d) as in the adverse pressure difference results. The fluid work follows average outflow because the adverse pressure difference was constant and had a peak value of 0.003 erg at a transmural pressure of 1 cmH₂O (Figure 35b,c). There was an optimal transmural pressure for greatest average outflow of 0.020 mL/hr (corresponding to minimum efficiency of 9.3%), which occurred during the reference conditions (Figure 35a). At transmural pressures greater than the optimal, there is increased force required to contract (Figure 35e,f), reducing the flow similarly to increasing the outlet pressure (Figure 35c).

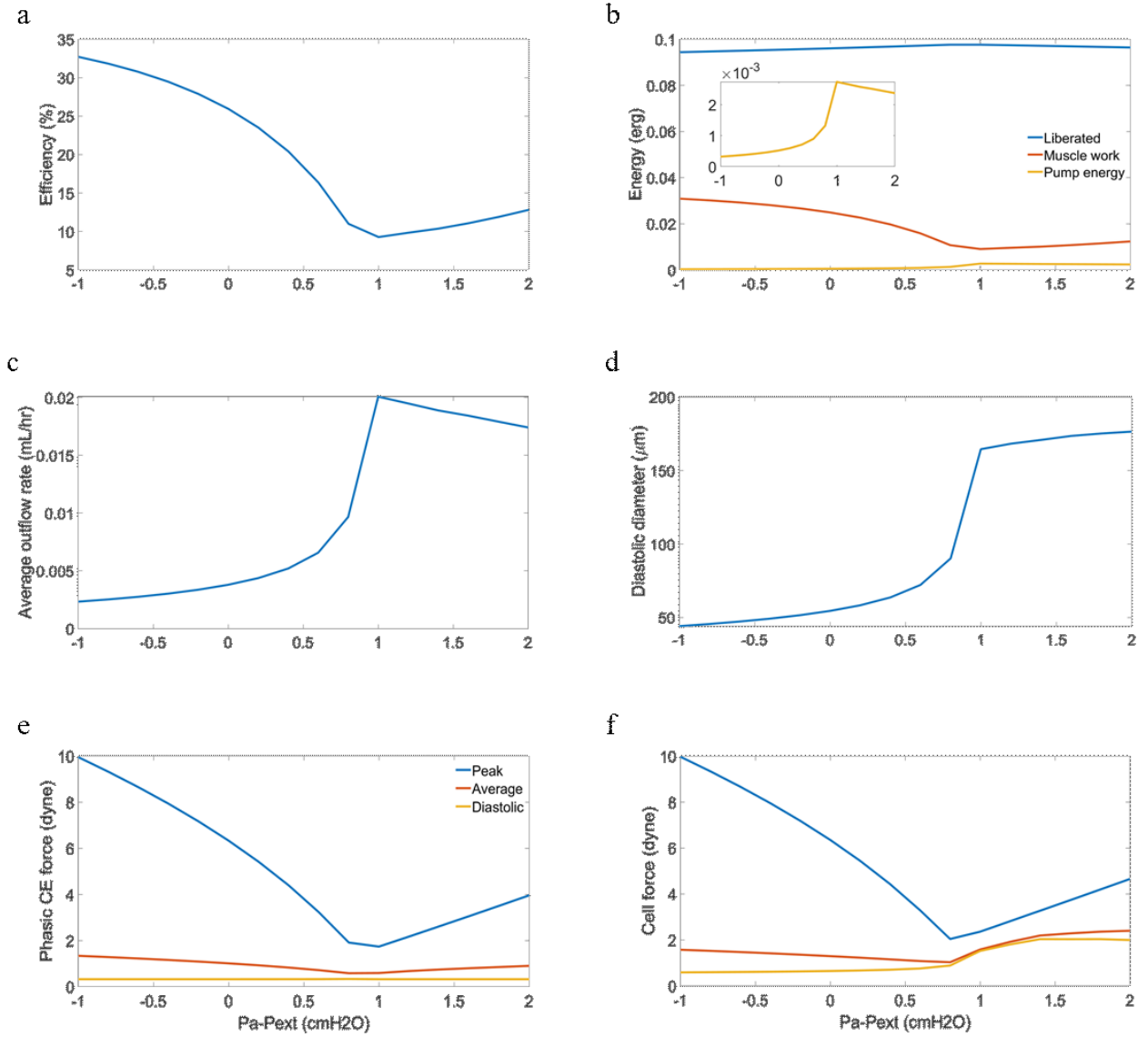


Figure 35: Panel of plots summarising the effect of simultaneously increasing inlet and outlet pressure (axial difference 0.1 cmH₂O) for constant external pressure (2 cmH₂O). (a) shows the efficiency of the muscle which follows an inverse relation to the average outflow (b) shows compares the energy liberated from ATP to the work done by the muscle and energy imparted to the fluid (c) shows the outflow change in response to varying transmural pressure with a peak of 0.0256 mL/hr at a transmural pressure of 1 cmH₂O (d) shows the collapse of lymphangions with transmural pressure lower than 1 cmH₂O, reducing the stroke volume available for pumping (e) shows variations in phasic force which was much greater in collapsed lymphangions (f) shows that the cell force follows phasic CE force

The muscle model increased its force at low transmural pressures (up to a peak of 9.95 dyne at -1 cmH₂O) whilst the prescribed contractions model had consistently low force (0.28 dyne at -1 cmH₂O) as shown by Figure 36c. This is due to the lymphangion collapse (44 μm and 50 μm at -1 cmH₂O for the muscle model and prescribed contraction model, respectively Figure 36a) and the diameter-dependence of force M_d . At higher transmural pressures, however, the diameter of the muscle and prescribed contraction models was higher (176.5 μm and 173.1 μm, respectively) and

both models increased their peak force (up to 3.96 dyne and 4.29 dyne at 2 cmH₂O, respectively). The peak flow (Figure 36b) of the prescribed contraction model (0.022 mL/hr) is slightly higher than the peak flow of the muscle model (0.020 mL/hr) and occurred at a slightly lower transmural pressure (0.8 cmH₂O compared to 1 cmH₂O). The average flow decreased faster for decreasing transmural pressure in the muscle model and for increasing transmural pressure in the prescribed contractions model. The response of muscle work (Figure 36d) to varying transmural pressure was the opposite in the muscle and prescribed contraction models with the prescribed contraction model's work following the average flow because the increased circumferential shortening velocity does not have a convection effect on the force generating capability in the prescribed contraction model.

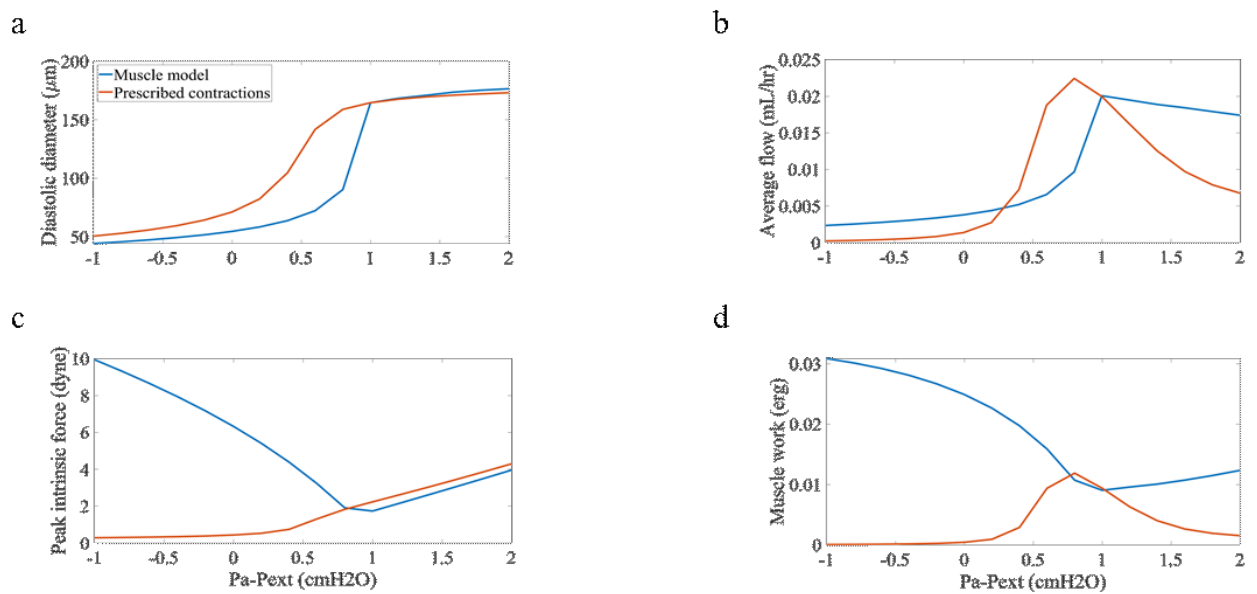


Figure 36: Panel of plots comparing the response of the muscle model and prescribed contractions model to variations in transmural pressure with a constant pressure difference along the lymphangion of 0.1 cmH₂O. (a) shows the response of diastolic diameter (b) the response of average flow (c) the response of the peak force and (d) the work done by intrinsic contractions

Including calcium oscillations (non-zero sinusoid amplitude in equation 35) increased the average flow rate (Figure 37a) with one oscillation at 1% amplitude causing only about a 0.3% increase. The oscillations without complete opening/closing of the outlet valve were still able to increase outflow because they opened the valve slightly. Oscillation peaks of course resulted in decreases in diameter (Figure 37b,c) with the greatest occurring at 1 Hz and 19% amplitude. The diameter decreases were

due to an increase in pressure (Figure 37d,e) as a result of the increased calcium allowing more heads to bind. There were low amplitude (compared to action potential, maximum peak was approximately 18.9% action potential peak) peaks in outflow with oscillatory increases in pressure from oscillations (Figure 37f,g). Valves start rapidly opening and closing at lower amplitudes when the frequency is greater (Figure 37h,i). The increase in flow became less sensitive to amplitude when the valves started to fully open and close with each depolarization. These results could not be compared to experimental data because none are available, so the discussion includes suggestions for potential experiments to investigate this.

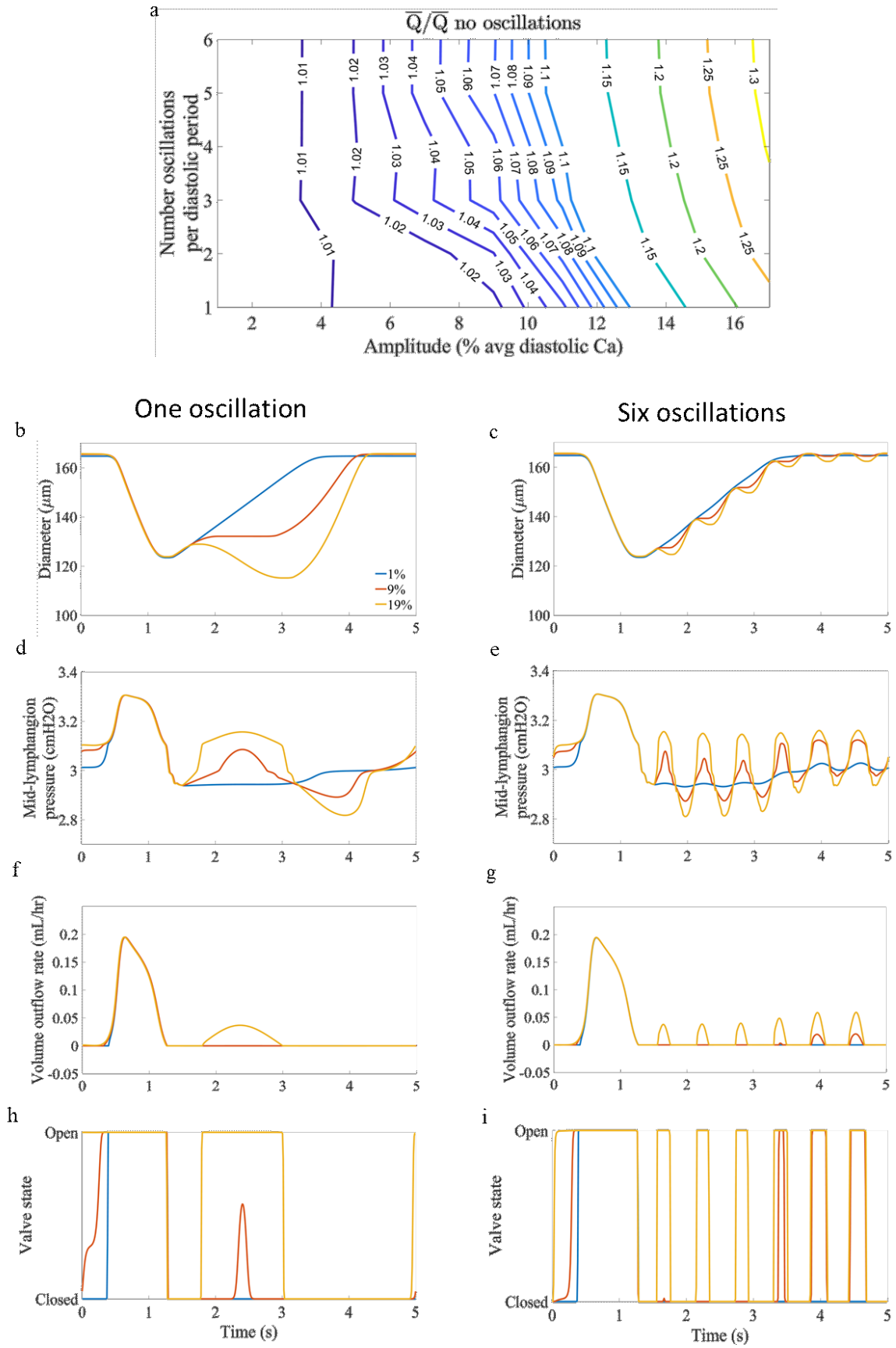


Figure 37: Panel of plots showing the effects of varying both amplitude and frequency of calcium oscillations with all combinations of amplitude and frequency increasing flow relative to the case without calcium oscillations. (a) contours of average outflow normalised to the results without calcium oscillations showing that higher flow is obtained at lower

amplitudes when the frequency is increased. (b,c) variation in time-dependence of diameter (d,e) variation in time-dependent mid-lymphangion pressure (f,g) variation in time-dependence of outflow (h,i) variation in time-dependence of outlet valve resistance, showing the opening and closing with calcium oscillations

A simulation was then run for a series connection of four simultaneously contracting (identical calcium inputs, equation 35) lymphangions with the cell viscosity suppressed because simulations varying viscoelasticity (see Appendix 1) showed little effect of viscosity on the model results and the series connection of lymphangions was unstable with it included. The external and inlet pressures were the same as used in the reference results for a single lymphangion (2 cmH₂O and 3 cmH₂O, respectively) and the outlet pressure was increased to 6 cmH₂O, giving an adverse pressure difference of 3 cmH₂O. Progressing down the lymphangion chain the efficiency of muscle contractions decreased (39.99 erg/s 39.54 erg/s 38.00 erg/s 35.13 erg/s) and the total efficiency (defined as the sum of work from each lymphangion divided by the sum of energy liberated in each lymphangion) was 38.15% (see Figure 38e). This decrease in efficiency was because the diameter contraction amplitude increased (20.83 μ m 21.10 μ m 22.12 μ m 23.79 μ m), meaning that there was more convection of heads progressing along the chain as shown in Figure 38a. The contractions in the model under these conditions were small, generating an average flow of 0.25mL/hr (see Figure 38b). The peak energy liberation rate increased along the chain (0.5093 erg/s 0.5122 erg/s 0.5178 erg/s 0.5258 erg/s), reflecting more turnover of myosin heads whilst the peak work rate decreased (0.2394 erg/s 0.2346 erg/s 0.2241 erg/s 0.2058 erg/s) showing that the decrease in force had more of an influence on work done than the increasing velocity. Diastolic diameter decreased slightly for each lymphangion along the chain (167.4657 μ m 166.4497 μ m 165.4496 μ m 164.7151 μ m) because the average tonic CE force increased slightly (0.3924dyne 0.3928dyne 0.3938dyne 0.3958dyne). This reduction in the diastolic diameter was the cause of the increased diameter change because the lymphangion was a cylinder of smaller volume, so pumping the same volume of lymph required a greater change in the diameter. The decreased diameter also meant that the phasic CEs were shorter and the phasic spring force was negligible (order 10^{-4} dyne, Figure 38e). The diameter recovery shape is closer to

exponential than the linear shape. The suction pressure was much smaller for a chain of lymphangions than for the single lymphangion (0.1283cmH₂O 0.1891cmH₂O 0.2062cmH₂O 0.2095cmH₂O below the inlet boundary condition, respectively). This may be because of the much greater adverse pressure prescribed in this simulation. It was necessary for the peak pressure to decrease along the chain (1.9191cmH₂O 1.7181cmH₂O 1.3077cmH₂O 0.6772cmH₂O over the outlet boundary condition, respectively) for flow to occur, corresponding to a decrease in the peak cell force (13.2035dyne 12.6987dyne 11.7070dyne 10.2311dyne), given in Figure 38c,d. The peak in contraction-based flow increased with progression between valves (0.1193mL/hr 0.1553mL/hr 0.3148mL/hr 0.4794mL/hr 0.6521mL/hr) whilst the suction-based flow peak decreased (0.1193mL/hr 0.0642mL/hr 0.0437mL/hr 0.0269mL/hr – 0.0001mL/hr). The adjusted prescribed contraction model was incapable of generating flow at this pressure difference. The efficiency of energy transfer to the lymph was calculated as the energy to lymph divided by the sum of work for all lymphangions and proved to be more efficient than for a single lymphangion (68.4% compared to 30.3%). This illustrates the ability of the muscle model to generate increased force in response to more adverse pressure through the reduced convection of myosin heads allowing more heads to attach and generate more force. The prescribed contraction model, however, was unable to capture this response due to the constant assigned peak tension (equivalently force).

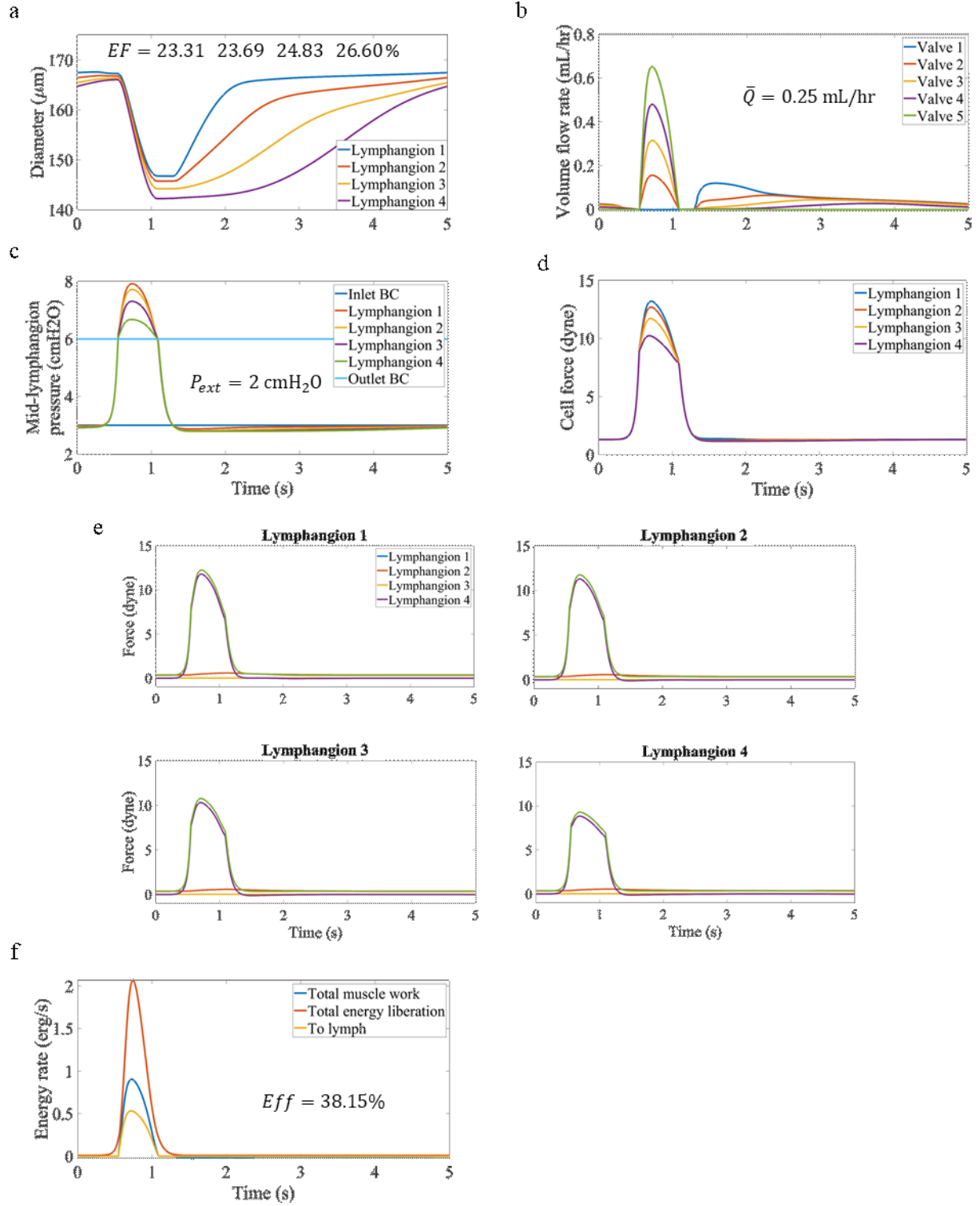


Figure 38: Panel of plots summarising the results for a series chain of four simultaneously contracting lymphangions with inlet pressure 3 cmH₂O outlet pressure 6 cmH₂O and external pressure 2 cmH₂O (a) diameter (b) volume flow rates (c) mid-lymphangion pressures (d) cell force (e) row force balance (f) energetics rates where the muscle rates are the sum of all lymphangions

3.5. Conclusions and discussion

We have developed a computer model of the subcellular mechanisms of lymphatic muscle

contraction that, on coupling with a well-characterised larger scale model of lymphangion pumping,

produces flow, diameter, and pressure traces similar to those from experiments on rat mesenteric lymphatics, and ejection fraction and average outflow under reference conditions are within the range previously reported from experiments (Davis et al., 2008, Davis et al., 2011, Davis et al., 2012, Scallan et al., 2016). This model is loosely based on the model of Brook and Jensen (Brook and Jensen, 2014) but is adapted to incorporate both phasic and tonic contractile elements (initially developed for tonic only). The particular arrangement of CEs with the phasic spring and tonic dashpot was the only one that produced physiologic results, out of the many we tried, giving some insight into the potential subcellular structure of LMCs and providing a basis for testing the potential of length-adaptation. Whilst this model contains many parameters, these were necessary to increase the detailed understanding of the various contractile and passive subcellular elements of lymphatic muscle cells beyond the current state and this model was developed to be as mechanistic as possible. Greater understanding of these subcellular mechanisms will be beneficial in developing interventions to promote lymph flow (both mechanical through the variation of external pressure and pharmacological). Most of the results in this model used a single lymphangion, but one simulation with a chain of four lymphangions showed that the energy liberation increased, and the work done by the muscle decreased along the chain, causing a decrease in the efficiency. In terms of conceptual ties to anatomical features, the phasic spring could represent the elasticity of titin while the tonic dashpot could represent the effects of a combination of tonic contractile machinery and the fluid environment around the smooth muscle components. Experiments to study the physical characteristics of the phasic spring and tonic dashpot would be useful. Smooth muscle contains a protein similar to titin, referred to as smitin (Kim and Keller III, 2002, Chi et al., 2005, Chi, 2007). Both titin and smitin can attach to smooth and striated actin and myosin (Kim and Keller III, 2002, Chi et al., 2005, Chi, 2007). This implies that titin, smitin, or some combination thereof can provide a direct connection between phasic and tonic CEs in LMCs.

A major overall inhibitor of studies on lymphatic muscle is the loss of contractile phenotype in previous attempts to culture LMCs. A bioreactor that mechanically stimulates cultured muscle cells

to maintain contractility is currently under development in Professor Moore Jr's research group. Cultured muscle cells will allow for more specific studies of lymphatic muscle (for example direct length-tension and force-velocity relationships without influence of other components of the lymphatic wall) and allow more accurate determination of the many parameters in this model, including the transition rates of the tonic component (currently left as the values of human airway smooth muscle, without detailed validation of the appropriateness for rat mesenteric lymphatic muscle). The suggested presence of titin and smitin should be investigated further using quantitative assays similar to (Muthuchamy et al., 2003) including determining the isoform(s) present and more detailed analysis of the relative concentrations of β -cardiac and SMB isoforms would provide additional clarity on the subcellular contractile element structure. Another highly useful investigation would be the use of specific inhibitors or genetic knockouts of the cardiac β -myosin/troponin or SMB isoforms/calmodulin to isolate the active phasic and tonic components of lymphatic muscle. Examples include the knockout of cardiac troponin as published by Huang and colleagues (Huang et al., 1999) or molecules that competitively bind to troponin, preventing the binding of calcium ions and keeping the actin binding sites blocked (see (Audran et al., 2013) for more information on calmodulin blockers) to isolate the active phasic and tonic components of lymphatic muscle. For example, in our current results the phasic component has a noticeable force during diastole though still significantly lower than the tonic force so it would be interesting to see if the diastolic force is non-zero if the tonic component is genetically knocked out. Note, however, that the genetic knockouts are in mice, not the rat which this model is based on. Understanding the molecular functioning of LMCs is a step towards more physiologic models of lymphatic function necessary for greater understanding of system performance (Margaris and Black, 2012) and is useful for identifying potential pharmaceutical interventions. One potential pharmacological intervention in oedema would be the inhibition of contractions during diastole to help with the refilling and allow for more lymph flow. Such a time-dependent suppression of force is impractical, however, so

suppression of the tonic force is suggested instead. Pharmacological intervention to optimise the calcium binding for flow is also indicated by the results of this model.

A parameter sensitivity analysis showed that the calcium binding properties of troponin, the detachment of phasic heads with negative displacement, the peak calcium concentration, and the number of LMCs around the circumference were the most sensitive parameters governing model outflow. There is a dearth of published calcium concentration measurements in rat mesenteric lymphatics so an updated study is recommended. Whilst the number of LMCs around the circumference was shown to be an important parameter, there is high confidence in the parameter estimate. The calcium binding properties of troponin would be facilitated by determining the isoforms of troponin that are present in rat mesenteric LMCs.

Our model provides the first estimates of the energetics and efficiency of individual LMCs, and their dependence on lymphangion upstream, downstream and external pressures. Unfortunately, there are no experimental data with which to directly compare the energy conversion predictions of the model. Energetics are included here as estimates that will hopefully be comparable with experimental estimations of ATP usage as is often performed by measuring the concentration of inorganic phosphate through, for example, fluorescent protein MDCC-PBP (He et al., 2000) and heat generation. The model calculates the efficiency of cross-bridge cycling converting chemical energy of ATP to useful work, ignoring the efficiency associated with the metabolism of storing energy in ATP. The thermodynamic cycling efficiency was calculated from the ratio of work done to free energy from ATP hydrolysis. Another commonly used measure of cross-bridge efficiency is mechanical, based on the ratio of work done to enthalpy (free energy + entropy \times temperature). The thermodynamic efficiency estimates from our model are within the ranges of published values for other muscle types. The thermodynamic efficiency of human skeletal muscle was reported as 40% at 20°C (He et al., 2000). Cardiac muscle from various species exhibited thermodynamic efficiencies of around 20% (Barclay et al., 2003, Barclay and Loiselle, 2020). The efficiency of vascular smooth

muscle (rabbit rectococcygeus) has been reported as 18% (Walker et al., 1994). Our model predicts a decline in efficiency at lower adverse pressure differences when there is less of a mechanical challenge to overcome. LMCs contain a large number of mitochondria (Ohhashi, 1987), so even small losses per mitochondria can sum up to cause losses comparable to cross-bridge cycling. By comparison, metabolic efficiency has been estimated as 80% for cardiac muscle; 4x the cross-bridge cycling efficiency (Barclay et al., 2003, Barclay and Loiselle, 2020). As described in Chapter 2, there are several limitations in the calculation of energetics when using the Huxley model. Additional states and pathways were not included in this model because there are no experimental data on lymphatic muscle energetics, so the additional complexity was deemed unnecessary for a first approximation. In future developments of the model, more head states could be included to model weak ATP powerstroke coupling.

The calculation of energetics is a useful development from this model because it may be an important factor in the shear- and pressure-dependent regulation of lymphatic contractions. For shear-dependent inhibition the theories are that when passive flow (passive pressure gradients driving flow) is possible, intrinsic contractions are unnecessary and (1) increase resistance to flow (2) waste energy (modelling the calcium-dependence on shear and diameter are currently underway and, with the energetics calculation of this model, will likely yield interesting results to better understand the regulation of lymphatic contractions that is not possible with existing models). Greater understanding of the feedback mechanisms may assist in the development of pharmacologic interventions to increase flow in oedema. The availability of energy may also be a limiting factor to lymph flow under certain conditions or with co-morbidities so enhanced understanding will facilitate treatments.

This was the first study (experimental or computational) to test the effects of varying amplitude and frequency of calcium oscillations in LMCs. Controlling these experimentally would be challenging, so the model presents a more tractable means of exploring the potential effects on pumping. Calcium

oscillations cause an increase in flow when strong enough to open the downstream valve, and this effect is stronger as frequency increases. Increased oscillation frequency also increases the AP frequency (not modelled here) for more phasic contractions as another means of increasing outflow. The pressure and diameter fluctuations caused by oscillations have been observed in previously published experiments. Contractile force generation should scale more-or-less linearly with the number of cells contracting in response to oscillations, which is encompassed in the varying of amplitude. Fluctuations in diameter and pressure have been observed experimentally in rat mesenteric lymphatics (Gashev et al., 2002, Zhang et al., 2007a, Dixon et al., 2006, Dixon et al., 2005). It has not, however, been confirmed that these fluctuations correspond to calcium fluctuations and this is still a matter of some debate. Detailed experimental observation of the effects of amplitude and frequency of calcium oscillations would be difficult to obtain. A commonly theorized cause of these oscillations is spontaneous transient depolarizations (STDs) though this is not unanimously agreed upon. Inhibitors and activators of STDs used for investigations in smooth muscle (for example inhibitors or blockers of inositol 1,4,5-triphosphate receptors or calcium-activated chloride channels (von der Weid et al., 2008)) could be applied to rat mesenteric lymphatics. However, studying the effect on diameter, pressure, and flow would be complicated by the lack of action potentials triggered by STDs.

Comparison of the muscle model with the prescribed contractions model showed that, under the reference conditions chosen for the muscle model, the muscle model was better able to capture the delayed suction recovery than the prescribed contractions model. The muscle model was also more capable of increasing force when the adverse pressure is increased (as observed experimentally (Davis et al., 2012, Scallan et al., 2012)) even without the regulatory feedback of calcium concentration. The muscle model also displays a more sensitive transmural pressure-dependence than the prescribed contraction model though this is not experimentally confirmed. This increased sensitivity to transmural pressure means that the muscle model more strongly supports the theory previously developed by the prescribed contraction model that application of compression bandages

is not necessarily the best treatment, and instead the external pressure should be optimised (potentially through applying suction). The major advantage of the muscle model was the ability to calculate the rate of energy liberation to better understand the metabolic requirements/limitations for lymphatic contractions. Splitting the phasic and tonic CE forces apart allows for greater understanding of their interactions under varying pressure conditions to indicate potential targeted therapies (for example the suppression of tone and altering the calcium binding of the phasic component) and provides an avenue for understanding the potential of lymphatic muscle to adapt to different conditions including through length adaptation (not included in this work as want to present the model first before investigating more sophisticated effects). The muscle model also showed a greater resistance to adverse pressure and had a sharper decrease in the flow with non-optimal transmural pressures. The work done by intrinsic contractions showed opposite responses to variations in pressure (transmural and adverse). Whilst the model increased the number of parameters in the model, it also moved towards more close inclusion of the experimental findings used as inputs (for example using actual calcium tracings from rat mesenteric lymphatics).

Calcium regulation by shear stress, diameter, and pressure conditions is not included in our model. LMC calcium regulation reduces contractile frequency at lower pressure differences, causing the LMCs to spend less time in the contracting state, potentially increasing the long-time-averaged efficiency. The increase in diameter that results from fewer contractions plus a notable relaxation in tone reduce resistance to pumping by upstream lymphangions. A future development will be to include calcium regulation with shear stress-, diameter- and voltage-dependent terms to represent calcium fluxes through different channels, following models of various smooth muscles (Bursztyn et al., 2007, Yang et al., 2003, Laforêt et al., 2011).

Sliding filament models have inaccuracies in energetics (Bagshaw, 1993), particularly during stretching of active muscle (included in our model during relaxation) and shortening at high velocity. The deviation in sliding filament estimates of energy liberation may be due to the tight coupling of

ATP hydrolysis and cross-bridge cycling (i.e. one hydrolysis per powerstroke) (Yanagida et al., 1985). It has also been suggested that not every powerstroke hydrolyses ATP (Yanagida et al., 1985). There have been several models of skeletal muscle which aim to improve energetics estimates by including the weak coupling of ATP hydrolysis and powerstroke cycles. These models included additional binding states (Piazzesi and Lombardi, 1995, Eisenberg et al., 1980) or additional rates (two attachment and two detachment) in the two-state model (Barclay, 1999).

When the length of a muscle cell is varied, its capability to generate force varies because the filaments slide past each other and the region of overlap is different. This means that the number of actin binding sites available is changed, so the number of attached heads is different. Overlap dependence is not included in the model, but could be through length-dependent variations in the number of myosin heads that are available for attachment following (Kocková and Cimrman, 2009, Zahalak and Motabarzadeh, 1997). A first required step would be to distribute the overall overlap-dependence of LMCs amongst the phasic and tonic CEs. Attributing the overlap-dependence entirely to the phasic CEs would be justified because of the physiologically low shortening velocity of tonic CEs enforced by the tonic dashpot. Another possible further development would be to model the structural rearrangement of contractile filaments in response to length changes. We could perform something similar to (Brook and Jensen, 2014) with an instantaneous change in the number of available heads. Unfortunately, there are no experimental data on which to base such a model or determine its parameters. Imaging capable of distinguishing the phasic and tonic CEs and their overlap would be useful for understanding the interactions of the two contraction types.

Another development will be to include the muscle model in a homogenisation scheme being developed in our group to model complete lymphatic vessel networks (covered in Chapter 4). We would likely want to simplify the muscle model to a distribution-moment model. The distribution-moment model assumes a Gaussian distribution of head states in displacement to obtain ODEs for force, energy, and stiffness (Zahalak, 1981, Zahalak, 1986). This increases error in force and velocity

estimates but reduces the computational demand. The four-state Huxley-Hai Murphy model for smooth muscle has also been implemented using the distribution-moment approximation (Rampadarath and Donovan, 2018). Some example results from the LMC model using the distribution-moment approximation are included in Appendix 1.

In conclusion, we have developed a model of the LMC that provides a first estimate of the energetics and efficiency of LMCs, and the effects of calcium oscillations on the average flow. In development of the model, some structural insights were obtained from the necessity of including a phasic spring and tonic dashpot to obtain physiologic contractions. A major discovery our model was the potential calcium oscillation-derived increase in outflow with transmural pressure. This model also provides estimates of the energy efficiency of lymphatic muscle which may be an important factor in the regulation of lymphatic contractions, important in promoting lymph flow in diseased conditions. It is hoped that this model will motivate further studies into the energetic aspects of lymphatic muscle function for a more comprehensive understanding of lymphatic muscle function, particularly the response to changes in pressure conditions as occur during lymphedema. This model is a step towards the more physiologic modelling of lymphatic pumping as required to increase our knowledge of the system's performance by mechanistically rather than phenomenologically modelling the intrinsic contractions.

CHAPTER 4 – HOMOGENISED MODEL OF LYMPHATIC NETWORKS

4.1. Introduction

The lymphatic system is vital for several aspects of physiologic function and is implicated in multiple diseased states. A major function of the lymphatic system is fluid homeostasis through the return of 4 – 8 L of interstitial fluid to the venous system per day. Failure of lymphatic fluid transport can result in a chronic debilitating condition involving tissue swelling known as lymphoedema. The interstitial fluid collected passes through lymph nodes which contain a high concentration of immune cells. The immune cells in lymph nodes sample lymph to detect pathogens and activate the adaptive immune response. Lymphatics are also one of the two main routes for cancer metastasis, the other being blood vasculature.

The basic unit of pumping in collecting lymphatic vessels is the lymphangion, a segment of lymphatic vessel bounded by two valves. These valves are bi-leaflet with a transmural pressure-dependent bias to the open position. Pumping is achieved by the intrinsic contractions of LMCs surrounding the lymphatic vessels which can be assisted by external compression (from, for example, skeletal muscle contraction and respiration, among others).

A major hindrance of lymphatic pumping research has been the difficulty with quantifying pressure, diameter, and flow *in vivo* in the human. This has led to the use of experimental animal models including rat, sheep, dog, and cow. *In vivo* experiments can be performed by exteriorising loops of vessel to track flow via cell movements and diameter but there is little control over pressure (also other factors affecting pumping such as temperature) and exteriorisation removes the surrounding tissue contributing external compressions. *In vitro* experiments can be performed by excising and cannulating lymphatic vessels, giving control of pressure conditions (and heat, among others) and diameter can still be tracked but flow measurements cannot be obtained, and external compressions are removed. The limitations with animal models have led to computational models based on the available experimental data. Additionally, the removal and cannulation of a large lymphatic network is impractical.

As covered in chapter 2, the first computational model of the lymphatic system was developed by Reddy and colleagues (Reddy, 1974, Reddy et al., 1977) and was a lumped-parameter model based on the reduction of the Navier-Stokes equations. More recent models are primarily also lumped-parameter models (Venugopal et al., 2003, Quick et al., 2007, Quick et al., 2008, Quick et al., 2009, Bertram et al., 2011, Bertram et al., 2014a) but Lattice-Boltzmann models have also been developed (Kunert et al., 2015, Ballard et al., 2018). A significant challenge in developing computer models of the lymphatic vasculature is the complexity of secondary valve dynamics, including their transmural pressure-dependent bias to the open position.

Scaling up models of lymphangion chains to model networks of lymphatic vessels is not simple and results in significant computational demand with the simulation of, for example, the arm lymphatics (hundreds of thousands of lymphangions) being impractical particularly with more complex models of valve dynamics to capture the bias of the valves to the open position. The network structure of lymphatics has not been mapped extensively and there is a great deal of uncertainty in (pressure) boundary conditions which, in addition to being difficult to measure, vary with both location and time and are specific to the individual. A lumped parameter model of lymphangions has previously been used to simulate a small idealised network of lymphangions (Jamalian et al., 2016). The results of this network model showed that a delay in contractions between lymphangions at branch points increased the flow rate and that having vessels of 10 lymphangions generated the highest flow over a wide range of adverse pressure differences. The presence of an optimal vessel length arises because increasing the series number of lymphangions is a balance between additional contractility and additional resistance.

Computational homogenisation (also known as coarse graining) is a method in which the boundary value problems of two scales are coupled. Macroscale parameters are used to set boundary values for a microscale representative volume element (RVE) that models a small segment at the microscale and is then homogenised over the macroscale. This means that the microscale need not

be simulated for the entire macroscale domain and greatly reduces computational demand.

Computational homogenisation is therefore a useful tool for scaling up the complex lymphangion models to network models. The size of the RVE is an important decision as it must be large enough to accurately model the microscale characteristics but small enough to ensure separation of scales between the macroscale and microscale (Geers et al., 2010). Various homogenisation techniques have been proposed but computational homogenisation is probably one of the most accurate for upscaling the nonlinear behaviour of a well-characterised microstructure (Geers et al., 2010). The basic concept of computational homogenisation is the return of a single effective parameter to represent the complex microscale function for use in a simpler evolution law at the larger scale.

Initial computational homogenisation models were restricted to small deformations or linear material behaviour, but the approach is fully general and has been generalised for large deformations with nonlinear material behaviour. Thus far, computational homogenisation has been applied primarily to materials science but some studies have applied it to fluid mechanics ((Kelly and Muske, 2004, Murphy et al., 2020) primarily porous flow (Chu et al., 2012, Bottaro, 2019, Lewińska et al., 2019, Bidier and Ehlers, 2014)) and other multiphysics problems (for example temperature (Lewińska et al., 2019, Larsson et al., 2010), electricity (Keip et al., 2013, Lu et al., 2018), chemistry (Polukhov and Keip, 2020, Yuan et al., 2014), and magnetism (Javili et al., 2013, Zabihyan et al., 2018)). Solid mechanics involves spatial homogenisation; however, we require both spatial and temporal homogenisation. The first-order method uses linearisation of the macroscale constitutive problem and is now quite established (Matsui et al., 2004, McVeigh et al., 2006, Temizer and Zohdi, 2006, Hain and Wriggers, 2008, Yuan and Fish, 2008). The first-order method, however, has its limitations: (1) the method complies with the principle of local action and the material point concept, meaning that in a non-modified form it is limited to a standard continuum mechanics theory at the macroscale (2) large spatial gradients at the macroscale cannot be resolved because of the requirement of separation of scales (3) the principle of local action mathematically enforces an infinitely small size to the RVE, meaning that size effects on the macroscale behaviour cannot be

properly studied. These limitations have led to a second-order method being developed to include the gradient of the macroscale constitutive relation (Geers et al., 2001, Kouznetsova et al., 2002, Kouznetsova et al., 2004, Kaczmarczyk et al., 2008). Homogenisation has previously been used to model noncontracting initial lymphatics (Roose and Swartz, 2012). A major advantage of computational homogenisation is that it is highly parallelisable with RVE models run simultaneously.

The aim of this study was therefore to develop a method for homogenising a lumped parameter model of short lymphangion chains to model large scale converging lymphatic networks. This model is then tested under typical physiological conditions and conditions with altered external pressure.

The overall goal is to examine the macroscale function of lymphatic pumping under various conditions to inform development of treatments for lymphoedema.

4.2. Methods

We have a well-validated lumped-parameter model of a small chain of lymphangions (Bertram et al., 2011, Jamalian et al., 2013, Bertram et al., 2014a, Jamalian et al., 2016, Jamalian et al., 2017) that is computationally intensive and to simulate the flow through a lymphatic network to better develop lymphedema therapies we use computational homogenisation for reduced computational intensity. To this end we have designed and implemented in MATLAB a multiscale nested lumped parameter model of lymphatic vessels with computational homogenisation that uses the lumped parameter model as a detailed microscale model that returns the solution as a single “compliance” that represents the link between microscale pressure and flow. This method is loosely based on the coupling of continuous porous media flow in nested discrete fluid networks as done by Chu and co-workers (Chu et al., 2012). Chu and colleagues developed a first-order homogenisation model to couple a macroscale conservation of mass with a discrete porous Darcy flow model at the microscale, focussing on coupling the pressures of the two scales. Capital parameters correspond to the macroscale and lower-case parameters to the microscale.

In this model we have two scales: the macroscale network (length scale of order m) and the microscale representative volume element (RVE) of a small chain of lymphangions (length scale of order mm). The macroscale is one-dimensional (length L and position X) and divided into a series of N elements (element lengths $\Delta X = L/N$) with one RVE prescribed to each element. Macroscale nodal values are indexed by a subscript I value (ranging from 1 to $N + 1$) and element midpoint values by $I \pm 0.5$. The macroscale includes an ODE for mass conservation and the main equation for solving at the macroscale is a simple constitutive relationship between pressure (P) and flow (Q) using the pressure difference from the microscale and the macroscale flow to calculate a single representative value linking the two scales. This constitutive relationship is used to update unknown pressures at the macroscale given a known (desired) flow.

Macroscale time T is split into multiple time steps and at each macroscale time step the macroscale parameters are passed down to the microscale RVE as boundary conditions (see Figure 39). The microscale boundary value problem is then solved and returns the pressure difference used to update the macroscale solution in the constitutive relationship and provide new microscale boundary conditions.

The microscale pressure difference represents the pressure difference that the lymphangions must generate to give the required flow for mass conservation at the macroscale. This is performed iteratively within each macroscale time step until the microscale solution has an insignificant effect on the macroscale and the following macroscale time step is begun (see Figure 42 for the relationship between macroscale and microscale times) for the relationship between the macroscale and microscale times). Vascular networks are commonly modelled as graphs with nodes (pressure values) and edges (flow values). In such models the edges also include a resistance term that relates the flow value to the difference in nodal pressure values. In our model this parameter is an overall representation of the microscale solution (pressure-flow relationship) referred to as tangent compliance (including total Poiseuille and valve resistances of the entire chain) though it is

complicated by the presence of intrinsic contractions in the lymphatics, reflected in the pressure difference generated by the RVE.

Pressure conditions (external P_{EXT} , inlet P_{IN} and outlet P_{OUT}) are prescribed at the macroscale. The model, however, must capture the interaction of lymphangions with both flow and pressure coupling, leading to the calculation of a flow boundary condition (Q_{IN}). An additional parameter is also included to capture the network branching (through parallel number of RVEs M , assuming all vessels at each generation of the network behave identically). External pressure and parallel vessel number are assigned at the left and right ends of the macroscale ($P_{EXT,L}$, $P_{EXT,R}$, M_L and M_R , respectively) and assumed to vary linearly (so can be linearly interpolated for the nodal values, as in equations 52 and 53). A major advantage of using computational homogenisation for this problem is the fact that detailed modelling of vessel junctions is not required.

$$P_{EXT,I} = P_{EXT,L} \left(1 - \frac{x_I}{L}\right) + P_{EXT,R} \frac{x_I}{L} \quad (52)$$

$$M_I = M_L \left(1 - \frac{x}{L}\right) + M_R \frac{x}{L} \quad (53)$$

4.2.1. Microscale

There are two types of RVE at the microscale, both lumped-parameter models of simultaneously contracting lymphangion chains (though inter-lymphangion contraction delay could easily be included). The number of lymphangions (n) in both types of RVE is assumed identical.

The first RVE type is the lymphangion model as developed previously with pressure-only boundary conditions and is used to calculate the network inflow for reasons covered below. This RVE is included outside of the macroscale as it is not actually part of the network being considered but is a representation of lymphatics upstream of the network being considered.

The second RVE is the same model with an upstream compliance unit added to allow for the prescription of inflow (as required for complete coupling of the lymphangions) without over-

prescribing the problem. These compliance RVEs are those assigned to each macroscale element of the network being considered.

RVE models are numerically stiff differential-algebraic equations, meaning that the time step required is much smaller than the macroscale time step and the RVE uses an adaptive time-step solver built into MATLAB (ODE15S) to accurately solve the model. RVEs use an extensively validated lumped parameter model for short lymphangion chains (Bertram et al., 2018, Bertram et al., 2017, Bertram et al., 2016b, Bertram et al., 2016a, Bertram et al., 2015, Bertram et al., 2014a, Bertram et al., 2014b, Jamalain et al., 2013, Bertram et al., 2011). This model has been through several iterations as covered in Chapter 2, and the prescribed functions for passive tube law, valve resistance, and intrinsic contractions are used here are the most recent versions as given in (Jamalain et al., 2017) and here as equations 54 to 60 (plotted in Chapter 3 as Figure 18, Figure 20, Figure 21, and Figure 22).

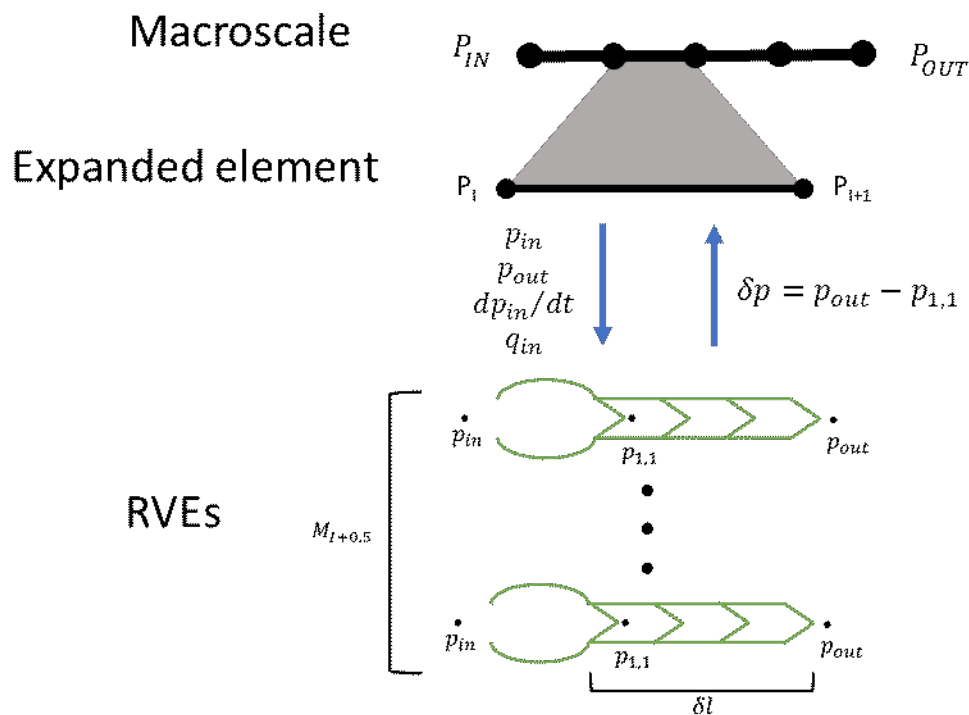


Figure 39: Coupling of the macroscale and microscale showing the inlet and outlet pressure boundary conditions prescribed at the macroscale. Below this is an expanded view of a single element and the coupling with the microscale compliance RVEs (passing down inlet and outlet pressure, the rate of change of inlet pressure, and the inflow to return the solution of pressure difference). The bottom figure shows the parallel RVEs with the pressure conditions and the upstream pressure within the first lymphangion, used in the calculation of returned pressure difference. The axial length of an RVE chain is also shown.

4.2.1.1. Unadapted lymphangion RVE

The unadapted model takes pressure boundary conditions and consists of an ordinary-differential equation for diameter from mass conservation (equation 54) and several momentum conservations (two each for the lymphangion body and the valves, equations 55a-d). Intrinsic contractions of the lymphangions are included through a wall-force balance (equation 60) relating the pressure in the middle of the lymphangion to the external pressure with a passive tube law (equation 61) and intrinsic contractions included through the prescription of diameter- and time-dependence (equations 58 and 59a-d) of intrinsic contractions. The passive tube law is a diameter-transmural pressure relationship of the wall with zero active force. The valve resistance is given by a sigmoidal relationship describing the resistance of the valve at different pressure differences across it (positive for decreasing pressure) and includes an experimentally observed bias to the open position. The flow generated by this RVE is then upscaled to the macroscale and used as a boundary condition for compliance RVEs.

$$\frac{d(d_i)}{dt} = \frac{2}{\pi d_i l_{lym}} (q_i - q_{i+1}) \quad (54)$$

where d is the lymphangion diameter, l_{lym} is the length of a lymphangion, q_i is the flow through valve i

$$p_{2,i-1} - p_{1,i} = R_{vi} q_i \quad (55a)$$

where p_2 is the downstream pressure, p_1 is the upstream pressure, R_v is the valve resistance

$$p_{1,i} - p_{m,i} = R_{ves} q_i \quad (55b)$$

where p_m is the mid-lymphangion pressure, R_{ves} is the Poiseuille resistance

$$p_{m,i} - p_{2,i} = R_{ves} q_{i+1} \quad (55c)$$

$$p_{2,i} - p_{1,i+1} = R_{vi+1} q_{i+1} \quad (55d)$$

$p_{2,i-1}$ and $p_{1,i+1}$ are the inlet and outlet pressure boundary conditions passed down from the macroscale.

$$R_v = R_{v,min} + R_{v,max} \left[1 / \left(1 + \exp(s_o(\Delta p - p_o)) \right) + 1 / \left(1 + \exp(-s_f(\Delta p - p_f)) \right) \right] \quad (56)$$

where R_v is the valve resistance, $R_{v,min}$ is the minimum (open) valve resistance, $R_{v,max}$ is the additional resistance on valve closure, s_o is the slope of valve opening, Δp is the pressure difference across the valve (positive for decreasing pressure), p_o is the opening pressure, s_f is the slope of valve failure, p_f is the pressure for valve failure

$$R_{ves} = 64\mu l_{lym} / \pi d^4 \quad (57)$$

$$M_t = \begin{cases} M_0 & \text{if } t_{temp} > 0.5(t_r + t_c) \\ M_a \left(1 - \cos\left(\frac{2\pi t_{temp}}{t_c}\right) \right) / 2 + M_0 & \text{if } t_{temp} > 0.5t_c \\ M_a \left(1 - \cos\left(\frac{2\pi(t_{temp} + 0.5(t_r + t_c))}{t_r}\right) \right) / 2 + M_0 & \text{if } 0.5t_c < t_{temp} < 0.5(t_r + t_c) \end{cases} \quad (58)$$

$$t_{temp} = \text{mod}(t, \text{cycletime})$$

$$\text{cycletime} = 0.5(t_r + t_c) + t_d$$

where *cycletime* is the duration of the contraction cycle, t_r is the duration of relaxation, t_c is the duration of contraction, t_d is the diastolic period, M_t is the time-dependence of intrinsic contractions, M_0 is the tonic tension, t_{temp} is the time from the beginning of the current contractile cycle, M_a is the additional tension on phasic intrinsic contraction

$$M_{d0} = 5.5 / \left(1 + \exp(-s_{d0}(D - D_0)) \right) \quad (59a)$$

$$M_{d1} = 0.5 / \left(1 + \exp(-s_{d1}(D - D_1)) \right) \quad (59b)$$

$$M_{d0} = 2 / \left(1 + \exp(s_{d2}(D - D_2)) \right) \quad (59c)$$

$$M_d = \frac{M_{d0} + M_{d1} + M_{d2} - 2}{6} \quad (59d)$$

where s_{d0} , D_0 , s_{d1} , D_1 , s_{d2} and D_2 are constitutive parameters with the same values as in the muscle model

$$p_{m,i} = p_{ext,i} + f_{pas,i} + 2M_{d,i}M_t/d_i \quad (60)$$

$$f_{pas,i} = c_1 \exp(c_2 d_i) + c_3 \exp(c_4 d_i) + c_5 d_i + c_6 - c_7/d_i^3 \quad (61)$$

where c_1 , c_2 , c_3 , c_4 , c_5 , c_6 , c_7 are constitutive parameters with the same values as in the muscle model

Parameter	Description	Value [units]
l_{lym}	Length of each lymphangion	0.3 [cm]
d_0	Initial diameter of each lymphangion	200 [μm]
C	Main RVE upstream compliance	10^{-12} [cm^5/dyne]
μ	Dynamic viscosity	10^{-4} [Pa s]
t_c	Contraction duration	2 [s]
t_r	Relaxation duration	2 [s]
t_d	Diastole duration	1.5 [s]
M_0	Tone tension	0 [dyne/cm]
M_a	Peak intrinsic tension	250 [dyne/cm]

4.2.1.2. Compliance RVE

The addition of a (zero-dimensional) compliance unit resulted in an additional equation for the charging of the pressure in the compliance (p_c) resulting from the upstream pressure boundary condition and the difference between the inflow boundary condition and the flow through the first valve of the lymphangion chain (q_{v1}), initialised to $p_c = p_{in}$

$$\frac{dp_c}{dt} = \frac{dp_{in}}{dt} + \frac{1}{C}(q_{in} - q_{v1}) \quad (62)$$

The opening of the first valve is then regulated by the difference between the compliance pressure and the pressure at the upstream end of the first lymphangion.

Note that the incoming boundary conditions are prescribed on the upstream compliance unit, and that flow and pressure at the actual inlet of the lymphangion chain can vary depending on the

behaviour of the compliance unit. Physically, this unit represents the compliance of upstream lymphangions and does not cause additional viscous pressure loss (i.e., resistance is zero).

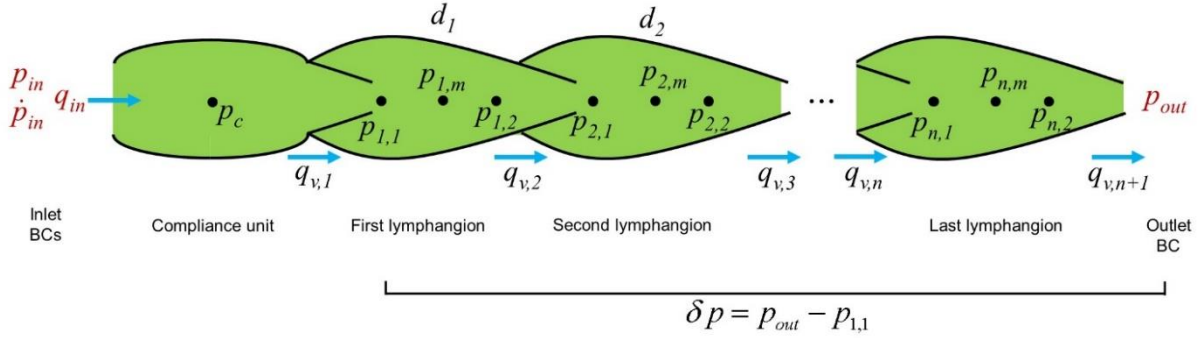


Figure 40: Schematic of the modified lymphangion pumping model as a microscale RVE. The compliance RVEs are assigned a mixture of pressure and flow boundary conditions. These RVEs calculate the pressure in the compliance, the diameter of each lymphangion, the flow through each valve, and three pressures per lymphangion (upstream, central and downstream). The instantaneous pressure difference across the RVE (δp) is the output returned to the macroscale.

The compliance of a passive lymphangion can be calculated from the passive tube law. This tube law provides a relationship between the transmural pressure and the diameter of passive lymphangions and, since we have assumed that the lymphangion is a radially expanding and contracting cylinder of constant axial length, we can use this to obtain a relationship between the transmural pressure and the lymphangion volume (v).

$$v_i = \pi l_{lym} \frac{d_i^2}{2} \quad (63)$$

This transmural pressure-volume relationship can then be differentiated with respect to the volume to get an equation for passive lymphangion compliance (Figure 41). We then use a constant value of the compliance that is representative of the values in the stiffening region of the passive tube law around a diameter of 200 μm . The result was a compliance value of $c = 10^{-12} \text{ cm}^5/\text{dyne}$.

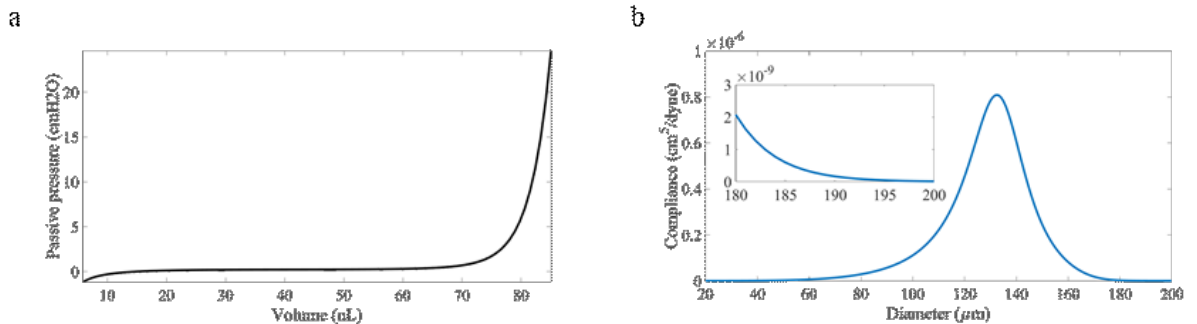


Figure 41: Plots showing the passive pressure-volume form of the passive tube law and the resultant compliance

4.2.2. Coupling the scales

Quasi-steady macroscale conditions are passed down to the microscale for solution of the RVE

models. In addition, the quasi-steady values passed down as microscale boundary conditions mean that there are initial transients for each RVE simulation, so several initial contraction cycles were run before the calculation of variables that are returned to influence the macroscale solution. Due to the periodic nature of the RVE model, the only important factor from macroscale timing is the time into the current contraction cycle (i.e., the position in the time-dependent tension). The RVE solution returns to the macroscale as either a flow (inlet RVE) or a pressure difference (compliance RVE).

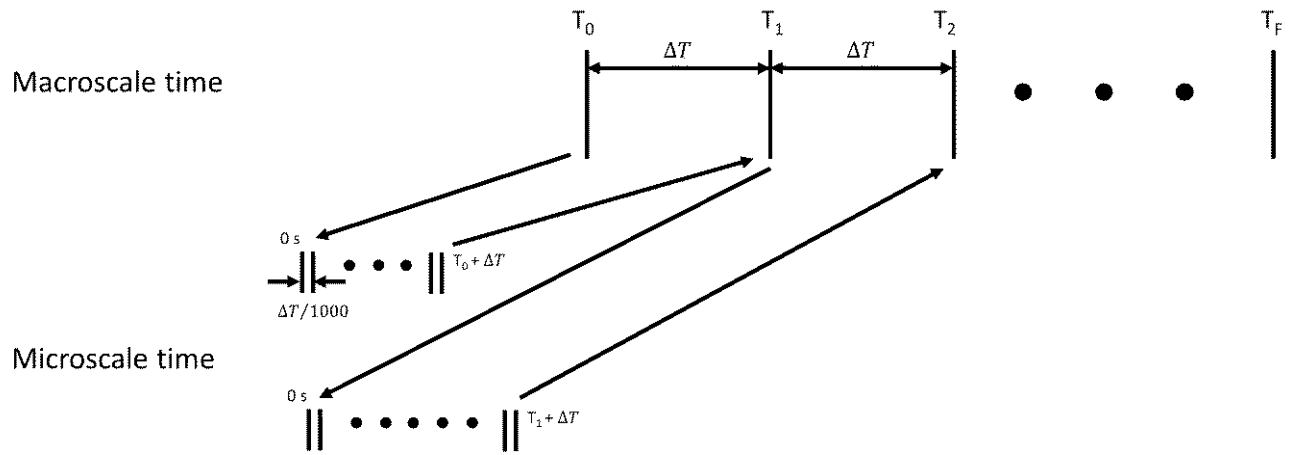


Figure 42: Diagram of the interaction between macroscale and microscale times

4.2.2.1. Inlet RVE

The inlet RVE is prescribed inlet and outlet pressure boundary conditions assuming a consistent pressure gradient with the main macroscale and is run only once per macroscale time step as changes in the macroscale solution do not affect the function of this inlet RVE (it is only dependent on the macroscale boundary conditions).

$$p_{in} = P_{IN} \quad (64a)$$

$$p_{out} = P_{IN} + \delta l (P_{OUT} - P_{IN})/L \quad (64b)$$

where δl is the length of an RVE

Additionally, the pressure external to the RVE is passed down as the external pressure at the left of the main network.

$$p_{ext} = P_{EXT,L} \quad (65)$$

Equations 54 to 61 are then solved with $p_{2,i-1} = p_{in}$ and $p_{1,i+1} = p_{out}$ and the solution stopping at the end of the macroscale time step. The instantaneous flow rate through the final valve in the lymphangion chain at the end of the macroscopic time step is returned to the macroscale by summing over the parallel number of RVEs at the inlet (M_L) to give network flow for use in the macroscopic solver and inlet boundary conditions in compliance RVEs.

$$Q_{IN} = M_L q \quad (66)$$

The radius of the RVE is stored as the instantaneous value of the radius at the end of the macroscale time step averaged between the lymphangions of the RVE chain (R). This is not used in the macroscale solution, but is required to keep track of the RVE size and prevent model instabilities with sudden differences in RVE radius between RVE calls.

$$R = \frac{\sum_{i=1}^n r_i}{n} \quad (67)$$

where n is the number of lymphangions in the RVE, r_i is the radius of the n^{th} lymphangion in the RVE

4.2.2.2. Compliance RVE

The compliance RVE is also passed both inlet and outlet pressure boundary conditions but is additionally assigned an inflow condition and the rate of change of inlet boundary pressure. These boundary conditions are assigned from the macroscale element values in which the RVE resides. This RVE is iteratively run with the macroscale solution giving updated boundary conditions.

The inlet and outlet pressure conditions are calculated from the midpoint macroscale pressure minus or plus the macroscale spatial gradient of pressure ($\nabla P_{I+0.5}$) multiplied by half of the RVE length (δl), respectively. This is part of the assumption of linear pressure variation between nodes.

$$p_{in} = P_{I+0.5} - \nabla P_{I+0.5} \frac{\delta l}{2} \quad (68a)$$

$$p_{out} = P_{I+0.5} - \nabla P_{I+0.5} \frac{\delta l}{2} \quad (68b)$$

$$\nabla P_{I+0.5} = (P_{I+1} - P_I) / \Delta X \quad (68c)$$

Differentiating equation 68a with respect to time gives the rate of change of inlet pressure as required by the compliance unit

$$\frac{dp_{in}}{dt} = \frac{\partial P_{I+0.5}}{\partial T} - \frac{\partial \nabla P_{I+0.5}}{\partial T} \frac{\delta l}{2} \quad (69)$$

The flow is calculated as the inflow from the inlet RVE divided by the number of parallel elements at the midpoint of the node (macroscale mass conservation assumes no spatial gradient in flow, so the inflow is evenly divided by the number of RVEs in parallel)

$$q_{in} = Q_{IN} / M_{I+0.5} \quad (70)$$

Again, external pressure is passed down but this time by averaging the nodal values on either side of the macroscale element the RVE is assigned to. External pressure is prescribed to the microscale as a single value (there can be spatial gradients in the external pressure at the macroscale, but they are assumed to give negligible differences at the microscale).

$$p_{ext} = \frac{P_{EXT,I} + P_{EXT,I+1}}{2} \quad (71)$$

After solution of the microscale model (equations 62 and 54 to 61 with $p_{2,i-1} = p_c$ and $p_{1,i+1} = p_{out}$) the pressure difference along the RVE (δp) is returned, reflecting the pressure difference that the lymphatics must generate to give the required flow for macroscale mass conservation.

$$\delta p = p_{out} - p_{1,1} \quad (72)$$

The radius is again stored for use in the following macroscale time step. A flowchart of the solution algorithm for this RVE is included as Figure 43.

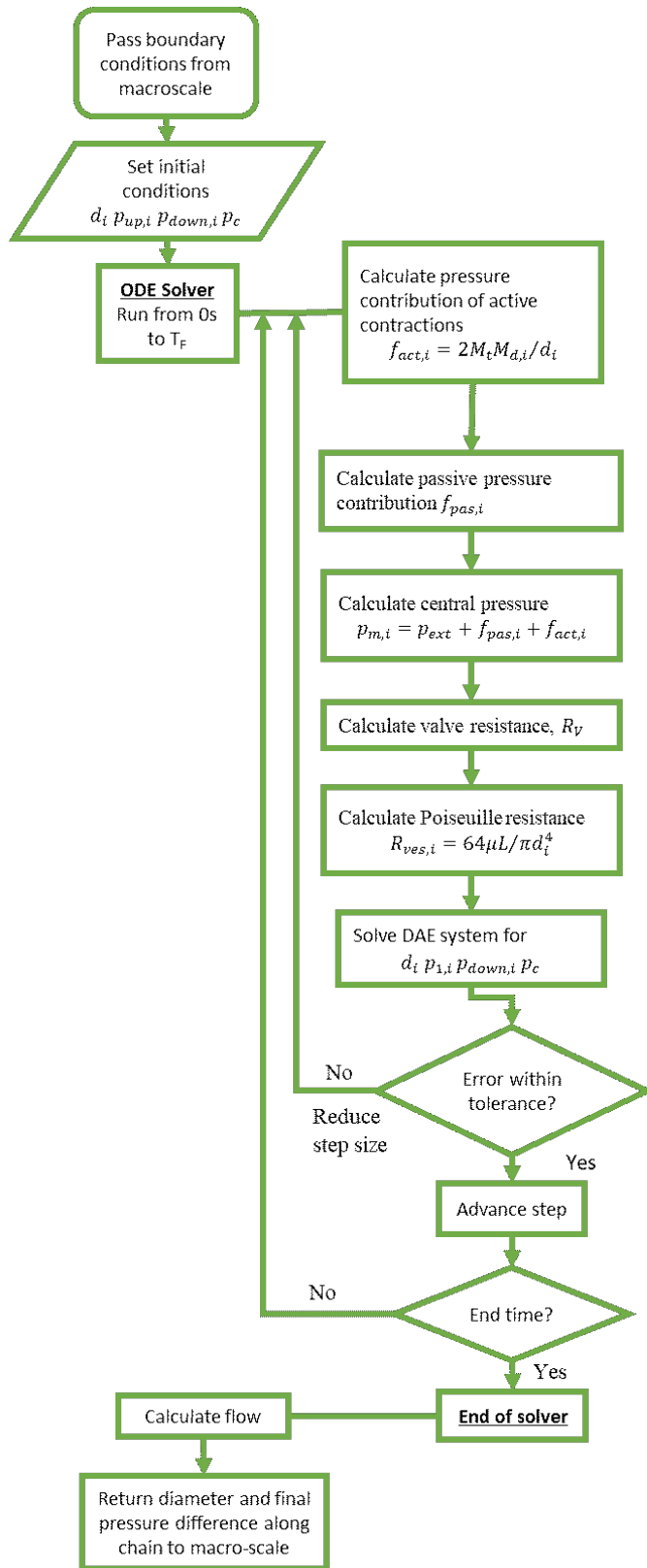


Figure 43: Solution algorithm for the compliance RVE

4.2.3. Macroscale solution

The objective of the macroscale scheme is to use results from the RVEs to determine the pressure profile along the network at all nodes except for external nodes as they are prescribed boundary

conditions. The initial values of these unknown internal nodal pressures at the very beginning of the simulation are assigned by linear interpolation between the boundary conditions at the left and right ends of the network.

$$P_I(T = 0) = P_{IN} \left(1 - \frac{x}{L}\right) + P_{OUT} \frac{x}{L} \quad (73)$$

Mass conservation at the macroscale is ensured by enforcing that the gradient in flow is zero.

$$\frac{\partial Q_I}{\partial x} = 0 \quad (74)$$

Momentum conservation then uses this mass conservation (which dictates the flow at every node and element midpoint) in a momentum conservation equation which uses a “resistance-type” term based on the microscale pressure difference. The objective of this is to determine the macroscale pressure shape that satisfies the mass conservation through sampling the detailed microscale model. The coupling between scales includes the macroscale flow from the conservation of mass with the inflow from the inlet RVE and momentum conservation from the microscale pressure gradient returned by the compliance RVEs.

The difference in macroscale flow between adjacent macroscale elements can be multiplied by the pressure gradient and its reciprocal.

$$\Delta Q_I = Q_{I+0.5} - Q_{I-0.5} = Q_{I+0.5} (\nabla P_{I+0.5})^{-1} \nabla P_{I+0.5} - Q_{I-0.5} (\nabla P_{I-0.5})^{-1} \nabla P_{I-0.5} \quad (75)$$

The gradient in macroscale pressure can be written as a finite difference such that the flow difference can be related to the unknown nodal pressures.

$$\Delta Q_I = Q_{I+0.5} - Q_{I-0.5} = Q_{I+0.5} (\nabla P_{I+0.5})^{-1} \frac{P_{I+1} - P_I}{\Delta x} - Q_{I-0.5} (\nabla P_{I-0.5})^{-1} \frac{P_I - P_{I-1}}{\Delta x} \quad (76)$$

The pressure gradient can also be written in terms of the microscale pressure difference by ensuring that both the macroscale and microscale pressure gradients are identical

$$\Delta Q_I = Q_{I+0.5} - Q_{I-0.5} = Q_{I+0.5} \left(\frac{\delta p}{\delta l}\right)^{-1} \frac{P_{I+1} - P_I}{\Delta x} - Q_{I-0.5} \left(\frac{\delta p}{\delta l}\right)^{-1} \frac{P_I - P_{I-1}}{\Delta x} \quad (77)$$

The macroscale pressure-flow momentum relation can then be obtained by defining the conductance term combining macroscale and microscale properties to couple the two scales

$$G_{I+0.5} = \frac{Q_{I+0.5}}{\delta p} \frac{\delta l}{\Delta X} \quad (78)$$

$$\Delta Q_I = Q_{I+0.5} - Q_{I-0.5} = G_{I+0.5}(P_{I+1} - P_I) - G_{I-0.5}(P_I - P_{I-1}) \quad (79)$$

This pressure-flow relation can then be applied to all macroscale elements and compared to the desired solution of zero flow difference \mathbf{H} from the conservation of mass to update the unknown macroscale pressures (vector \mathbf{P}).

$$\mathbf{H}(2:N) = 0 \quad (80)$$

The flow difference across the first node and last node are special cases. The flow difference across the first node is simply the inflow

$$\mathbf{H}(1) = Q_{IN} \quad (81)$$

The flow difference across the final node is the midpoint flow minus the conductance of the final element midpoint multiplied by the outlet pressure boundary condition.

$$\mathbf{H}(N+1) = Q_{N+0.5} - G_{N+0.5}P_{OUT} \quad (82)$$

$$[\mathbf{G}] = \begin{bmatrix} -G_{0.5} & G_{0.5} & 0 & \cdots & 0 \\ G_{0.5} & -G_{0.5} - G_{1.5} & G_{1.5} & 0 & 0 \\ 0 & G_{1.5} & \ddots & \ddots & 0 \\ \vdots & \ddots & \ddots & -G_{N-1.5} - G_{N-0.5} & G_{N-1.5} \\ 0 & \cdots & 0 & G_{N-1.5} & -G_{N-1.5} - G_{N-0.5} \end{bmatrix} \quad (83a)$$

$$\{\mathbf{P}\} = \begin{Bmatrix} P_{IN} \\ P_1 \\ \vdots \\ P_{N-2} \\ P_{N-1} \end{Bmatrix} \quad (83b)$$

The macroscale constitutive equation for momentum conservation is then (in vector-matrix format)

$$\{\mathbf{H}\} = [\mathbf{G}]\{\mathbf{P}\} \quad (83c)$$

So the pressure can then be updated iteratively within each macroscale time step using

$$\{\mathbf{P}\}^{k+1} = [\mathbf{G}]^{-1} \{\mathbf{H}\}^k \quad (84)$$

where k is the current macroscale time step

The nodal pressures are forced to be at least equal to the inlet pressure to ensure that there is no backflow during diastole.

$$P_I = P_{IN} \quad \text{if} \quad P_I < P_{IN} \quad (85)$$

The pressure is considered converged when the L2-error of the pressure (change in pressure between successive iterations) decreases to below 10^{-2}

$$\text{err}_P = \frac{\|\mathbf{p}^{k+1} - \mathbf{p}^k\|}{\|\mathbf{p}^{k+1}\|} < 10^{-2} \quad (86)$$

Once this convergence criterion is reached, the model progresses to the following macroscale time step, with a new flow rate calculated from the inlet RVE (due to the different position in the time-dependence of intrinsic contraction). The boundary conditions of the inlet RVE are not changed, but the network inflow is updated as a result. The macroscale solution algorithm flowchart is included as Figure 44.

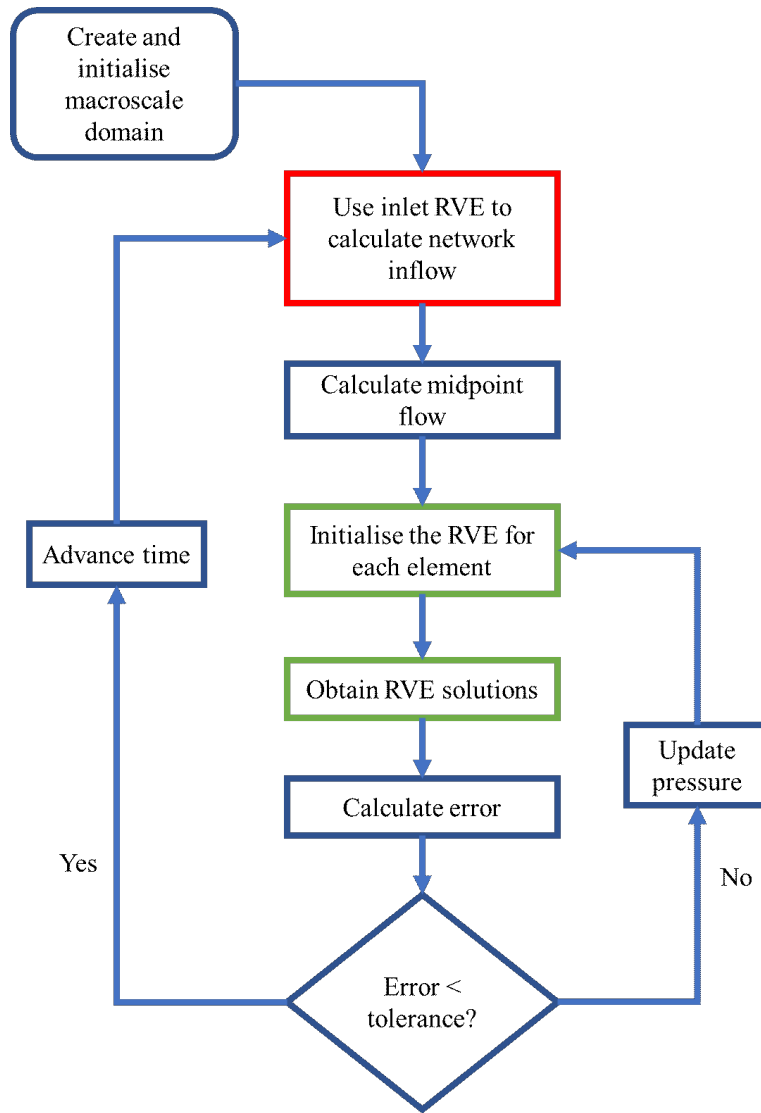


Figure 44: Solution algorithm for the macroscale homogenisation. The red box indicates calling the unmodified RVE function with the solution algorithm as used previously and green boxes represent calling the compliance RVE (algorithm in Figure 43).

Symbol	Description	Value [units]
T_0	Start time for macroscale	24.5 [s]
T_F	End time for macroscale	28.0 [s]
ΔT	Macroscale time step	0.25 [s]
N	Number of macroscale elements	5
n	Number of lymphangions per RVE	5
L	Length of the macroscale domain	7.5 [cm] (equivalent to 25 lymphangions in series)
P_{IN}	Inlet pressure boundary condition	5 [cmH ₂ O]
P_{OUT}	Outlet pressure boundary condition	8 [cmH ₂ O]
P_{EXT}	External pressure	2 [cmH ₂ O] (unless otherwise specified)

4.3. Results

Under reference conditions of inlet pressure 5 cmH₂O, outlet pressure 8 cmH₂O and external pressure 2 cmH₂O, the homogenised diameter and pressure both increase with inflow (Figure 45c,e). This is different from the results of a direct simulation of a 25-lymphangion chain in the lymphangion model (essentially a long inlet RVE) under the same pressure conditions that shows a decrease in diameter as occurs *in vivo*. The increasing diameter from the homogenised model is because the single peak flow from the inlet pressure RVE (Figure 45a) overwhelms the intrinsic contractions of the compliance RVE lymphangions. The homogenised model contains a single peak in flow because the flow through the outlet valve of the inlet RVE is prescribed to every RVE in the homogenised model, so there is no second peak and no suction pressure (minimum pressure is enforced to be at least the inlet pressure). The direct simulation, however, shows two peaks in flow through each of the internal valves (i.e. not the inlet or outlet valve) with the second peak corresponding to a decrease in the pressure along the chain. The homogenised pressure during diastole is constant at the inlet boundary condition along the macroscale except in the final element which has an increased value of 6.5 cmH₂O in order to meet the outlet pressure boundary condition. The direct model, however, has a diastolic pressure decrease of 0.76 cmH₂O along the chain (Figure 45d). At peak flow, the homogenised pressure of course decreases along the macroscale (12.9 cmH₂O in the first macroscale element to 8.6 cmH₂O in the final element). This is to ensure that the flow is constant through all RVEs (as prescribed by the macroscale mass conservation) as the diameter along the chain varies by only 1.5% at this time, meaning that the resistance to flow varies little (Figure 45c). The diastolic diameter of the direct model is significantly greater than that of the homogenised model (average along the chain of 181.0 μ m in direct model and 175.8 μ m in the homogenised model), see Figure 45e. This is because of the suction-based filling in the direct model that is absent in the homogenised model causes more fluid uptake. For the cases run here, the direct model took approximately 4 minutes whilst the homogenised model took

approximately 5 hours on a laptop with an AMD Ryzen 7 3700U processor (quad core 2.3GHz per core) and 8GB of RAM.

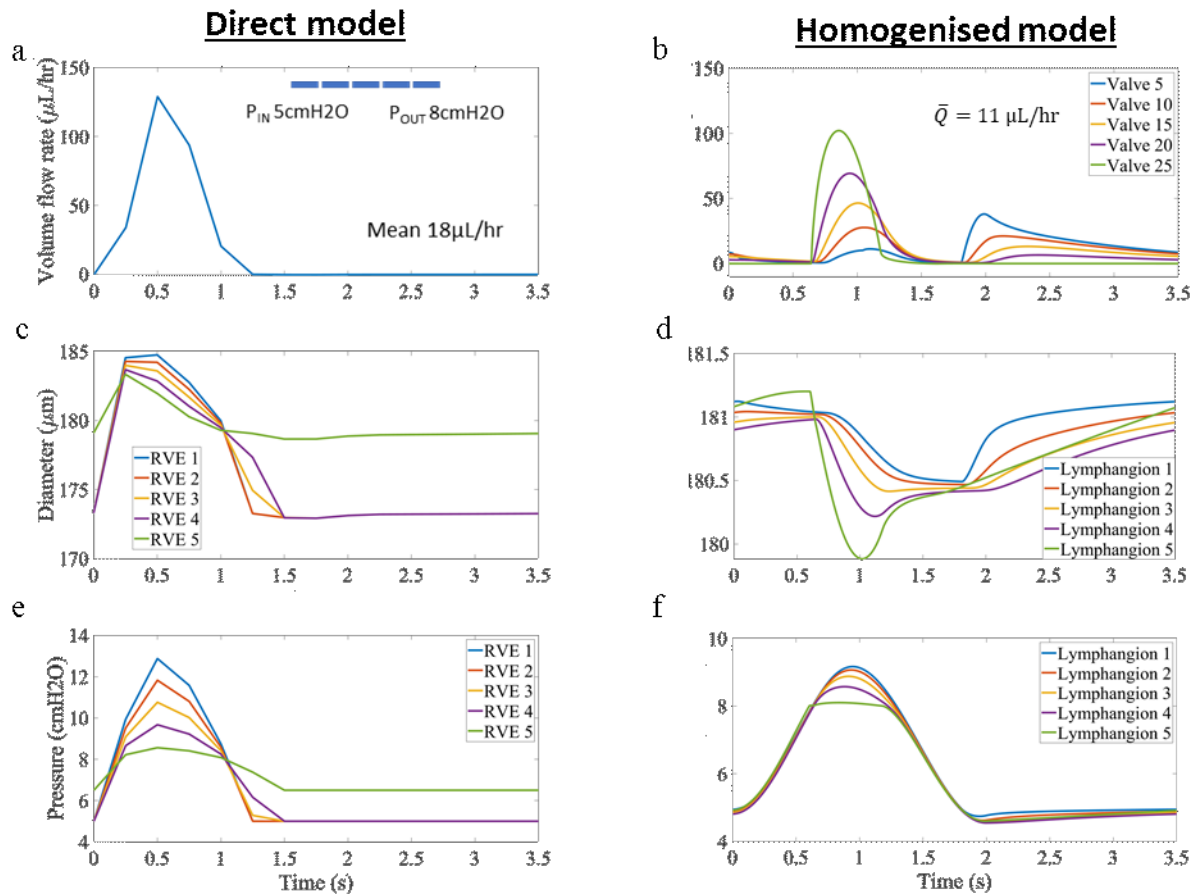


Figure 45: Panel of plots comparing the time-dependence of results from the homogenised model and a direct pressure boundary condition lymphangion chain (long inlet RVE) of 25 lymphangions under the same pressure conditions (inlet 5 cmH₂O, outlet 8 cmH₂O and external 2 cmH₂O). (a) shows the flow through the homogenised network (b) shows the flow through several valves in the direct simulation (c) shows the diameter of the homogenised network (d) shows the diameter of lymphangions in the direct simulation (e) shows the pressure in the homogenised model and (f) the diameter of some lymphangions in the direct simulation

Increasing external pressure at the inlet from 2 cmH₂O (Figure 46a,b) to 5 cmH₂O (Figure 46c,d) caused reduced average flow through the network (3 $\mu\text{L/hr}$ compared to 18 $\mu\text{L/hr}$). This is because the inlet lymphangions had reduced transmural pressure (first macroscale element 0.28 cmH₂O for 5 cmH₂O and 0.30 cmH₂O for 5 cmH₂O to 2 cmH₂O compared to 3 cmH₂O for 2 cmH₂O and 2.7 cmH₂O for 2 cmH₂O to 5 cmH₂O) as shown in Figure 46f, resulting in a smaller diameter (first macroscale element 78 μm for 5 cmH₂O and 79 μm for 5 cmH₂O to 2 cmH₂O compared to 173 μm for 2 cmH₂O and 172 μm for 2 cmH₂O to 5 cmH₂O) so there was a smaller volume of lymph

available to pump (see Figure 46e). Because of the increase in internal pressure along the network, transmural pressure is not a mirror image for the increasing and decreasing gradients in external pressure, causing the diameter to not be a mirror image.

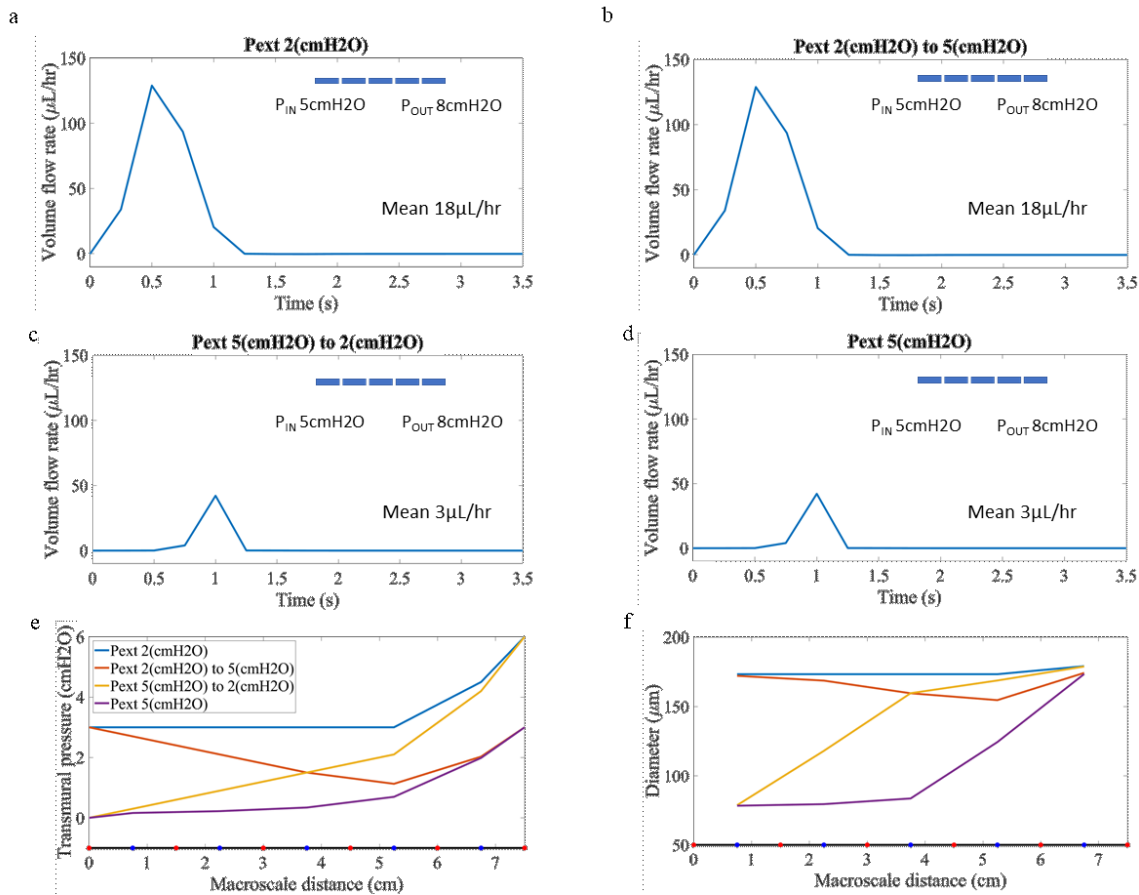


Figure 46: Panel of plots showing the effects of varying external pressure in the homogenised model for a single vessel 25 lymphangions long with an inlet pressure of 5 cmH₂O, outlet pressure of 8 cmH₂O and external pressure of 2 cmH₂O. (a-d) show the time-dependent network flow (e) shows the variation of diastolic diameter along the macroscale and (f) shows the variation of diastolic transmural pressure along the macroscale. In (e) and (f) red circles show the position of nodes and blue circles the positions of macroscale element midpoints.

The flow through the network increases linearly with the parallel number of vessels at the inlet (Figure 47a) because the pressure conditions are the same, so the inlet RVE produces the same amount of flow (18 μL/hr), and then is summed over the parallel number of vessels. The pressure curves during contraction for converging networks become concave (Figure 47b,d). This is because there is consistent flow along the network and the total cross-sectional area along the chain decreases (due to the decreasing number of vessels in parallel), increasing the resistance to flow so more of a pressure drop is required to produce the same flow in more downstream elements. There

is only a very slight difference in diameter with more parallel vessels (the maximum diameter in the first macroscale element increased from 185 μm with a single vessel to 186 μm for 5 parallel inlet vessels and 187 μm for 10 parallel inlet vessels) (see Figure 47e-g) because the lymphangions are in the very stiff region of the passive tube law, causing the lymphangions to be unable to reduce their resistance. The increased pressure difference required for downstream elements meant that the highest pressure in the first element increased (12.9 cmH_2O for a single vessel to 16.5 cmH_2O for 5 parallel inlet vessels and 18.2 cmH_2O for 10 parallel inlet vessels).

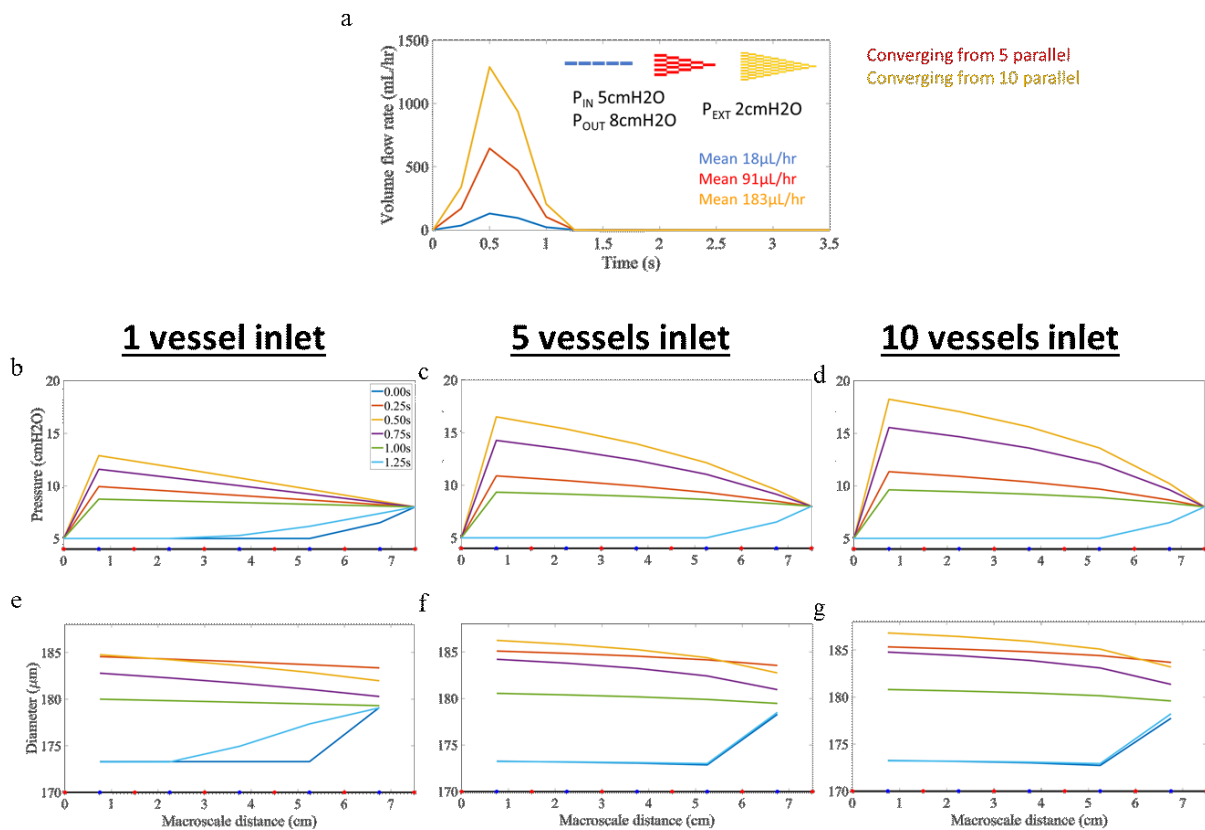


Figure 47: Panel of plots showing the effects of varying the parallel number of vessels at the inlet of the network 25 lymphangions long. Pressure conditions are kept constant with an inlet of 5 cmH_2O , outlet of 8 cmH_2O , and external of 2 cmH_2O . (a) shows the time-dependence of network flow which scales linearly with the parallel number of vessels (b-d) show the profiles of pressure along the macroscale at different time points and (e-g) show the diameter profiles along the macroscale at different time points.

The effects of external pressure on a converging network of lymphatic vessels (Figure 48) are similar to those on a single vessel. As discussed in the results from varying the parallel number of vessels at the inlet, the flow has increased proportionally so for each set of external pressure conditions, so the flow here is 10 times the flow for a single vessel under the same pressure conditions. The diastolic

diameter for inlet vessels again decreased with higher external pressure at the inlet (first macroscale element 71 μm for 5 cmH_2O and 79 μm for 5 cmH_2O to 2 cmH_2O compared to 173 μm for 2 cmH_2O and 172 μm for 2 cmH_2O to 5 cmH_2O) due to a smaller diastolic transmural pressure (first macroscale element 0.0 cmH_2O for 5 cmH_2O and 0.3 cmH_2O for 5 cmH_2O to 2 cmH_2O compared to 3 cmH_2O for 2 cmH_2O and 2.7 cmH_2O for 2 cmH_2O to 5 cmH_2O).

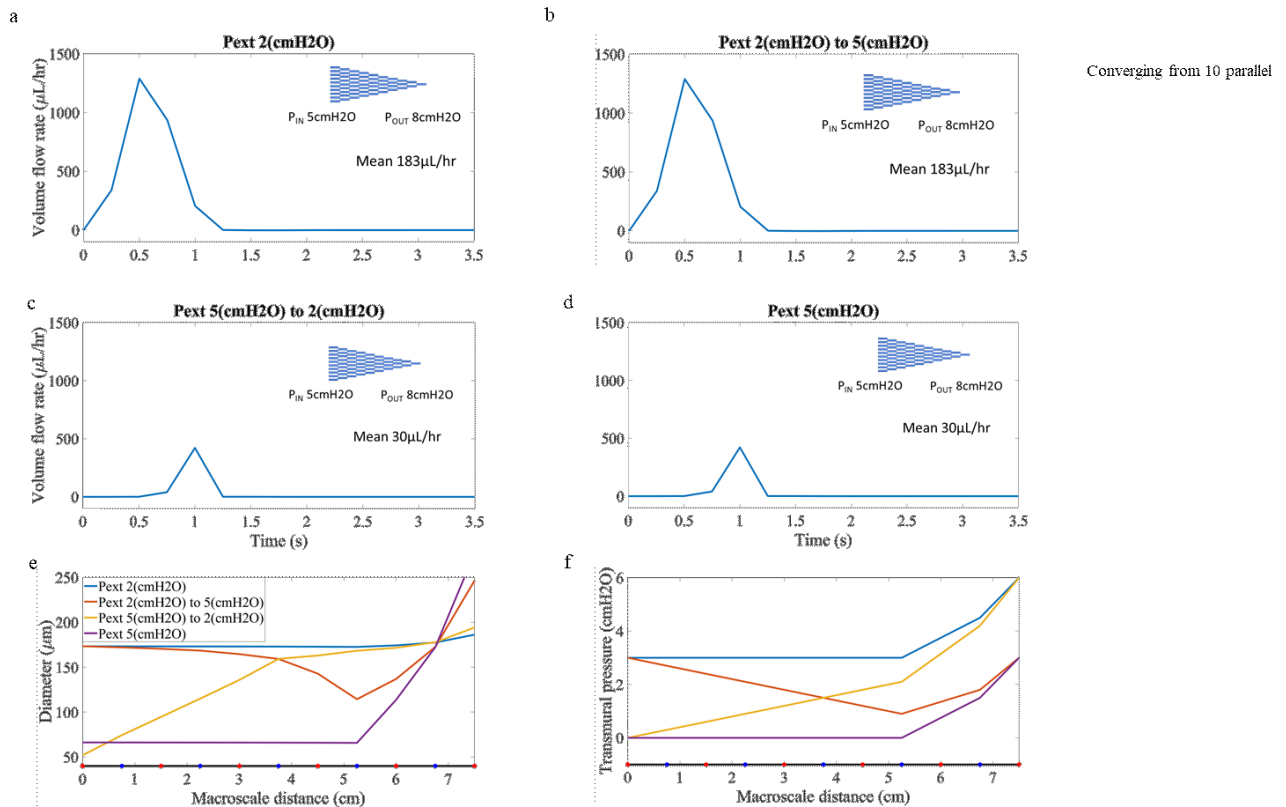


Figure 48: Panel of plots showing the effects of varying the external pressure for a network 25 lymphangions long converging from 10 parallel vessels at the inlet to a single vessel at the outlet with an inlet pressure of 5 cmH_2O and outlet pressure of 8 cmH_2O . (a-d) show the time-dependence of flow through the network (e) shows the variation of diastolic diameter along the macroscale and (f) shows the variation of diastolic transmural pressure along the macroscale. In (e) and (f) red circles show the position of nodes and blue circles the positions of macroscale element midpoints.

4.4. Discussion

One of the key functions of the lymphatic vessels is to maintain fluid homeostasis, which can breakdown to result in lymphoedema. In this chapter I have covered our progress in developing a model of large lymphatic networks that can represent multiple different geometries without re-deriving the model for each change of network geometry. The motivation behind developing such a model is that the small functional elements of the lymphatic system (lymphangions) interact in very large networks and that lymphoedema occurs on the network scale. Management/treatment

strategies for lymphoedema such as external pressure modulation also work at the network scale.

This means that to better understand lymphoedema and improve management/treatments we need to model the interaction of large networks of lymphangions. A computational model is warranted as it is not feasible to remove and cannulate such large networks.

The model in its current form does not reflect the actuality of lymphatic networks. Prescription of the same inflow to each RVE does not reflect the *in vivo* conditions where the outflow from each lymphangion forms the inflow for the following lymphangion, so future developments should use the more accurate mass conservation that accounts for different volume changes between RVEs as considered in the lymphangion model. The issue with this is deciding which condition to include for each macroscale time step's convergence. As a result of prescribing the same inflow to each RVE, the homogenised model gives a diameter increase during the intrinsic contractions of lymphatic muscle which is not the case observed *in vivo*. The prescription of consistent flow throughout the network means that, during contraction, the pressure must decrease along the chain after the first RVE. Effectively, the entry RVE is providing the input flow and the other RVEs are just dynamic resistors that contribute no pumping. Instead, the flow from the entry RVE should input into the first macroscale element's RVE, and the output from each RVE should be the input for the adjacent downstream RVE with the macroscale mass conservation adjusted to allow for temporary storage of lymph in RVEs (i.e. include a volume change in the macroscale mass conservation as in the microscale conservation). The homogenised model does not capture the suction-based refilling characteristic of lymphatic function due to the prescription of a single flow peak, neglecting the suction-based refilling peak. Flow through the outlet valve on the inlet RVE does not produce a two-peak flow as occurs in lymphangions due to lymph expulsion during contraction followed by refilling with suction. This is a model limitation that could potentially be overcome by returning the flow through the penultimate valve. Preventing the macroscale pressure from reducing below the inlet boundary condition also prevents the model from capturing the important characteristic of suction-based refilling. The use of an RVE outside of the macroscale domain without any variations in the

outlet pressure condition is not particularly physiological, so it may be useful to move this RVE into the first macroscale element. The length scales considered are only a few orders of magnitude, so it is also suggested to transition to a second-order homogenisation. The homogenised model took longer than the direct model in the reference case presented here because the network is relatively short and we are simulating all lymphangions at the microscale to characterise the model under conditions where the results will be most similar to the direct model. At longer network scales (hundreds to thousands of lymphangions) where the homogenised model is sampling the microscale as in its final intended use, the direct simulation will take significantly longer. For example, the simulations for 25 lymphangions both took around 5 hours when the homogenised model used 25 lymphangions in 5 RVEs. These simulations, however, were run without any parallelisation and the time taken will reduce when this is implemented. A key development will be to update the model such that the resulting flow out of each RVE forms the inflow for the following RVE (the reason for implementing the compliance unit).

Model results obtained so far show that increased external pressure at the inlet reduces flow which is consistent with the results from previous publications (Jamalian et al., 2016, Jamalian et al., 2013). This implies that increased external pressure as occurs in the commonly used compression bandage treatment for lymphoedema can cause decreased flow within the lymphatic vessels. Compression bandages can still work, however, because the lymphatics are not the only fluid compartment, so inducing pressure gradients can cause flow through the interstitium or alter the flow of plasma out of blood vessels to reduce interstitial fluid accumulation. There are also devices that apply varying external pressure to the arm. The model predicts a different pressure shape between single vessels and converging networks. This is likely the case, but the limitations of the model mean that the actual pressure profiles predicted are likely not correct.

This model is intended to represent the entire lymphatic vasculature, which would require representation of the lymph nodes. Lymph nodes provide significant resistance to flow (Jafarnejad et

al., 2015), so a resistance unit should be included. There is also fluid exchange in the lymph nodes from the lymphatics directly into the blood (Jafarnejad et al., 2015), indicating the applicability of a point sink or source.

Other potential updates include diameter-dependent effects on the passive tube law and diameter-dependence of intrinsic force because of increased vessel diameters with progression through the network. The feedback models developed by Moore Jr and Bertram for shear- and transmural-pressure could also be incorporated to investigate the effects of local regulation on the overall network (Bertram et al., 2019, Bertram et al., 2018, Bertram et al., 2017).

CHAPTER 5 – CONCLUSIONS AND FUTURE WORK

5.1. Conclusions

The lymphatic vasculature has a major role in many physiologic functions including maintaining fluid homeostasis, immunology, cancer, and obesity, among others, but is understudied in comparison to the blood vasculature. Lymphatic vessels return interstitial fluid to the venous system by localised contractions of vessel segments bounded by valves, called lymphangions. Deficient lymphatic pumping can result in a chronic debilitating condition called lymphoedema involving the accumulation of fluid and proteins in the interstitium. The effectiveness of treatments for lymphoedema is limited and this can be attributed to a lack of understanding of the biomechanics of lymphatic pumping, including the contractility of specialised muscle lining the vessels. This muscle is called lymphatic muscle and exhibits both phasic and tonic contractions. *In vivo* and *in vitro* experiments performed on lymphangions are limited in that they cannot simultaneously measure pressure, diameter, and flow. This motivated the previous development of a lumped parameter model of lymphangion contractions by the research group. This thesis covers the development of two multiscale computational models to improve our understanding of lymphatic pumping across scales.

The first model examined the subcellular mechanisms of force generation in lymphatic muscle, and their effects on lymphangion-scale pumping. This model combines the sliding filament model of Huxley (Huxley, 1957) with its adaptation for smooth muscle (Mijailovich et al., 2000, Fredberg et al., 1999). These models were then structurally arranged with passive viscoelastic elements to model the contractility of lymphatic muscle cells. Multiple structural organisations were trialled but only one provided physiologic results. The muscle model was then incorporated into the group's existing lymphangion model for comparison with experimental results. This was the first model to study the mechanical and energetic aspects of lymphatic contraction at the subcellular scale. I showed that the model produces results that are qualitatively and quantitatively similar to experimental results from

rat mesenteric lymphangions whilst additionally estimating the thermodynamic efficiency of cross-bridge cycling. I then investigated the effects of varying pressure conditions on efficiency, predicting a decrease in lymphatic efficiency with low adverse pressure differences in the absence of mechanical feedback to excitation-contraction coupling. The maximum reported efficiency was approximately 35%, in the upper range reported from a range of muscle types. Finally, I investigated the effect of calcium oscillations with varying amplitudes and frequencies. The results show that, in the range of values tested, the oscillations can increase lymphangion outflow by up to 40%. The key advances of this model compared to the current state-of-the-art and the existing lumped-parameter lymphangion model are the prediction of energy aspects which will hopefully allow further insight into the reasoning behind lymphatic regulation and act as a step towards understanding the signalling pathways involved to possibly intervene and promote lymph flow. Energetics is also the other of the two key aspects of muscle function (besides mechanical as has already been investigated) and it is hoped that this model will spark increased interest in understanding this. This model is also a more mechanistic and detailed representation of the subcellular mechanisms of lymphatic muscle contraction and progresses towards physiologic modelling of lymphatic system function. The coupled muscle-lymphangion model is more sensitive to transmural pressure than was previously predicted in the prescribed contraction model, suggesting even more heavily that treatments for lymphedema should carefully consider the external pressure around lymphatics and its effect on the active pumping capability. A sensitivity analysis was also performed, finding that the muscle model is sensitive to calcium binding properties of troponin, the detachment of phasic heads with negative displacement, the peak calcium concentration, and the number of LMCs around the circumference. This has led to the suggestion for future experimental studies to gain more accurate values for these parameters, as covered in the following section.

The second model examined the interaction of lymphangions in a large network. A previous model of smaller idealised lymphatic networks based on the lumped parameter lymphangion model has been developed in the group (Jamalian et al., 2016). It was found that the lymphangion model was

prohibitively complex for limb-scale or larger lymphatic networks. Our new model uses computational homogenisation to reduce computational intensity by not modelling every lymphangion in the network. In the homogenised model we do not have to model the details of flow at junctions. The homogenised model also means that we do not have to re-derive the model equations for every change in geometry. I then compared the results from the homogenised model to a direct simulation of a chain of lymphangions. These results showed different behaviour for the homogenised and direct simulations, primarily in the fact that the homogenised model shows diameter increases during contraction whilst the direct simulation shows a diameter decrease. This is due to the prescription of the same flow at every RVE with mass conservation assuming that the spatial gradient of macroscale flow is zero. The homogenised model also doesn't capture the suction-based refilling. We cover suggested future changes to the model that will correct these deviations from true lymphatic function in the following section. Comparing the timing for the homogenised model and direct simulation showed that, in the case run here, the homogenised model took longer. Simulating longer networks, however, will cause the direct simulation to take longer than the homogenised model. I studied the effects of varying the external pressure, showing that high external pressure at the network inlet can collapse the upstream lymphangions, and that this disruption of individual lymphangions reduces the overall flow through the network. I also studied the effect of network branching, showing that the pressure profile along the network is different for single vessel and converging vessels with a linear decrease for a single vessel and a concave shape for a converging network.

5.2. Future work

In the muscle model, the CE forces scale with the number of myosin heads and the number of parallel rows of CEs. There are some images in the literature that could be used to estimate the number of CE rows (for example in (Muthuchamy et al., 2003)), but there is still significant uncertainty.

The muscle model has suggested multiple useful experiments yet to be performed. Obtaining more up-to-date recordings of the dimensional (rather than expression as a ratio of Fura-2 intensities as in (Souza-Smith et al., 2011)) calcium concentration in lymphatic muscle would be beneficial. Whilst there have already been some studies (for example (Souza-Smith et al., 2011, Shirasawa and Benoit, 2003)), further investigation into the response of calcium concentration and calcium sensitisation to variations in shear and transmural pressure would be beneficial in separating the regulation of lymphatic muscle into changes in calcium concentration and in calcium binding, especially since the binding properties of troponin and the peak calcium concentration were both shown to be important parameters in muscle function. This sensitivity to troponin also prompts further studies into the isoform(s) of troponin present. The increased sensitivity of lymphatics to transmural pressure shown by the muscle model compared to the prescribed contraction model suggests experiments where the external pressure is varied in active and pharmacologically reduced activation lymphangions to test whether the inhibition of muscle allows more consistent flow over a wider range of external pressures with potential implications in treatments for patients with oedema. Such experiments may be performed with the use of specific inhibitors or genetic knockouts of the cardiac β -myosin/troponin or SMB isoforms/calmodulin. Examples include the knockout of cardiac troponin as published by Huang and colleagues (Huang et al., 1999) or molecules that competitively bind to troponin, preventing the binding of calcium ions and keeping the actin binding sites blocked (see (Audran et al., 2013) for more information on calmodulin blockers) to isolate the active phasic and tonic components of lymphatic muscle. The suggested presence of titin and smitin should be investigated further using quantitative assays similar to (Muthuchamy et al., 2003) including determining the isoform(s) present and more detailed analysis of the relative concentrations of β -cardiac and SMB isoforms would provide additional clarity on the subcellular contractile element structure. It is suggested that inhibitors and activators of STDs used for investigation in smooth muscle (for example inhibitors or blockers of inositol 1,4,5-triphosphate receptors or calcium-activated chloride channels (von der Weid et al., 2008)) be applied to

lymphatics as this model shows that calcium oscillations may significantly affect the flow generated. Finally, the addition of energetics estimates in this model require further experimental investigation so that they can be validated. Such investigations could potentially be performed by measuring the concentration of inorganic phosphate through, for example, fluorescent protein MDCC-PBP (He et al., 2000) and heat generation. Investigating the energetics variations under various pressure and flow conditions may allow better understanding of the reasoning for regulation of lymphatic muscle which would be useful for developing treatments for lymphedema.

Future developments to the muscle model will include incorporating mechanical feedback through shear- and pressure-dependent variations in excitation-contraction coupling. The model will include shear-dependent decreases in calcium concentration (through nitric oxide) and transmural pressure-dependent increases in the calcium concentration and calcium sensitivity. This is motivated by the well-documented effects of shear- and transmural pressure-dependent effects on lymphatic pumping. The major anticipated insight is how the regulatory feedback optimises the energy efficiency of lymphatic muscle under different mechanical conditions, primarily a reduction in efficiency decrease at lower adverse pressure differences. Studying the effects of shear regulation on average flow and efficiency will also yield some interesting insights.

Additional potential developments may be to include overlap-dependence of the muscle contraction whereby the number of myosin heads that are available for attachment varies with muscle length due to the overlapping of filaments varying the number of myosin heads with actin sites in attachment range. This is motivated by the documented effects of overlap on force generation in all muscles, and additionally the potential importance of length adaptation in optimising flow over a large range of lymphangion diameters. The third development may be to include additional rates or head states to incorporate the weak ATP coupling that has been observed experimentally in striated muscles for improved energetics estimates. Experimental studies on lymphatic muscle energetics such as measuring ATP consumption and heat generation would be a very useful development. The

model could also be used to simulate lymphangion chains for improved correlation with some cannulated experiments.

The two models covered in this thesis could be combined such that the homogenised model includes a mechanistic basis for contractions. This would involve a simplification of the muscle model by using distribution-moment approximations in both types of contractile element based on previous derivations (Rampadarath and Donovan, 2018, Zahalak, 1981).

There are several potential developments of the homogenised model, though first the model needs to be updated to capture physiologic lymphangion characteristics (decreased diameter with contraction and suction-based refilling). The homogenised model is limited through the prescription of identical flow to all RVEs at every macroscale time step. The first step in future development of the homogenised model will be to use the outflow from each RVE as the inflow boundary condition for the following RVE. This will also involve changing the macroscale conservation of mass to allow for temporary storage of flow in RVEs by including a term for changes in lymphangion volume as is used at the microscale. The average flow over a contraction cycle, however, needs to be consistent for all macroscale elements, potentially requiring an additional condition for model solution. This is expected to cause the homogenised model to reproduce the diameter reduction observed *in vivo* and in the direct simulation. Prescription of the flow through the final valve means that there is only one flow peak which does not capture the suction-based refilling of lymphatics. One potential method to rectify this is to use the flow through the penultimate valve. The capture of suction-based flow would also require the limit that macroscale pressure never decreases below the inlet pressure be removed. Additionally, the pressure boundary condition RVE could be moved into the first macroscale element so that it has an updating downstream pressure condition which reflects the *in vivo* case of the afterload of one lymphangion being the preload of the downstream lymphangion. Finally, the separation of scales between the macroscale and microscale is not that large (only a few

orders of magnitude) in our model, suggesting the transition to a second-order homogenisation method.

This model is intended to model the entire lymphatic vasculature, which would require representation of the lymph nodes. Lymph nodes provide significant resistance to flow (Jafarnejad et al., 2015), so a resistance unit should be included. There is also fluid exchange in the lymph nodes from the lymphatics directly into the blood (Jafarnejad et al., 2015), indicating the applicability of a point sink or source.

A source term could be included to provide a better representation of initial lymphatics, e.g. through space- and/or time-dependence of additional flow into the RVE. It has been shown that the suction effect created by collecting lymphatics can open the primary valves to allow fluid uptake from the interstitium into initial lymphatics (Jamalian et al., 2017), so a coupling between the source term and macroscale pressure could be warranted. We may additionally include diameter-dependent effects on the passive tube law because of increased vessel diameters with progression through the network. The feedback models developed by Moore Jr and Bertram for shear- and transmural-pressure could also be incorporated to investigate the effects of local regulation on the overall network (Bertram et al., 2019, Bertram et al., 2018, Bertram et al., 2017).

REFERENCES

- ALLEN, J. M., MCHALE, N. G. & ROONEY, B. M. 1983. Effect of norepinephrine on contractility of isolated mesenteric lymphatics. *American Journal of Physiology - Heart and Circulatory Physiology*, 244, H479-H486.
- ANGELI, V., LLODRÁ, J., RONG, J. X., SATOH, K., ISHII, S., SHIMIZU, T., FISHER, E. A. & RANDOLPH, G. J. 2004. Dyslipidemia associated with atherosclerotic disease systemically alters dendritic cell mobilization. *Immunity*, 21, 561-574.
- ASPELUND, A., ANTILA, S., PROULX, S. T., KARLSEN, T. V., KARAMAN, S., DETMAR, M., WIIG, H. & ALITALO, K. 2015. A dural lymphatic vascular system that drains brain interstitial fluid and macromolecules. *The Journal of Experimental Medicine*, 212, 991-999.
- ASPELUND, A., TAMMELA, T., ANTILA, S., NURMI, H., LEPPÄNEN, G., ZARKADA, G., STANCZUK, L., FRANCOIS, M., MÄKINEN, T., SAHARINEN, P., IKKA, I. & KARI, A. 2014. The Schlemm's canal is a VEGF-C/VEGFR-3-responsive lymphatic-like vessel. *The Journal of Clinical Investigation*, 124, 3975-3986.
- AUDRAN, E., DAGHER, R., GIORIA, S., TSETKOV, P. O., KULIKOVA, A. A., DIDIER, B., VILLA, P., MAKAROV, A. A., KILHOFFER, M.-C. & HAIECH, J. 2013. A general framework to characterize inhibitors of calmodulin: use of calmodulin inhibitors to study the interaction between calmodulin and its calmodulin binding domains. *Biochimica et Biophysica Acta*, 1833, 1720-1731.
- AUKLAND, K. & REED, R. K. 1993. Interstitial-lymphatic mechanisms in the control of extracellular fluid volume. *Physiological Reviews*, 73, 1-78.
- AZUMA, T., OHHASHI, T. & SAKAGUCHI, M. 1977. Electrical activity of lymphatic smooth muscles. *Proceedings of the Society for Experimental Biology and Medicine*, 155, 270-273.
- BAGSHAW, C. R. 1993. *Muscle Contraction*, London, UK, Chapman & Hall.
- BAISH, J. W., KUNERT, C., PADERA, T. P. & MUNN, L. L. 2016. Synchronization and random triggering of lymphatic vessel contractions. *PLoS Computational Biology* [Online], 12.
- BALDAZZI, V., PACI, P., BERNASCHI, M. & CASTIGLIONI, F. 2009. Modeling lymphocyte homing and encounters in lymph nodes. *BMC Biomechanics*, 10.
- BALLARD, M., WOLF, K. T., NEPIYUSHCHIKH, Z., DIXON, J. B. & ALEXEEV, A. 2018. Probing the effect of morphology on lymphatic valve dynamic function. *Biomechanics and Modeling in Mechanobiology*, 17, 1343-1356.
- BAR AD, V., DUTTA, P. R., SOLIN, L. J., HWANG, W.-T., TAN, K. S., BOTH, S., CHEVILLE, A. & HARRIS, E. R. 2010. Time-course of arm lymphedema and potential risk factors for progression of lymphedema after breast conservation treatment for early stage breast cancer. *International Journal of Radiation Oncology Biology Physics*, 76, 85-90.
- BARCLAY, C. J. 1999. A weakly coupled version of the Huxley crossbridge model can simulate energetics of amphibian and mammalian skeletal muscle. *Journal of Muscle Research and Cell Motility*, 20, 163-176.
- BARCLAY, C. J. & LOISELLE, D. S. 2020. An equivocal final link - quantitative determination of the thermal efficiency of ATP hydrolysis - sullies the chain of electric, ionic, metabolic and chemical steps underlying cardiac contraction. *Frontiers in Physiology*, 11, Article 183.
- BARCLAY, C. J., WIDÉN, C. & MELLORS, L. J. 2003. Initial mechanical efficiency of isolated cardiac muscle. *The Journal of Experimental Biology*, 206, 2725-2732.
- BEHRINGER, E. J., SCALLAN, J. P., JAFARNEJAD, M., CASTORENA-GONZALEZ, J. A., ZAWIEJA, S. D., MOORE JR., J. E., DAVIS, M. J. & SEGAL, S. S. 2017. Calcium and electrical dynamics of the lymphatic endothelium. *The Journal of Physiology*, 595, 7347-7368.
- BEN-BARUCH, A. 2008. Organ selectivity in metastasis: regulation by chemokines and their receptors. *Clinical & Experimental Metastasis*, 25, 345-356.
- BENOIT, J. N., ZAWIEJA, D. C., GOODMAN, A. H. & GRANGER, H. J. 1989. Characterization of intact mesenteric lymphatic pump and its responsiveness to acute edemagenic stress. *American Journal of Physiology*, 257, H2059-H2069.

- BERTRAM, C. D. 2020. Modelling secondary lymphatic valves with a flexible vessel wall: how geometry and material properties combine to provide function. *Biomechanics and Modelling in Mechanobiology*, 19, 2081-2098.
- BERTRAM, C. D., MACASKILL, C., DAVIS, M. J. & MOORE, J. E., JR. 2014a. Development of a model of a multi-lymphangion lymphatic vessel incorporating realistic and measured parameter values. *Biomech Model Mechanobiol*, 13, 401-16.
- BERTRAM, C. D., MACASKILL, C., DAVIS, M. J. & MOORE JR, J. E. 2017. Valve-related modes of pump failure in collecting lymphatics: numerical and experimental investigation. *Biomechanics and Modeling in Mechanobiology*, 16, 1987-2003.
- BERTRAM, C. D., MACASKILL, C., DAVIS, M. J. & MOORE JR., J. E. 2016a. Consequences of intravascular lymphatic valve properties: a study of contraction timing in a multi-lymphangion model. *American Journal Physiology - Heart and Circulatory Physiology*, 310, H847-H860.
- BERTRAM, C. D., MACASKILL, C., DAVIS, M. J. & MOORE JR., J. E. 2018. Contraction of collecting lymphatics: organization of pressure-dependent rate for multiple lymphangions. *Biomechanics and Modelling in Mechanobiology*, 17, 1513-1532.
- BERTRAM, C. D., MACASKILL, C. & MOORE JR., J. E. 2011. Simulation of a chain of collapsible contracting lymphangions with progressive valve closure. *Journal of Biomechanical Engineering*, 133.
- BERTRAM, C. D., MACASKILL, C. & MOORE JR., J. E. 2014b. Incorporating measured valve properties into a numerical model of a lymphatic vessel. *Computer Methods in Biomechanics and Biomedical Engineering*, 17, 1519-1534.
- BERTRAM, C. D., MACASKILL, C. & MOORE JR., J. E. 2015. An improved model of an actively contracting lymphatic vessel consisting of multiple lymphangions: pumping characteristics.
- BERTRAM, C. D., MACASKILL, C. & MOORE JR., J. E. 2016b. Pump function curve shape for a model lymphatic vessel. *Medical Engineering and Physics*, 38, 656-663.
- BERTRAM, C. D., MACASKILL, C. & MOORE JR., J. E. 2019. Inhibition of contraction strength and frequency by wall shear stress in a single-lymphangion model. *Journal of Biomechanical Engineering*, 141.
- BIDIER, S. & EHLERS, W. Particle-based modelling and computational homogenisation of granular media. 11th World Congress on Computational Mechanics, 2014 Barcelona, Spain.
- BOGGON, R. P. & PALFREY, A. J. 1973. The microscopic anatomy of human lymphatic trunks. *Journal of Anatomy*, 114, 389-405.
- BOHLEN, H. G., GASHEVA, O. Y. & ZAWIEJA, D. C. 2011. Nitric oxide formation by lymphatic bulb and valves is a major regulatory component in lymphatic pumping. *American Journal of Physiology - Heart and Circulatory Physiology*, 301, H1897-H1906.
- BOHLEN, H. G., WANG, W., GASHEV, A. A., GASHEVA, O. & ZAWIEJA, D. C. 2009. Phasic contractions of rat mesenteric lymphatics increase basal and phasic nitric oxide generation in vivo. *American Journal of Physiology - Heart and Circulatory Physiology*, 297, H1319-H1328.
- BOTTARO, A. 2019. Flow over natural or engineered surfaces: an adjoint homogenization perspective. *Journal of Fluid Mechanics*, 877.
- BRICE, G., CHILD, A. H., EVANS, A., BELL, R., MANSOUR, S., BURNAND, K., SARFARAZI, M., JEFFERY, S. & MORTIMER, P. 2005. Milroy disease and the VEGFR-3 mutation phenotype. *Journal of Medical Genetics*, 42, 98-102.
- BRIDENBAUGH, E. A., GASHEV, A. A. & ZAWIEJA, D. C. 2003. Lymphatic muscle: a review of contractile function. *Lymphatic Research and Biology*, 1, 147-158.
- BRIGGS BOEDTKJER, D., RUMESSEN, J., BAANDRUP, U., MIKKELSEN, M. S., TELINIUS, N., PILEGAARD, H., AALKJAER, C. & HJORTDAL, V. 2013. Identification of interstitial cajal-like cells in the human thoracic duct. *Cells Tissue Organs*, 197, 145-158.

- BROOK, B. S. 2014. Emergence of airway smooth muscle mechanical behavior through dynamic reorganization of contractile units and force transmission pathways. *Journal of Applied Physiology*, 116, 980-997.
- BROOK, B. S. & JENSEN, O. E. 2014. The role of contractile unit reorganization in force generation in airway smooth muscle. *Mathematical Medicine and Biology*, 31, 99-124.
- BROWSE, N. L., LORD, R. S. A. & TAYLOR, A. 1971. Pressure waves and gradients in the canine thoracic duct. *The Journal of Physiology*, 213, 507-524.
- BROWSE, N. L., RUTT, D. R., SIZELAND, D. & TAYLOR, A. 1974. The velocity of lymph flow in the canine thoracic duct. *The Journal of Physiology*, 237, 401-413.
- BURSZTYN, L., EYTAN, O., JAFFA, A. J. & ELAD, D. 2007. Mathematical model of excitation-contraction in a uterine smooth muscle cell. *American Journal of Physiology - Cell Physiology*, 292, C1816-C1829.
- CANNELL, M. B. & ALLEN, D. G. 1984. Model of calcium movements during activation in the sarcomere of frog skeletal muscle. *Biophysical Journal*, 45, 913-925.
- CASTORENA-GONZALEZ, J. A., ZAWIEJA, S. D., LI, M., SRINIVASAN, R. S., SIMON, A. M., DE WIT, C., DE LA TORRE, R., MARTINEZ-LEMUS, L. A., HENNIG, G. W. & DAVIS, M. J. 2018. Mechanisms of connexin-related lymphedema: a critical role for Cx45, but not Cx47, in the entrainment of spontaneous lymphatic contractions. *Integrative Physiology*, 123, 964-985.
- CAULK, A. W., DIXON, J. B. & GLEASON JR., R. L. 2016. A lumped parameter model of mechanically mediated acute and long-term adaptations of contractility and geometry in lymphatics for characterization of lymphedema. *Biomechanics and Modeling in Mechanobiology* [Online]. [Accessed 31/10/2016].
- CAULK, A. W., NEPIYUSHCHIKH, Z. V., SHAW, R., DIXON, J. B. & GLEASON, R. L. J. 2015. Quantification of the passive and active biaxial mechanical behaviour and microstructural organization of rat thoracic ducts. *Journal of the Royal Society, Interface*, 12.
- CHAPMAN, B. & LOISELLE, D. 2016. Thermodynamics and kinetics of the F_0F_1 -ATPase: application of the probability isotherm. *Royal Society Open Science*, 3.
- CHI, R. J. 2007. *Smooth muscle titin interactions with alpha-actinin*. PhD, The Florida State University.
- CHI, R. J., OLENYCH, S. G., KIM, K. & KELLER III, T. C. S. 2005. Smooth muscle α -actinin interaction with smitin. *The International Journal of Biochemistry & Cell Biology*, 37, 1470-1482.
- CHU, J., ENGQUIST, B., PRODANOVIĆ, M. & TSAI, R. 2012. A multiscale method coupling network and continuum models in porous media I: steady-state single phase flow. *Multiscale Modeling & Simulation*, 10, 515-549.
- COCCARELLI, A., EDWARDS, D. H., AGGAWARL, A., NITHIARASU, P. & PATHIMUS, D. 2018. A multiscale active structural model of the arterial wall accounting for smooth muscle dynamics. *Journal of the Royal Society Interface* [Online], 15.
- CONTARINO, C. & TORO, E. 2018. A one-dimensional mathematical model of collecting lymphatics coupled with an electro-fluid-mechanical contraction model and valve dynamics. *Biomechanics and Modeling in Mechanobiology*, 17, 1687-1714.
- COOPER, L. J., J.P., H., CLOUGH, G. F., GANAPATHISUBRAMANI, B. & ROOSE, T. 2016. An image-based model of fluid flow through lymph nodes. *Bulletin of Mathematical Biology*, 78, 52-71.
- CROWE, M. J., VON DER WEID, P. Y., BROCK, J. A. & VAN HELDEN, D. F. 1997. Co-ordination of contractile activity in guinea-pig mesenteric lymphatics. *The Journal of Physiology*, 500, 235-244.
- DAO, T. T. & HO BA THO, M.-C. 2018. A systematic review of continuum modeling of skeletal muscles: current trends, limitations, and recommendations. *Applied Bionics and Biomechanics*.
- DAS, S. & SKOBE, M. 2008. Lymphatic vessel activation in cancer. *Annals of the New York Academy of Sciences*, 1131, 235-241.

- DAVIS, M. J., DAVIS, A. M., KU, C. W. & GASHEV, A. A. 2009a. Myogenic constriction and dilation of isolated lymphatic vessels. *American Journal of Physiology - Heart and Circulatory Physiology*, 296, H293-H302.
- DAVIS, M. J., DAVIS, A. M., LANE, M. M., KU, C. W. & GASHEV, A. A. 2009b. Rate-sensitive contractile responses of lymphatic vessels to circumferential stretch. *Journal of Physiology*, 587, 165-182.
- DAVIS, M. J., LANE, M. M., DAVIS, A. M., DURTSCHI, D., ZAWIEJA, D. C., MUTHUCHAMY, M. & GASHEV, A. A. 2008. Modulation of lymphatic muscle contractility by the neuropeptide substance P. *American Journal of Physiology - Heart and Circulatory Physiology*, 295, H587-H597.
- DAVIS, M. J., RAHBAR, E., GASHEV, A. A., ZAWIEJA, D. C. & MOORE JR., J. E. 2011. Determinants of valve gating in collecting lymphatic vessels From rat mesentery. *American Journal of Physiology - Heart and Circulatory Physiology*, 301, H48-H60.
- DAVIS, M. J., SCALLAN, J. P., WOLPERS, J. H., MUTHUCHAMY, M., GASHEV, A. A. & ZAWIEJA, D. C. 2012. Intrinsic increase in lymphangion muscle contractility in response to elevated afterload. *American Journal of Physiology - Heart and Circulatory Physiology*, 303, H795-H808.
- DILLON, P. F., AKSOY, M. P., DRISKA, S. P. & MURPHY, R. A. 1981. Myosin phosphorylation and the cross-bridge cycle in arterial smooth muscle. *Science*, 211, 495-497.
- DISIPIO, T., RYE, S., NEWMAN, B. & HAYES, S. 2013. Incidence of unilateral arm lymphoedema after breast cancer: a systematic review and meta-analysis. *The Lancet Oncology*, 14, 500-515.
- DIXON, J. B. 2006. *A biomedical engineering approach to investigating flow and wall shear stress in contracting lymphatics*. Doctor of Philosophy, Texas A&M.
- DIXON, J. B., GREINER, S. T., GASHEV, A. A., COTE, G. L., MOORE JR., J. E. & ZAWIEJA, D. C. 2006. Lymph flow, shear stress, and lymphocyte velocity in rat mesenteric prenodal lymphatics. *Microcirculation*, 13, 597-610.
- DIXON, J. B., ZAWIEJA, D. C., GASHEV, A. A. & COTÉ, G. L. 2005. Measuring microlymphatic flow using fast video microscopy. *Journal of Biomedical Optics*, 10.
- DOUGHERTY, P. J., DAVIS, M. J., ZAWIEJA, D. C. & MUTHUCHAMY, M. 2008. Calcium sensitivity and cooperativity of permeabilized rat mesenteric lymphatics. *American Journal of Physiology - Regulatory, Integrative and Comparative Physiology*, 294, R1524-R1532.
- DOUGHERTY, P. J., NEPIYUSHCHIKH, Z. V., CHAKRABORTY, S., WANG, W., DAVIS, M. J., ZAWIEJA, D. C. & MUTHUCHAMY, M. 2014. PKC activation increases Ca^{2+} sensitivity of permeabilized lymphatic muscle via myosin light chain 20 phosphorylation-dependent and -independent mechanisms. *American Journal of Physiology - Heart and Circulatory Physiology*, 306, H674-H683.
- EISENBERG, E. & GREENE, L. E. 1980. The relation of muscle biochemistry to muscle physiology. *Annual Review of Physiology*, 42, 293-309.
- EISENBERG, E., HILL, T. L. & CHEN, Y.-D. 1980. Cross-bridge model of muscle contraction: Quantitative analysis. *Biophysical Journal*, 29, 195-227.
- EL MAKSSOUD, H., GUIRAUD, D., POIGNET, P., HAYASHIBE, M., WIEBER, P.-B., YOSHIDA, K. & AZEVEDO-COSTE, C. 2011. Multiscale modeling of skeletal muscle properties and experimental validations in isometric conditions. *Biological Cybernetics*, 105, 121-138.
- FAAS, G. C. & MODY, I. 2012. Measuring the kinetics of calcium binding proteins with flash photolysis. *Biochimica et Biophysica Acta*, 1820, 1195-1204.
- FAJMUT, A., BRUMEN, M. & SCHUSTER, S. 2005a. Theoretical model of the interactions between Ca^{2+} , calmodulin and myosin light chain kinase. *FEBS Letters*, 15, 4361-4366.
- FAJMUT, A., JAGODI Č, M. & BRUMEN, M. 2005b. Mathematical modeling of the myosin light chain kinase activation. *Journal of Chemical Information and Modeling*, 45, 1605-1609.

- FERNANDEZ, J. W., BUIST, M. L., NICKERSON, D. P. & HUNTER, P. J. 2005. Modelling the passive and nerve activated response of the rectus femoris muscle to a flexion loading: A finite element framework. *Medical Engineering & Physics*, 27, 862-870.
- FERRELL, R. E., BATY, C. J., KIMAK, M. A., KARLSSON, J. M., LAWRENCE, E. C., FRANKE-SNYDER, M., MERINEY, S. D., FEINGOLD, E. & FINEGOLD, D. N. 2010. GJC2 missense mutations cause human lymphedema. *The American Journal of Human Genetics*, 86, 943-948.
- FINEGOLD, D. N., BATY, C. J., KNICKELBEIN, K. Z., PERSCHKE, S., NOON, S. E., CAMPBELL, D., KARLSSON, J. M., HUANG, D., KIMAK, M. A., LAWRENCE, E. C., FEINGOLD, E., MERINEY, S. D., BRUFISKY, A. M. & FERRELL, R. E. 2012. Connexin 47 mutations increase risk for secondary lymphedema following breast cancer treatment. *Clinical Cancer Research*, 18, 2382-2390.
- FREDBERG, J. J., INOUE, D. S., MIJAILOVICH, S. M. & BUTLER, J. P. 1999. Perturbed equilibrium of myosin binding in airway smooth muscle and its implications in bronchospasm. *American Journal of Respiratory and Critical Care Medicine*, 159, 959-967.
- FU, M. R. 2014. Breast cancer-related lymphedema: symptoms, diagnosis, risk reduction, and management. *World Journal of Clinical Oncology*, 5, 241-247.
- FUNG, Y.-C. 1993. *Biomechanics: Mechanical Properties of Living Tissues*, New York, Springer.
- GALIE, P. & SPILKER, R. L. 2009. A two-dimensional computational model of lymph transport across primary lymphatic valves. *Journal of Biomechanical Engineering*, 131.
- GASHEV, A. A. 2002. Physiologic activity of lymphatic contractile function: current perspectives. *Annals of the New York Academy of Sciences*, 979, 178-187.
- GASHEV, A. A. 2008. Lymphatic vessels: pressure- and flow-dependent regulatory reactions. *Annals of the New York Academy of Sciences*, 1131, 100-109.
- GASHEV, A. A. 2010. Basic mechanisms controlling lymph transport in the mesenteric lymphatic net. *Annals of the New York Academy of Sciences*, 12072, E16-E20.
- GASHEV, A. A., DAVIS, M. J., DELP, M. D. & ZAWIEJA, D. C. 2004. Regional variations of contractile activity in isolated rat lymphatics. *Microcirculation*, 11, 477-492.
- GASHEV, A. A., DAVIS, M. J. & ZAWIEJA, D. C. 2002. Inhibition of the active lymph pump by flow in rat mesenteric lymphatics and thoracic duct. *The Journal of Physiology*, 540, 1023-1037.
- GASHEV, A. A., ZHANG, R. Z., MUTHACHAMY, M., ZAWIEJA, D. C. & DAVIS, M. J. 2012. Regional heterogeneity of length-tension relationships in rat lymph vessels. *Lymphatic Research and Biology*, 10, 14-19.
- GASHEVA, O. Y., ZAWIEJA, D. C. & GASHEV, A. A. 2006. Contraction-initiated NO-dependent lymphatic relaxation: a self-regulatory mechanism in rat thoracic duct. *The Journal of Physiology*, 575, 821-832.
- GEERS, M. G. D., KOUZNETSOVA, V. & BREKELMANS, W. A. M. 2001. Gradient-enhanced computational homogenization for the micro-macro scale transition. *Le Journal de Physiologie IV*, 11, 145-152.
- GEERS, M. G. D., KOUZNETSOVA, V. G. & BREKELMANS, W. A. M. 2010. Multi-scale computational homogenization: trends and challenges. *Journal of Computational and Applied Mathematics*, 234, 2175-2182.
- GILLESPIE, T. C., SAYEGH, H. E., BRUNELLE, C. L., DANIELL, K. M. & TAGHIAN, A. G. 2018. Breast cancer-related lymphedema: risk factors, precautionary measures, and treatments. *Gland Surgery*, 7, 379-403.
- GONG, C., MATTILA, J. T., MILLER, M., FLYNN, J. L., LINDERMAN, J. J. & KIRSCHNER, D. 2013. Predicting lymph node output efficiency using systems biology. *Journal of Theoretical Biology*, 335, 169-184.
- GROOD, E. S., MATES, R. E. & FALSETTI, H. 1974. A model of cardiac muscle dynamics. *Circulation Research*, 35, 184-196.
- GUCCIONE, J. M. & MCCULLOCH, A. D. 1993. Mechanics of active contraction in cardiac muscle: Part I—constitutive relations for fiber stress that describe deactivation. *Journal of Biomechanical Engineering*, 115, 72-81.

- GUCCIONE, J. M., WALDMAN, L. K. & MCCULLOCH, A. D. 1993. Mechanics of active contraction in cardiac muscle: Part II — cylindrical models of the systolic left ventricle. *Journal of Biomechanical Engineering*, 115, 82-90.
- GUYTON, A. C., GRANGER, H. J. & TAYLOR, A. E. 1971. Interstitial fluid pressure. *Physiological Reviews*, 51, 527-563.
- HAI, C.-M. & MURPHY, R. A. 1988a. Cross-bridge phosphorylation and regulation of latch state in smooth muscle. *American Journal of Physiology*, 254, C99-C106.
- HAI, C.-M. & MURPHY, R. A. 1988b. Regulation of shortening velocity by cross-bridge phosphorylation in smooth muscle. *American Journal of Physiology*, 255, C86-C94.
- HAI, C. M. & MURPHY, R. A. 1992. Adenosine 5'-triphosphate consumption as predicted by the coupled four-state crossbridge model. *Biophysical Journal*, 61, 530-541.
- HAIR, M. & WRIGGERS, P. 2008. Computational homogenization of micro-structural damage due to frost in hardened cement paste. *Finite Elements in Analysis and Design*, 44, 233-244.
- HALD, B. O., CASTORENO-GONZALEZ, J. A., ZAWIEJA, S. D., GUI, P. & DAVIS, M. J. 2018. Electrical communication in lymphangions. *Biophysical Journal*, 115, 936-949.
- HALL, J. G., MORRIS, B. & WOOLLEY, G. 1965. Intrinsic rhythmic propulsion of lymph in the unanaesthetized sheep. *The Journal of Physiology*, 180, 336-349.
- HANLEY, C. A., ELIAS, R. M. & JOHNSTON, M. G. 1992. Is endothelium necessary for transmural pressure-induced contractions of bovine truncal lymphatics? *Microvascular Research*, 43, 134-146.
- HARTEN, A., LAX, P. D. & VAN LEER, B. 1983. On upstream differencing and Godunov-type schemes for hyperbolic conservation laws. *SIAM Review*, 25, 35-61.
- HASHIMOTO, S., KAWAI, Y. & OHHASHI, T. 1994. Effects of vasoactive substances on the pig isolated lymphatic vessels. *The Journal of Pharmacology and Experimental Therapeutics*, 269, 482-488.
- HE, Z.-H., BOTTINELLI, R., PELLEGRINO, M. A., FERENCZI, M. A. & REGGIANI, C. 2000. ATP consumption and efficiency of human single muscle fibers with different myosin isoform composition. *Biophysical Journal*, 79, 945-961.
- HEPPELL, C., RICHARDSON, G. & ROOSE, T. 2013. A model for fluid drainage by the lymphatic system. *Bulletin of Mathematical Biology*, 75 49-81.
- HEPPELL, C. W. 2013. *Modelling the Fluid Drainage Through Primary Lymphatic Valves*. Doctor of Philosophy, University of Southampton.
- HILL, A. V. 1938. The heat of shortening and the dynamic constants of muscle. *Proceedings of the Royal Society of London. Series B, Biological Sciences*, 126, 136-195.
- HILL, T. L. 1974. Theoretical formalism for the sliding filament model of contraction of striated muscle Part I. *Progress in Biophysics and Molecular Biology*, 28, 267-340.
- HIORNS, J. E., JENSEN, O. E. & BROOK, B. S. 2014. Nonlinear compliance modulates dynamic bronchoconstriction in a multiscale airway model. *Biophysical Journal*, 107, 3030-3042.
- HUANG, X., PI, Y., LEE, K. J., HENKEL, A. S., GREGG, R. G., POWERS, P. A. & WALKER, J. W. 1999. Cardiac troponin I gene knockout: a mouse model of myocardial troponin I deficiency. *Circulation Research*, 84, 1-8.
- HUXLEY, A. F. 1957. Muscle structure and theories of contraction. In: BUTLER, J. A. V. & KATZ, B. (eds.) *Progress in Biophysics and Biophysical Chemistry*. New York: The MacMillan Company.
- HUXLEY, A. F. 1973. A note suggesting that the cross-bridge attachment during muscle contraction may take place in two stages. *Proceedings of the Royal Society B - Biological Sciences*, 183, 83-86.
- HUXLEY, A. F. & SIMMONS, R. M. 1971. Proposed mechanism of force generation in striated muscle. *Nature*, 233, 533-538.
- IOOSS, B. & LEMAÎTRE, P. 2015. A review on global sensitivity analysis methods. In: DELLINO, G. & MELONI, C. (eds.) *Uncertainty Management in Simulation-Optimization of Complex Systems*. New York: Springer.

- IVANOVIĆ, M., STOJANOVIĆ, B., KAPLAVERIĆ-MALIŠIĆ, A., GILBERT, R. & MIJAILOVICH, S. 2016. Distributed multi-scale muscle simulation in a hybrid MPI-CUDA computational environment. *Simulation: Transactions of the Society for Modeling and Simulation International*, 92, 19-31.
- JAFARNEJAD, M., WOODRUFF, M. C., ZAWIEJA, D. C., CARROLL, M. C. & MOORE JR, J. E. 2015. Modeling lymph flow and fluid exchange with blood vessels in lymph nodes. *Lymphatic Research and Biology*, 13, 234-247.
- JAMALIAN, S., BERTRAM, C. D., RICHARDSON, W. J. & MOORE, J., J.E. 2013. Parameter sensitivity analysis of a lumped-parameter model of a chain of lymphangions in series. *American Journal of Physiology - Heart and Circulatory Physiology*, 305, H1709-H1717.
- JAMALIAN, S., DAVIS, M. J., ZAWIEJA, D. C. & MOORE JR., J. E. 2016. Network scale modeling of lymph transport and its effective pumping parameters. *Plos ONE* [Online], 11.
- JAMALIAN, S., JAFARNEJAD, M., ZAWIEJA, S. D., BERTRAM, C. D., GASHEV, A. A., ZAWIEJA, D. C., DAVIS, M. J. & MOORE JR., J. E. 2017. Demonstration and analysis of the suction effect for pumping lymph from tissue beds at subatmospheric pressure. *Scientific Reports*, 7.
- JAVILI, A., CHATZIGEORGIOU, G. & STEINMANN, P. 2013. Computational homogenization in magneto-mechanics. *International Journal of Solids and Structures*, 50, 4197-4216.
- JUNG, G. S. & BUEHLER, M. J. 2017. Multi-scale modeling of muscular-skeletal systems. *Annual Review of Biomedical Engineering*, 19, 435-457.
- KACZMARCZYK, L., PEARCE, C. J. & BIĆANIĆ, N. 2008. Scale transition and enforcement of RVE boundary conditions in second-order computational homogenization. *International Journal for Numerical Methods in Engineering*, 74, 506-522.
- KARPANEN, T. & ALITALO, K. 2008. Molecular biology and pathology of lymphangiogenesis. *Annual Review of Pathology*, 3, 367-397.
- KEENER, J. & SNEYD, J. 2009. *Mathematical Physiology II: Systems Physiology*, New York, NY, Springer Science+Business Media, LLC.
- KEIP, M.-A., LABUSCH, M. & SHRÖDER, J. 2013. Two-scale computational homogenization of magneto-electric composites. *Proceedings in Mathematics and Mechanics*, 13, 529-532.
- KELLERMAYER, M. S. Z., BUSTAMANTE, C. & GRANZIER, H. L. 2003. Mechanics and structure of titin oligomers explored with atomic force microscopy. *Biochimica et Biophysica Acta*, 1604, 105-114.
- KELLY, W. J. & MUSKE, K. R. 2004. Optimal operation of high-pressure homogenization for intracellular product recovery. *Bioprocess and Biosystems Engineering*, 27, 25-37.
- KHALAFVAND, S. S., NG, E. Y. K. & ZHONG, L. 2011. CFD simulation of flow through heart: a perspective review. *Computer Methods in Biomechanics and Biomedical Engineering*, 14, 113-132.
- KIM, K. & KELLER III, T. C. S. 2002. Smitin, a novel smooth muscle titin-like protein, interacts with myosin filaments in vitro and in vivo. *Journal of Cell Biology*, 156, 101-112.
- KIRKPATRICK, C. T. & MCHALE, N. G. 1977. Electrical and mechanical activity of isolated lymphatic vessels. *Journal of Physiology*, 272, 33P-34P.
- KNUDSON, D. 2007. *Fundamentals of Biomechanics*, New York, Springer.
- KOCKOVÁ, H. & CIMRMAN, R. 2009. Implementation of skeletal muscle with advanced activation control. *Applied and Computational Mechanics*, 3, 305-318.
- KOENIGSBERGER, M., SAUSER, R., LAMBOLEY, M., BÉNY, J.-L. & MEISTER, J.-J. 2004. Ca^{2+} Dynamics in a population of smooth muscle cells: modeling the recruitment and synchronization. *Biophysical Journal*, 87, 92-104.
- KOUZNETSOVA, V., GEERS, M. G. D. & BREKELMANS, W. A. M. 2002. Multi-scale constitutive modelling of heterogeneous materials with a gradient-enhanced computational homogenization scheme. *International Journal for Numerical Methods in Engineering*, 54, 1235-1260.

- KOUZNETSOVA, V. G., GEERS, M. G. D. & BREKELMANS, W. A. M. 2004. Multi-scale second-order computational homogenization of multi-phase materials: a nested finite element solution study. *Computer Methods in Applied Mechanics and Engineering*, 193, 5525-5550.
- KUNERT, C., BAISH, J. W., LIAO, S., PADERA, T. P. & MUNN, L. L. 2015. Mechanobiological oscillators control lymph flow. *Proceedings of the National Academy of Sciences (PNAS)*, 112, 10938-10943.
- LABEIT, D., WATANABE, K., WITT, C., FUJITA, H., WU, Y., LAHMERS, S., FUNCK, T., LABEIT, S. & GRANZIER, H. 2003. Calcium-dependent molecular spring elements in the giant protein titin. *Proceedings of the National Academy of Sciences of the United States of America*, 100, 13716-13721.
- LAFORÊT, J., GUIRAUD, D., ANDREU, D., TAILLADES, H. & AZEVEDO-COSTE, C. 2011. Smooth muscle modeling and experimental identification: application to isometric bladder contraction. *Journal of Neural Engineering*, 8.
- LAMBERT, R. K., PARÉ, P. D. & SEOW, C. Y. 2004. Mathematical description of geometric and kinematic aspects of smooth muscle plasticity and some related morphometrics. *Journal of Applied Physiology*, 96, 469-476.
- LANDESBURG, A. & SIDEMAN, S. 1994. Mechanical Regulation of Cardiac Muscle by Coupling Calcium Kinetics with Cross-Bridge Cycling: a dynamic model. *American Journal of Physiology - Heart and Circulatory Physiology*, 267, H779-H795.
- LARSSON, F., RUNESSON, K. & SU, F. 2010. Variationally consistent computational homogenization of transient heat flow. *International Journal for Numerical Methods in Engineering*, 81, 1659-1686.
- LAUZON, A.-M., BATES, J. H. T., DONOVAN, G., TAWHAI, M., SNEYD, J. & SANDERSON, M. J. 2012. A multi-scale approach to airway hyperresponsiveness: from molecule to organ. *Frontiers in Physiology*, 3.
- LEAK, L. V. & BURKE, J. F. 1968. Ultrastructural studies on the lymphatic anchoring filaments. *The Journal of Cell Biology*, 36, 129-149.
- LEE, S., ROIZES, S. & VON DER WEID, P.-Y. 2014. Distinct roles of L- and T-type voltage-dependent Ca^{2+} channels in regulation of lymphatic vessel contractile activity. *Journal of Physiology*, 592, 5409-5427.
- LEMAIRE, K. K., BAAN, G. C., R.T., J. & VAN SOEST, A. J. 2016. Comparison of the validity of Hill and Huxley muscle-tendon complex models using experimental data obtained from rat m. soleus in situ. *Journal of Experimental Biology*, 219, 977-987.
- LEVICK, J. R. & MICHEL, C. C. 2010. Microvascular fluid exchange and the revised Starling principle. *Cardiovascular Research*, 87, 198-210.
- LEWIŃSKA, M. A., KOUZNETSOVA, V. G., VAN DOMMELEN, J. A. W. & GEERS, M. G. D. 2019. Computational homogenisation of acoustic metafoams. *European Journal of Mechanics / A Solids*, 77.
- LI, B., SILVER, I., SZALAI, J. P. & JOHNSTON, M. G. 1998. Pressure-volume relationships in sheep mesenteric lymphatic vessels in situ: response to hypovolemia. *Microvascular Research*, 56, 127-138.
- LINKE, W. A. & GRÜTZNER, A. 2008. Pulling single molecules of titin by AFM - recent advances and physiological implications. *Pflügers Archiv*, 456, 101-115.
- LOISELLE, D. S., TRAN, K. T., CRAMPIN, E. J. & CURTIN, N. A. 2010. Why has reversal of the actin-myosin cross-bridge cycle not been observed experimentally? *Journal of Applied Physiology*, 108, 1465-1471.
- LOPEZ-PEREZ, A., SEBASTIAN, R. & FERRERO, J. M. 2015. Three-dimensional cardiac computational modelling: methods, features and applications. *BioMedical Engineering OnLine* [Online], 14.
- LOUVEAU, A., SMIRNOV, I., KEYES, T. J., ECCLES, J. D., ROUHIN, S. J., PESKE, J. D., DERECKI, N. D., CASTLE, D., MANDELL, J. W., LEE, K. S., HARRIS, T. H. & KIPNIS, J. 2015. Structural and functional features of central nervous system lymphatic vessels. *Nature*, 523, 337-341.

- LU, X., GIOVANIS, D. G., YVONNET, J., PAPADOPOULOS, V., DETREZ, F. & BAI, J. 2018. A data-driven computational homogenization method based on neural networks for the nonlinear anisotropic electrical response of graphene/polymer nanocomposites. *Computational Mechanics*, 64, 307-321.
- LU, Y., JEFFRIES, C. M. & TREWHELLA, J. 2011. Invited review: probing the structures of muscle regulatory proteins using small-angle solution scattering. *Biopolymers*, 95, 505-516.
- LUTTER, S., XIE, S., TATIN, F. & MAKINEN, T. 2012. Smooth muscle-endothelial cell communication activates Reelin signaling and regulates lymphatic vessel formation. *The Journal of Cell Biology*, 197, 837-849.
- MACDONALD, A. 2008. *The Computational Modelling of Collecting Lymphatic Vessels*. PhD, University of Exeter.
- MACDONALD, A. J., ARKILL, K. P., TABOR, G. R., MCHALE, N. G. & WINLOVE, C. P. 2008. Modelling flow in collecting lymphatic vessels: one-dimensional flow through a series of contractile elements. *American Journal of Physiology - Heart and Circulatory Physiology*, 295, H305-H313.
- MAGGIO, C. D., JENNINGS, S. R., ROBICHAUX, J. L., STAPOR, P. C. & HYMAN, J. M. 2012. A modified Hai-Murphy model of uterine smooth muscle contraction. *Bulletin of Mathematical Biology*, 74, 143-158.
- MARGARIS, K. N. & BLACK, R. A. 2012. Modelling the lymphatic system: challenges and opportunities. *Journal of the Royal Society, Interface*, 9, 601-612.
- MARINO, S., HOGUE, I. B., RAY, C. J. & KIRSCHNER, D. E. 2008. A methodology for performing global uncertainty and sensitivity analysis in systems biology. *Journal of Theoretical Biology*, 254, 178-196.
- MARSTON, S. B. & REDWOOD, C. S. 1993. The essential role of tropomyosin in cooperative regulation of smooth muscle thin filament activity by caldesmon. *The Journal of Biological Chemistry*, 268, 12317-12320.
- MATSUI, K., TERADA, K. & YUGE, K. 2004. Two-scale finite element analysis of heterogeneous solids with periodic microstructures. *Computers & Structures*, 82, 593-606.
- MCCLOSKEY, K. D., TOLAND, H. M., HOLLYWOOD, M. A., THORNBURY, K. D. & MCHALE, N. G. 1999. Hyperpolarisation-activated inward current in isolated sheep mesenteric lymphatic smooth muscle. *The Journal of Physiology*, 521, 201-211.
- MCHALE, N. G., RODDIE, I. C. & THORNBURY, K. D. 1980. Nervous modulation of spontaneous contractions in bovine mesenteric lymphatics. *The Journal of Physiology*, 309, 461-472.
- MCMASTER, P. D. 1937. Changes in the cutaneous lymphatics of human beings and in the lymph flow under normal and pathological conditions. *Journal of Experimental Medicine*, 65, 347-372.
- MCVEIGH, C., VERNEREY, F., LIU, W. K. & BRINSON, L. C. 2006. Multiresolution analysis for material design. *Computer Methods in Applied Mechanics and Engineering*, 195, 5053-5076.
- MELLOR, R. H., TATE, N., STANTON, A. W. B., HUBERT, C., T., M., SMITH, A., BURNAND, K. G., JEFFERY, S., LEVICK, J. R. & MORTIMER, P. S. 2011. Mutations in FOXC2 in humans (lymphoedema distichiasis syndrome) causes lymphatic dysfunction on dependency. *Journal of Vascular Research*, 48, 397-407.
- MENDOZA, E. & SCHMID-SCHÖNBEIN, G. W. 2003. A model for mechanics of primary lymphatic valves. *Journal of Biomechanical Engineering*, 125, 407-414.
- MIJAILOVICH, S. M., BUTLER, J. P. & FREDBERG, J. J. 2000. Perturbed equilibria of myosin binding in airway smooth muscle: bond-length distributions, mechanics and ATP metabolism. *Biophysical Journal*, 79, 2667-2681.
- MIZUNO, R., DÖRNYEI, G., KOLLER, A. & KALEY, G. 1997. Myogenic responses of isolated lymphatics: modulation by endothelium. *Microcirculation*, 4, 413-420.
- MOORE JR., J. E. & BERTRAM, C. D. 2018. Lymphatic system flows. *Annual Review of Fluid Mechanics*, 50, 459-482.

- MUNN, L. L. 2015. Mechanobiology of lymphatic contractions. *Seminars in Cell & Developmental Biology*, 38, 67-74.
- MURPHY, N. B., CHERKAEV, E., ZHU, J., XIN, J. & GOLDEN, K. M. 2020. Spectral analysis and computational for homogenization of advection diffusion processes in steady flows. *Journal of Mathematical Physics*, 61.
- MURPHY, R. A. & REMBOLD, C. M. 2005. The latch-bridge hypothesis of smooth muscle contraction. *Canadian Journal of Physiology and Pharmacology*, 83, 857-864.
- MURTADA, S.-L., HUMPHREY, J. D. & HOLZAPFEL, G. A. 2017. Multiscale and multiaxial mechanical aspects of vascular smooth muscle. *Biophysical Journal*, 113, 714-727.
- MUTHUCHAMY, M., GASHEV, A., BOSWELL, N., DAWSON, N. & ZAWIEJA, D. 2003. Molecular and functional analyses of the contractile apparatus in lymphatic muscle. *The FASEB Journal* [Online], 17.
- NEGRINI, D., MORIONDO, A. & MUKENGE, S. 2004. Transmural pressure during cardiogenic oscillations in rodent diaphragmatic lymphatic vessels. *Lymphatic Research and Biology*, 2, 69-81.
- NEGRONI, J. A. & LASCANO, E. C. 1996. A cardiac muscle model relating sarcomere dynamics to calcium kinetics. *Journal of Molecular and Cellular Cardiology*, 28, 915-929.
- NIEDERER, S. A., CAMPBELL, K. S. & CAMPBELL, S. G. 2019. A short history of the development of mathematical models of cardiac mechanics. *Journal of Molecular and Cellular Cardiology*, 127, 11-19.
- NIZAMUTDINOVA, I. T., MAEJIMA, D., NAGAI, T., BRIDENBAUGH, E., THANGASWAMY, S., CHATTERJEE, V., MEININGER, C. J. & GASHEV, A. A. 2014. Involvement of histamine in endothelium-dependent relaxation of mesenteric lymphatic vessels. *Microcirculation*, 21, 640-648.
- NIZAMUTDINOVA, I. T., MAEJIMA, D., NAGAI, T., MEININGER, C. J. & GASHEV, A. A. 2017. Histamine as an endothelium-derived relaxing factor in aged mesenteric lymphatic vessels. *Lymphatic Research and Biology*, 15, 136-145.
- OHHASHI, T. 1987. Comparison of viscoelastic properties of walls and functional characteristics of valves in lymphatic and venous vessels. *Lymphology*, 20, 219-223.
- OHHASHI, T., AZUMA, T. & SAKAGUCHI, M. 1980. Active and passive mechanical characteristics of bovine mesenteric lymphatics. *American Journal of Physiology - Heart and Circulatory Physiology*, 8, 88-95.
- OHHASHI, T., KAWAI, Y. & AZUMA, T. 1978. The response of lymphatic smooth muscles to vasoactive substances. *Pflügers Archiv*, 375, 183-188.
- OHTANI, O., OHTANI, Y., CARATI, C. J. & GANNON, B. J. 2003. Fluid and cellular pathways of rat lymph nodes in relation to lymphatic labyrinths and Aquaporin-1 expression. *Archives of Histology and Cytology*, 66, 261-272.
- OLSZEWSKI, W. L. 2002. Contractility patterns of normal and pathologically changed human lymphatics. *Annals of the New York Academy of Sciences*, 979, 52-63.
- OLSZEWSKI, W. L. & ENGESET, A. 1980. Intrinsic contractility of prenodal lymph vessels and lymph flow in human leg. *American Journal of Physiology - Heart and Circulatory Physiology*, 239, H775-H783.
- PADERA, T. P., MEIJER, E. F. J. & MUNN, L. L. 2016. The lymphatic system in disease processes and cancer progression. *Annual Review of Biomedical Engineering*, 18, 125-158.
- PARSONS, R. J. & MCMASTER, P. D. 1938. The effect of the pulse upon the formation and flow of lymph. *Journal of Experimental Medicine*, 68, 353-376.
- PARTHIMOS, D., EDWARDS, D. H. & GRIFFITH, T. M. 1999. Minimal model of arterial chaos generated by coupled intracellular and membrane Ca^{2+} oscillators. *American Journal of Physiology - Heart and Circulatory Physiology*, 277, H1119-H1144.

- PAUPERT, J., SOUNNI, N. E. & NOËL, A. 2011. Lymphangiogenesis in post-natal tissue remodeling: lymphatic endothelial cell connection with its environment. *Molecular Aspects of Medicine*, 32, 146-158.
- PFARR, K. M., DEBRAH, A. Y., SPECHT, S. & HOERAUF, A. 2009. Filariasis and lymphoedema. *Parasite Immunology*, 31, 664-672.
- PFITZER, G. 2001. Regulation of myosin phosphorylation in smooth muscle. *Journal of Applied Physiology*, 91, 497-503.
- PIAZZESI, G. & LOMBARDI, V. 1995. A cross-bridge model that is able to explain mechanical and energetic properties of shortening muscle. *Biophysical Journal*, 68, 1966-1979.
- PIAZZESI, G., RECONDITI, M., LINARI, M., LUCII, L., BIANCO, P., BRUNELLO, E., DEOSTRE, V., STEWART, A., GORE, D. B., IRVING, T. C., IRVING, M. & LOMBARDI, V. 2007. Skeletal muscle performance determined by modulation of number of myosin motors rather than motor force or stroke size. *Cell Press*, 131, 784-795.
- PODGRABINSKA, S. & SKOBA, M. 2014. Role of lymphatic vasculature in regional and distant metastases. *Microvascular Research*, 95, 46-52.
- POLITI, A. Z., DONOVAN, G. M., TAWHAI, M. H., SANDERSON, M. J., LAUZON, A.-M., BATES, J. H. T. & SNEYD, J. 2010. A multiscale, spatially-distributed model of asthmatic airway hyper-responsiveness. *Journal of Theoretical Biology*, 266, 614-624.
- POLUKHOV, E. & KEIP, M.-A. 2020. Computational homogenization of transient chemo-mechanical process based on a variational minimization principle. *Advanced Modeling and Simulation in Engineering Sciences*, 7.
- QUICK, C. M., NGO, B. L., VENUGOPAL, A. M. & STEWART, R. H. 2009. Lymphatic pump-conduit duality: contraction of postnodal lymphatic vessels inhibits passive flow. *American Journal of Physiology - Heart and Circulatory Physiology*, 296, H662-H668.
- QUICK, C. M., VENUGOPAL, A. M., DONGAONKAR, R. M., LAINE, G. A. & STEWART, R. H. 2008. First-order approximation for the pressure-flow relationship of spontaneously contracting lymphangions. *American Journal of Physiology - Heart and Circulatory Physiology*, 294, H2144-H2149.
- QUICK, C. M., VENUGOPAL, A. M., GASHEV, A. A., ZAWIEJA, D. C. & STEWART, R. H. 2007. Intrinsic pump-conduit behavior of lymphangions. *American Journal of Physiology - Regulatory, Integrative and Comparative Physiology*, 292, R1510-R1518.
- RAHBAR, E. & MOORE JR., J. E. 2011. A model of a radially expanding and contracting lymphangion. *Journal of Biomechanics*, 44, 1001-1007.
- RAMPADARATH, A. K. & DONOVAN, G. M. 2018. A distribution-moment approximation for coupled dynamics of the airway wall and airway smooth muscle. *Biophysical Journal*, 114, 493-501.
- RAZAVI, M. S., DIXON, J. B. & GLEASON, R. L. 2020. Characterization of rat tail lymphatic contractility biomechanics: incorporating nitric oxide-mediated vasoregulation. *Journal of the Royal Society - Interface*, 17.
- RAZAVI, M. S., NELSON, T. S., NEPIYUSHCHIKH, Z., GLEASON, R. L. & DIXON, J. B. 2017. The relationship between lymphangion chain length and maximum pressure generation established through in vivo imaging and computational modeling. *American Journal of Physiology - Heart and Circulatory Physiology*, 313, H1249-H1260.
- REDDY, N. P. 1974. *A discrete model of the lymphatic system*. PhD, Texas A&M.
- REDDY, N. P. 1980. A note on the lymphatic vessel network design. *Journal of Biomechanics*, 13, 529-531.
- REDDY, N. P., KROUSKOP, T. A. & NEWELL JR., P. H. 1977. A computer model of the lymphatic system. *Computers in Biology and Medicine*, 7, 181-197.
- REGAZZONI, F., DEDE, L. & QUARTERONI, A. 2021. Active force generation in cardiac muscle cells: mathematical modeling and numerical simulation of the actin-myosin interaction. *Vietnam Journal of Mathematics*, 49, 87-118.

- RENKIN, E. M. 1986. Some consequences of capillary permeability to macromolecules: Starling's hypothesis reconsidered. *American Journal of Physiology - Heart and Circulatory Physiology*, 250, H706-H710.
- RICE, J. J. & DE TOMBE, P. P. 2004. Approaches to modeling crossbridges and calcium-dependent activation in cardiac muscle. *Progress in Biophysics & Molecular Biology*, 85, 179-195.
- RICE, J. J., WANG, F., BERS, D. M. & DE TOMBE, P. P. 2008. Approximate model of cooperative activation and crossbridge cycling in cardiac muscle using ordinary differential equations. *Biophysical Journal*, 95, 2368-2390.
- ROBERTSON, S. P., JOHNSON, J. D. & POTTER, J. D. 1981. The time-course of Ca^{2+} exchange with calmodulin, troponin, parvalbumin, and myosin in response to transient increases in Ca^{2+} . *Biophysical Journal*, 34, 559-569.
- ROCKSON, S. G. & KAHEALANI, K. R. 2008. Estimating the population burden of lymphedema. *Annals of the New York Academy of Sciences*, 1131, 147-154.
- ROE, P. L. 1986. Characteristic-based schemes for the Euler equations. *Annual Review of Fluid Mechanics*, 18, 337-365.
- ROOSE, T. & SWARTZ, M. A. 2012. Multiscale modeling of lymphatic drainage from tissues using homogenization theory. *Journal of Biomechanics*, 45, 107-115.
- RÖHRLE, G., DAVIDSON, J. B. & PULLAN, A. J. 2012. A physiologically based, multi-scale model of skeletal muscle structure and function. *Frontiers in Physiology* [Online], 3.
- SANDERS, K. M. & WARD, S. M. 2008. Interstitial cells of Cajal: a new perspective on smooth muscle function. *The Journal of Physiology*, 576, 721-726.
- SCALLAN, J. P., WOLPERS, J. H. & DAVIS, M. J. 2013. Constriction of isolated collecting lymphatic vessels in response to acute increases in downstream pressure. *The Journal of Physiology*, 591, 443-459.
- SCALLAN, J. P., WOLPERS, J. H., DAVIS, M. J., MUTHUCHAMY, M., ZAWIEJA, D. C. & GASHEV, A. A. 2012. Independent and interactive effects of preload and afterload on the pump function of the isolated lymphangion. *American Journal of Physiology - Heart and Circulatory Physiology*, 303, H809-H824.
- SCALLAN, J. P., ZAWIEJA, S. D., CASTORENA-GONZALEZ, J. A. & DAVIS, M. J. 2016. Lymphatic pumping: mechanics, mechanisms and malfunction. *The Journal of Physiology*, 594, 5749-5768.
- SCHAD, H., FLOWACZNY, H., BRECHTELSBAUER, H. & BIRKENFELD, G. 1978. The significance of respiration for thoracic duct flow in relation to other driving forces of lymph flow. *Pflügers Archiv*, 378, 121-125.
- SCHMID-SCHÖNBEIN, G. W. 1990. Microlymphatics and lymph flow. *Physiological Reviews*, 70, 987-1028.
- SCHROEDL, F., KASER-EICHBERGER, A., SCHLERETH, S. L., BOCK, F., REGENFUSS, B., REITSAMER, H. A., LUTTY, G. A., MARUYAMA, K., CHEN, L., LUTJEN-DRECOLL, E., DANA, R., KERJASCHKI, D., ALITALO, K., DE STEFANO, M. E., JUNGHANS, B. M., HEINDL, L. M. & CURSIEFEN, C. 2014. Consensus statement on the immunohistochemical detection of ocular lymphatic vessels. *Investigative Ophthalmology & Visual Science*, 55, 6440-6442.
- SEOW, C. Y. 2013. Hill's equation of muscle performance and its hidden insight on molecular mechanisms. *The Journal of General Physiology*, 142, 561-573.
- SEOW, C. Y. 2016. *Introduction to Smooth Muscle Mechanics*, Victoria, Canada, FriesenPress.
- SHIELDS, J. D., FLEURY, M. D., YONG, C., TOMEI, A. A., RANDOLPH, G. J. & SWARTZ, M. A. 2007. Autologous chemotaxis as a mechanism of tumor cell homing to lymphatics via interstitial flow and autocrine CCR7 signaling. *Cancer Cell*, 11, 526-538.
- SHIRASAWA, Y. & BENOIT, J. N. 2003. Stretch-induced calcium sensitization of rat lymphatic smooth muscle. *American Journal of Physiology - Heart and Circulatory Physiology*, 285, H2573-H2577.

- SKOBE, M., HAWIGHORST, T., JACKSON, D. G., PREVO, R., JANES, L., VELASCO, P., RICCARDI, L., ALITALO, K., CLAFFEY, K. & DETMAR, M. 2001. Induction of tumor lymphangiogenesis by VEGF-C promotes breast cancer metastasis. *Nature*, 7, 192-198.
- SMITH, C. W. J. 1985. *Thin Filament Linked Regulation of Vascular Smooth Muscle Contraction*. PhD, University of London.
- SOLITO, R., ALESSANDRINI, C., FRUSCHELLI, M., PUCCI, A. & GERLI, R. 1997. An immunological correlation between the anchoring filaments of the initial lymph vessels and the neighboring elastic fibers: a unified morphofunctional concept. *Lymphology*, 30, 194-202.
- SOMLYO, A. P. & SOMLYO, A. V. 1994. Signal transduction and regulation in smooth muscle. *Nature*, 372, 231-236.
- SOUZA-SMITH, F. M., KURTZ, K. M. & BRESLIN, J. W. 2011. Measurement of cytosolic Ca^{2+} in isolated contractile lymphatics. *Journal of Visualized Experiments*, 58.
- STACKER, S. A., CESAR, C., BALDWIN, M. E., THORNTON, G. E., WILLIAMS, R. A., PREVO, R., JACKSON, D. G., NISHIKAWA, S.-I., KUBO, H. & ACHEN, M. G. 2001. VEGF-D promotes the metastatic spread of tumor cells via the lymphatics. *Nature Medicine*, 7, 186-191.
- STACKER, S. A., WILLIAMS, S. P., KARNEZIS, S., SHAYAN, R., FOX, S. B. & ACHEN, M. G. 2014. Lymphangiogenesis and lymphatic vessel remodelling in cancer. *Nature Reviews Cancer*, 14, 159-172.
- SUGA, H. & SAGAWA, K. 1972. Mathematical interrelationship between instantaneous ventricular pressure-volume ratio and myocardial force-velocity relation. *Annals of Biomedical Engineering*, 1, 160-181.
- SUGA, H. & SAGAWA, K. 1974. Instantaneous pressure-volume relationships and their ratio in the excised, supported canine left ventricle. *Circulation Research*, 35, 117-126.
- SUGA, H., SAGAWA, K. & SHOUKAS, A. A. 1973. Load independence of the instantaneous pressure-volume ratio of the canine left ventricle and effects of epinephrine and heart rate on the ratio. *Circulation Research*, 32, 314-322.
- TAKAHASHI, N., KAWAI, Y. & OHHASHI, T. 1990. Effects of vasoconstrictive and vasodilative agents on lymphatic smooth muscles in isolated canine thoracic ducts. *The Journal of Pharmacology and Experimental Therapeutics*, 254, 165-170.
- TAWHAI, M. H. & BATES, J. H. 2011. Multi-scale lung modeling. *Journal of Applied Physiology*, 110, 1466-1472.
- TEMIZER, I. & ZOHDI, T. I. 2006. A numerical method for homogenization in non-linear elasticity. *Computational Mechanics*, 40, 281-298.
- TOLAND, H. M., MCCLOSKEY, K. D., THORNBURY, K. D., MCHALE, N. G. & HOLLYWOOD, M. A. 2000. Ca^{2+} -activated Cl^- current in sheep lymphatic smooth muscle. *American Journal of Physiology - Cell Physiology*, 279, C1327-C1335.
- TREPAT, X., DENG, L., AN, S. S., NAVAJAS, D., TSCHUMPERLIN, D. J., GERTHOFFER, W. T., BUTLER, J. P. & FREDBERG, J. J. 2007. Universal physical responses to stretch in the living cell. *Nature*, 447, 592-595.
- TRZEWIK, J., MALLIPATTU, S., ARTMANN, G. M., DELANO, F. & SCHMID-SCHÖNBEIN, G. W. 2001. Evidence for a second valve system in lymphatics: endothelial microvalves. *The FASEB Journal*, 15, 1711-1717.
- UNTHANK, J. L. & BOHLEN, H. G. 1988. Lymphatic pathways and role of valves in lymph propulsion from small intestine. *American Journal of Physiology - Gastrointestinal and Liver Physiology*, 254, G389-G398.
- VAN HELDEN, D. F. 1993. Pacemaker potentials in lymphatic smooth muscle of the guinea-pig mesentery. *The Journal of Physiology*, 471, 465-479.
- VENUGOPAL, A. M., STEWART, R. H., LAINE, G. A., DONGAONKAR, R. M. & QUICK, C. M. 2007. Lymphangion coordination minimally affects mean flow in lymphatic vessels. *American Journal of Physiology - Heart and Circulatory Physiology*, 293, H1183-H1189.

- VENUGOPAL, A. M., STEWART, R. H., LAINE, G. A. & QUICK, C. M. 2010. Nonlinear lymphangion pressure-volume relationship minimizes edema. *American Journal of Physiology - Heart and Circulatory Physiology*, 299, H876-H882.
- VENUGOPAL, A. M., STEWART, R. H., RAJAGOPALAN, S., LAINE, G. A. & QUICK, C. M. 2004. Optimal lymphatic vessel structure. *The 26th Annual International Conference of the IEEE Engineering in Medicine and Biology Society*.
- VENUGOPAL, A. M., STEWART, R. H., RAJAGOPALAN, S., ZAWIEJA, D. C., LAINE, G. A. & QUICK, C. M. 2003. Applying the time-varying elastance concept to determine the optimum coordination of lymphangion contraction in a lymphatic vessel. *Annual International Conference of the IEEE EMBS*. Cancun, Mexico.
- VON DER WEID, P.-Y. 2013. Lymphatic myogenic constriction - how lymphatic vessels pump lymph uphill. *The Journal of Physiology*, 591, 391-392.
- VON DER WEID, P.-Y. 2019. Lymphatic vessel pumping. In: HASHITANI, H. & LANG, R. (eds.) *Smooth Muscle Spontaneous Activity*. Singapore: Springer.
- VON DER WEID, P.-Y., LEE, S., IMTIAZ, M. S., ZAWIEJA, D. C. & DAVIS, M. J. 2014. Electrophysiological properties of rat mesenteric lymphatic vessels and their regulation by stretch. *Lymphatic Research and Biology*, 12, 66-75.
- VON DER WEID, P.-Y. & MUTHUCHAMY, M. 2010. Regulatory mechanisms in lymphatic vessel contraction under normal and inflammatory conditions. *Pathophysiology*, 17, 263-276.
- VON DER WEID, P.-Y., RAHMAN, M., IMTIAZ, M. S. & VAN HELDEN, D. F. 2008. Spontaneous transient depolarizations in lymphatic vessels of the guinea pig mesentery: pharmacology and implication for spontaneous contractility. *American Journal of Physiology - Heart and Circulatory Physiology*, 295, H1989-H2000.
- VON DER WEID, P.-Y. & VAN HELDEN, D. F. 1997. Functional electrical properties of the endothelium in lymphatic vessels of the guinea-pig mesentery. *The Journal of Physiology*, 504, 439-451.
- VON DER WEID, P. Y. 2001. Review article: lymphatic vessel pumping and inflammation the role of spontaneous constrictions and underlying electrical pacemaker potentials. *Alimentary Pharmacology and Therapeutics*, 15, 1115-1129.
- VON DER WEID, P. Y., CROWE, M. J. & VAN HELDEN, D. F. 1996. Endothelium-dependent modulation of pacemaking in lymphatic vessels of the guinea-pig mesentery. *Journal of Physiology*, 493, 563-575.
- VON DER WEID, P. Y. & ZAWIEJA, D. C. 2004. Lymphatic smooth muscle: the motor unit of lymph drainage. *The International Journal of Biochemistry & Cell Biology*, 36, 1147-1153.
- WALKER, J. S., WINGARD, C. J. & MURPHY, R. J. 1994. Energetics of crossbridge phosphorylation and contraction in vascular smooth muscle. *Hypertension*, 23, 1106-1112.
- WALMSLEY, J. G., GORE, R. W., DACEY JR., R. G., DAMON, D. N. & DULING, B. R. 1982. Quantitative morphology of arterioles from the hamster cheek pouch related to mechanical analysis. *Microvascular Research*, 24, 249-271.
- WANG, I., POLITI, A. Z., TANIA, N., BAI, Y., SANDERSON, M. J. & SNEYD, J. 2008. A mathematical model of airway and pulmonary arteriole smooth muscle. *Biophysical Journal*, 94, 2053-2064.
- WANG, W., NEPIYUSHCHIKH, Z., ZAWIEJA, D. C., CHAKRABORTY, S., ZAWIEJA, S. D., GASHEV, A. A., DAVIS, M. J. & MUTHUCHAMY, M. 2009. Inhibition of myosin light chain phosphorylation decreases rat mesenteric lymphatic contractile activity. *American Journal of Physiology - Heart and Circulatory Physiology*, 297, H726-H734.
- WARD, S. M., SANDERS, K. M., THORNBURY, K. D. & MCHALE, N. G. 1991. Spontaneous electrical activity in isolated bovine lymphatics recorded by intracellular microelectrodes. *Journal of Physiology*, 596, 168P.
- WASHIO, T., OKADA, J.-I., SUGIURA, S. & HISADA, T. 2012. Approximation for cooperative interactions of a spatially-detailed cardiac sarcomere model. *Cellular and Molecular Bioengineering*, 5, 113-126.

- WATSON, D. J., SAZONOV, I., ZAWIEJA, D. C., MOORE JR, J. E. & VAN LOON, R. 2017. Integrated geometric and mechanical analysis of an image-based lymphatic valve. *Journal of Biomechanics*, 7, 172-179.
- WEBB JR, R. C. & STARZL, T. E. 1953. The effect of blood vessel pulsations on lymph pressure in large lymphatics. *Bulletin of the Johns Hopkins Hospital*, 93, 401-407.
- WHITE, J. C., FIELD, M. E. & DRINKER, C. K. 1932. On the protein content and normal flow of lymph from the foot of the dog. *American Journal of Physiology*, 103, 34-44.
- WHO 2008. Global programme to eliminate lymphatic filariasis. *Weekly Epidemiological Record*, 83, 333-341.
- WILKINSON, J. M. 1980. Troponin C from rabbit slow skeletal and cardiac muscle is the product of a single gene. *European Journal of Biochemistry*, 103, 179-188.
- WILSON, J. T., VAN LOON, R., WANG, W., ZAWIEJA, D. C. & MOORE JR., J. E. 2015. Determining the combined effect of the lymphatic valve leaflets and sinus on resistance to forward flow. *Journal of Biomechanics*, 48, 3584-3590.
- WILSON, J. T., WANG, W., HELLERSTEDT, A. H., ZAWIEJA, D. C. & MOORE JR., J. E. 2013. Confocal image-based modeling of nitric oxide transport in a rat mesenteric lymphatic vessel. *Journal of Biomechanical Engineering*, 135, 0510051–0510058.
- WINTERS, J. M. 1990. Hill-based muscle models: a systems engineering perspective. In: WINTERS, J. M. & WOO, S. L.-Y. (eds.) *Multiple Muscle Systems: Biomechanics and Movement Organization*. New York: Springer-Verlag.
- WONG, A. Y. K. 1971. Mechanics of cardiac muscle, based on Huxley's model: mathematical simulation of isometric contraction. *Journal of Biomechanics*, 4, 529-540.
- WONG, A. Y. K. 1972. Mechanics of cardiac muscle, based on Huxley's model: simulation of active state and force-velocity relation. *Journal of Biomechanics*, 5, 107-117.
- WONG, A. Y. K. 1976. A model of excitation-contraction coupling in frog cardiac muscle. *Journal of Biomechanics*, 9, 319-332.
- WORD, R. A., TANG, D.-C. & KAMM, K. E. 1994. Activation properties of myosin light chain kinase during contraction/relaxation cycles of tonic and phasic smooth muscle. *The Journal of Biological Chemistry*, 269, 21596-21602.
- YANAGIDA, T., ARATA, T. & OOSAMA, F. 1985. Sliding distance of actin filament induced by a myosin crossbridge during one ATP hydrolysis cycle. *Nature*, 316, 366-369.
- YANG, J., CLARK JR., J. W., BRYAN, R. M. & ROBERTSON, C. 2003. The myogenic response in isolated rat cerebrovascular arteries: smooth muscle cell model. *Medical Engineering & Physics*, 25, 691-709.
- YOCHUM, M., LAFORÊT, J. & MARQUE, C. Uterine smooth muscle cell force generation from electrical properties. International Conference on Clinical and BioEngineering for Women's Health, 2015 Porto, Portugal. CRC Press.
- YOFFEY, J. M. & COURTICE, F. C. 1956. *Lymphatics, Lymph, and Lymphoid Tissue*, London, Edward Arnold (Publishers) Ltd.
- YOFFEY, J. M. & COURTICE, F. C. 1970. *Lymphatics Lymph and the Lymphomyeloid Complex*, London, Academic Press, Inc.
- YU, S.-N., CRAGO, P. E. & CHIEL, H. J. 1997. A nonisometric kinetic model for smooth muscle. *American Journal of Physiology - Cell Physiology*, 272, C1025-C1039.
- YUAN, Z. & FISH, J. 2008. Toward realization of computer homogenization in practice. *International Journal for Numerical Methods in Engineering*, 73, 361-380.
- YUAN, Z., JIANG, T., FISH, J. & MORSCHER, G. 2014. Reduced-order multiscale-multiphysics model for heterogeneous materials. 12, 45-64.
- ZABIHYAN, R., MERGHEIM, J., JAVILI, A. & STEINMANN, P. 2018. Aspects of computational homogenization in magneto-mechanics: boundary conditions, RVE size and microstructure composition. *International Journal of Solids and Structures*, 130-131, 105-121.

- ZAHALAK, G. I. 1981. A distribution-moment approximation for kinetic theories of muscular contraction. *Mathematical Biosciences*, 55, 89-114.
- ZAHALAK, G. I. 1986. A comparison of the mechanical behavior of the cat soleus muscle with a distribution-moment model. *Journal of Biomechanical Engineering*, 108, 131-140.
- ZAHALAK, G. I. & MA, S.-P. 1990. Muscle activation and contraction: constitutive relations based directly on cross-bridge kinetics. *Journal of Biomechanical Engineering*, 112, 52-62.
- ZAHALAK, G. I. & MOTABARZADEH, I. 1997. A re-examination of calcium activation in the Huxley cross-bridge model. *Journal of Biomechanical Engineering*, 119, 20-29.
- ZAMPELL, J. C., ELHADAD, S., AVRAHAM, T., WEITMAN, E., ASCHEN, S., YAN, A. & MEHRARA, B. J. 2012. Toll-like receptor deficiency worsens inflammation and lymphedema after lymphatic injury. *American Journal of Physiology - Cell Physiology*, 302, C709-C719.
- ZAMPELL, J. C., YAN, A., AVRAHAM, T., ANDRADE, V., MALLIARIS, S., ASCHEN, S., ROCKSON, S. G. & MEHRARA, B. J. 2011. Temporal and spatial patterns of endogenous danger signal expression after wound healing and in response to lymphedema. *American Journal of Physiology - Cell Physiology*, 300, C1107-C1121.
- ZAWIEJA, D. C. 2009. Contractile physiology of lymphatics. *Lymphatic Research and Biology*, 7, 87-96.
- ZAWIEJA, D. C., DAVIS, K. L., SCHUSTER, R., HINDS, W. M. & GRANGER, H. J. 1993. Distribution, propagation, and coordination of contractile activity in lymphatics. *American Journal of Physiology - Heart and Circulatory Physiology*, 264, H1283-H1291.
- ZAWIEJA, D. C., KOSSMAN, E. & PULLMAN, J. 1999. Dynamics of the microlymphatic system. *Progress in Applied Microcirculation*, 23, 33-41.
- ZAWIEJA, D. C., VON DER WEID, P.-Y. & GASHEV, A. A. 2011. Microlymphatic biology. *Handbook of Physiology, The Cardiovascular System, Microcirculation*.
- ZHANG, R., GASHEV, A. A., ZAWIEJA, D. C., LANE, M. M. & DAVIS, M. J. 2007a. Length-dependence of lymphatic phasic contractile activity under isometric and isobaric conditions. *Microcirculation*, 14, 613-625.
- ZHANG, R., TAUCER, A. I., GASHEV, A. A., MUTHUCHAMY, M., ZAWIEJA, D. C. & DAVIS, M. J. 2013. Maximum shortening velocity of lymphatic muscle approaches that of striated muscle. *American Journal of Physiology - Heart and Circulatory Physiology*, 305, H1494-H1507.
- ZHANG, R.-Z., GASHEV, A. A., ZAWIEJA, D. C. & DAVIS, M. J. 2007b. Length-tension relationships of small arteries, veins and lymphatics from the rat mesenteric microcirculation. *American Journal of Physiology - Heart and Circulatory Physiology*, 292, H1943-H1952.
- ZWEIFACH, B. W. & PRATHER, J. W. 1975. Micromanipulation of pressure in terminal lymphatics in the mesentery. *American Journal of Physiology*, 228, 1326-1335.

APPENDIX 1 – MUSCLE MODEL

Alternate CE arrangements (Original rate functions and values)

Parallel CEs

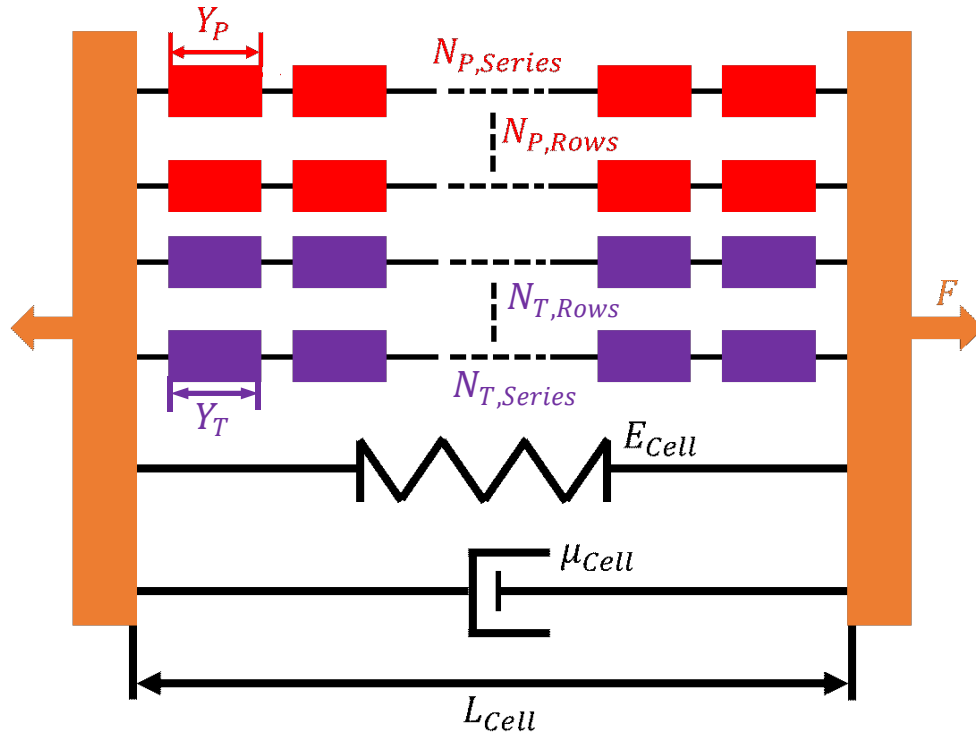


Figure 49: Diagram of an LMC with CEs in parallel with parallel spring and dashpot to model passive cell viscoelasticity. Y_P is the length of phasic CEs, $N_{P,Series}$ is the series number of phasic CEs, $N_{P,Rows}$ is the parallel number of phasic CEs, Y_T is the length of tonic CEs, $N_{T,Series}$ is the series number of tonic CEs, $N_{T,Rows}$ is the parallel number of tonic CEs, E_{Cell} is the stiffness of the LMC, μ_{Cell} is the viscosity of the LMC, L_{Cell} is the length of the LMC

The total length of CEs must be the length of the LMC

$$L_{Cell} = N_{P,Series}Y_P + N_{T,Series}Y_T$$

The force of the cell is the sum of parallel contributions

$$F = N_{P,Rows}F_P + N_{T,Rows}F_T + E_{Cell}(L_{Cell} - L_{ref}) + \mu_{Cell} \frac{dL_{Cell}}{dt}$$

Series numbers of contractile elements per row were maintained (i.e. in series connection had 14 of either type in series, so here have 28 of one CE type in series). The total parallel number of CE rows had a phasic:tonic ratio of 50:50 with a total of 1e4 (i.e. 5e3 of either type). Other values were consistent with the reference results in Chapter 2. The results show that, during phasic contractions,

the tonic force resists contractions. This is because of the phasic CEs dragging tonic myosin heads to negative displacements.

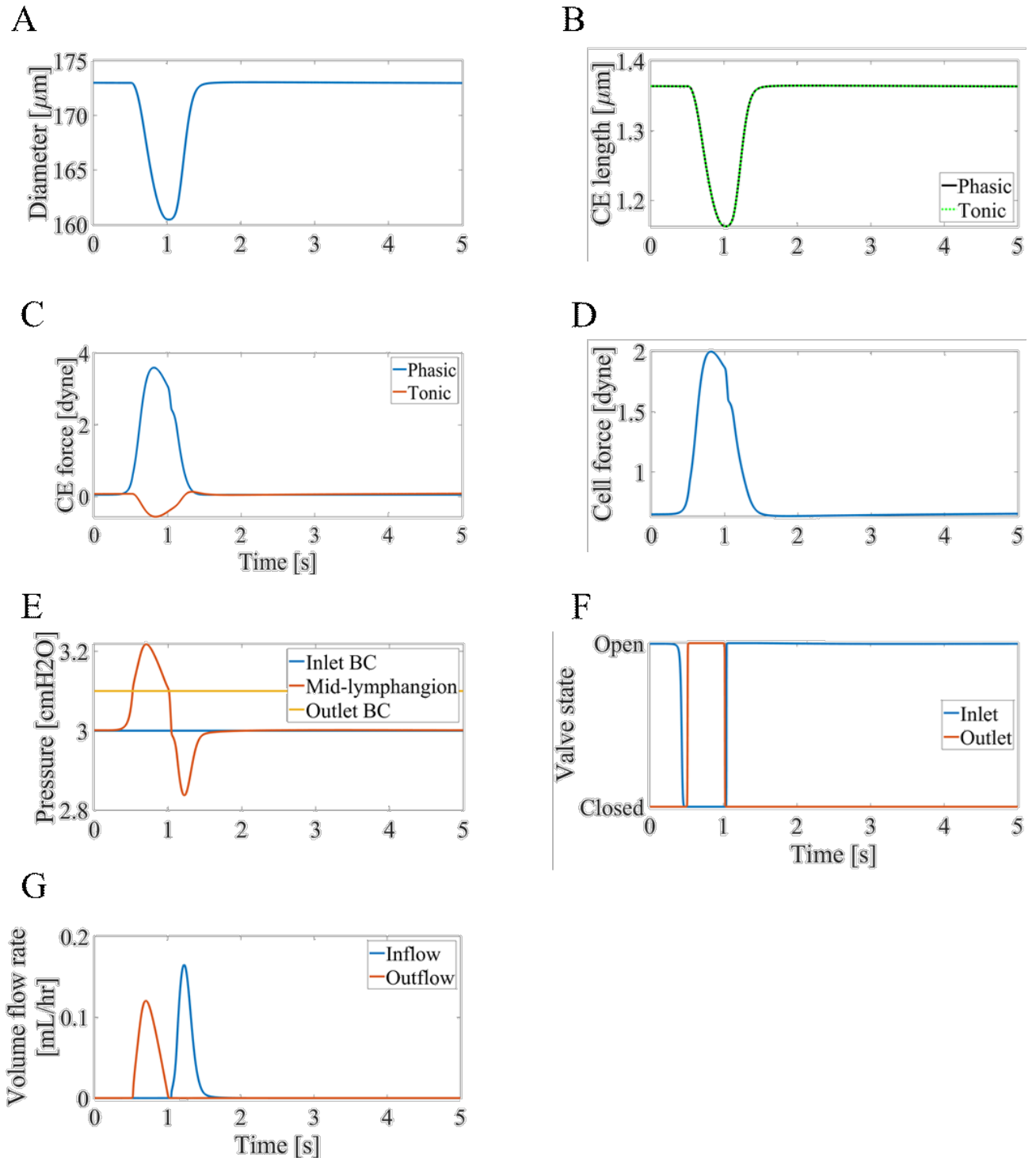


Figure 50: Panel of plots summarising the results for contractile elements in parallel. (A) is the diameter, (B) shows that the contractile elements have the same length (C) shows that the tonic force is negative during phasic contractions (D) shows the overall force from an LMC, (E) shows the pressure (F) shows the states of both valves and (G) shows the flow through valves

Series CEs phasic parallel spring, dashpot

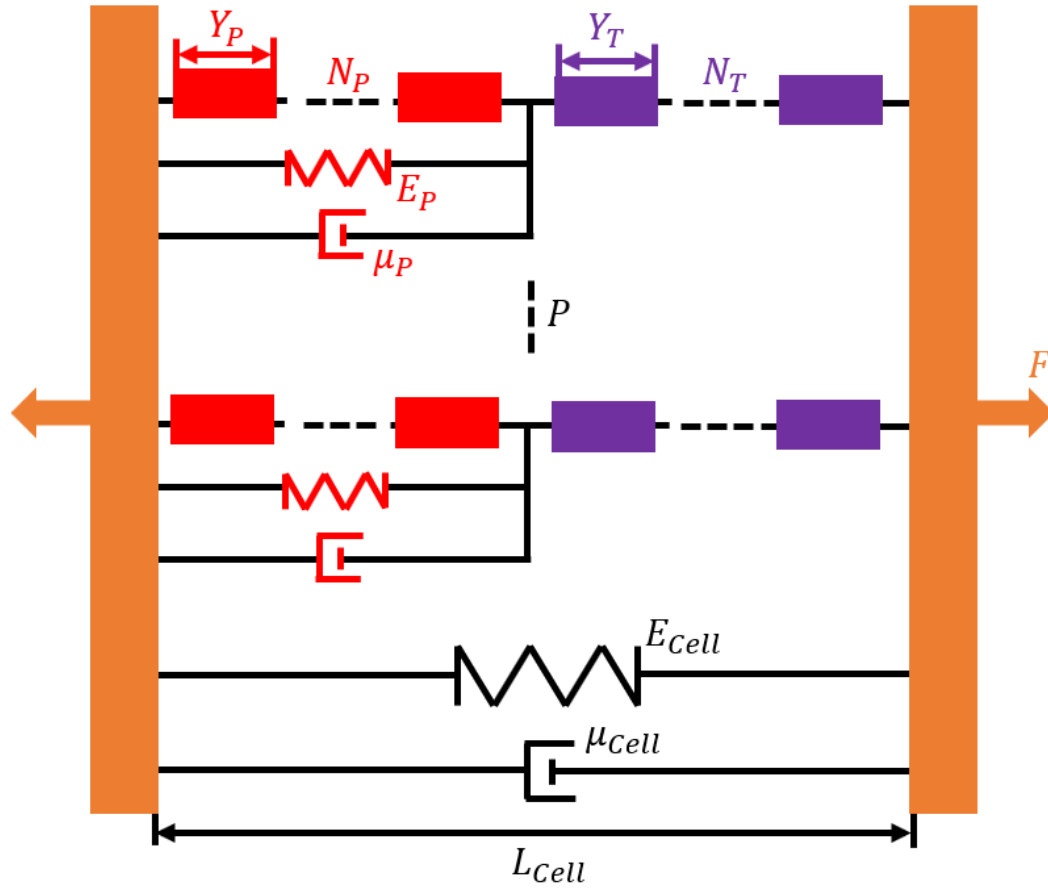


Figure 51: Diagram of an LMC with CEs in series. Phasic contractile elements have a spring and dashpot in parallel. The cell also has a spring and dashpot in parallel with contractile element rows to model passive cell viscoelasticity. Y_P is the length of phasic CEs, $N_{P, Series}$ is the series number of phasic CEs, $N_{P, Rows}$ is the parallel number of phasic CEs, Y_T is the length of tonic CEs, $N_{T, Series}$ is the series number of tonic CEs, $N_{T, Rows}$ is the parallel number of tonic CEs, E_{Cell} is the stiffness of the LMC, μ_{Cell} is the viscosity of the LMC, L_{Cell} is the length of the LMC

The shortening velocity of phasic CEs is obtained by rearranging the series force balance

$$\frac{dY_P}{dt} = [F_{Tonic,i} - F_{Phasic,i} - E_P(N_{Phasic}Y_{Phasic,i} - L_{P,Ref})]/(\mu_P N_{Phasic})$$

The shortening velocity of tonic CEs is obtained by rearranging and differentiating the series length balance

$$\frac{dY_T}{dt} = \frac{dL_{Cell}/dt - N_P dY_P/dt}{N_T}$$

The force from a single row of contractile elements is the force from CEs with the phasic spring and dashpot

$$F_{Row} = F_T = F_P + E_P N_P Y_P + \mu_P N_P \frac{dY_P}{dt}$$

The force from an LMC is the sum of row forces with contributions from cell viscosity and elasticity

$$F = PF_{Row} + E_{Cell}(L - L_{ref}) + \mu_{Cell} \frac{dL_{Cell}}{dt}$$

In this model, the phasic spring was not strain-stiffening, instead the stiffness was maintained at a constant value of 0.0128 dyne/cm. The phasic dashpot viscosity had a value of 0.0128 dyne s/cm. The parallel number of CE rows was 1e4 in agreement with the total number for the parallel CEs model. All other values were the same as the reference results in Chapter 2.

The results showed that there was no phasic contraction because the passive elements in parallel with the phasic contractile elements made it so that the row force was only the tonic force. This meant that the pressure variation was insufficient to exceed the outlet pressure, so the outlet valve didn't open and there was negligible flow.

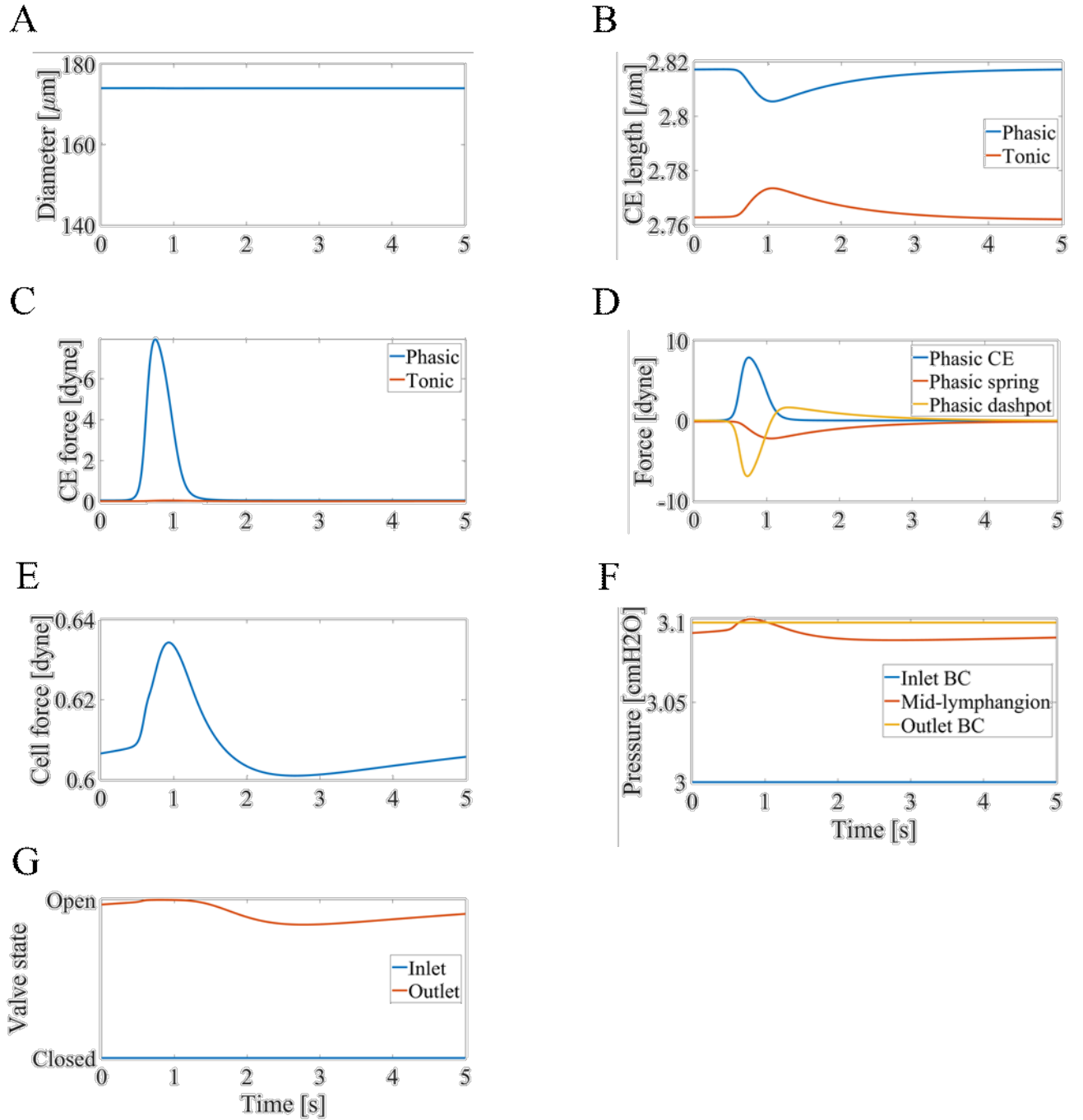


Figure 52: Panel of plots summarising results from a dashpot and spring in parallel with phasic CEs. (A) shows that there is negligible diameter change (B) shows that the shortening of phasic CEs causes an extension of tonic CEs (C) shows the phasic and tonic CE forces (D) shows the phasic CE, phasic spring, and phasic viscosity forces (E) shows the overall force from an LMC (F) shows the pressure without any suction for refilling and (G) shows that there is no complete opening or closing of valves.

Series CEs tonic parallel spring, dashpot

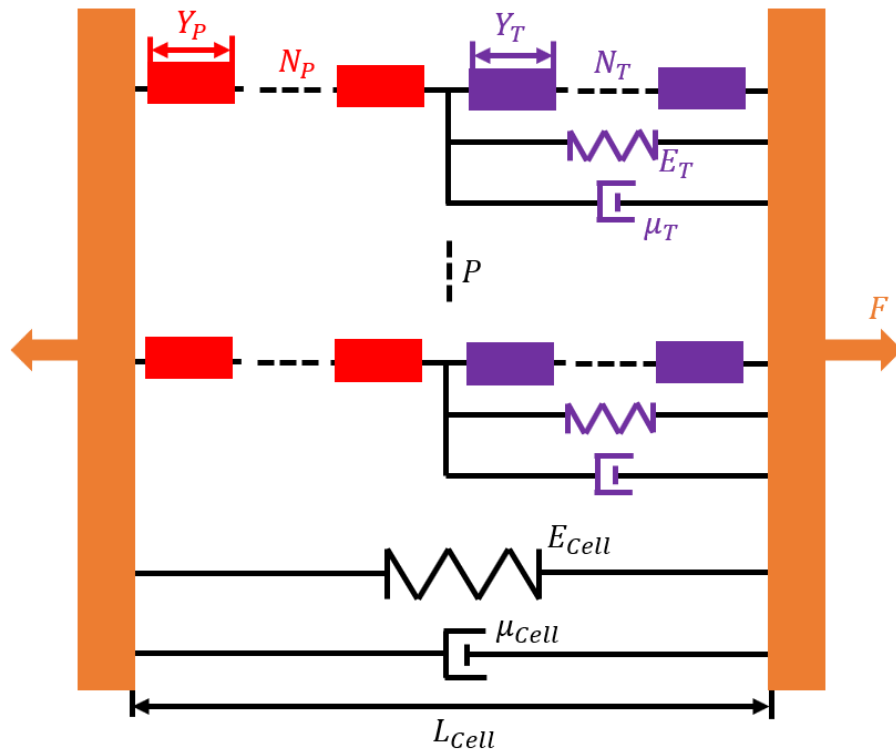


Figure 53: Diagram showing an LMC with series connections of CEs. Tonic contractile elements have a spring and dashpot in parallel. The cell also has a spring and dashpot in parallel with contractile element rows to model the cell viscoelasticity. Y_P is the length of phasic CEs, $N_{P,series}$ is the series number of phasic CEs, $N_{P,rows}$ is the parallel number of phasic CEs, Y_T is the length of tonic CEs, $N_{T,series}$ is the series number of tonic CEs, $N_{T,rows}$ is the parallel number of tonic CEs, E_{Cell} is the stiffness of the LMC, μ_{Cell} is the viscosity of the LMC, L_{Cell} is the length of the LMC

$$\frac{dY_T}{dt} = [F_{Phasic,i} - F_{Tonic,i} - E_T(N_{Tonic}Y_{Tonic,i} - L_{T,Ref})]/(\mu_T N_{Tonic})$$

$$\frac{dY_P}{dt} = \frac{dL_{Cell}/dt - N_T dY_T/dt}{N_P}$$

$$F_{Row} = F_P = F_T + E_T N_T Y_T + \mu_T N_T \frac{dY_T}{dt}$$

$$F = P F_{Row} + E_{Cell}(L - L_{ref}) + \mu_{Cell} \frac{dL_{Cell}}{dt}$$

In this model the tonic spring stiffness was maintained at a constant value of 0.0128 dyne/cm. The tonic dashpot viscosity had a value of 0.0128 dyne s/cm. The parallel number of CE rows was 1e4 in agreement with the total number for the parallel CEs model. All other values were the same as the reference results in Chapter 2.

The passive elements in parallel with tonic contractile elements now meant that the cell force was only dependent on phasic force, meaning that there was pumping but that tonic force could not constrict the lymphangion.

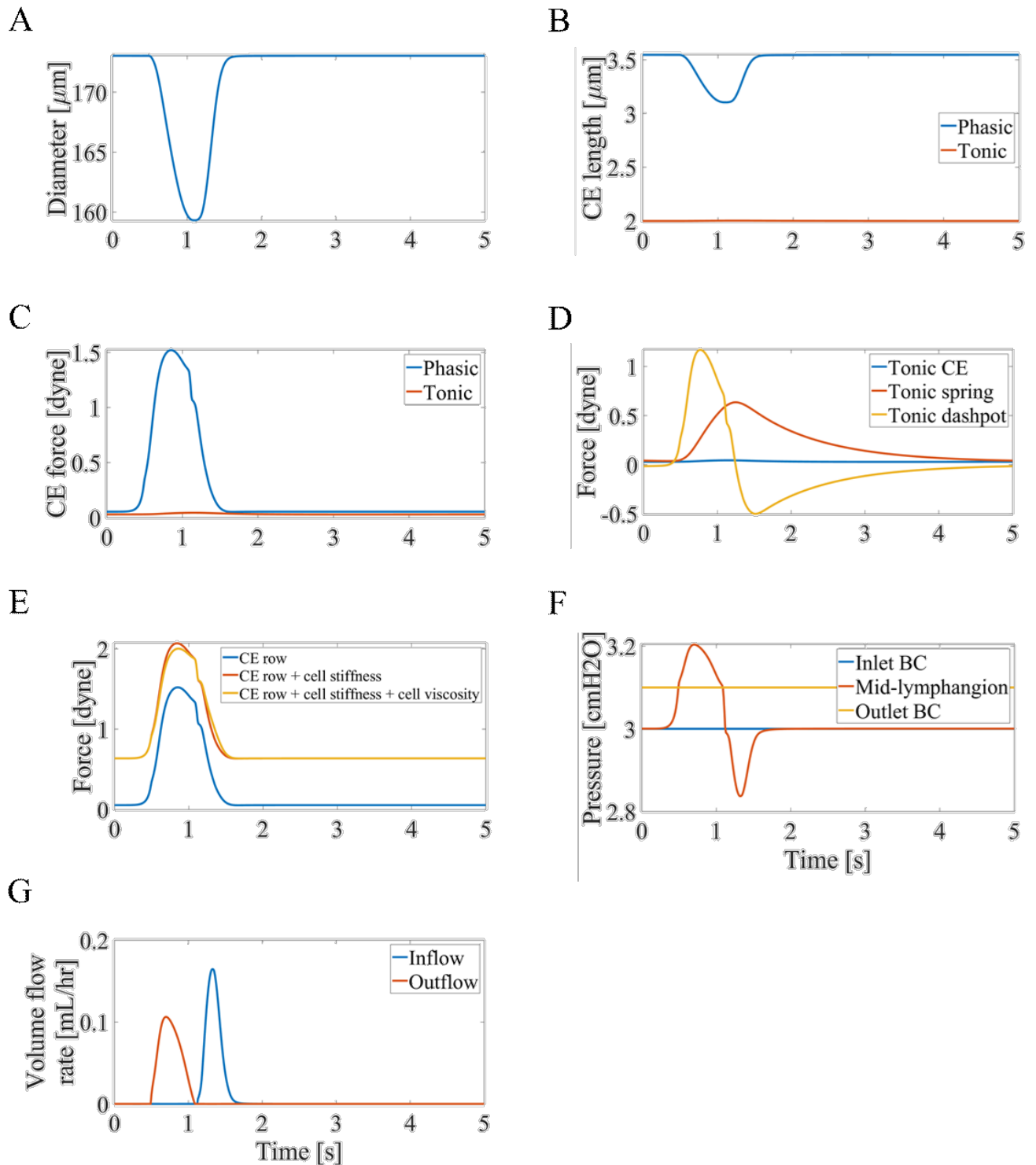


Figure 54: Panel of plots summarising the results for a muscle cell with a spring and dashpot in parallel with tonic contractile elements. (A) shows the diameter (B) shows that the tonic CE length is virtually consistent compared to the phasic CE length (C) shows the CE forces (D) shows the tonic CE, tonic spring, and tonic dashpot forces (E) compares the row force with the effects of cell stiffness and viscosity (F) shows the pressure and (G) shows the flow rates

Original rate function (Before smoothed transition)

The reference rates of (Huxley, 1957) were multiplied by various factors. All other values were maintained at the reference values used in Chapter 3.

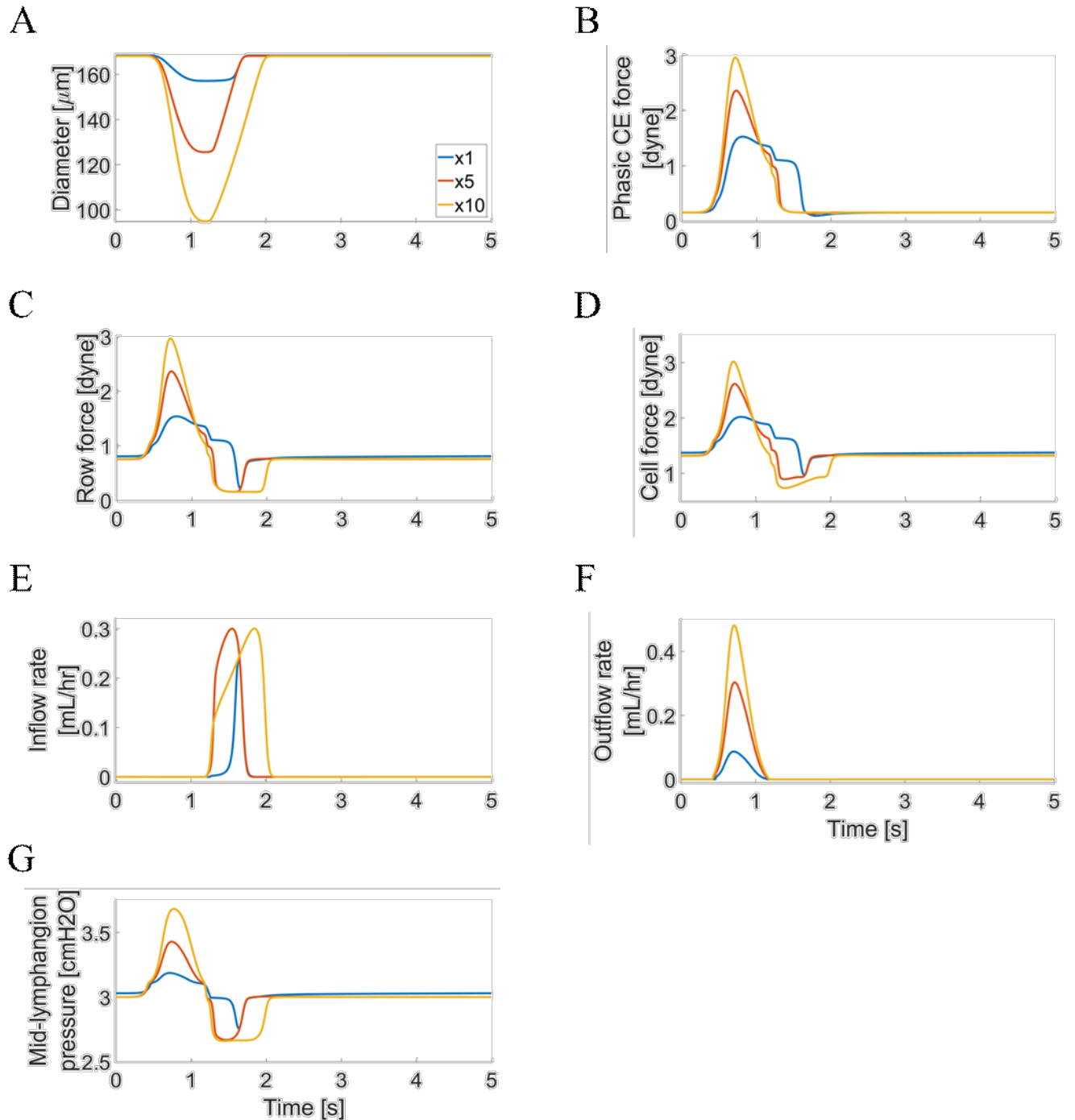


Figure 55: Panel of plots summarising the effect of varying the phasic attachment and detachment rate constants in the original Huxley rate functions. Results were obtained using the final cell model (phasic parallel spring, tonic parallel dashpot) with reference values other than phasic rates. (A) shows diameter (B) shows the force from phasic CEs (C) shows the force from CE rows (D) shows the force from an LMC (E) shows the inflow (F) shows the outflow (G) shows the pressure

Constant detachment for $x > h$ (Before smoothed transition)

The phasic rate functions originally used by Huxley (Huxley, 1957) were modified so that the

detachment rate had a constant value as given in Chapter 3.

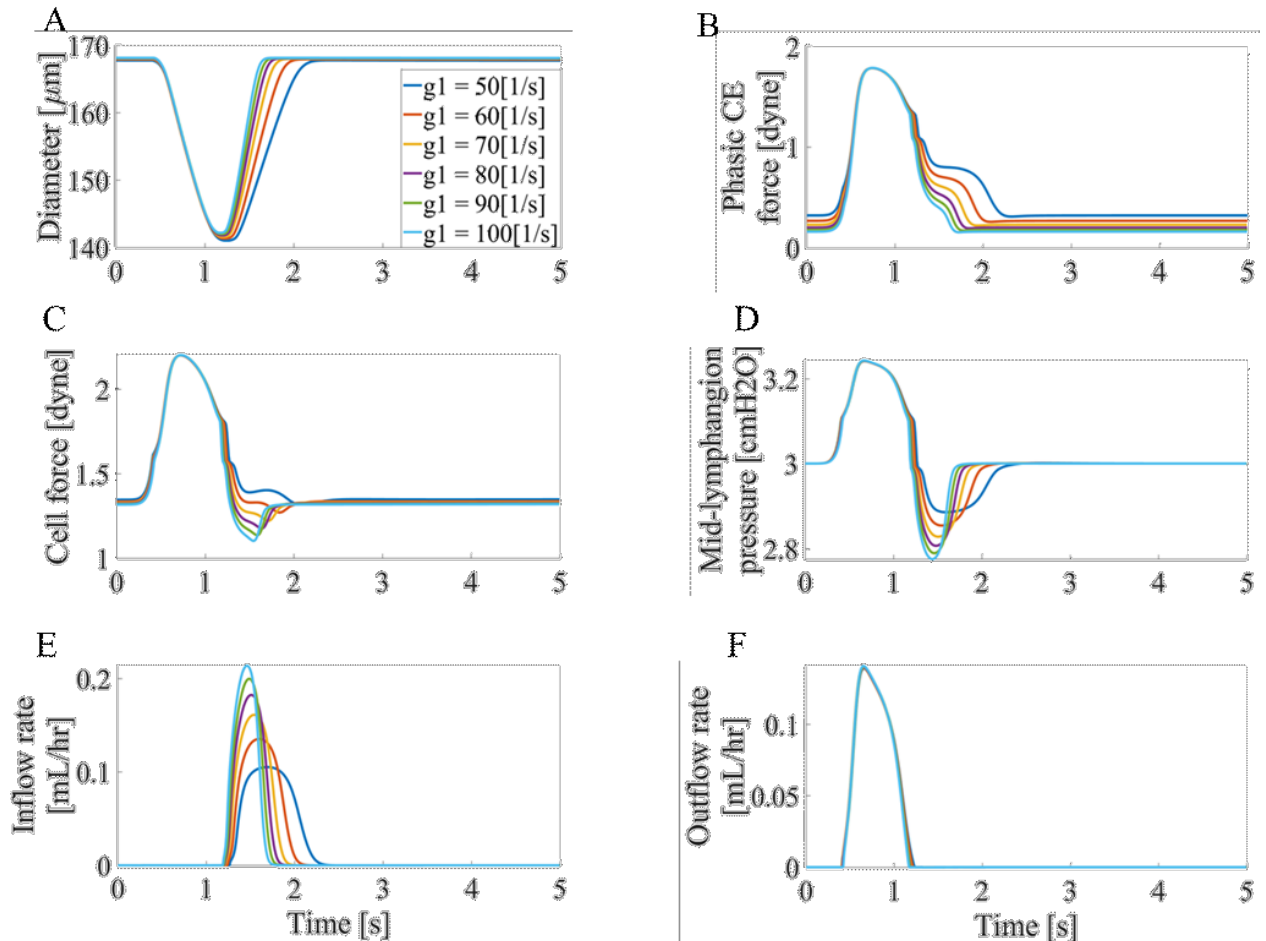


Figure 56: Panel of plots summarising the effects of varying $g1$ in a modified phasic rate function with constant detachment ($g1$) for positive displacements greater than the powerstroke length without part sine smoothing. Results were obtained using the final cell model (phasic parallel spring, tonic parallel dashpot) with reference values other than $g1$. (A) shows diameter (B) shows the force from phasic CEs (C) shows the cell force (D) shows the pressure (E) shows the inflow rate and (F) shows the outflow rate

Smoothed varying $g1_{Hux}$ (constant detachment for $x > h$)

The transitions in rate functions were given by part sine rate functions as described in the Methods

section (3.2.).

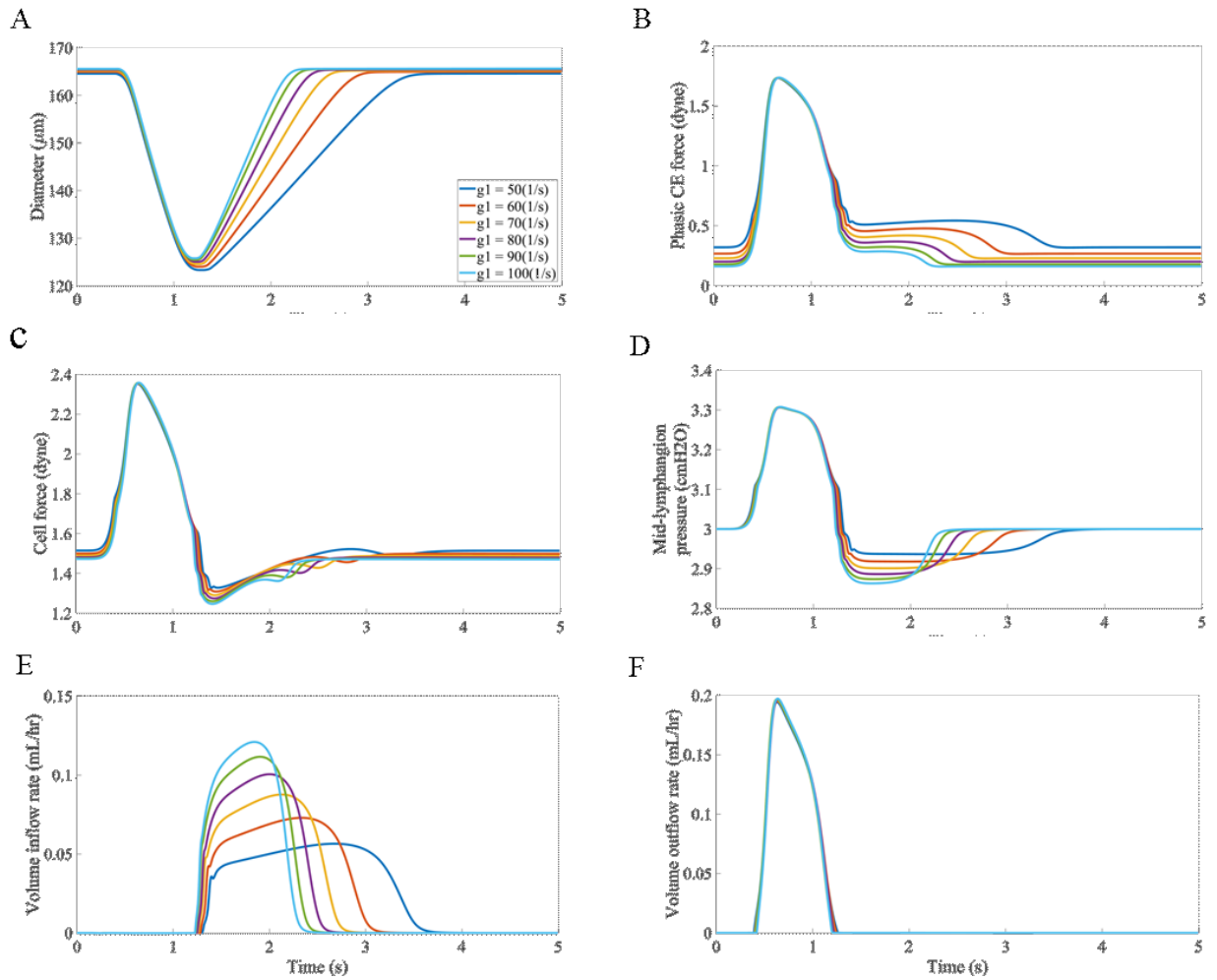
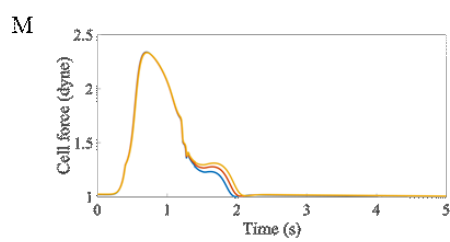
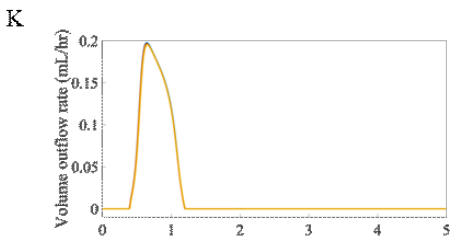
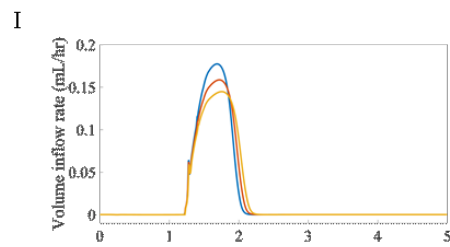
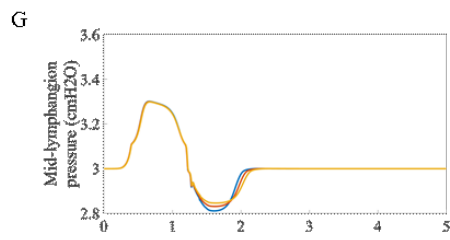
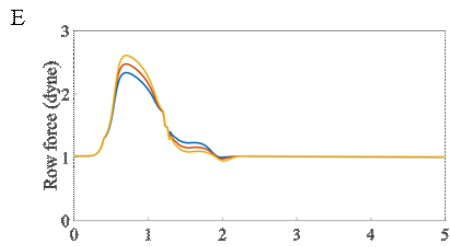
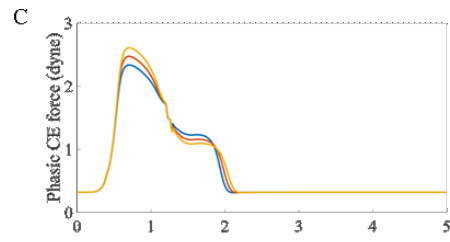
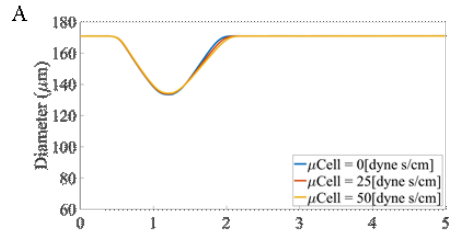


Figure 57: Panel of plots summarising the effects of varying $g1$ in a modified phasic rate function with constant detachment ($g1$) for positive displacements greater than the powerstroke length with part sine smoothing. Results were obtained using the final cell model (phasic parallel spring, tonic parallel dashpot) with reference values other than $g1$. (A) shows diameter (B) shows the force from phasic CEs (C) shows the cell force (D) shows the pressure (E) shows the inflow rate and (F) shows the outflow rate

Cell viscoelasticity

The viscosity and elasticity of the cell were co-varied, showing that increased stiffness caused greater contraction and delayed relaxation. The viscosity delayed both contraction and relaxation slightly.

$E_{cell} = 0[\text{dyne/cm}]$



$E_{cell} = 50[\text{dyne/cm}]$

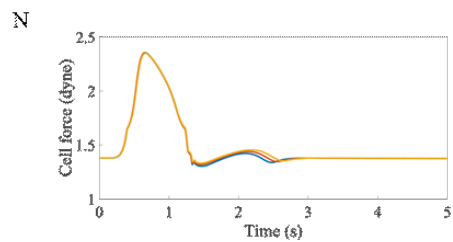
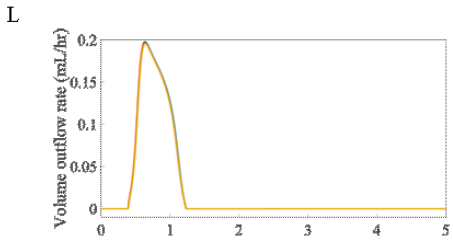
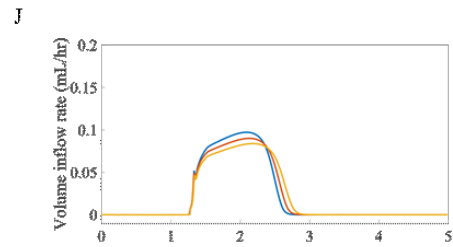
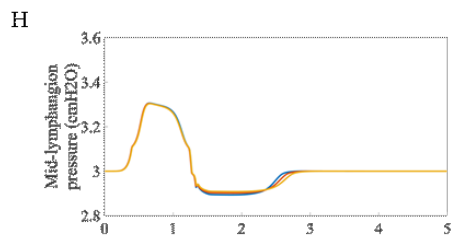
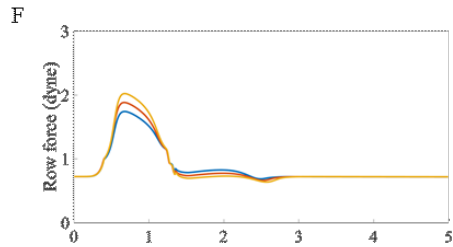
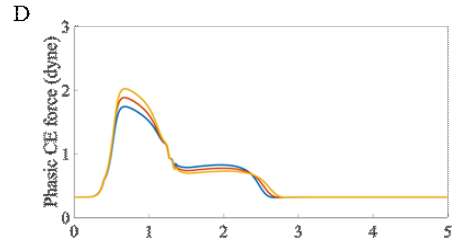
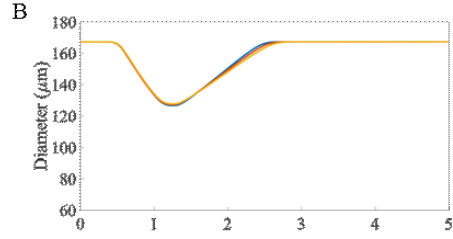


Figure 58: Panel of plots showing the effects of varying cell viscoelasticity. Results were obtained using the final cell model (phasic parallel spring, tonic parallel dashpot) with reference values other than cell viscoelasticity.

Time step check

It was verified that halving the time step used by the model did not noticeably alter the model results.

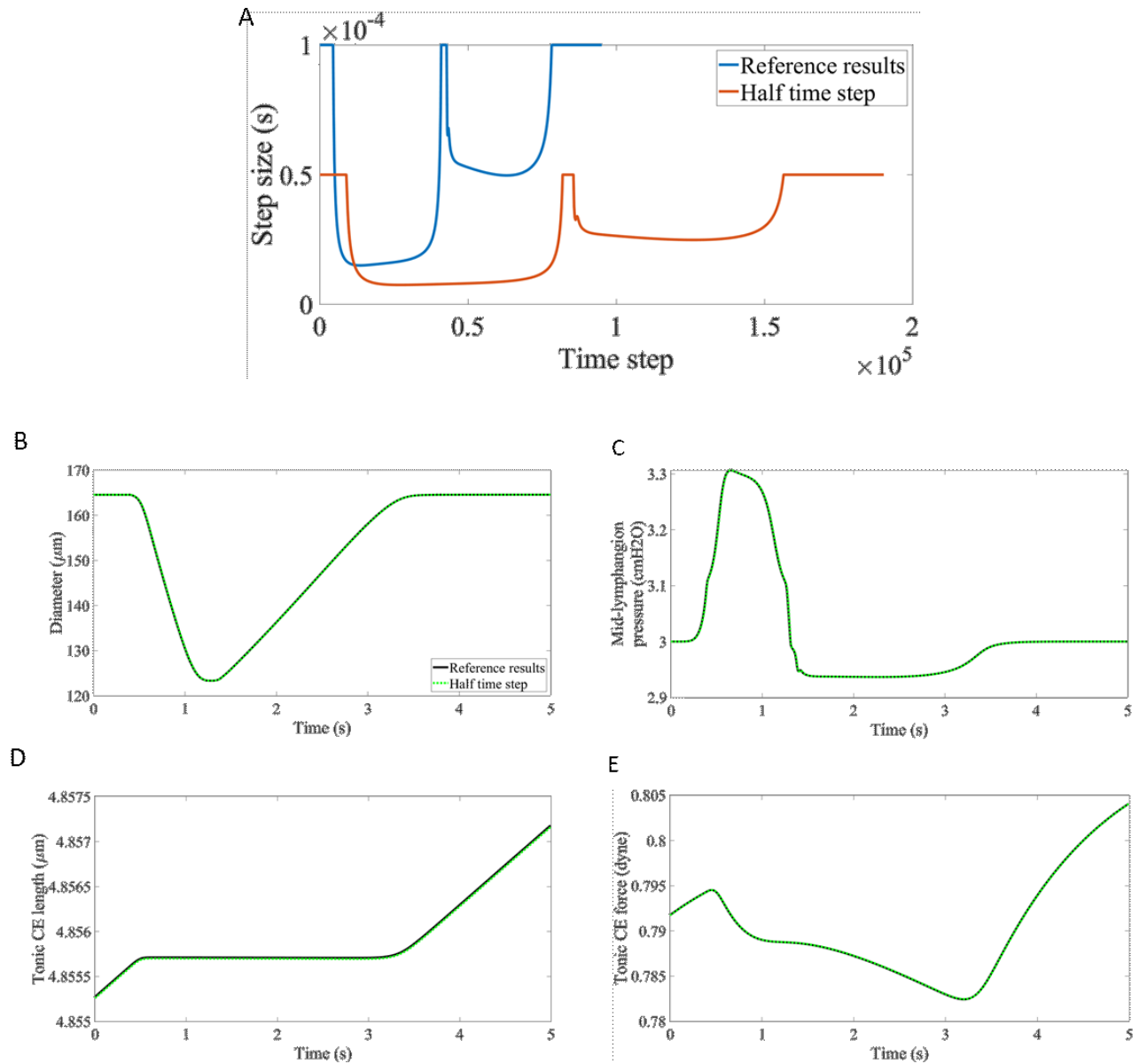


Figure 59: Panel of plots summarising the effects of halving the time step in simulations under reference conditions.

Table 6: Effects of halving the time step on key model outputs

Time step	AMP [μm]	EF [%]	Qbar [mL/hr]
Original	41.23	43.83	0.0201
Half	41.23	43.83	0.0201
% difference	-7.28e-04	0.003	0.0058

Periodicity conditions check

The simulation for reference conditions was initially run until periodicity conditions were met and was then run for an additional five cycles to check that there was negligible change. The main model outputs of diameter, pressure, and flow did not change (Figure 38 A-D). There is still some variation in tonic CE force and length but they are small (Figure 38 E,F see axes).

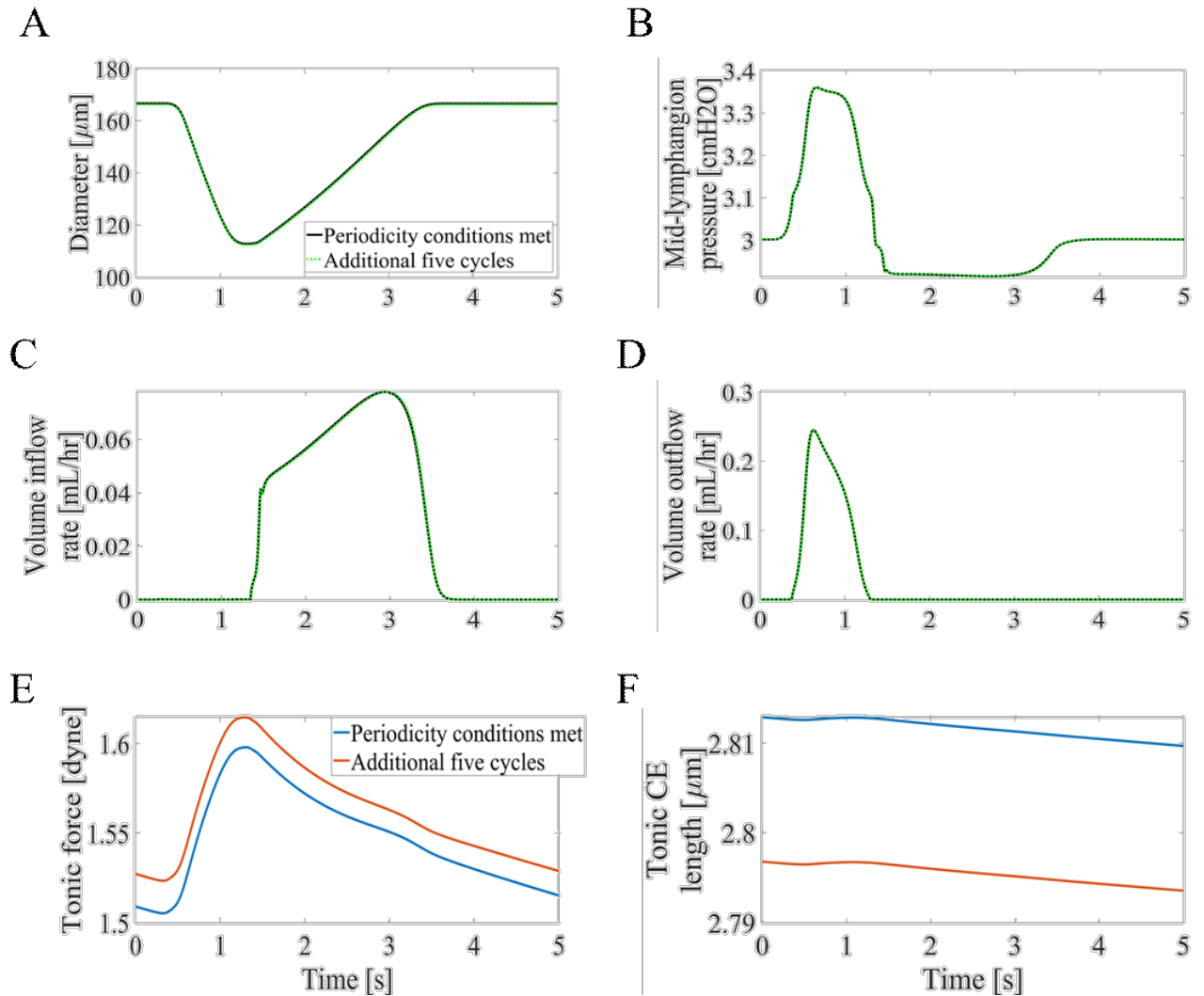


Figure 60: Panel of plots verifying that the periodicity conditions ensure that the results have reached periodicity. (A) shows that the diameter change is negligible (B) shows that the pressure change is negligible (C) shows that the change in inflow is negligible (D) shows that the outflow rate is negligible (E) shows that there is some variation in tonic CE force and (F) shows that there is some variation in tonic CE length

Time step	AMP [μm]	EF [%]	Qbar [mL/hr]
Original	41.2339	43.8320	0.0201
Half	41.3529	43.9132	0.0201
% difference	-0.2886	-0.1852	0

Results from MacCormack predictor corrector

For each head state in the phasic and tonic models n the displacement-distribution of heads is

updated using a prediction step

$$n^p(j) = \begin{cases} n(j) - V(dt/dx)[n(j) - n(i+1)] + S(j)n(j) \\ n(j) - V(dt/dx)[n(j-1) - n(j)] + S(j)n(j) \end{cases}$$

where n^p is a temporary variable used in the update, V is the shortening velocity, dt is the time step, dx is the displacement discretisation and S is the source/sink term (the transition rates)

and a correction step

$$n(j) = \begin{cases} \frac{n(j) + n^p(j)}{2} - \frac{1}{2} \frac{dt}{dx} V[n^p(j) - n^p(j+1)] + 0.5S(j)n(j) \\ \frac{n(j) + n^p(j)}{2} - \frac{1}{2} \frac{dt}{dx} V[n^p(j-1) - n^p(j)] + 0.5S(j)n(j) \end{cases}$$

With n now updated to a new value

The results obtained using this MacCormack scheme under conditions corresponding to the reference results are very similar to those obtained using the second order Godunov scheme.

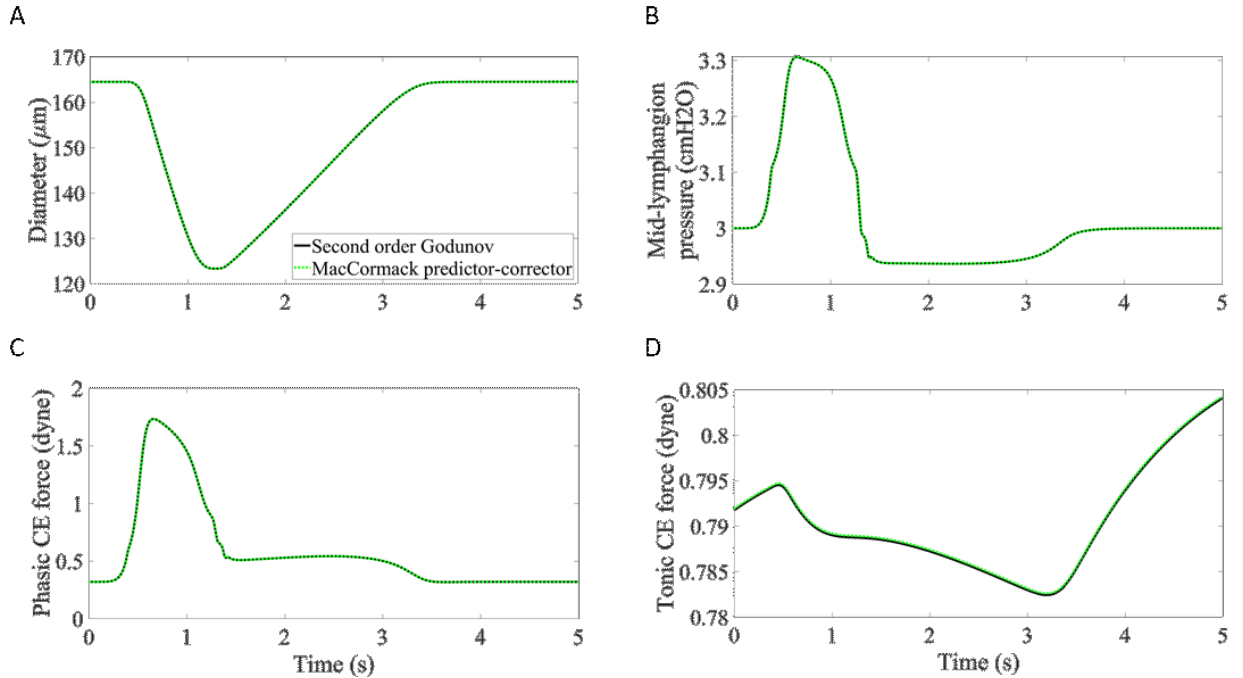


Figure 61: Panel of plots comparing model results under reference conditions when obtained with the second order Godunov solver and obtained with the MacCormack predictor-corrector (A) compares diameter (B) compares the mid-lymphangion pressure (C) compares the phasic CE force and (D) compares the tonic CE force

Time step	AMP [um]	EF [%]	Qbar [mL/hr]
Original	41.2339	43.8320	0.0201
Half	41.2267	43.8254	0.0201
% difference	0.0175	0.0151	0.0114

Muscle cell energy balance

The balance of work done, energy stored and energy lost for a muscle cell was calculated for the reference results from Chapter 2.

Phasic CE work done + Tonic CE work done – Tonic dashpot loss – Cell dashpot loss + Phasic spring storage input + Cell spring storage input = Cell work done

Phasic CE work rate

$$\frac{dW_P}{dt} = PF_P \times -N_P \frac{dY_P}{dt}$$

where the minus sign is included because the muscle does work to reduce the CE length

Tonic CE work rate

$$\frac{dW_T}{dt} = PF_T \times -N_T \frac{dY_T}{dt}$$

Cell work rate

$$\frac{dW}{dt} = F \times -\frac{dL}{dt}$$

Phasic spring storage rate

$$\frac{dStore_P}{dt} = PE_P N_P Y_P \times N_P \frac{dY_P}{dt}$$

Tonic dashpot loss rate

$$\frac{dLoss_T}{dt} = P\mu_T N_T \frac{dY_T}{dt} \times N_T \frac{dY_T}{dt}$$

Cell spring storage rate

$$\frac{dStore}{dt} = \mu_{cell} \frac{dL}{dt} \times \frac{dL}{dt}$$

Cell dashpot loss rate

$$\frac{dLoss}{dt} = E_{cell} L \times \frac{dL}{dt}$$

The changes in spring storages were calculated by initialising the value to zero, and then energy released from springs was calculated as the decrease in stored energy (i.e. changing the sign).

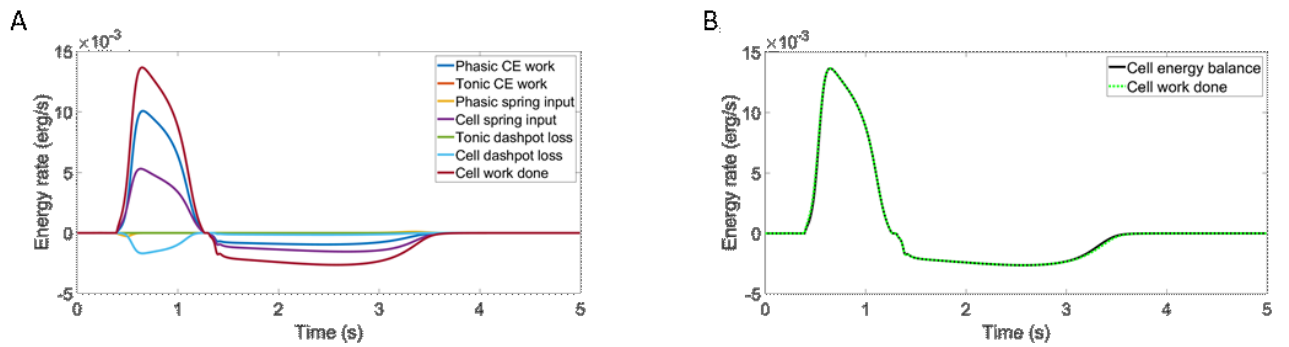


Figure 62: Energetics of an LMC. (A) Time-dependent rates of energy level changes in each form within a muscle cell (note that negative values indicate energy lost as heat/work done on the muscle and positive values indicate work done by the muscle/energy input into pumping). (B) Energy balance showing that the work done by the cell is the sum of work done by CEs, energy released from the spring stores and (negative) energy lost to viscosity.

Displacement discretisation insensitivity

Decreasing the displacement discretization from $h/20$ to $h/40$ had a negligible effect on the results

under reference conditions. Average flow differed between the two discretisations by only 0.01%.

The efficiency of muscle was 9.3% and the efficiency of transfer of muscle work to lymph was

30.2% in both cases.

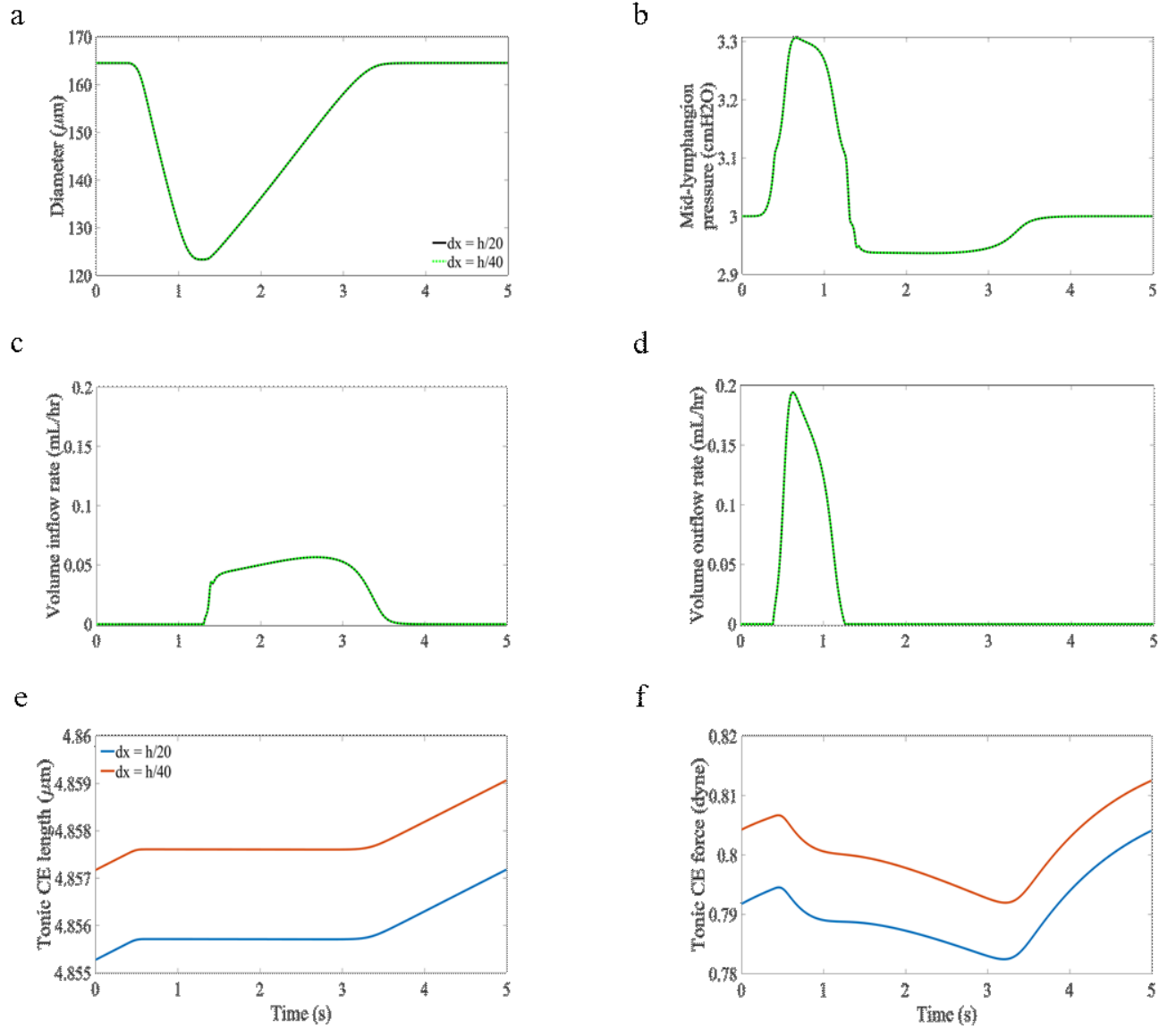


Figure 63: Panel of plots showing that halving the displacement discretization had a negligible effect on the main output parameters of the model

Time step	AMP [μm]	EF [%]	Qbar [mL/hr]
Original	41.2339	43.8320	0.0201
Half	41.2300	43.8212	0.0201
% difference	0.0095	0.0246	0.0107

One-at-a-time sensitivity analysis results

Table 7: Table of results showing the sensitivity measures obtained for each parameter from the one-at-a-time sensitivity analysis. Rows in bold indicate the variables considered sensitive and included in the Latin hypercube analysis

Parameter	Input values			S		
a_2 [s^{-6}]	12.085	48.34	120.85	0.1909	0.0844	0.0450
a_p [dyne/cm]	5.1282e-24	1.0256e-22	5.1282e-22	-0.0188	-0.0061	-0.0024
b_2 [s^{-6}]	0.2639	1.0556	2.639	-0.3899	-0.1839	-0.1010
b_p [$1/\text{cm}$]	73.8382	738.3821		-0.0274	-0.0301	
Ca_{amp} [M]	1.2e-7	4.8e-7	1.2e-6	2.0067	0.5065	0.0003

Ca_d [M]	7e-8	2.8e-7	7.0e-7	0.6196 -1.0000 -0.2500
E_{cell} [dyne/cm]	7.5	150	750	0.0594 -0.6729 -0.1032
f_1 [1/s]	62	1240	6200	0.6050 -0.6009 -0.1061
$K_{3,1}$ [1/s]	0.088	1.76	8.80	1.0e-04 * 0.3037 -0.3800 -0.0467
g_1 [1/s]	5	100	500	1.0910 -0.0231 -0.0186
$K_{7,1}$ [1/s]	0.01	0.2	1	1.0e-03 * 0.0444 -0.1320 -0.0433
g_2 [1/s]	21	420	2100	2.4213 0.4602 0.0142
$K_{4,1}$ [1/s]	0.022	0.44	2.2	1.0e-04 * 0.4355 -0.3182 -0.0313
h [cm]	7.8e-7	3.12e-6	7.8e-6	1.0e-05 * -0.4358 -0.5938 -0.7047
K_1 [1/s]	0.035	0.7	3.5	-0.0134 0.0121 0.0013
K_2 [1/s]	0.01	0.2	1	-0.0134 0.0121 0.0013
K_{HHM} [dyne/cm]	0.18	3.6	18	1.0e-04 * 0.2936 -0.4351 -0.1296
K_{Hux} [dyne/cm]	0.04	0.8	4	0.6402 -0.6034 -0.1064
m []	3	12	30	-0.9598 -0.3994 -0.1799
μ_{cell} [dyne s/cm]	5	10	25	-0.0258 -0.0256 -0.0252
μ_T [dyne s/cm]	1	20	100	-0.0122 -0.0008 -0.0002
N_{cell} []	3	5	10	3.9802 0.7651 0.6196
N_{Tonic} []	7	28	50	0.0320 0.0151 0.0094
N_{Phasic} []	7	28	50	0.8798 0.6108 0.3853
$c_{0.5, CaM}$ [M]	4e-6	20e-6		1.0e-04 * 0.2782 0.0389
n_{mCaM} []	0.5	1	2	1.0e-03 * 0.7910 0.2688 -0.0802
N_{Rows} []	1.8e3	3.6e4	1.8e5	0.6141 -0.6034 -0.1064
Num_P []	450	9000	45000	0.6402 -0.6034 -0.1064
Num_T []	100	2000	10000	-0.0220 -0.0071 -0.0026
ρ [1/cm]	6e4	1.2e6	6e6	0.6402 -0.6034 -0.1064

Distribution-moment approximation

The displacement-distribution of attached heads (n) is assumed to be Gaussian

$$n = M_0 \exp\left(-\frac{(x-p)^2}{2q^2}\right)$$

$$\frac{dM_0}{dt} = b_0 - F_0(M_0, M_1, M_2)$$

$$\frac{dM_1}{dt} = b_1 - F_1(M_0, M_1, M_2) - vM_0$$

$$\frac{dM_2}{dt} = b_2 - F_2(M_0, M_1, M_2) - 2vM_1$$

where M_0, M_1, M_2 are the zeroth, first and second moments of attached head distribution over displacement, initialised to 0.00001, 0.00001 and 0.00002, respectively

$$b_0 = \int_{x_0}^{x_1} S_{Trop} f_1 x \, dx$$

$$b_1 = \int_{x_0}^{x_1} S_{Trop} f_1 x^2 \, dx$$

$$b_2 = \int_{x_0}^{x_1} S_{Trop} f_1 x^3 \, dx$$

$$F_0 = \frac{M_0}{\sqrt{2\pi}q} \left[\int_{-\infty}^{x_0} g_2 \exp\left(-\frac{(x-p)^2}{2q^2}\right) dx + \int_{x_0}^{x_1} (S_{Trop} f_1 + g_1) x \exp\left(-\frac{(x-p)^2}{2q^2}\right) dx + \int_{x_1}^{\infty} g_1 \exp\left(-\frac{(x-p)^2}{2q^2}\right) dx \right]$$

$$F_1 = \frac{M_0}{\sqrt{2\pi}q} \left[\int_{-\infty}^{x_0} g_2 x \exp\left(-\frac{(x-p)^2}{2q^2}\right) dx + \int_{x_0}^{x_1} (S_{Trop} f_1 + g_1) x^2 \exp\left(-\frac{(x-p)^2}{2q^2}\right) dx + \int_{x_1}^{\infty} g_1 x \exp\left(-\frac{(x-p)^2}{2q^2}\right) dx \right]$$

$$F_2 = \frac{M_0}{\sqrt{2\pi}q} \left[\int_{-\infty}^{x_0} g_2 x^2 \exp\left(-\frac{(x-p)^2}{2q^2}\right) dx + \int_{x_0}^{x_1} (S_{Trop} f_1 + g_1) x^3 \exp\left(-\frac{(x-p)^2}{2q^2}\right) dx + \int_{x_1}^{\infty} g_1 x^2 \exp\left(-\frac{(x-p)^2}{2q^2}\right) dx \right]$$

$$p = \frac{M_0}{M_1}$$

$$q = \sqrt{\frac{M_2}{M_0} - \left(\frac{M_1}{M_0}\right)^2}$$

HHM

$$\frac{dM_{10}}{dt} = A_0 - B_0 + C_0 - k_{2HHM}M_{10}$$

$$\frac{dM_{11}}{dt} = A_1 - B_1 + C_1 - k_{2HHM}M_{11} - v_T M_{10}$$

$$\frac{dM_{12}}{dt} = A_2 - B_2 + C_2 - k_{2HHM}M_{12} - 2v_T M_{11}$$

$$\frac{dM_{20}}{dt} = D_0 - E_0 - S_{CaM}k_{1HHM}M_{20}$$

$$\frac{dM_{21}}{dt} = D_1 - E_1 - S_{CaM}k_{1HHM}M_{21} - v_T M_{20}$$

$$\frac{dM_{22}}{dt} = D_2 - E_2 - S_{CaM}k_{1HHM}M_{22} - 2v_T M_{21}$$

$$\frac{dc}{dt} = -S_{CaM}k_{1HHM}c + (1 - c)k_{2HHM}$$

where M_{10}, M_{11}, M_{12} are the zeroth, first and second displacement-distribution moments of attached phosphorylated heads (initialised to 0.00001, 0.00001 and 0.00002, respectively), M_{20}, M_{21}, M_{22} are the zeroth, first and second displacement-distribution moments of attached dephosphorylated heads, c is the sum of the zeroth moments of attached dephosphorylated and detached dephosphorylated myosin heads (initialised to 0.9999)

$$y = \frac{x - p_a}{q_a}$$

$$\varphi_1(0) = \frac{1}{\sqrt{2\pi}} \int_{-\infty}^{y=0} \exp(0.5y^2) dy$$

$$\varphi_1(1) = \frac{1}{\sqrt{2\pi}} \int_{-\infty}^{y=1} \exp(0.5y^2) dy$$

$$J_1(0) = p_a \varphi_1(0) - \frac{q_a}{\sqrt{2\pi}}$$

$$J_1(1) = p_a \varphi_1(1) - \frac{q_a \exp(-0.5)}{\sqrt{2\pi}}$$

$$J_2(0) = p_a^2 \varphi_1(0) - \frac{2p_a q_a}{\sqrt{2\pi}} + q_a^2 \varphi_1(0)$$

$$J_2(1) = p_a^2 \varphi_1(1) - \frac{2p_a q_a \exp(-0.5)}{\sqrt{2\pi}} + q_a^2 \left[\varphi_1(1) - \frac{\exp(-0.5)}{\sqrt{2\pi}} \right]$$

$$J_3(0) = p_a^3 \varphi_1(0) - \frac{3p_a^2 q_a}{\sqrt{2\pi}} + 3p_a q_a^2 \varphi_1(0) - \frac{2q_a^3}{\sqrt{2\pi}}$$

$$J_3(1) = p_a^3 \varphi_1(1) - \frac{3p_a^2 q_a \exp(-0.5)}{\sqrt{2\pi}} + 3p_a q_a^2 \left[\varphi_1(1) - \frac{\exp(-0.5)}{\sqrt{2\pi}} \right] - \frac{q_a^3 \exp(-0.5)}{\sqrt{2\pi}}$$

$$A_0 = \frac{f_{p1HHM}(1-c)}{2h} - f_{p1HHM}(J_1(1) - J_1(0))M_{10}$$

$$A_1 = \frac{f_{p1HHM}(1-c)}{3h} - f_{p1HHM}(J_2(1) - J_2(0))M_{10}$$

$$A_2 = \frac{f_{p1HHM}(1-c)}{4h} - f_{p1HHM}(J_3(1) - J_3(0))M_{10}$$

$$B_0 = \frac{M_{10}}{\sqrt{2\pi}q_a h} \left[\int_{-\infty}^{x_0} g_{p2HHM} \exp\left(-\frac{(x-p_a)^2}{2q_a^2}\right) dx + \int_{x_0}^{x_1} g_{p1HHM} x \exp\left(-\frac{(x-p_a)^2}{2q_a^2}\right) dx \right. \\ \left. + \int_{x_1}^{\infty} (g_{p1HHM} + g_{p3HHM}) x \exp\left(-\frac{(x-p_a)^2}{2q_a^2}\right) dx \right]$$

$$B_1 = \frac{M_{10}}{\sqrt{2\pi}q_a h} \left[\int_{-\infty}^{x_0} g_{p2HHM} x \exp\left(-\frac{(x-p_a)^2}{2q_a^2}\right) dx + \int_{x_0}^{x_1} g_{p1HHM} x^2 \exp\left(-\frac{(x-p_a)^2}{2q_a^2}\right) dx \right. \\ \left. + \int_{x_1}^{\infty} (g_{p1HHM} + g_{p3HHM}) x^2 \exp\left(-\frac{(x-p_a)^2}{2q_a^2}\right) dx \right]$$

$$B_2 = \frac{M_{10}}{\sqrt{2\pi}q_a h} \left[\int_{-\infty}^{x_0} g_{p2HHM} x^2 \exp\left(-\frac{(x-p_a)^2}{2q_a^2}\right) dx + \int_{x_0}^{x_1} g_{p1HHM} x^3 \exp\left(-\frac{(x-p_a)^2}{2q_a^2}\right) dx \right. \\ \left. + \int_{x_1}^{\infty} (g_{p1HHM} + g_{p3HHM}) x^3 \exp\left(-\frac{(x-p_a)^2}{2q_a^2}\right) dx \right]$$

$$C_0 = \frac{S_{CaM} k_{1HHM} M_{20}}{\sqrt{2\pi}q_b h} \left[\int_{-\infty}^{x_0} \exp\left(-\frac{(x-p_b)^2}{2q_b^2}\right) dx + \int_{x_0}^{x_1} x \exp\left(-\frac{(x-p_b)^2}{2q_b^2}\right) dx \right. \\ \left. + \int_{x_1}^{\infty} \exp\left(-\frac{(x-p_b)^2}{2q_b^2}\right) dx \right]$$

$$C_1 = \frac{S_{CaM} k_{1HHM} M_{20}}{\sqrt{2\pi}q_b h} \left[\int_{-\infty}^{x_0} x \exp\left(-\frac{(x-p_b)^2}{2q_b^2}\right) dx + \int_{x_0}^{x_1} x^2 \exp\left(-\frac{(x-p_b)^2}{2q_b^2}\right) dx \right. \\ \left. + \int_{x_1}^{\infty} x \exp\left(-\frac{(x-p_b)^2}{2q_b^2}\right) dx \right]$$

$$C_2 = \frac{S_{CaM} k_{1HHM} M_{20}}{\sqrt{2\pi}q_b h} \left[\int_{-\infty}^{x_0} x^2 \exp\left(-\frac{(x-p_b)^2}{2q_b^2}\right) dx + \int_{x_0}^{x_1} x^3 \exp\left(-\frac{(x-p_b)^2}{2q_b^2}\right) dx \right. \\ \left. + \int_{x_1}^{\infty} x^2 \exp\left(-\frac{(x-p_b)^2}{2q_b^2}\right) dx \right]$$

$$D_0 = \frac{k_{2HHM} M_{10}}{\sqrt{2\pi}q_a h} \left[\int_{-\infty}^{x_0} \exp\left(-\frac{(x-p_a)^2}{2q_a^2}\right) dx + \int_{x_0}^{x_1} \exp\left(-\frac{(x-p_a)^2}{2q_a^2}\right) dx \right. \\ \left. + \int_{x_1}^{\infty} \exp\left(-\frac{(x-p_a)^2}{2q_a^2}\right) dx \right]$$

$$D_1 = \frac{k_{2HHM} M_{10}}{\sqrt{2\pi}q_a h} \left[\int_{-\infty}^{x_0} x \exp\left(-\frac{(x-p_a)^2}{2q_a^2}\right) dx + \int_{x_0}^{x_1} x \exp\left(-\frac{(x-p_a)^2}{2q_a^2}\right) dx \right. \\ \left. + \int_{x_1}^{\infty} x \exp\left(-\frac{(x-p_a)^2}{2q_a^2}\right) dx \right]$$

$$D_2 = \frac{k_{2HHM}M_{10}}{\sqrt{2\pi}q_a h} \left[\int_{-\infty}^{x_0} x^2 \exp\left(-\frac{(x-p_a)^2}{2q_a^2}\right) dx + \int_{x_0}^{x_1} x^2 \exp\left(-\frac{(x-p_a)^2}{2q_a^2}\right) dx \right. \\ \left. + \int_{x_1}^{\infty} x^2 \exp\left(-\frac{(x-p_a)^2}{2q_a^2}\right) dx \right]$$

$$E_0 = \frac{M_{20}}{\sqrt{2\pi}q_b h} \left[\int_{-\infty}^{x_0} g_{2HHM} \exp\left(-\frac{(x-p_b)^2}{2q_b^2}\right) dx + \int_{x_0}^{x_1} g_{1HHM} x \exp\left(-\frac{(x-p_b)^2}{2q_b^2}\right) dx \right. \\ \left. + \int_{x_1}^{\infty} (g_{1HHM} + g_{3HHM}) x \exp\left(-\frac{(x-p_b)^2}{2q_b^2}\right) dx \right]$$

$$E_1 = \frac{M_{20}}{\sqrt{2\pi}q_b h} \left[\int_{-\infty}^{x_0} g_{2HHM} x \exp\left(-\frac{(x-p_b)^2}{2q_b^2}\right) dx + \int_{x_0}^{x_1} g_{1HHM} x^2 \exp\left(-\frac{(x-p_b)^2}{2q_b^2}\right) dx \right. \\ \left. + \int_{x_1}^{\infty} (g_{1HHM} + g_{3HHM}) x^2 \exp\left(-\frac{(x-p_b)^2}{2q_b^2}\right) dx \right]$$

$$E_2 = \frac{M_{20}}{\sqrt{2\pi}q_b h} \left[\int_{-\infty}^{x_0} g_{2HHM} x^2 \exp\left(-\frac{(x-p_b)^2}{2q_b^2}\right) dx + \int_{x_0}^{x_1} g_{1HHM} x^3 \exp\left(-\frac{(x-p_b)^2}{2q_b^2}\right) dx \right. \\ \left. + \int_{x_1}^{\infty} (g_{1HHM} + g_{3HHM}) x^3 \exp\left(-\frac{(x-p_b)^2}{2q_b^2}\right) dx \right]$$

$$p_a = \frac{M_{11}}{M_{10}}$$

$$q_a = \sqrt{\frac{M_{12}}{M_{10}} - \left(\frac{M_{11}}{M_{10}}\right)^2}$$

$$p_b = \frac{M_{21}}{M_{20}}$$

$$q_b = \sqrt{\frac{M_{22}}{M_{20}} - \left(\frac{M_{21}}{M_{20}}\right)^2}$$

Comparing the results of a distribution-moment model with the full partial-differential equation model under reference conditions showed that the distribution-moment model can capture the qualitative features of the full model but that further tuning of the rate parameters is required. The diastolic diameter is very similar (165 μm in the original model and 162 μm in the distribution-moment model) whilst the systolic diameter is significantly larger for the distribution-moment model (142 μm) than the original muscle model (123 μm). This is due to weaker contractions in the distribution-moment model (peak cell force 2.1 dyne compared to 2.4 dyne) causing lower peak pressures (0.1 cmH_2O compared to 0.2 cmH_2O) and smaller outflow (peak value 0.09 mL/hr compared to 0.19 mL/hr and average value 0.01 mL/hr compared to 0.02 mL/hr). The suction-based refilling is also slower due to a reduced suction pressure amplitude (0.02 cmH_2O below the inlet pressure compared to 0.06 cmH_2O). These result in lower rates of work (0.05 erg/s compared to 0.02 erg/s) and energy transfer (0.0025 erg/s compared to 0.0053 erg/s) to the lymph. Additional work is required to calculate the energy liberation through hydrolysis of ATP in the distribution-moment model.

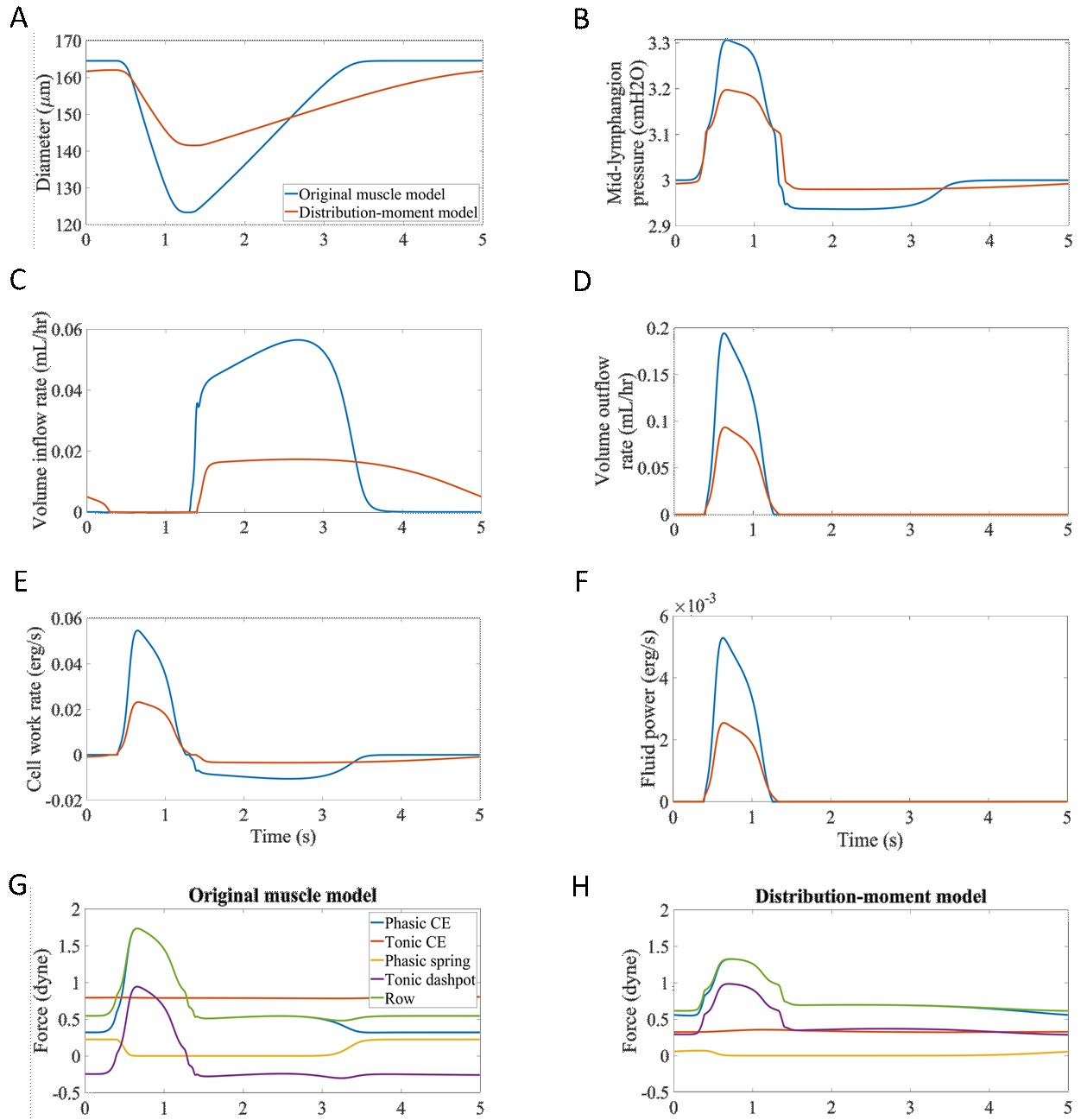


Figure 64: Comparison of the fully-resolved displacement-distribution of myosin heads with the Gaussian distribution-moment model (A) compares diameter (B) compares mid-lymphangion pressure (C) compares volume inflow rate (D) compares volume outflow rate (E) compares the work rate (F) compares the rate of energy transfer to fluid (G) shows the subcellular forces from the full model and (H) shows the subcellular forces from the distribution-moment model

APPENDIX 2 – PERMISSIONS DOCUMENTS FOR REPRINT

Order Date	02-Sep-2020	Type of Use	Republish in a thesis/dissertation
Order license ID	1060205-1	Publisher	ANNUAL REVIEWS
ISSN	1545-4479	Portion	Image/photo/illustration

LICENSED CONTENT			
Publication Title	Annual review of fluid mechanics	Rightholder	Annual Reviews, Inc.
Date	01/01/1969	Publication Type	e-Journal
Language	English	URL	http://arjournals.annualreviews.org/loi/fluid
Country	United States of America		

REQUEST DETAILS			
Portion Type	Image/photo/illustration	Distribution	Worldwide
Number of images / photos / illustrations	1	Translation	Original language of publication
Format (select all that apply)	Print, Electronic	Copies for the disabled?	No
		Minor editing privileges?	No

Who will republish the content?	Academic institution	Incidental promotional use?	No
Duration of Use	Life of current and all future editions	Currency	GBP
Lifetime Unit Quantity	Up to 499		
Rights Requested	Main product		

NEW WORK DETAILS			
Title	Multi-scale computer models of lymphatic pumping	Institution name	Imperial College London
		Expected presentation date	2021-01-01
Instructor name	Prof James Moore Jr		

ADDITIONAL DETAILS			
Order reference number	N/A	The requesting person / organization to appear on the license	Christopher Morris

REUSE CONTENT DETAILS			
Title, description or numeric reference of the portion(s)	Figure 2	Title of the article/chapter the portion is from	Lymphatic system flows

Editor of portion(s)	N/A	Author of portion(s)	Moore Jr., J.E. and Bertram, C.D
Volume of serial or monograph	N/A	Issue, if republishing an article from a serial	N/A
Page or page range of portion	461	Publication date of portion	2018-01-31

Lymphangiogenesis and lymphatic vessel remodelling in cancer

Author: Steven A. Stacker et al

Publication: Nature Reviews Cancer

Publisher: Springer Nature

Date: Feb 13, 2014

Copyright © 2014, Springer Nature

SPRINGER NATURE

Order Completed

Thank you for your order.

This Agreement between Chris ("You") and Springer Nature ("Springer Nature") consists of your license details and the terms and conditions provided by Springer Nature and Copyright Clearance Center.

Your confirmation email will contain your order number for future reference.

License Number 4862611296757

[Printable Details](#)

License date Jul 05, 2020

Licensed Content

Licensed Content Publisher	Springer Nature
Licensed Content Publication	Nature Reviews Cancer
Licensed Content Title	Lymphangiogenesis and lymphatic vessel remodelling in cancer
Licensed Content Author	Steven A. Stacker et al
Licensed Content Date	Feb 13, 2014

Order Details

Type of Use	Thesis/Dissertation
Requestor type	academic/university or research institute
Format	print and electronic
Portion	figures/tables/illustrations
Number of figures/tables/illustrations	1
High-res required	no
Will you be translating?	no
Circulation/distribution	30 - 99
Author of this Springer Nature content	no

About Your Work

Title	Multi-scale computer models of lymphatic pumping
Institution name	Imperial College London
Expected presentation date	Jan 2021

Additional Data

Portions	Figure 1
----------	----------

Requestor Location

Chris
21 Keswick Road

Requestor Location
London, Greater London Br4
9ar
United Kingdom
Attn: Chris

Tax Details

\$ Price

Total 0.00 GBP

Total: 0.00 GBP



Mechanobiology of lymphatic contractions

Author: Lance L. Munn

Publication: Seminars in Cell & Developmental Biology

Publisher: Elsevier

Date: February 2015

Copyright © 2015 Elsevier Ltd. All rights reserved.

Order Completed

Thank you for your order.

This Agreement between Chris ("You") and Elsevier ("Elsevier") consists of your license details and the terms and conditions provided by Elsevier and Copyright Clearance Center.

Your confirmation email will contain your order number for future reference.

License Number 4862610397677

[Printable Details](#)

License date Jul 05, 2020

Licensed Content

Licensed Content Publisher	Elsevier
Licensed Content Publication	Seminars in Cell & Developmental Biology
Licensed Content Title	Mechanobiology of lymphatic contractions
Licensed Content Author	Lance L. Munn
Licensed Content Date	Feb 1, 2015
Licensed Content Volume	38
Licensed Content Issue	n/a
Licensed Content Pages	8
Journal Type	S&T

Order Details

Type of Use	reuse in a thesis/dissertation
Portion	figures/tables/illustrations
Number of figures/tables/illustrations	1
Format	both print and electronic
Are you the author of this Elsevier article?	No
Will you be translating?	No

About Your Work

Title	Multi-scale computer models of lymphatic pumping
Institution name	Imperial College London
Expected presentation date	Jan 2021

Additional Data

Portions	Adaptation of Figure 3
----------	------------------------

Requestor Location

Requestor Location	Chris 21 Keswick Road London, Greater London Br4 9ar United Kingdom Attn: Chris
--------------------	---

Tax Details

Publisher Tax ID	GB 494 6272 12
------------------	----------------

\$ Price

Total	0.00 GBP
-------	----------

**Book:** Microcirculation in Chronic Venous Insufficiency**Chapter:** Dynamics of the Microlymphatic System**Author:** Zawieja , Kossmann , Pullin**Publisher:** Karger Publishers**Date:** Jul 1, 1999

Copyright © 1999, Karger Publishers

Order Completed

Thank you for your order.

This Agreement between Chris ("You") and Karger Publishers ("Karger Publishers") consists of your license details and the terms and conditions provided by Karger Publishers and Copyright Clearance Center.

Your confirmation email will contain your order number for future reference.

License Number 4862620433644

[Printable Details](#)

License date Jul 05, 2020

✓ Licensed Content

Licensed Content Publisher	Karger Publishers
Licensed Content Publication	Karger Book
Licensed Content Title	Dynamics of the Microlymphatic System
Licensed copyright line	Copyright © 1999, Karger Publishers
Licensed Content Author	Zawieja , Kossmann , Pullin
Licensed Content Date	Jul 1, 1999
Licensed Content Volume	23

📄 Order Details

Type of use	Thesis/Dissertation
Requestor type	student
Format	Print, Electronic
Portion	figures/tables/illustrations
Number of figures/tables/illustrations	1
Include Image file	no
Rights for	Main product
Duration of use	Life of current edition/presentation
Creation of copies for the disabled	no
With minor editing privileges	no
In the following language(s)	Original language of publication
For distribution to	Worldwide
With incidental promotional use	no
Lifetime unit quantity of new product	100

📄 About Your Work

Title	Multi-scale computer models of lymphatic pumping
Institution name	Imperial College London
Expected presentation date	Jan 2021

📄 Additional Data

Portions	Figure 3
The requesting person/organization	Christopher Morris



A model of a radially expanding and contracting lymphangion

Author: Elaheh Rahbar, James E. Moore

Publication: Journal of Biomechanics

Publisher: Elsevier

Date: 7 April 2011

Copyright © 2011 Elsevier Ltd. All rights reserved.

Order Completed

Thank you for your order.

This Agreement between Chris ("You") and Elsevier ("Elsevier") consists of your license details and the terms and conditions provided by Elsevier and Copyright Clearance Center.

Your confirmation email will contain your order number for future reference.

License Number 5105441482354

[Printable Details](#)

License date Jul 10, 2021

Licensed Content

Licensed Content Publisher	Elsevier
Licensed Content Publication	Journal of Biomechanics
Licensed Content Title	A model of a radially expanding and contracting lymphangion
Licensed Content Author	Elaheh Rahbar, James E. Moore
Licensed Content Date	Apr 7, 2011
Licensed Content Volume	44
Licensed Content Issue	6
Licensed Content Pages	7

Order Details

Type of Use	reuse in a thesis/dissertation
Portion	figures/tables/illustrations
Number of figures/tables/illustrations	1
Format	both print and electronic
Are you the author of this Elsevier article?	No
Will you be translating?	No

About Your Work

Title	Multi-scale computer models of lymphatic pumping
Institution name	Imperial College London
Expected presentation date	Sep 2021

Additional Data

Portions	Figure 1 of the original paper
----------	--------------------------------

Requestor Location

	Chris 21 Keswick Road
Requestor Location	London, Greater London Br4 9ar United Kingdom Attn: Chris

Tax Details

Publisher Tax ID	GB 494 6272 12
------------------	----------------

\$ Price

Total	0.00 GBP
-------	----------

A one-dimensional mathematical model of collecting lymphatics coupled with an electro-fluid-mechanical contraction model and valve dynamics

SPRINGER NATURE

Author: Christian Contarino et al

Publication: Biomechanics and Modeling in Mechanobiology

Publisher: Springer Nature

Date: Jul 14, 2018

Copyright © 2018, Springer-Verlag GmbH Germany, part of Springer Nature

Order Completed

Thank you for your order.

This Agreement between Chris ("You") and Springer Nature ("Springer Nature") consists of your license details and the terms and conditions provided by Springer Nature and Copyright Clearance Center.

Your confirmation email will contain your order number for future reference.

License Number 5106000447019

[Printable Details](#)

License date Jul 11, 2021

Licensed Content

Licensed Content Publisher Springer Nature

Licensed Content Publication Biomechanics and Modeling in Mechanobiology

Licensed Content Title A one-dimensional mathematical model of collecting lymphatics coupled with an electro-fluid-mechanical contraction model and valve dynamics

Licensed Content Author Christian Contarino et al

Licensed Content Date Jul 14, 2018

Order Details

Type of Use Thesis/Dissertation

Requestor type academic/university or research institute

Format print and electronic

Portion figures/tables/illustrations

Number of figures/tables/illustrations 2

Will you be translating? no

Circulation/distribution 30 - 99

Author of this Springer Nature content no

About Your Work

Title Multi-scale computer models of lymphatic pumping

Institution name Imperial College London

Expected presentation date Sep 2021

Additional Data

Portions Figures 2 and 7 of the original publication

Requestor Location

Chris
21 Keswick Road

Requestor Location

London, Greater London Br4
9ar
United Kingdom
Attn: Chris

Tax Details

\$ Price

Total 0.00 USD

Total: 0.00 USD



Integrated geometric and mechanical analysis of an image-based lymphatic valve

Author: Daniel J. Watson,Igor Sazonov,David C. Zawieja,James E. Moore,Raoul van Loon

Publication: Journal of Biomechanics

Publisher: Elsevier

Date: 7 November 2017

© 2017 Elsevier Ltd. All rights reserved.

Order Completed

Thank you for your order.

This Agreement between Chris ("You") and Elsevier ("Elsevier") consists of your license details and the terms and conditions provided by Elsevier and Copyright Clearance Center.

Your confirmation email will contain your order number for future reference.

License Number 5105360245674

[Printable Details](#)

License date Jul 10, 2021

☒ Licensed Content

Licensed Content Publisher	Elsevier
Licensed Content Publication	Journal of Biomechanics
Licensed Content Title	Integrated geometric and mechanical analysis of an image-based lymphatic valve
Licensed Content Author	Daniel J. Watson,Igor Sazonov,David C. Zawieja,James E. Moore,Raoul van Loon
Licensed Content Date	Nov 7, 2017
Licensed Content Volume	64
Licensed Content Issue	n/a
Licensed Content Pages	8

☐ Order Details

Type of Use	reuse in a thesis/dissertation
Portion	figures/tables/illustrations
Number of figures/tables/illustrations	1
Format	both print and electronic
Are you the author of this Elsevier article?	No
Will you be translating?	No

☐ About Your Work

Title	Multi-scale computer models of lymphatic pumping
Institution name	Imperial College London
Expected presentation date	Sep 2021

☐ Additional Data

Portions	Figure 2 from the original paper
----------	----------------------------------

Hill-Based Muscle Models: A Systems Engineering Perspective

Author: Jack M. Winters

Publication: Springer eBook

Publisher: Springer Nature

Date: Jan 1, 1990

Copyright © 1990, Springer-Verlag

SPRINGER NATURE

Order Completed

Thank you for your order.

This Agreement between Chris ("You") and Springer Nature ("Springer Nature") consists of your license details and the terms and conditions provided by Springer Nature and Copyright Clearance Center.

Your confirmation email will contain your order number for future reference.

License Number 5104900366417

[Printable Details](#)

License date Jul 09, 2021

Licensed Content

Licensed Content Publisher	Springer Nature
Licensed Content Publication	Springer eBook
Licensed Content Title	Hill-Based Muscle Models: A Systems Engineering Perspective
Licensed Content Author	Jack M. Winters
Licensed Content Date	Jan 1, 1990

Order Details

Type of Use	Thesis/Dissertation
Requestor type	academic/university or research institute
Format	print and electronic
Portion	figures/tables/illustrations
Number of figures/tables/illustrations	1
Will you be translating?	no
Circulation/distribution	30 - 99
Author of this Springer Nature content	no

About Your Work

Title	Multi-scale computer models of lymphatic pumping
Institution name	Imperial College London
Expected presentation date	Sep 2021

Additional Data

Portions	Figure 5.1 of the original publication
----------	--

Requestor Location

Requestor Location	Chris 21 Keswick Road London, Greater London Br4 9ar United Kingdom Attn: Chris
--------------------	---

Tax Details

Price

Total	0.00 GBP
-------	----------

Total: 0.00 GBP

[CLOSE WINDOW](#)

[ORDER MORE](#)



Perturbed Equilibria of Myosin Binding in Airway Smooth Muscle: Bond-Length Distributions, Mechanics, and ATP Metabolism

Author: Srboj M. Mijailovich, James P. Butler, Jeffrey J. Fredberg

Publication: Biophysical Journal

Publisher: Elsevier

Date: November 2000

Copyright © 2000 The Biophysical Society. Published by Elsevier Inc. All rights reserved.

Review Order

Please review the order details and the associated [terms and conditions](#).

No royalties will be charged for this reuse request although you are required to obtain a license and comply with the license terms and conditions. To obtain the license, click the Accept button below.

Licensed Content

Licensed Content Publisher	Elsevier
Licensed Content Publication	Biophysical Journal
Licensed Content Title	Perturbed Equilibria of Myosin Binding in Airway Smooth Muscle: Bond-Length Distributions, Mechanics, and ATP Metabolism
Licensed Content Author	Srboj M. Mijailovich, James P. Butler, Jeffrey J. Fredberg
Licensed Content Date	November 2000
Licensed Content Volume	79
Licensed Content Issue	5
Licensed Content Pages	15

Order Details

Type of Use	reuse in a thesis/dissertation
Portion	figures/tables/illustrations
Number of figures/tables/illustrations	1
Format	both print and electronic
Are you the author of this Elsevier article?	No
Will you be translating?	No

About Your Work

Title	Multi-scale computer models of lymphatic pumping
Institution name	Imperial College London
Expected presentation date	Sep 2021

Additional Data

Portions	Figure 1 of the original publication
----------	--------------------------------------

Requestor Location

Requestor Location	Chris 21 Keswick Road London, Greater London Br4 9ar United Kingdom Attn: Chris
--------------------	---

Tax Details

Publisher Tax ID	GB 494 6272 12
------------------	----------------

\$ Price

Total	0.00 GBP
-------	----------



The role of contractile unit reorganization in force generation in airway smooth muscle

Author: Brook, B. S.; Jensen, O. E.

Publication: Mathematical Medicine and Biology

Publisher: Oxford University Press

Date: 2013-01-28

Copyright © 2013, Oxford University Press

Order Completed

Thank you for your order.

This Agreement between Chris ("You") and Oxford University Press ("Oxford University Press") consists of your license details and the terms and conditions provided by Oxford University Press and Copyright Clearance Center.

Your confirmation email will contain your order number for future reference.

License Number 5095391271831

[Printable Details](#)

License date Jun 24, 2021

Licensed Content

Licensed Content Publisher	Oxford University Press
Licensed Content Publication	Mathematical Medicine and Biology
Licensed Content Title	The role of contractile unit reorganization in force generation in airway smooth muscle
Licensed Content Author	Brook, B. S.; Jensen, O. E.
Licensed Content Date	Jan 28, 2013
Licensed Content Volume	31
Licensed Content Issue	2

Order Details

Type of Use	Thesis/Dissertation
Requestor type	Educational Institution/Non-commercial/ Not for-profit
Format	Print and electronic
Portion	Figure/table
Number of figures/tables	1
Will you be translating?	No

About Your Work

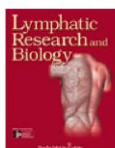
Title	Multi-scale computer models of lymphatic pumping
Institution name	Imperial College London
Expected presentation date	Jun 2021

Additional Data

Portions	Figure 3
----------	----------

📍 Requestor Location		📄 Tax Details	
	Chris 21 Keswick Road	Publisher Tax ID	GB125506730
Requestor Location	London, Greater London Br4 9ar United Kingdom Attn: Chris		
\$ Price			
Total	0.00 GBP		

Total: 0.00 GBP



Contractile Physiology of Lymphatics

Author: David C. Zawieja

Publication: Lymphatic Research and Biology

Publisher: Mary Ann Liebert, Inc.

Date: Jun 1, 2009

Copyright © 2009, Mary Ann Liebert, Inc.

Order Completed

Thank you for your order.

This Agreement between Chris ("You") and Mary Ann Liebert, Inc. ("Mary Ann Liebert, Inc.") consists of your license details and the terms and conditions provided by Mary Ann Liebert, Inc. and Copyright Clearance Center.

Your confirmation email will contain your order number for future reference.

License Number 5106630574427

[Printable Details](#)

License date Jul 12, 2021

Licensed Content

Licensed Content Publisher	Mary Ann Liebert, Inc.
Licensed Content Publication	Lymphatic Research and Biology
Licensed Content Title	Contractile Physiology of Lymphatics
Licensed Content Author	David C. Zawieja
Licensed Content Date	Jun 1, 2009
Licensed Content Volume	7
Licensed Content Issue	2

Order Details

Type of Use	CME Materials
Requestor type	academic
Format	print and electronic
Portion	charts/graphs/tables
Number of charts/graphs/tables	1
Translating...	no
Distribution quantity	100

About Your Work

Title	Multiscale computer models of lymphatic pumping
Client / Sponsor	Imperial College London
Expected presentation date	Jul 2021

Additional Data

Portions	Figure 4A of the original publication
----------	---------------------------------------

Requestor Location

Requestor Location	Chris 21 Keswick Road London, Greater London Br4 9ar United Kingdom Attn: Chris
--------------------	---

Tax Details

Billing Information

Billing Type	Credit Card
Credit card info	Visa ending in 3155
Credit card expiration	09/2022

\$ Price

Total	94.83 GBP
-------	-----------